CHALMERS
UNIVERSITY OF TECHNOLOGY

Design and Modeling of a Modular Payload Carrying Tethered Drone System

A Systematic Research and Design of a Modular Tethered Hexacopter Platform with System Modeling, Control, and Simulation

Master's thesis in Product development and Systems, control and mechatronics

OSCAR SCHYUM
FREDRIK NYGREN

DEPARTMENT OF ELECTRICAL ENGINEERING

CHALMERS UNIVERSITY OF TECHNOLOGY
Gothenburg, Sweden 2025
www.chalmers.se

Master's thesis 2025

Design and Modeling of a Modular Payload Carrying Tethered Drone System

A systematic research and design of a modular tethered hexacopter platform with system modeling, control, and simulation

Oscar Schyum
Fredrik Nygren

CHALMERS
UNIVERSITY OF TECHNOLOGY

Department of Electrical Engineering
Division of Systems and Control
Chalmers University of Technology
Gothenburg, Sweden 2025

Design and Modeling of a Modular Payload Carrying Tethered Drone System
A systematic research and design of a modular tethered hexacopter platform with system modeling, control, and simulation
OSCAR SCHYUM & FREDRIK NYGREN

Supervisor: Niklas Eisele & Jens Grönberg , Saab Surveillance
Examiner: Martin Fabian, Electrical Engineering

Master's Thesis 2025
Department of Electrical Engineering
Division of Systems and Control
Chalmers University of Technology
SE-412 96 Gothenburg
Telephone +46 31 772 1000

Cover: AI generated image of a hovering tethered hexacopter with payload black-boxes

Typeset in LaTeX
Printed by Chalmers Reproservice
Gothenburg, Sweden 2025

Design and Modeling of a Modular Payload Carrying Tethered Drone System
A systematic research and design of a modular tethered hexacopter platform with system modeling, control, and simulation
OSCAR SCHYUM & FREDRIK NYGREN
Department of Electrical Engineering
Chalmers University of Technology

Abstract

Unmanned Aerial Vehicles (UAVs) are currently employed in a plethora of applications, spanning both military and civilian sectors. A key limitation of conventional UAVs is their restricted flight time and operational range. Efforts to extend this range often come at the expense of reduced payload capacity. Tethered drones offer a promising solution to overcome these limitations, where power and communication are transmitted through a tether, allowing the system to achieve substantially longer flight times compared to conventional drones.

This thesis defines the capabilities and limitations of a tethered drone designed for high-capacity and modular payload applications. The system is constrained by predefined dimensions for the drone, ground base, and the upper and lower payload. The system is separated into different subsystems, each of which is investigated individually based on a series of research questions. Design decisions are based on the predefined constraints, along with additional requirements derived from a range of potential applications. Furthermore, a concept generation and evaluation phase is conducted, during which concepts are iteratively assessed through performance-based comparisons. A hexacopter with three-bladed foldable propellers, capable of landing in any yaw-angle, emerges as the most suitable solution. This concept offers additional margins in thrust compared to other viable solutions. This additional thrust can be allocated to increase acceleration, extend tether length, enhance payload capacity, or prolong untethered flight duration.

Following this, the hexacopter and tether are modeled using the Euler Lagrange method, with the tether modeled as a lumped mass model. The modeling, based on a comprehensive literature review, identifies the appropriate governing system equations and results in a coupled system of ADEs. The system is subsequently controlled using cascaded PID control and simulated in Simulink to validate the system design and to assess its performance in terms of stability, robustness and redundancy. Key performance metrics, including recommended tether tension, optimal payload distribution, and maximum operating time are also computed by means of simulation under various environmental conditions and payload variations.

Keywords: UAV, tUAV, drone, tether, hexacopter, propeller, payload, Euler-Lagrange, PID.

Acknowledgements

First and foremost, we would like to express our sincere gratitude to our supervisors at Saab, Jens Grönberg and Niklas Eisele, for their constant involvement, enthusiasm, and valuable support throughout the project. We would also like to extend our thanks to our examiner, Martin Fabian, for his guidance and support throughout this project, always being readily available to answer all of our questions and concerns. Additionally, to Emmanuel Dean for his support and insightful discussions regarding the model. A special thanks goes to our masters-thesis colleagues, Gustav Mosséen and Simon Nygren, for making our days at Saab even more enjoyable. Additionally, we would like to thank all of our amazing friends, families and loved ones, for supporting us during these past years, this would not have been possible without you. Lastly, we would like to express a special thanks to each other, for many pleasurable and rewarding moments over the past six months working on this project together, as well as throughout the previous years of our joint Chalmers journey.

Oscar Schyum & Fredrik Nygren, Gothenburg, June 2025

"For once you have tasted flight you will walk the earth with your eyes turned skyward, for there you have been and there you will long to return."

— Leonardo da Vinci *(attributed)*

List of Acronyms

Below is the list of acronyms that have been used throughout this thesis listed in alphabetical order:

ADE	Algebraic differential equations
BEMT	Blade element momentum theory
BET	Blade element theory
BLDC	Brushless direct current
CADAC	Computer aided design of aerospace concepts
CoM	Center of mass
COTS	Commercial off the shelf
DAE	Differential algebraic equation
DOF	Degrees of freedom
EMI	Electromagnetic interference
ESC	Electronic speed controller
FEM	Finite element method
FPV	First person view
FORJ	Fiber optic rotary joint
LMM	Lumped mass model
IMU	Inertial measurement unit
INS	Inertial navigation system
ISR	Intelligence, surveillance, and reconnaissance
MPC	Model predictive control
MT	Momentum theory
OASPL	Overall sound pressure level
ODE	Ordinary differential equation
PID	Proportional integral derivative
RMSE	Root mean square error
tUAV	Tethered unmanned aerial vehicle
UAV	Unmanned aerial vehicle
USV	Unmanned surface vehicle

Contents

List of Figures

List of Tables

1
Introduction

The following chapter provides a brief introduction to the thesis. The problem background is established, followed by the project's objectives. This includes a concise overview of the primary subsystems addressed in the thesis, along with the predefined dimensional constraints for both the payloads and the ground bound system base. Finally, the chapter outlines the limitations related to the project's scope.

1.1 Background

Unmanned Aerial Vehicles (UAVs) are constantly being subjected to extensive research and development, driven by their expanding role across a wide and growing range of applications. Until recently, the exploration and research of UAV technology have been predominately conducted for military applications, where benefits include the rapid and portable deployment capabilities, as well as effectiveness in challenging environments. These systems are employed primarily for intelligence, surveillance, and reconnaissance (ISR) missions, enabling real-time monitoring of enemy movements and assessments of potential threats. However, advances in technology have rendered UAVs more accessible and popular for civilian applications, where benefits include large coverage, modular payload capabilities and a high cost-effectiveness. Nevertheless, a key limitation of traditional UAVs are their restricted flight time and range. Efforts to extend the flight time often come at the expense of reduced payload capacity, since the battery mass increases, and vice versa. This highlights the present trade-off between endurance and payload versatility.

To overcome the present limitations in flight time, tethered drone system are being implemented. A tethered drone refers to a drone that is attached via a physical link to the ground or an object at all times during flight. Typically, power and communication are transmitted through the tether, allowing these systems to remain largely unaffected by the mentioned trade-off. With a continuous power supply, such systems can achieve substantially longer flight times, compared to conventional drones. An example of such a tethered drone system is shown in Figure 1.1. Meanwhile, as the tether drastically restricts the maneuverability of the drone, its specific characteristics provide other appealing benefits for a variety of use cases, spanning both military and civilian applications. The benefits of the tethered system varies accordingly. Military applications benefit from the system's ability to carry additional payload, since the battery weight is largely removed. The civilian applications leverage things such as the drone's extended flight time for continuous surveillance.

Figure 1.1: Elistair's tethered drone system, Khronos [1].

1.2 Project objectives

The principal objective of this thesis is to define the capabilities and limitations of a payload-carrying drone tethered to a base with an integrated power source. The allowed size of the drone and the ground base, together with the payload weight and dimensions are specified prior to the project, acting as constraints. The system can be considered physically larger than most existing tethered drone systems and should allow for a high payload capacity. Choices made regarding the system should ensure modular payload capabilities. The system will be designed and evaluated through an iterative product development process. The drone system will be separated into different subsystems, each of which will be investigated individually. Design decisions for these subsystems will be based on the predefined constraints, along with additional requirements derived from a range of potential applications. Following this, a concept generation and evaluation phase will take place, during which the concepts will be assessed through a theoretical performance-based comparison. The final drone concept will then be modeled, controlled and simulated, in order to validate the overall design, assess the fulfillment of certain requirements, and derive some of the specific capability and performance metrics.

1.2.1 Primary subsystems

In order to define these capabilities, possibilities and limitations, a set of primary subsystems are identified and considered in the development, each of which will encompass all the other subsystems further on in the development. The primary subsystems considered are the:

- *Drone* - The unmanned aerial vehicle (UAV) that the payload is mounted on. The drone receives its energy from the power supply through the tether. The drone itself consists of several subsystems, such as the chassis, onboard electronics, motors, propellers, etc.
- *Tether* - The cable that connects the drone to the base. It provides power and data transmission, as well as tensile strength, which enables constant tension for stability and counteraction against tether impulses, and contributes with resistance against breakage. Additionally, the tether serves as a controlled mechanism for retracting the drone.
- *Base* - The base houses the power supply that delivers energy to the drone via the tether, a winding mechanism for spooling and storing the tether, in addition to a landing platform and a ground control station.

1.2.2 Payloads

To maximize the modularity and versatility of the system, it has been considered advantageous to support payload mounting both above and below the drone. This enables a wider range of operational applications. Some restricting dimensions for the payloads have therefore been given in the form of two black-boxes denoted *upper payload* and *lower payload*, see Figure 1.2. The combined payload weight shall be at least 15 kg, with the flexibility to distribute this weight freely between the upper and lower payload.

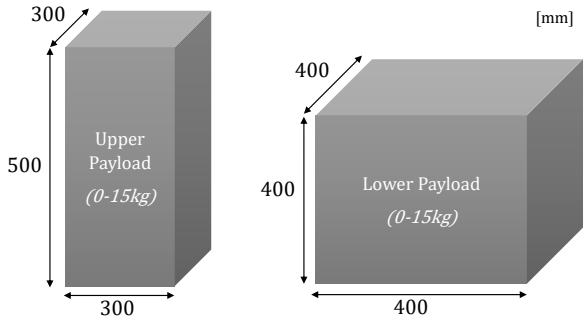

Figure 1.2: Upper and lower payload black-boxes.

1.2.3 System base

In addition to the payload black-boxes, some restricting dimensions for the *base* and the *drone* itself have been given, see Figure 1.3. The dimensions relating to the drone are associated with the dimensions during storage or transportation. Some measurements relating to the height of certain sections are set as optional, allowing for some degree of design flexibility. However, minimizing these dimensions is still deemed advantageous.

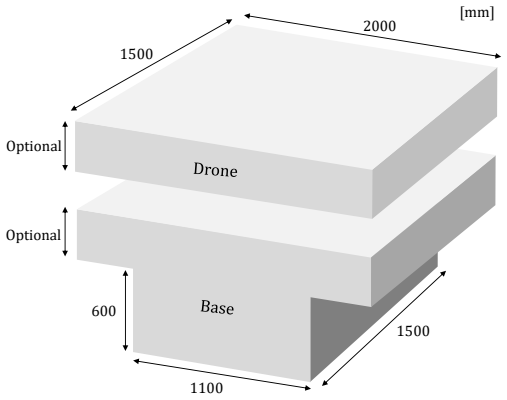

Figure 1.3: Base and drone dimensions.

1.3 Limitations

For this project, the focus will be on designing, dimensioning, and evaluating the drone solution at the system level. As such, specific components will not be examined in detail, except as references during the evaluation, elimination, and at the assessment of requirement fulfillment. The design process will involve specifying and defining the optimal properties of different subsystems, but no detailed design of any subsystem or the interface between the systems will be conducted, beyond in terms of assuring compatibility and estimating weight.

Some subsystems will be completely excluded from the investigation. These include the control station and the landing platform. Additionally, the chassis, including landing gear/feet and arms, together with the propeller protection, will only be considered in terms of estimated weight, its effect on the overall center of mass, drag, and moment of inertia. The specific design or the interfaces between the systems will not be considered. The design of the tether winding mechanism will only be considered in terms of spatial dimensions. No specific onboard electronics will be selected, instead they will be considered only in terms of estimated weight.

The development will be carried out on a theoretical level, involving several assumptions and estimations. Available product data will be used as references to compare and determine the capabilities of different concepts. The same approach applies to the modeling, control, and simulation of the system, where assumptions and simplifications will be made in order to keep complexity manageable, to enable a validation of the design. For instance, while the tether winch itself will not be modeled, the tension it generates will be incorporated into the model. Additionally, the drone's control system will be designed solely to enable simulation of the system, and will not be intended for use in a potential final product. The simulations of the system are also limited in terms of computational time, where a balance between the accuracy of the results and feasible simulation times is desirable.

2
Application and system analysis

The following chapter examines potential applications for this modular system, categorized into both civilian and military. Based on these applications, customer needs are identified, and together with requirements provided directly by Saab, a requirement specification list is constructed, aiming to guide the development of the system. To address the requirements, key subsystems are identified, including their individual functions within the overall system, along with their interaction with one another. This analysis establishes a structured basis for the detailed subsystem research presented in the subsequent chapter.

2.1 Customer and stakeholder identification

Usually in the planning stage of product development work, customers and stakeholders are identified prior to performing a customers needs analysis. This is crucial in order to allow the creation of a solution aligned with the latent needs of the customers. However, as stated, this system is supposed to have modular payload capabilities, and therefore the project does not consider specific payloads, and in turn specific applications or customers. Saab could be considered a customer, especially since some needs and requirements come directly from them, as seen in Section 1.2. However, the secondary customers, who would be the end users of the product and whose needs are of the greatest interest, remain unidentified.

For this reason, no qualitative or quantitative methods, such as interviews or surveys, could be used to identify any customer needs, beyond those already proposed by Saab. Instead, these needs were derived from an analysis of the system's potential applications. These were identified through existing literature, in addition to prior Saab knowledge and research, and dialog with internal company parties.

2.2 Applications

The project aims, as stated, to explore a drone system with modular payload capabilities, which would naturally support a plethora of applications in both civilian and military sectors. Given its versatility, it is essential to consider a variety of potential applications and the specific needs and requirements they bring. The following are some identified, already available applications of such a system, based on existing literature, as well as additional applications identified through Saab's prior

knowledge, and discussions with internal company stakeholders. Due to the systems modularity, the applications are not merely limited to those mentioned here.

2.2.1 Civilian applications

Civilian applications are numerous and span a wide range of industries. While the specific use cases may differ, many of the underlying needs and requirements generally remain consistent across applications.

2.2.1.1 Temporary communication

One identified application is the use of tethered drones for temporary communication, with for example a 5G antenna as payload. Tethered UAVs could be used to extend the coverage of telecommunication networks for temporary situations, such as during disasters where normal telecommunication infrastructure is compromised, or at public events where network demand temporarily exceeds normal capacity [2].

Relay in disaster areas
A number of different natural disasters, such as hurricanes, earthquakes, tornadoes, floods or severe snowstorms can in multiple cases result in devastating consequences for telecommunication infrastructures [3], [4]. Similarly, damage due to malicious attacks could yield the same severe results [5]. If the existing cellular base stations and ground communication infrastructure were compromised, due to damage, or them even being destroyed, the communication network could be significantly overloaded [4]. Therefore, there is a growing demand for the ability to temporarily boost wireless network communication in a large area when infrastructure has failed. This capability is crucial to ensure, among other things, public safety communication, with the ultimate goal of saving lives [4]. Replacing telecommunication ground base stations with an UAV is a viable, fast and flexible solution for these situations [3].

Conventional untethered UAV communication has two main drawbacks. Firstly, the UAV inherits a limited battery power supply, and therefore a limited flight time, which becomes a huge constraint in the case of network infrastructure collapse. Most current UAVs can only operate for an hour maximum, leading to the need for frequent ground visits for recharges [6]. This temporarily leads to loss of the coverage that was provided by the UAV. Moreover, an UAV also requires an extra wireless backhaul link to connect users to the core network [3], [7]. A tethered system could be the critical solution for providing the required power to the UAVs. This solves the problem of limited battery lifetime, enabling the possibility of flight times of up to multiple days [6]. This while still maintaining quick and flexible deployment and fast data transfer, due to the enabling of connection directly to the core network [3], [7]. A tethered drone could also be designed to support heavier payloads [3], since the need for carrying extra battery weight is obsolete. Additionally, the motor power demand is not as limited as for a non-tethered drone. Numerical results show that a tethered UAV, compared to an untethered UAV, has an increased coverage performance when its tether length is above 75 m (where an increased altitude results in increased coverage). This is true under the assumption that the untethered UAV

is has an availability of 80% due the limitations of the battery [7].

Communication spike due to public events
In the situations where an public event temporarily increases the network demand in specific geographical areas, UAV assisted communication can offer a near instant and cost-efficient solution to offload some of the traffic in a reliable way [7]. Examples of this can be public events, including concerts, and sports matches etc. where an increased data demand can be expected prior to the event.

It is apparent that a product that could be used in these applications have a great need for long continuous flight times, which also means that the maintenance should be sparse, and quick to perform. It would be beneficial to have a long tether for larger coverage. Having fast deployment and retraction capabilities in disaster areas are of great significance, along with a flexibility in the deployment. This is including both an ease of transportation, and the ability to deploy the drone from uneven terrain. For safety reasons, there is a great need for system redundancy. This refers to both redundancy in the case of motor failures, and the inclusion of backup systems onboard, like a backup battery in case power from the tether is lost. The propeller should also be protected, for both the safety of people and the drone itself. For these applications there is also a need for the drone to operate in, and withstand harsh weather and other challenging environments. Generally, the price is also an important factor, since multiple drones might need to be used for larger coverage.

2.2.1.2 Continuous surveillance at large public events

In addition to using tethered drones to handle communication spikes due to public events, another application could be the usage of tethered drones for public surveillance at these large events. In the modern fast-paced world it has become an increasingly complex challenge to ensure the safety of public events. A tethered drone system could provide huge advantages when it comes to real-time monitoring, crowd control, and rapid response capabilities. The bird's eye of view of a tUAV could allow it to cover large areas efficiently. The modular payload capabilities of the proposed tethered drone could allow for the mounting of various equipment that could be used for this surveillance, including high-definition cameras, night vision cameras, thermal imaging sensors, along with other advanced sensors. This could ensure coverage of the monitored event regardless of the time of day. It would be beneficial to be able to use this modular platform, rather than relying on fixed installations that quickly become outdated or may not meet the right needs.

This continuous surveillance could allow security personnel to respond quickly to potential threats and incidents, such as crowd disturbances or suspicious activities. The ability to respond fast plays an important role in maintaining order and keeping a high level of security at large events [8]. The system could also be used to ensure that emergency exits are unobstructed at all times. The key benefit of this tethered system, over a traditional non-tethered drone, is still the possibility to perform continuous surveillance. There are a number of real-life examples where tethered systems have played important roles, such as at a Guns N' Roses concert, where

these were used for surveillance and event security [8].A modular system could also potentially allow for the simultaneously fitting of these cameras for event surveillance and the previously mentioned communication antennas.

By looking at this application, it becomes clear how changing the payload can greatly amplify the number of use cases. Therefore, allowing for modular payload capabilities, with regards to weight, size, and placement, is an important need. For the usage at public events, it is of great importance for the system to be as quiet as possible, in order to not disturb the people around it, or draw too much attention away from the event in question. This is in particular true at events that themselves do not emit much sound (contrary to e.g. the mentioned rock concerts).

2.2.1.3 Other civilian applications

Other civilian applications of a tethered drone system are for example monitoring of traffic [9]. In this application sensors can offer an aerial view of the traffic, that can help authorities to efficiently identify and act on incidents, or allow for the monitoring of traffic density and its flow patterns. The tethered drone could also be used in police operations, where its continuous surveillance of a target area could allow for real time coordination of tactical responses to hostile situations [10]. Equipping the drone with thermal imaging could also assist in the monitoring of building fires and forest fires. This could assist the fire brigade in the allocation of resources, and help keeping responders safe [10]. The platform could also be used for maritime security applications. The drone could increase the line of sight, and provide surveillance and detection of e.g. illegal fishing, illicit drug and migrant trafficking, and surveillance over vessels that could be deemed as suspicious [11]. It could also be used for search and rescue operations, utilizing its bird's eye view. Other things include infrastructure inspection (of bridges, harbors etc.), and environmental monitoring [11]. All maritime UAV applications could greatly utilize the tether for easier and more reliable landings. This is because the need to track a (moving) boat whilst landing, is rendered obsolete, when you can retract the drone by pulling the tether.

As intended, the applications of a tethered drone system with modular payload capabilities are, as can be seen, nearly endless. These mentioned applications also reinforce the need for modular payload capabilities, fast deployment, among other things. A lot of the needs from the different potential stakeholders tends to be similar between the cases. Some needs could also be derived generally from all applications. It would for example be beneficial to minimize the heat development in the system, in order to minimize energy loss, and minimize the IR-image (for stealthiness in police operations). Since the product is aimed for development by, or in association with Saab, there should be an overall high durability and reliability, to meet the existing Saab quality standards. The tether component that is performing the information exchange should be free from disturbances , have a high data transfer speed, and be reliable. If the focus is directed towards the system's main functionality, and the mentioned applications, the system could be regarded as merely an elevator, aimed to raise payload. Therefore, there is a greater need for z-direction maneuverability, compared to maneuverability in the xy-plane.

2.2.2 Military applications

Due to the secrecy of the conducted work, no specific military applications will be disclosed in any specific detail. However, it could be argued that military applications would benefit from all of the same requirements and needs as discussed in the civilian applications above. These are things such as fast deployment, long flight time, low maintenance, modular payload capabilities (weight, size, placement), high flight altitude, redundancy, etc.

2.3 Customer needs list

Given the system's modular payload capability and the absence of a specific defined end-user application, customer needs have not been gathered through direct interaction with specific users. Instead, they have been derived from an analysis of potential applications identified through literature, internal Saab knowledge, and stakeholder discussions. Although the motivations behind certain needs may vary across applications, the needs themselves are recurring and overlapping. All identified needs are presented in Table 2.1.

Need	**Motivation**
Modular payload capabilities	Weight, size, placement Allow a wide range of applications
Long flight time/low maintenance	Continuous operation
Tether length above 75 m	Larger coverage
Fast deployment/retraction	In disaster areas
Flexibility in deployment	Ease of transportation and deployment from uneven terrain
Quiet	To not disturb
Redundancy	Safety
Backup systems	Eg. backup-battery, for safety
Protected propellers	Safety
Operable in harsh environment	Operate in & withstand harsh weather and other challenging environments
Cost-effectiveness	Enable usage of multiple for larger coverage, increased accessibility
Minimize heat development	Minimize energy loss, and IR-image
Meet Saab quality standards	Durability and reliability in unity with present product range
Disturbances free information exchange	Safety
Light, reliable, high speed data transfer	Not limit payload Improved range of usage
Great maneuverability in z-direction	Perform within its main functionality
Maneuverability in xy-plane	Increase maneuverability and stability

Table 2.1: Customer needs list based on mentioned applications and other general system considerations, together with a short motivation for the respective need.

2.4 Requirement specification

In order to make full use of the identified customer needs, a requirement specification is created, utilizing these stated needs. Some requirements are also directly given by Saab, such as the payload weight and dimensions, and the limitation in dimensions during transportation, see sections 1.2.2 and 1.2.3. The creation of the requirement specification list aims to guide the development work, by providing clarity in what should to be addressed, as these requirements are what will dictate the design of the system.

Some of the categories in the requirement specification were directly derived from the customer needs. This was complemented with other categories that were found relevant from a predefined checklist proposed by Pugh [12]. This ensured a wide range of requirements, and allowed for a broader consideration of the entire system. However, because of the limitations of the project, and the project aim, certain requirements are neglected and will not be addressed. These requirements are more closely associated with a finalized product, where the level of detail extends down to individual components or specific detailed designs. The requirements that are outside of the system level are requirements regarding testing, installation, and aesthetics. Due to the complexity of the product, an emphasis is set on an limited number of requirements relating to the key issues of the problem being addressed. These are what mainly guides the development, and are summarized in the list below. The complete requirement specification is given in Appendix A.

1. The system, including the generator and tether, must be able to be safely transported within given dimensions
2. The tether must have a length greater than 70 [m]
3. The system must have modular payload capabilities, where it must be able to carry a top mounted and bottom mounted payload of given dimension, and a given combined payload weight
4. The system must have great maneuverability in the z-direction
5. The system must be designed with redundancy, such that it is operable with loss of one motor
6. Backup systems, such as an onboard battery, must be present
7. The propellers must be protected
8. The tether must allow for disturbance free and high speed information exchange, and provide sufficient power to payload
9. The system must be able to get power supplied from a (COTS) power supply
10. The system should give away minimal noise
11. The system must be operable in harsh environments
12. The system must have fast deployment and retraction capabilities, and be deployable from and be able to land on uneven terrain
13. The drone must fit within the given dimensions in one direction while landing

2.5 Subsystem identification

To meet these requirements, the system's compliance with the stated criteria will primarily be investigated on the subsystem or system level, as opposed to on a detailed component level. Therefore, these subsystems must be identified so that they can be researched individually, with the ultimate goal of ensuring that the system meets the requirements. However, some of these subsystems might ultimately consist of just a single component.

The subsystems are derived from research, such as online resources, knowledge gathered during the application analysis, and the creation of the customer needs list and requirement specification. Although there are variations between different types of drones, most of the components are common and essential for the proper functionality of the drone system. The following components are considered relevant and are present in the tethered-drone system that this project aims to design and analyze. The main parts of the tethered drone system is the drone itself, the tether, and the ground base, see overview in Figure 2.1.

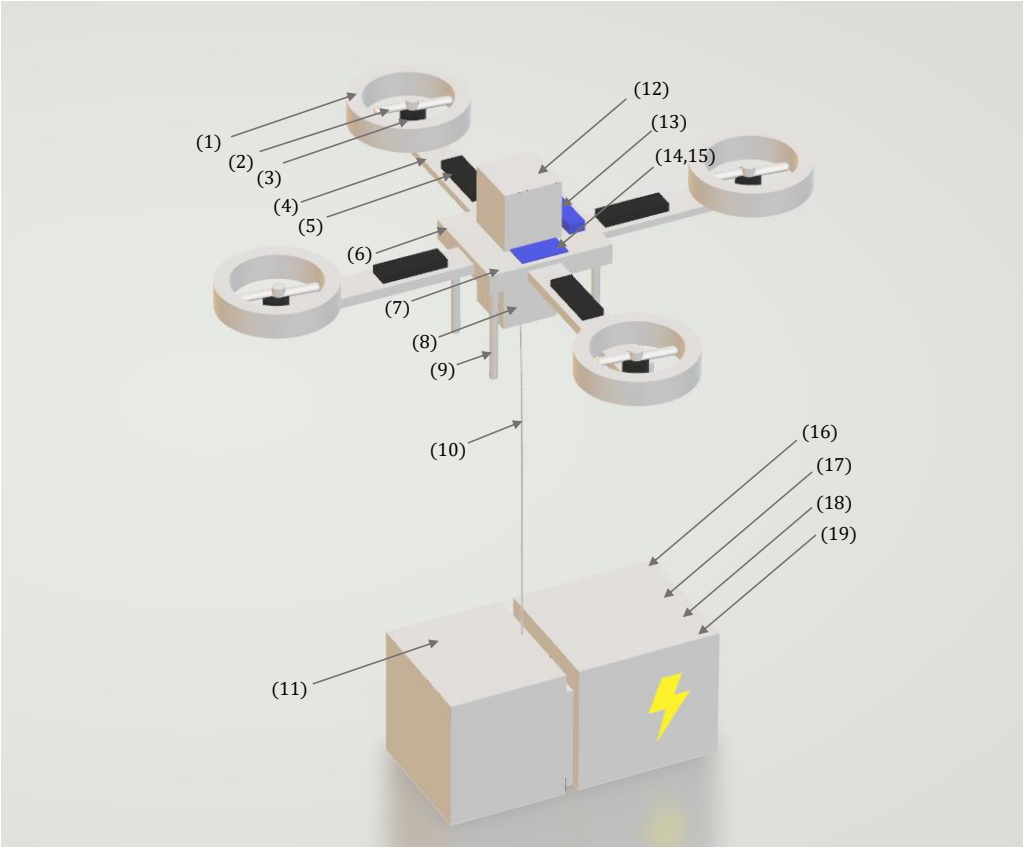

Figure 2.1: Overview of general drone subsystems/components. Illustrated with a quadcopter, but the number of rotors does not affect the constituent components.

All components of the drone are held together by a main chassis or frame (6). There are different types of drone frames (all with their own advantages), which mainly correspond to different geometric form [13]. The drone arms (4) are attached to the

main chassis and serves to support the motors. In some cases they are a part of the main chassis, but are here considered separately. The motors (3) are what generates rotation of the propellers, and the propellers (2) are in turn what generates the thrust and lift of the system [14]. Electronic speed controllers (ESCs) (5) adjust the speed of the motors. These are usually attached to the arms or chassis directly. One or several DC-to-DC converter(s) (7) regulate the voltage given to the ESCs. A flight controller (14) sends instructions regarding how the ESCs should control the motors in order to perform a given task. The flight controller can be considered the brain of the drone [15], and gets input from components such as the IMU (15). The IMU (Inertial Measurement Unit), estimates the acceleration and orientation of the drone. A backup battery (13) aims to provide power to the system if the main power supply (through the tether) were to be interrupted. Both the converters and battery are attached to the chassis. Propeller protections (1) are placed on the arms. The payload itself could also be considered as a part of this tethered system, which is placed on the chassis, either on the top (12), bottom (8), or a combination of the two. Drones also contain some kind of landing gear or feet (9) to safely take off and land without damaging the drone or payload.

The tether (10) provides power to the airborne system, along with transferring data, to and from the drone. In addition to this, the tether also functions as a fast and controlled means of landing by pulling the tether while the drone keeps the tether in tension. Furthermore, by keeping a constant tension in the tether flight stability is increased. The tether attachment point affects the stability of the system, where keeping it as close as possible to the CoM is beneficial.

A separate ground base houses the power supply (16), which is from where the power for the system originates. This power passes through an AC-to-DC (17) converter before being fed through the tether [16]. The base also houses the landing platform (18), which could serve both as a means for the drone to land safely and as protection for the drone during transportation. A control station (19), that controls, and processes the data from the drone is also a part of the base. Additionally, the base contains a tether-winding mechanism (11), which provides landing capabilities by pulling the drone down, and also maintains cable tension in order to stabilize the flight.

2.5.1 Functional description

It is beneficial to create a visualization over the system and its subsystems in order to get an better overview over how the different parts are connected. This can be done by creating a functional description, through functional modeling. One strategy of conducting functional modeling, is by using function-means modeling. Here the system is broken down into its basic functions and the corresponding means that can realize that function [17]. Functions-means modeling is useful for both transforming and purpose functions, compared to something like a process (flow) model, which is mainly used for transforming functions.

Usually multiple means for the same functions indicate multiple alternative means to implementing a function, described by Malmqvist [17]. In this model, multiple means for the same functions instead describes the different parallel means needed to implement a function. Multiple functions for one mean, indicates that there are a number of necessary functions due to the chosen mean.

To create this model, the research that was conducted during the subsystem identification, was used to identify the different means. Brainstorming was used, together with the the requirement specification, to derive different necessary functions. The main function, raise payload, is derived directly from the aim of the project. The function-means modeling is shown in Figure 2.2.

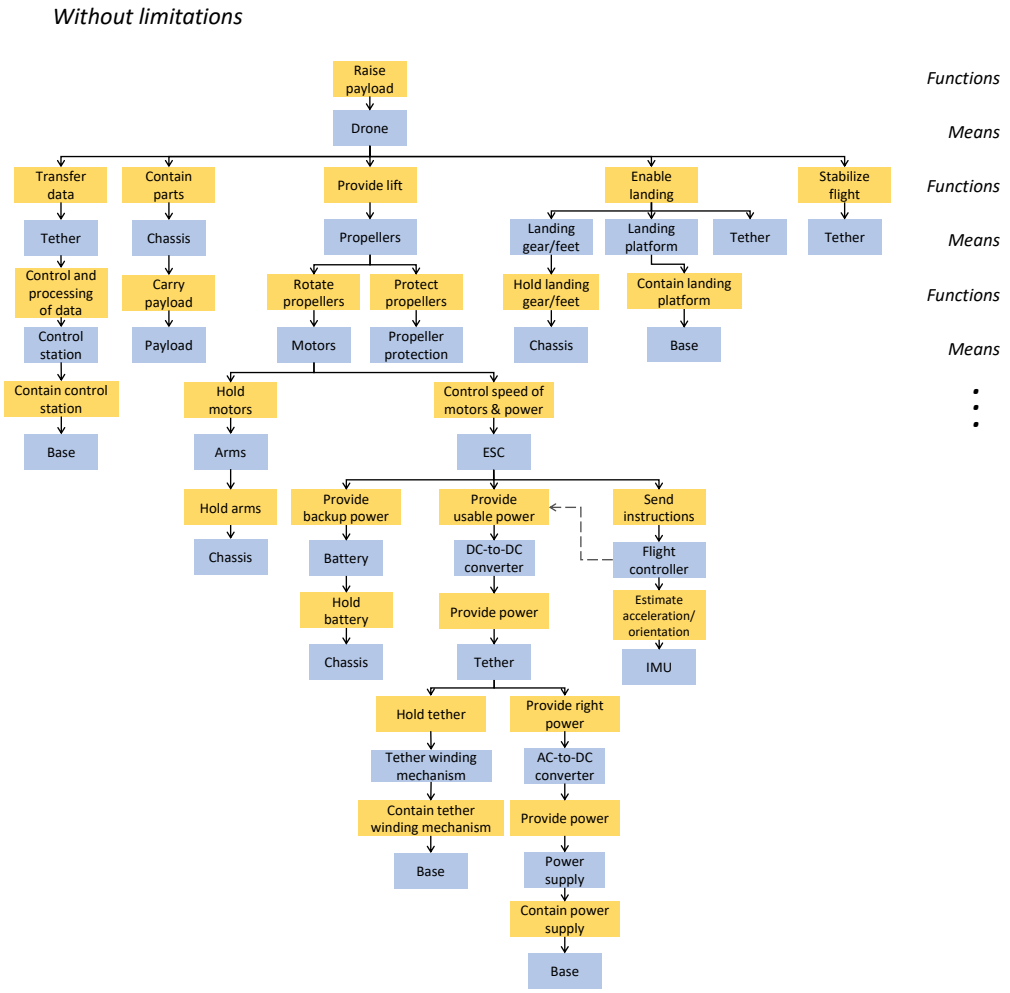

Figure 2.2: Function-means modeling of the system, without limitations.

In this function-means model, all the identified subsystems, and their connections, are displayed. To show the limitations of the project, a version of this function-means model was created to clarify which subsystems that are deemed most relevant to the project scope and given limitations, see Figure 2.3.

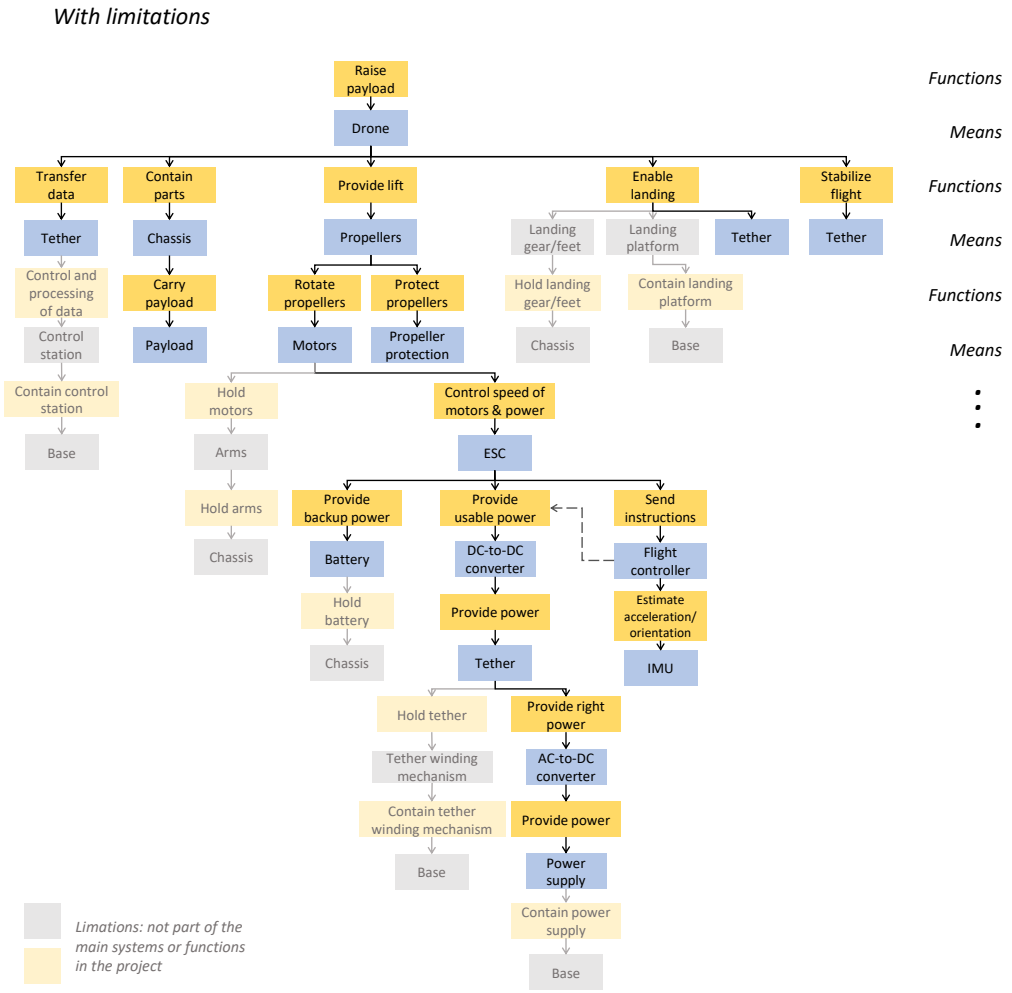

Figure 2.3: Function-means modeling of the system, with limitations.

The most relevant subsystems are the ones that will undergo the most detailed research in following chapters. Parts that are deemed as not part of the main systems or function in the project, will still to some degree be considered, but mostly regarding the way they affect the main systems. For example, the *tether winding mechanism* is something deemed outside the scope of the project, but will still be considered, as it effects the dimensions of the *base* and therefore the dimensions of the drone, see the requirement specification in Appendix A. For this reason, an estimate of its size will at least have to be made. The power supply is also contained inside the base, and will be similarly considered in terms of size. However, this will also have to be further investigated, since it effects the power input to the system. The chassis, arms, and landing gear/feet of the drone will be considered in terms of estimated weight (and CoM), drag, and moment of inertia, but not their exact design or the interfaces between them.

3
Detailed subsystem research

In this chapter, a detailed research into the different subsystem will be conducted, with the aim to discover how the design, dimensioning and choices relating to the different subsystems affect the system and its performance, with relation to the requirements stated in the requirement specification, see Appendix A. The research will focus on each subsystem independently, and be guided by a number of research questions. Some research questions might touch upon eventual trade-offs and compatibility between the different subsystems. The questions will be answered based on research of various sources of literature.

The main systems that have to be researched can be seen in the function-means model of the system, see Figure 2.3. These are the *motors*, *propellers*, and *tether*. The motor is divided into the *motor configuration* which relates to the number of motors and their placement, and the *motors* themselves. Other subsystems such as the power supply, backup battery, ESC, flight controller, IMU, and propeller protection, will be considered mainly in terms of weight, together with their effect on the overall system performance, and their compatibility with the other systems.

3.1 Motor configuration

The drone motors provide the lift and control necessary for the drone system to fly. Drones can be found with different numbers of motors, and with different motor placements. This affects the stability, load capacity, efficiency, redundancy, and maneuverability of the system. Each motor is driving a rotor, but sometimes no distinction (between motor and rotor) is made. Some drones have arms of different length, rotors placed on different heights, or multiple rotors operating in the same rotational axis. The following is an investigation based on a number of research question that aim to determine how the number of rotors, and their configuration influence the performance of the system.

- How does the number of rotors affect the system's performance?
- How does the placement of the rotors affect the performance (unevenly/evenly spaced, equal/non-equal arm length)?
- How does a coaxial configuration affect the performance of the system? What is the affect of z-direction separation?

3.1.1 Number of motors

UAVs can usually be categorized into different types, such as quadcopters (4), hexacopters (6), octocopters (8), and so forth, based on the number of rotors they contain, see Figure 3.1. A general term is *multirotor*, but that typically refers to drones with more than four rotors [18].

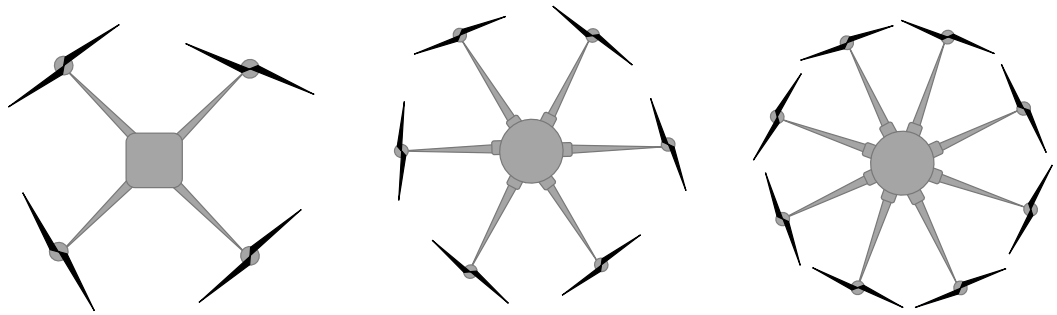

Figure 3.1: From left to right: quadcopter, hexacopter, octocopter.

Quadcopter
A quadcopter has four rotors. This is what can be referred to as the "classic" drone, because of its commercial popularity that is due to its maneuverability, simplicity and stability. The quadcopters have a comparably simpler design with their fewer number of motors, and are also lighter, which makes them agile. However, this simultaneously limits their lifting capacity [18]. Thanks to the lower number of motors, quadcopters are also normally cheaper than their higher motor counterparts [19]. One drawback of a quadcopter is that it has no redundancy, meaning that there is no allowable points of failure. If one motor stops working, the drone cannot maintain a controlled flight and will crash [20].

Hexacopter
A hexacopter has six rotors. Usually this achieves increased stability and payload capacities [21], due to the higher number of motors. Due to this, the power consumption increases, compared to a quadcopter [21]. In a hexacopter at least one rotor can also be considered redundant [20]. This means that it can maintain a relatively controlled flight in the case of a motor failure, which should enable a safe landing.

Octocopter
An octocopter has eight rotors. This enables it to lift even heavier payloads due to the increased thrust produced by the additional motors (if no limits in size are present). However, this also leads to additional power consumption. An increase in the number of motors also lead to an increased weight, from the motors themselves, but also from more propellers, ESCs, and a larger frame (due to more arms, and

housing of more components). Octocopters inherit a high level of stability and redundancy, which makes them suitable for demanding applications. In a octocopter, at least one rotor can be considered redundant. This should maintain a even more controlled flight with one motor failure, compared to the hexacopter.

A drone with an odd number of rotors, such as tricopters (3) or pentacopters (5), lack the paired propellers that the above mentioned configurations benefit from. This means an increased complexity in the yaw mechanism, which makes them harder to control. In addition to this, the tricopters lack thrust with their few number of rotors, and therefore struggles to support larger weights [20].

Generally, for a rotary wing aircraft, when the number of rotors increase, so does the disk loading ratio (the ratio between the weight and the rotor disk area). Having a low disk loading increases the rotor efficiency, through a minimization of the velocity change of the air that passes through the rotor [22]. This can be illustrated by considering a single-rotor helicopter, which achieves a very low disk loading and, therefore, a high rotor efficiency. With an increase in rotors, the drone's footprint usually also increases [23]. However, there is a limiting factor given in this project relating to the drone and the base dimensions. Therefore, an analysis is conducted that is specifically connected to these geometrical limitations, where the theoretical maximum rotor diameter and rotor (sweep) area is calculated. Since the rotor area is one of the main things that affects the thrust, see Section 3.3.2, this is considered relevant to investigate.

3.1.1.1 Area analysis

The area analysis looks at the maximum rotor diameters and rotor areas based on the different number of rotors, and different *configurations* that the motors could be placed in. The configurations relate to different design choices, such as if the propellers are foldable or not, or if the drone should be able to land in any yaw angle or only a specified few. To be clear, it might not be optimal to maximize the rotor area within the given dimensions. A smaller rotor area might be found sufficient for the required payload weight, and other trade-offs are perhaps more important. However, this is not the focus here. Instead it is of relevance to see how the individual propeller size, and maximum area differs between the different number of rotors and the different configurations, and also which are using the available space most efficiently.

Since this section only focuses on the number of motors and how that affects the performance of the system, some assumptions will be made in this analysis. For each configuration with a respective number of rotors, all arms are assumed to be of even length, such that all rotors are placed at an equal distance from the center of the drone. All rotors are evenly spaced, and all propellers are of uniform size. The arms are also assumed to be fixed, meaning that they can not be folded. The mean position between the rotors must also be the position of the drone center. Another research question related to the motor configuration is an analysis of how a coaxial configuration (where two rotors operate in the same rotational axis) affects the performance of the system. Because of this, all rotors in this analysis will be

assumed to be limited by the largest, bottom mounted payload, to enable the usage of the same areas for the coaxial configurations if that were to be relevant. Since the calculations are of the theoretical maximum area, it is also assumed that there are no margins between parts (propellers-propellers and propellers-payload). Propeller protection and motors are considered infinitely thin. Therefore, in actuality, the area for all of these configurations are smaller than initially stated here.

Configurations
The analysis will consist of different *configurations*, which will be combined with the different amount of rotors (four, six, or eight). These configurations all have their unique characteristics, which are explained below.

- **Non-limited configuration** acts as a reference, where the propeller area is maximized given the payload and base dimensions, without further restrictions, see Figure 3.2.

- **Configuration 1** maximizes the area given the payload and base dimensions. Additionally, the area is limited by requirement R14.2 (see Appendix A), that the size of the drone is restricted in positive y-direction when landing. Recall that the non-limited configuration, see Figure 3.2, is an example when this is not the case. The propellers are also assumed to be foldable, and the drone can only land in a specific yaw angle.

- **Configuration 2** maximizes the area given the payload and base dimensions, with addition to the restriction in positive y-direction when landing (R14.2). The propellers are assumed foldable, and the drone can land regardless of yaw angle.

- **Configuration 3** maximizes the area given the payload- and base dimensions, with addition to the restriction in positive y-direction when landing (R14.2). The propellers are assumed non-foldable. It is deemed of interest to investigate the maximum area without foldable propellers. Since it might be complicated and time-consuming to fold propellers and remove propeller protection, based on requirements R12.1 and R12.3 (fast deployment and retraction capabilities, see Appendix A). Configuration 3 only allows the drone to land in a specific yaw angle.

- **Configuration 4** maximizes the area given the payload and base dimensions, with addition to the restriction in positive y-direction when landing (R14.2). The propellers are assumed non-foldable, and the drone can land regardless of yaw angle.

Quadcopter: Non-limited configuration
This is an example of a quadcopter with maximized propeller area given the payload and base dimensions, that is not restricted within the positive y-direction (as per requirement R14.2), see Figure 3.2. The red lines indicate the area that is outside of the usable directions whilst landing. Therefore, this will not be further considered, and all upcoming configurations will be restricted within the base dimension in this direction. Since only even length arms and evenly spaced rotors are considered in this stage, the dashed square represents the drone, and the light gray circle is where all the rotors are placed. The multiple (dark) dashed circles represent the rotor area. The light gray rectangle represents the system base (which as stated includes the landing platform, power supply, tether winding mechanism, control station, etc.). The dimensions of the base, and the payload black-boxes can be found in the requirement specification, Appendix A.

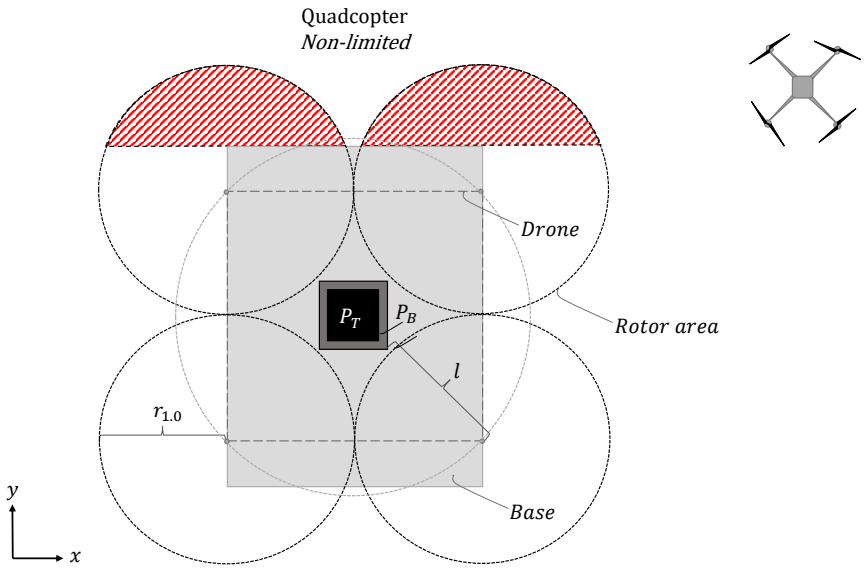

Figure 3.2: Non-limited (reference) configuration. The figure shows a quadcopter with some rotor segments outside of the usable dimension. For $l > r_{1.0}$, the propellers limit themselves before being limited by the payload.

The shortest distance between a rotor center and a payload black-box is denoted l. This is used to evaluate if the propeller sizes are limited by themselves or by the payload. P_B is the bottom payload black-box, and P_T is the top payload black-box. The radius of a propeller is denoted $r_{a.b}$, where a relates to if it is a quad-, hexa-, or octocopter, whilst b relates to the configuration used (note that a $b = 1$ is not always Configuration 1, but instead just the first configuration considered with that number of rotors, as will be the case for the hexa- and octocopter, since multiple configurations are the same). In this example, the propeller size is limited by the propellers themselves, before being limited by the payload black-boxes.

Quadcopter: Configuration 1

A quadcopter with maximized area in Configuration 1 is shown in Figure 3.3, left. For Configuration 1 the propellers are assumed to be foldable. It can be noted that even if they were not foldable, the propellers could still be inside the base dimensions if they had only one blade that could be rotated in place. Representing the rotors as circles ensures that all blades are guaranteed to be inside, for the non-foldable configurations 3 and 4, regardless of the number of blades. A quadcopter in Configuration 1, has its propeller size limited by the payload black-box dimensions, and not the other propellers. A trigonometric expression for the rotor radius $r_{1.1}$ was derived, and by leveraging the knowledge regarding the limiting payload and base dimensions it could be numerically solved in Matlab. The radius was calculated as:

$$r_{1.1} \approx 566.548\ mm.$$

The theoretical maximum area for one rotor, and the total theoretical maximum area for all four rotors combined for this quadcopter configuration is:

$$A_{1.1} \approx 1.008\,\mathrm{m}^2, \quad A_{1.1(\mathrm{total})} = 4 \cdot A_{1.1} \approx 4.035\,\mathrm{m}^2.$$

Quadcopter: Configuration 2

A quadcopter with maximized area in Configuration 2 is shown in Figure 3.3, right. For Configuration 2 the propellers are assumed to be foldable. The propeller size is limited by the propellers themselves, before being limited by the payload black-boxes. The expression for the rotor radius $r_{1.2}$, is derived as:

$$r_{1.2} = \frac{\sqrt{750^2 + 750^2}}{2} \approx 530.330\,mm.$$

The theoretical maximum area for one rotor, and the total theoretical maximum area for all four rotors combined for this quadcopter configuration is:

$$A_{1.2} \approx 0.887\,\mathrm{m}^2, \quad A_{1.2(\mathrm{total})} = 4 \cdot A_{1.2} \approx 3.534\,\mathrm{m}^2.$$

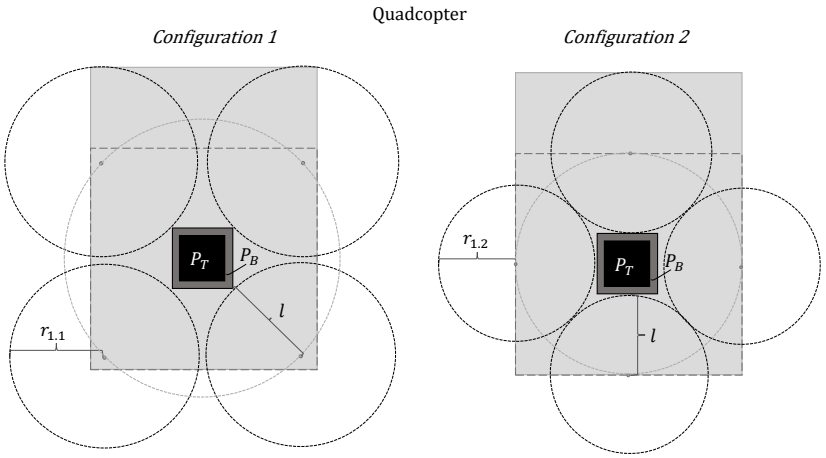

Figure 3.3: Quadcopter; Configuration 1 to the left, Configuration 2 to the right. For $l = r_{1.1}$, the payload black-box dimensions limit the propeller size. For $l > r_{1.2}$, the propellers limit themselves before being limited by the payload.

Quadcopter: Configuration 3
A quadcopter with maximized area in Configuration 3 is shown in Figure 3.4, left. A quadcopter in this configuration has its propeller size limited by the payload black-box dimensions and not by the other propellers. The expression for the rotor radius $r_{1.3}$, is calculated as:

$$r_{1.3} = \frac{\sqrt{1500^2 + 1500^2} - \sqrt{400^2 + 400^2}}{2 \cdot (1 + \sqrt{2})} \approx 322.183\,mm.$$

The theoretical maximum area for one rotor, and the total theoretical maximum area for all four rotors combined for this quadcopter configuration is:

$$A_{1.3} \approx 0.326\,\mathrm{m}^2, \quad A_{1.3(\mathrm{total})} = 4 \cdot A_{1.3} \approx 1.304\,\mathrm{m}^2.$$

Quadcopter: Configuration 4
A quadcopter with maximized area in configuration 4 can be seen in Figure 3.4. A quadcopter in this configuration, has its propeller size limited by the payload black-box dimensions, and not the other propellers. The expression for the rotor radius $r_{1.4}$, is derived as:

$$r_{1.4} = \frac{1500 - 400}{4} = 275\,mm$$

The theoretical maximum area for one rotor, and the total theoretical maximum area for all four rotors combined for this quadcopter configuration is:

$$A_{1.4} \approx 0.238\,\mathrm{m}^2, \quad A_{1.4(\mathrm{total})} = 4 \cdot A_{1.4} \approx 0.950\,\mathrm{m}^2.$$

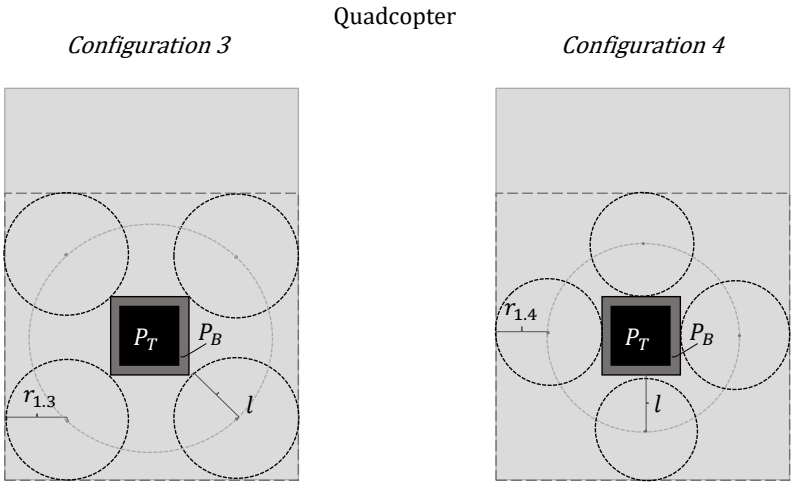

Figure 3.4: Quadcopter; Configuration 3 to the left, Configuration 4 to the right.

Hexacopter: Configurations 1 and 2
A hexacopter with maximized area in Configuration 1, is identical to the one in Configuration 2. This is always the case when the rotor radius is smaller than the difference between the length of the drone "square" and the base in the y-direction

(500 [mm]), and that the propeller size is limited by the propellers themselves. This can be seen in Figure 3.5, left. The rotor radius $r_{2.1}$, is derived as:

$$r_{2.1} = 1500/4 = 375\,mm.$$

The theoretical maximum area for one rotor, and the total theoretical maximum area for all six rotors combined for this hexacopter configuration is:

$$A_{2.1} \approx 0.4418\,\mathrm{m}^2, \quad A_{2.1(\mathrm{total})} = 6 \cdot A_{2.1} \approx 2.651\,\mathrm{m}^2.$$

Hexacopter: Configurations 3 and 4

A hexacopter with maximized area in Configuration 3, is not identical to the one in Configuration 4. In Configuration 3, the area is slightly larger, since the payload black-box dimensions just limit the rotor radius at specific yaw angles. However, since this angle is very small compared to the one in Configuration 3, it will be considered negligible, and these configurations will be considered together. This is shown in Figure 3.5, right. In these configurations, an estimate of the rotor radius will be made. In actuality there is a clash between a rotor and the side of the base at one yaw angle, and there is a clash between a rotor and the payload black-boxes at another yaw angle. However, these will be considered to happen simultaneously when calculating the rotor radius. Therefore, the rotor radius $r_{2.2}$, is estimated as:

$$r_{2.2} \approx 233.579\,mm$$

The theoretical maximum area for one rotor, and the total theoretical maximum area for all six rotors combined for this hexacopter configuration is estimated as:

$$A_{2.2} \approx 0.1714\,\mathrm{m}^2, \quad A_{2.2(\mathrm{total})} = 6 \cdot A_{2.2} \approx 1.028\,\mathrm{m}^2.$$

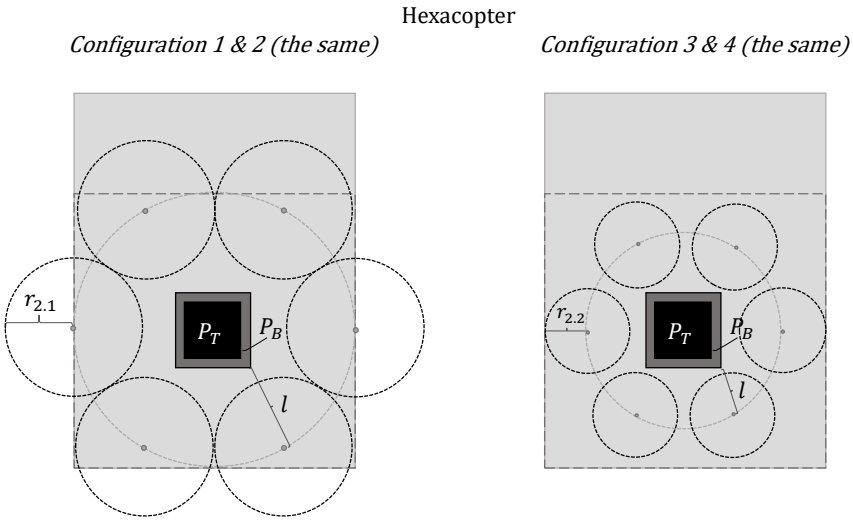

Figure 3.5: Hexacopter; configurations 1 and 2 to the left, configurations 3 and 4 to the right. For $l > r_{2.1}$, propellers limit themselves before being limited by payload. For $l = r_{2.2}$, payload black-box dimensions limit propeller size.

Octocopter: Configurations 1 and 2
An octocopter with a maximized area in Configuration 1, is identical to the one in Configuration 1. This is for the same reason as previously stated. This is shown in Figure 3.6, left. The propeller size is once again limited by the propellers themselves, before being limited by the payload black-box dimensions. The trigonometric expression for the rotor radius $r_{3.1}$, is derived as:

$$r_{3.1} = \sin(22.5) \cdot 750 \approx 287.013\,mm.$$

The theoretical maximum area for one rotor, and the total theoretical maximum area for all eight rotors combined for this octocopter configuration is:

$$A_{3.1} \approx 0.2588\,\mathrm{m}^2, \quad A_{3.1(\text{total})} = 8 \cdot A_{3.1} \approx 2.070\,\mathrm{m}^2.$$

Octocopter: Configuration 3 and 4
An octocopter with maximized area in Configuration 3, is not identical to the one in Configuration 4, but the difference is once again considered negligible. This is shown in Figure 3.6, right. The propeller size is limited by the propellers themselves (with small yaw angle), before being limited by the payload black-box dimensions. The expression for the rotor radius $r_{3.1}$, is derived as:

$$r_{3.2} = \frac{\sin(22.5) \cdot 750}{1 + sin(22.5)} \approx 207.576\,mm.$$

The theoretical maximum area for one rotor, and the total theoretical maximum area for all eight rotors combined for this octocopter configuration is:

$$A_{3.2} \approx 0.135\,\mathrm{m}^2, \quad A_{3.2(\text{total})} = 8 \cdot A_{3.2} \approx 1.083\,\mathrm{m}^2.$$

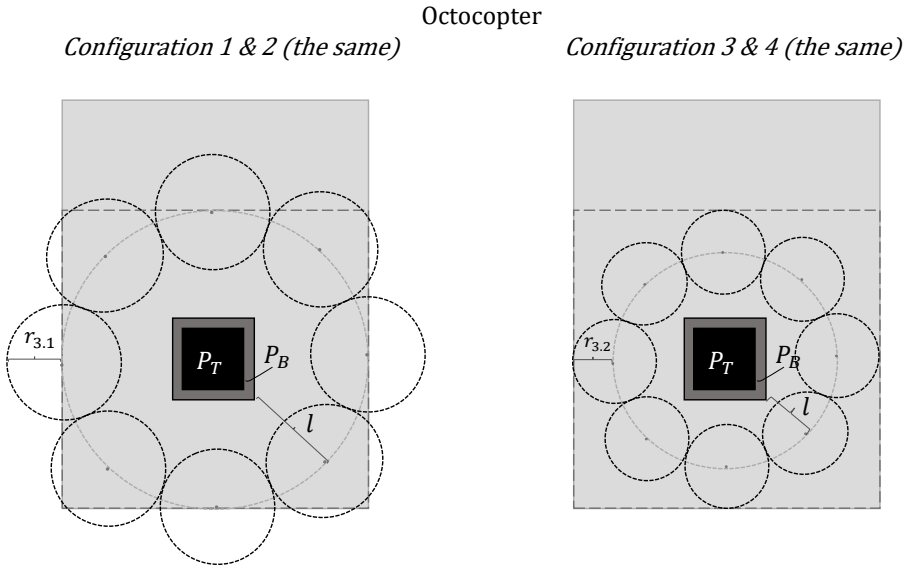

Figure 3.6: Octocopter, to the left: configuration 1 and 2, to the right: configuration 3 and 4. $l > r \rightarrow$ propeller limit themselves before being limited by payload.

Conclusion
A compilation of the radii, for the different number of rotors and configurations, is given in Table 3.1.

Configuration	1	2	3	4
Quadcopter	566.548	530.330	322.183	275.000
Hexacopter	375.000	375.000	233.579	233.579
Octocopter	287.013	287.013	207.576	207.576

Table 3.1: Compilation of radii [mm], based on configuration and number of rotors.

The areas are also compiled and ranked based on the different configurations and the number of rotors, see Table 3.2.

Configuration	1	2	3	4
Largest area	Quad: 4.035	Quad: 3.534	Quad: 1.304	Octo: 1.083
Second largest area	Hex: 2.651	Hex: 2.651	Octo: 1.083	Hex: 1.028
Smallest area	Octo: 2.070	Octo: 2.070	Hex: 1.028	Quad: 0.950

Table 3.2: Compilation of areas [m^2], ranked based on configuration and number of rotors.

It could be argued that this compilation of the total rotor areas is not entirely relevant, since the relationship between rotor radii and thrust is not entirely linear (as discussed in Section 3.3.2). This results in the total area not being the decisive factor when it comes to maximum thrust production. However, the total area still directly affects the disk-loading ratio (the ratio between the total rotor area and drone weight) which is beneficial to minimize in order to maximize efficiency. For example, in practice, a total rotor area of $1.028\,m^2$ for a hexacopter would most likely produce more thrust than an octocopter with a total rotor area of $1.083\,m^2$.

An interesting conclusion from this analysis is that, based on which configuration is preferred, a different number of rotors lead to the largest maximized area, see Table 3.2. It is evident that except for the quadcopter, no area is lost by enabling landing in any yaw direction. The thing that has the greatest impact on the maximized area, with each number of rotors, is if the propellers are assumed to be foldable or not. However, it is important to note that these are the theoretical maximums. As stated, assumptions were made that there were no margins between parts, and that the motors and propeller protection were infinitely thin. In reality, this is not the case. Since the area is nonlinear with regards to the radius, this would have a nonlinear effect on the total areas. Something that could have an effect on which configuration actually leads to the largest area with the different number of rotors.

Distance between propellers
A gap between the propellers would not only function as a safety margin against the vibrations of the arms and/or propeller blades during flight (to hinder a collision), but it could also keep air-flow interference down. Air flow interference would

otherwise make the drone less efficient and decrease its thrust. There does not seem to be any specific established minimum distance between the propellers on a drone. However, some recommendations seem to be generally adopted across the industry and in literature. Some literature states that 1/3 of the diameter should be used as a gap between the propeller tips [24]. This would mean a loss of 1/7th of the rotor radii dimensions. Other discuss that it is of good praxis to keep one propeller diameter as a gap between two opposite placed propellers, or 1/3 of the diameter as a gap between two adjacent propellers [25]. The latter is the same as the first mentioned, and thus also decreases the radii by 1/7th. This lower boundary will be used for all configurations radii, even though some are, as can be seen, limited by the payload before the propellers. This would in actuality lead to a propeller-propeller gap of more than 1/3 of the diameter. However, it could be argued that it would be good practice to have the same distance from the propellers to the payload as well. Especially when landing gear/feet, and maybe an additional tether attachment point have to be considered in the same limited space.

A paper also states that the lifting force of the drone is connected to the distances between the propellers, along with the propeller diameter and pitch [26]. This lifting force generally increases with an increased distance, up to an certain threshold. However, in order to make some general guideline concerning the distance between the propellers, it could be stated that a larger distance (larger gap between the propellers) is desired, if the diameter of the propellers could be unchanged. Therefore, the upper limit of the distance between the propellers is drawn from the limiting dimensions of the base. Clearly, this lengthening of the arms would also increase the weight. This leads to a non-trivial optimization problem, which might later have to be analyzed for a specific chosen drone configuration. Longer arms may also introduce extra strain on the body of the drone, if flying in turbulent conditions. There is also a desire to keep the deployed footprint minimal. An increased distance between propellers also increases the inertia, which leads to a worse maneuverability or a slower response, but an increased stability.

The stated 1/7th will be used as a fixed reduction of all the different configurations radii, and are used for the calculation of the areas found in Table 3.2. The 1/7th radius reduction, corresponding to a 1/3 diameter gap, is also meant to cover the size of the propeller protection, and the actual size of the, previously assumed infinitely thin, motors. A compilation of the new radii is given in Table 3.3, which includes the gap between the propellers.

Configuration	**1**	**2**	**3**	**4**
Quadcopter	485.613	454.569	276.156	235.714
Hexacopter	321.429	321.429	200.211	200.211
Octocopter	246.011	246.011	171.609	171.609

Table 3.3: Compilation of radii [mm], with 1/7th fixed reduction for gap, based on configuration and number of rotors.

The corresponding areas are given in Table 3.4.

Configuration	1	2	3	4
Largest area	Quad: 2.963	Quad: 2.597	Quad: 0.958	Octo: 0.796
Second largest area	Hex: 1.947	Hex: 1.947	Octo: 0.796	Hex: 0.756
Smallest area	Octo: 1.521	Octo: 1.521	Hex: 0.756	Quad: 0.698

Table 3.4: Compilation of areas $[m^2]$, with 1/7th fixed radii reduction for gap, ranked based on configuration and number of rotors.

There has not been any change of the ranking over the maximized area, based on the different configurations and number of rotors, when this propeller gap was introduced. However, it is clear that drones with fewer, larger rotors were more heavily affected by this gap between propellers, because of the nonlinear radius-area relationship. Something that could also have been derived before this analysis, is that as a result of a quadcopter's lack of redundancy, it will not be a feasible option, as per requirement R7.4 (must be designed with redundancy, such it is operable with loss of one motor, Appendix A). However, thanks to the upcoming look into the coaxial configuration, these area calculations could still be relevant, as they could be used for the coaxial "quad" setup, see Section 3.1.3.

A conclusion that could be drawn from looking into this research question in its entirety, is that generally, as the number of rotors increases, so does the price, weight, payload weight capabilities (if the size is not limited), maneuverability, stability, size, redundancy, complexity, and power consumption of the drone (just looking at the number of motors). The complexity in turn also increases the required maintenance [18] of the drone. Also, when the number of rotors increase, which generally reduces the total rotor area, the disk-loading ratio increases, which reduces the efficiency of the rotors and therefore the system.

3.1.2 Placement of motors

In the previous section it was assumed that all arms were of equal length and all rotors evenly spaced. However, this is not a qualification for the drone system to function. Since the given base and drone footprint is rectangular, this area could theoretically be better utilized if the motors were placed in with uneven separation.

Arms of non-equal length
If there is no need to enable landing in any yaw angle, arms of non-equal length could increase the total rotor area with a set number of rotors. It could also increase the mean arm length, which increases the stability of the system, as a consequence of an increased moment of inertia, but would simultaneously negatively affect the maneuverability. An example of a configuration with these characteristics has been made for a hexacopter, see Figure 3.7. Here, the dashed rectangle represents the drone, and the light gray dashed rectangle is where all the rotors are placed (compare to a square and circle, with the evenly spaced arms/rotors of equal length).

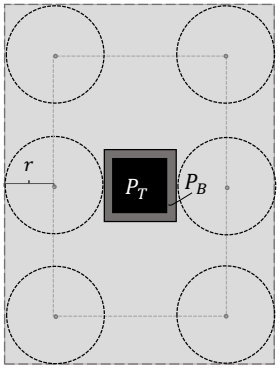

Figure 3.7: Example of hexacopter with arms of non-equal length. For $l > r$, propellers limit themselves before being limited by the payload.

This setup can be directly compared to configurations 3 and 4 for a hexacopter in the preceding analysis. Here, there is an increase in the total rotor area of 32% for the theoretical maximum, and a 39% increase of the area, if the estimated gap distance is considered. This in turn could increase the thrust and payload capabilities of the drone. However, landing in a very specific yaw angle requires very high precision, and for that there are high demands on the control. This could also interfere with one of the tether's functions, to enable quick landing of the drone my pulling it down. With a precise yaw angle requirement, that pulling has to be simultaneously assisted by an additional system, which would most likely lead to longer landing times. Furthermore, using arms of non-equal length would increase the complexity of the modeling and control.

Asymmetric configuration
If the motors are placed asymmetrically, the system also becomes harder to control [27]. This could be the case if a design would have to be adjusted to accommodate certain payload shapes or weight distributions. For a quadcopter, the system is underactuated, since the number of inputs (rotors) are fewer than the six DOFs, and the drone cannot move in the xy-plane without rolling or pitching. This is further discussed in Chapter 7. Either way, correcting for this in the control is generally harder if the drone is asymmetric. For a hexa-, or octocopter the number of inputs are sufficient with regards to the DOFs. However, the additional rotors are linearly dependent with the preexisting, since they all work in the same plane. Therefore, movement in the xy-plane is still coupled with roll and pitch. Because of this, the control of an asymmetric hexa-, or octocopter can also be deemed more complicated.

Motors on different heights
Even though not previously mentioned, all the rotors have been assumed to be on the same plane. Yet, drones with rotors placed on different heights exists [28]. The reason for this could for example be a certain payload that must have an increased field of view in a direction, enabled by moving some rotors higher up. Or the need for an increase in the total rotor area, where overlapping rotors could be used to increase the individual rotor diameters. However, this could cause problems related

to efficiency since some of the rotors could cause an interference when blowing air into others, something that could also negatively affect the drone's stability. Others argue for an increase in efficiency when lifting some of the rotors, since you get more "clean air" whilst flying forward [29]. Since this system is bound by a tether, there will be a limited amount of forward flying. Nevertheless, this would also increase the complexity of the frame design, which could reduce its reliability, and increase the amount of service needed. This extra frame weight could also outweigh the potential aerodynamic gains.

Foldable arms
One of the main benefits of arms of non-equal length or rotors on different heights would be an increase in the rotor area within the given base dimensions. Another means of increasing this area could be to use foldable arms. This would separate the problem of a large rotor area but limited base dimensions, in time. If the arms could be folded after landing, the drone could be kept within its limiting landing dimensions, while allowing a larger size when flying. This could increase the rotor area significantly, and also, if necessary, be used to increase the arm length for higher stability. It could also make it more portable and enable easier and more secure storage and transportation. However, this could also have a large effect on the yaw angles that the drone could land in, which as mentioned requires high precision, and puts high demands on the system control. Foldable arms, just like any moving part, increases the complexity. This in turn increases the cost and maintenance required (due to mechanical wear), and potentially also reduces the drone's reliability. It is also evident that foldable arm would have a negative effect on the deployment and retraction times. When the arms are extended they also have to be aligned with high precision in order to ensure that the motors are in the correct position. If they are not aligned properly when unfolded, the drone could experience an imbalanced thrust, something that could cause instabilities in the flight or a drift in the position. There is also a desire to minimize the drone footprint in the air, so an increase in the drones deployed size is not desired, unless required. If it becomes evident that foldable arms are indeed required in order to reach a sufficient rotor area for the given payload weight, a solution that would render the requirement R14.2 (restricted landing in 1 direction) obsolete, would most likely have to be developed.

To conclude, due to the mentioned drawbacks, the design should focus on an even and symmetric placement of motors, at the same height, with non-foldable arms of equal length. This reduces both the mechanical complexity and the complexity in modeling and control.

3.1.3 Coaxial configuration

Something that has been previously repeatedly stated, is the clear connection between an increased rotor area and thrust output. The quadcopter had, in many of the defined configurations, the largest area, but has been described as non feasible for this application in terms of redundancy. However, as mentioned, a coaxial motor configuration could be used on the quadcopter design (along with on the hexa-, and

octocopter). A coaxial motor configuration refers to where two rotors operate in the same rotational axis, but in different directions [23], see Figure 3.8. This increases the thrust, while retaining the volume of the platform, all while allowing for redundancy in case of motors loss. The reason for the opposite working directions of the motors, is because the torques produced by the motors then compensates one another, which balances the system. Noteworthy is that the bottom propeller is inverted, in order for both of the propellers to move air in the same direction. The thrust benefits are also more evident when the propellers rotates in opposite directions of each other, compared to in the same direction [30].

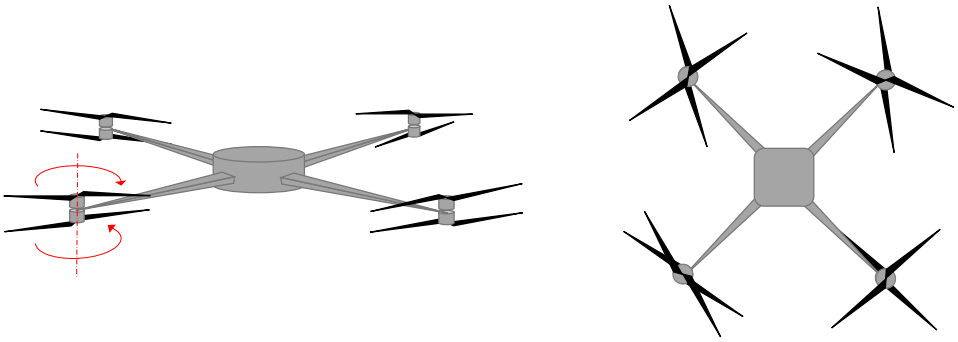

Figure 3.8: Coaxial quadcopter, 3D and top view.

In the calculations of the theoretical maximum area, all the propellers were limited by the lower payload dimensions (the larger one), to account for potential coaxial setups. Therefore, the theoretical rotor area for the coaxial configurations would be double of what is stated in Tables 3.2 and 3.4. By simply doubling the area, through a doubling of the number of rotors, would the output thrust also be doubled, given a constant power input per motor? The answer is no [31], since in the coaxial configuration the lower propeller loses thrust when operating in the prop wash (the airflow generated by the upper propeller). This can also be considered a loss of efficiency, as the thrust output could be set as equal to or double that of a drone with isolated motors, but at the cost of increased power demand (if the motor and propeller would allow for that). It is interesting to determine how significant this reduction in efficiency or thrust is.

Thrust reduction

Usually in a coaxial configuration, the upper propeller acts as a tractor, pulling the drone, keeping its rotor axis under tension. Whilst the lower propeller acts as a pusher, and pushes the drone, having its rotor axis under compression, see Figure 3.9. The upper tractor is more efficient and operates at a similar performance to that of a single isolated rotor [32], whilst the lower propeller have a significant efficiency loss because of its operation in the uppers propellers developed slipstream. The thrust reduction effect is solely aerodynamic and could be estimated using CFD analysis. However, this is deemed outside of the scope of the project and therefore available literature will be used to estimate the reduction in efficiency or thrust.

Glauert's theory is a simple method that can be used to predict the behavior of a coaxial configuration, and estimate its reduction of efficiency/thrust. It is based upon the assumption that the propellers can be approximated by an actuating disk with zero thickness, with a pressure difference occurring over it, and a thrust force applied to it. Glauert's theory is also referred to as the one-dimensional momentum theory, and applies the laws of conversation of mass, momentum and energy, to the system. It does not take viscid losses or the compressibility of fluids, into account [33]. However, it is still estimated to provide a sufficient approximation, as several conducted experiments conclude that the predictions presented by the theory were within an error of around 5% [33]. One paper studies the hover flight mode, and uses the Glauert's theory to deduce an approximate of the efficiency loss in a coaxial system, for multiple different cases. Firstly, if the two propellers were assumed to share the same plane (whilst working in the same rotational axis) and are operated at the same thrust. The application of the Glauert's theory estimates that the coaxial system requires approximately 41% more power to produce the same thrust, in comparison to two isolated propellers [33]. If the lower propeller is placed on a distance where the velocity of the air from the upper propeller has stabilized, known as the "far" wake, and both propellers operate with identical thrust. The coaxial system can be estimated to require an additional 28% power, compared to two isolated propellers, in order to produce the same total thrust. If the lower propeller is placed in the "far" wake of the upper, but the propellers are instead operated at matching power. The coaxial system only require 22% additional power, to produce the same total thrust, compared to two isolated propellers.

One study estimates a average loss of total thrust of a coaxial quadcopter, compared to a design with 8 single isolated propellers, to around 14%, where equal RPM was used for both motors. [34]

Another paper performs experimental verifications, to estimate efficiency of the coaxial configuration. It is concluded that a pair of motors in a coaxial configuration, produce less thrust compared to a isolated motor, when operating at the same total power. This loss of efficiency is dependent on the propeller size, but does not change notably with an change of propeller RPM. Larger propellers provide significant gain in efficiency, but the performance of the coaxial configuration decreases. For a test with 26″ propellers, the efficiency of the coaxial configuration was about 77% of that of the isolated unit. For 16″ and 10″ propellers, the efficiency was estimated to around 85% [31]. To draw a parallel to the area analysis, these propeller sizes serves as a better estimate given the available dimensions. The coaxial configuration requires an additional 17% power to generate the same thrust, if useful thrust is considered (which includes the motors' weight) [31]. However, as stated, this setup inherits a high thrust to occupied volume ratio. Meaning that even though additional power is needed to generate the same thrust, the total thrust that could be generated within the given footprint is significantly higher. Considering the 10″ and 16″ propeller, the thrust gain, looking at the useful thrust (the real thrust minus the difference of weight between the configurations), are 40.6% and 43.7% respectively [31].

An additional study proposes that for conventional torque-balanced co-axial configuration, there can be seen a 22% reduction in efficiency, when compared to two isolated motors [32]. The momentum theory (Glauert's theory) predicts a 26% increase in the required power for the system.

Propeller separation in z-direction
The distance between the propellers have a minimum value, governed by for instance the thickness of the arm, and the height of the rotors. However, this vertical separation l_R might want to be controlled in order to maximize the systems performance. See Figure 3.9 for a profile view of a coaxial propeller pair.

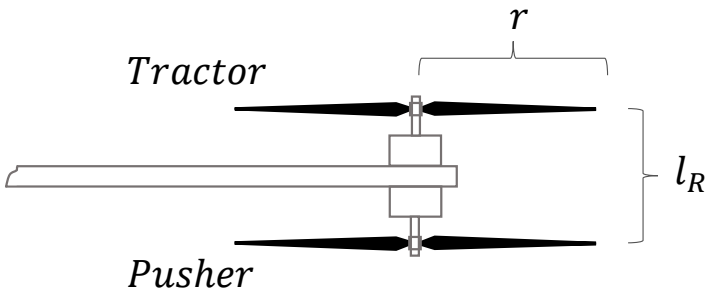

Figure 3.9: Vertical separation between tractor and pusher, with l_R as the rotor separation distance, and r as the rotor radius.

One study discusses the fact that the velocity of the air just above and below the propeller are equal, but progressively increases after passing through the propeller, finally stabilizing after a certain distance known as the "far" wake [33]. Based on the Glauert's theory it is predicted that a coaxial system with maximum efficiency have its lower propeller located at the "far" wake of the upper propeller. This distance, l_R, is approximately equal to the radius of the propeller, r. In the investigation of the thrust reduction for a coaxial configuration, this "far" wake point was mentioned and used for the cases when 28% and 22% extra power was needed respectively to produce the same total thrust, compared to two isolated propellers.

Another paper also suggests that usually the distance between the two propellers, l_R, is approximately equal to the radius, r of the propeller. This distance is said to affect the efficiency of the system, where an increased distance also increases the total thrust of the system, since the two propellers act more and more like two independent systems the further they move from each other (but the thrust is always less than double that generated by an isolated propeller). However, the first paper states that the distance, l_R, between the propellers have little influence over the efficiency of the coaxial system, if it is placed at or beyond the point of the "far" wake [33]. This would suggest that there is no need to move further away from the point of the "far" wake, which would also be beneficial considering the desire to minimize the deployed footprint of the drone. Experiments also show that the ratio of distance to propeller radius is not recommended to be less than ($l_R/r \geq 0.357$) [30].

Other coaxial considerations

It has been previously stated that the two rotors operate in the same rotational axis, but in different directions, and that this is related to a compensation of torque. However, it is not actually required for the rotors to operate in different directions, since there is an even number of coaxial propeller pairs in the quad-, hexa-, and octocopter configuration. This means that diagonally opposite placed rotors can rotate in different directions, whilst the rotors in the same pair rotate in the same direction, and still even the torque out on a system level. Note that in this case one of the propellers are no longer inverted. An experiment suggests that the rotational directions have little influence on the efficiency of the system, but that rotating the propellers in the same direction yields a lower motor operating temperature [33]. Something that could be important due to the requirement regarding a minimization of the heat development in the system. Another source do suggest that different rotational directions of the upper and lower propeller results in a higher total thrust [30]. Additionally, it is stated that if the upper propeller were to be rotated faster than the lower propeller, the total thrust increases significantly. However, this is still not recommended, since it makes the system harder to control and induces an unbalance of torque in each individual coaxial rotor pair [30].

To conclude, a coaxial configuration increases the systems thrust while retaining the dimensions within a given volume. It introduces redundancy to a quadcopter design, and increases the redundancy of a hexa- and octocopter configuration. Different papers propose that somewhere in the range of 16.3-28.2% extra power is needed to obtain the same thrust of the system, if a coaxial configuration is introduced. This is something that can be compared to a 14-22% reduction in thrust, compared to a non-coaxial isolated system (for a given power input). By looking at the useful thrust, a more than 40% thrust gain could be achieved with a propeller size of around 254-406.4 mm, when utilizing a coaxial configuration. The distance, l_R, between the propellers is usually (and should be) set (at a minimum) to the radius of the propeller, r, as this corresponds to the point of the "far" wake. It should not be placed at a distance any less than a factor of 0.357 of the radius, r, ($l_R/r \geq 0.357$). A counter-rotating propeller configuration should be used, and both the upper and lower propeller should be operated with the same input power.

3.2 Motors

The drones motors are crucial components of the drone system, as they are what provides the necessary lift that enables flight. They do this by converting electrical energy into mechanical energy, in the form of rotation of the propellers. This enables the drone to lift, maintain flight, and maneuver through the air. The motors that are mounted diagonally across from each other rotate in the same direction, while adjacent propellers rotate in opposite direction, in order to counter torque and balance the flight. The design of the drone motors varies widely and is depending on the requirements of the system. Generally, it consists of a rotor and a stator. The rotor is the rotating part of the motor, which has its magnets interact with the magnetic field generated by the stator in order to create the necessary thrust for the drone. Following is an investigation based on a number of research question, aimed to determine how the drone motors influences the performance of the system.

- How does the motor type affect the performance?
- How does other motor design parameters, such as motor size, Kv rating, torque, N and P ratings, and motor winding, affect the performance?
- How would a *counter-rotating drone motor* affect the performance?
- Does a coaxial motor configuration have any impact on the choice of motors?

3.2.1 Motor type

There are a number of different motor types, which are characterized by their working principle and the type of current they draw. The most common motor types are the brushed DC motor, brushless DC motor, and the AC motor.

Brushed DC motors are distinguished by their use of a mechanical system, including a commutator and brushes. The brushes maintain contact with the commutator (which is mounted to the rotor) to supply current. The stator creates a permanent magnetic field, and the rotor (armature) is energized to act as an electromagnet. The interaction between the magnetic fields of the stator and the rotor generates motion. Brushed DC motors are characterized by their simple design, and cost effectiveness [35]. They do not need an electronic speed controller (ESC), which simplifies their control. However, they lack in some other key areas. They have a low efficiency, since they have to overcome the brush friction, which also leads to an increased buildup of heat. The brushes also reduces the lifespan of the motors, and increases the required maintenance [35]. Brushed DC motors are generally used in low performance applications, where less power is required [36].

Brushless DC motors consists of a stator, usually with copper windings, and a rotor with permanent magnets. Instead of using brushes, they utilize an electronic mechanism, in the form of an ESC, to control the switching of current in the stator windings. This creates a rotating magnetic field that rotates the rotor. BLDC motors benefit from an higher energy efficiency, since there is no brushes. The friction of the motor is reduced [37], and the electronic switching reduces the energy

loss [38]. This also increases the service life, and reduces the required maintenance of the motor. BLDC motors themselves are also quieter during operation since they lack components prone to wear and friction. These motors are also smaller in size which contributes to an increased efficiency, since less energy are dissipated as heat. BLDC motors also provide a greater torque-to-weight ratio [36], and are able to provide a more constant torque (compared to AC motors, which often loses torque as speed increases) [37]. Additionally, they offer a superior stability of speed, since integrated sensors can adjust the switching sequence for accurate speed regulation.

Just like BLDC motors, AC motors have no brushes. Instead they use the same electronic mechanism to transfer current, by switching the current in the stator winding in a controlled manner. The AC motors operate by using an alternating current that creates a rotating magnetic field that drives the rotor. AC motors have an high efficiency, similar to that of the BLDC motor (since they both lack brushes), but is typically less expensive. However, as stated, the AC motor experiences a loss of torque as its speed increases [37]. They are also more complex in their design, and have a higher weight. In addition to this, AC motors also have a lower controllability than the BLDC motor, in addition to a lower starting torque [38].

For the above reasons, AC motors are deemed as inappropriate with regards to the requirements of the system. As a general conclusion, BLDC motors are a clearly favorable choice over their brushed counterparts, for any drone that is intended for non-hobby use, which requires an increased reliability and conditions that allows for heavy lift usage. They have an appealing combination of high efficiency, beneficial power-to-weight ratio, low maintenance, and precise speed control.

Inrunner vs. Outrunner motors

Inrunner and outrunner motors are two different types of BLDC motors, where an outrunner motor is characterized by having its permanent magnets fixed to a rotor ring, located on the outside of the stator. See Figure 3.10. This results in the outrunner motor consisting of a rotating ring, instead of a rotating shaft, leading to the center of the motor being fixed in position.

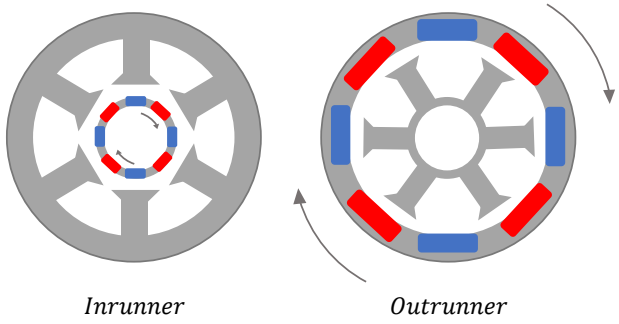

Figure 3.10: Brushless DC inrunner and outrunner motors.

The main advantage of an outrunner motor, lies in their ability to generate a greater amount of torque, within a given build volume. Something that is especially relevant

when high payload capabilities are required. This increased torque is an attribute of a longer torque lever arm for the outrunner motors, which is generated from the force being exerted further away from the motors center of rotation, when the rotor diameter is larger. In addition to this, the larger air gap surface area in the outrunner motor, allows for a more substantial passage for electromagnetic field lines from the rotor to the stator, which leads to a significantly increased torque [37]. In comparison, an inrunner motor has its rotor placed on the inside of the stator, and as a consequence of this reduced torque arm length, often struggles with lower torque outputs. Often the solution lies with the incorporation of transmissions or gearboxes. However, this introduces further complexities, weight, and higher maintenance needs [37], [39]. Generally, outrunner motors have a larger diameter but lower height compared to inrunner motors of comparable weight [39]. Outrunner motors also usually have a lower Kv rating (RPM per volt), than their inrunner counterparts, something that is inversely proportional to the torque. A drawback of the outrunner motors are their somewhat lower efficiency, as a consequence of worse heat dissipation. This is a result of the stator winding (where the heat generation mainly occurs) being located in the center of the motor. For this reason, cooling vents are usually introduced to allow air to flow over the winding directly [39]. Looking at multirotor vehicles in general, outrunner motors are the preferred choice, as the usage benefit from the increased reliability, reduced weight and maintenance, and the increased torque that can be generated.

3.2.2 Motor parameters

A number of different parameters affect the drone's performance, which have to be carefully considered in order to meet the set requirements of the system.

Motor size and thrust-to-weight ratio

One parameter that plays a key role into the performance of a motor is its size. The size of the motor is generally denoted by XXYY, where XX is the width (diameter) of the stator, and YY is the height of the stator, in [mm]. As explained earlier, outrunner motors have their stator located on the inside of the motor, with the rotor rotating around it. Regardless of whether it's an inrunner or outrunner motor, the XXYY designation refers to the stator dimensions. Therefore, the total dimensions of an outrunner motor would be larger than the stated XXYY. Larger motors (with a larger stator) generally offer greater torque and thrust, since increasing either the width or height, increases the size of the permanent magnets and the electromagnetic stator coils. This motor can then support larger propellers, but will have an increased weight and decreased responsiveness [36], [37]. This is since an increased stator width leads to greater inertia, which decreases the responsiveness of the system. However, increasing the width allows for larger bearings, an enhanced durability, and an increased efficiency and stability. Wider stators are also better in terms of cooling, since the surface area is increased. Using a motor with a narrow stator, increases the responsiveness, but might lead to problems with regards to cooling. Keeping the temperature low is crucial for the motor performance, since the motors ability to generate magnetic flux decreases as the temperature increase,

which impacts the efficiency and torque generation of the motor [40]. Looking at the requirement of rather large payload capabilities, wider motors are preferred, whereas responsiveness is deemed as less critical.

It is recommended to opt for a desired thrust-to-weight ratio of the entire drone system, and then selecting the smallest motor that fulfills those specifications. This is in order to balance the required power, responsiveness and weight for an all together efficient setup [37]. A fundamental guideline is to aim for a total maximum thrust that is at least double that of the drones weight, in order to ensure lifting capabilities at takeoff, and to allow for the maneuverability needed for controlled flight [37]. A 2:1 ratio allows the drone to hover at half throttle. Some drones have a ratio of 3:1, 4:1, or even up to 14:1 (for racing drones), if extra maneuverability is needed [35]. However, for this application, an at minimum 2:1 ratio is deemed sufficient, since the drone will mostly be at static hover with its tether extended.

Kv rating
The Kv rating of an electric motor is a number that corresponds to the RPM per volt (RPM/V), which indicates the motors speed at a given voltage. More specifically the RPM an unloaded motor produce at full throttle when given an 1 volt input. Therefore, given the Kv rating, the RPM of a motor can also be estimated, by multiplying the Kv value fo the motor by the power source output voltage. The Kv value is as stated inversely proportional to the torque. Therefore, lower Kv ratings are suitable for heavier drones, where a higher torque is required to drive larger propellers, whereas higher Kv values are beneficial for faster drones with smaller propellers [36]. Just to illustrate, pairing a high Kv rating motor with a heavy (large) propeller makes it attempt to rotate the propeller at its maximum speed, which requires an increased torque and therefore draws increased current. If an inappropriate Kv rating is chosen, there is a great risk of burning power system components out [39], which would drastically decrease the systems reliability, and increase the required maintenance. Conversely, using a low Kv rating, with a lighter (smaller) propeller might result in a inadequate thrust generation [37].

When a motor with a low Kv rating produces more torque, it enables faster changes in the propeller speed, which in turn allows the drone to adapt quicker to given control inputs. This increases the maneuverability of the system, and increases the stability in for example windy conditions [36]. However, an excessive torque might lead to jerky movements, and an difficulty performing delicate maneuvers, which highlights the importance of a balance between torque and efficiency in order to optimize the performance. Motors with a high Kv rating usually have shorter windings and lower internal resistance. This reduces the maximum voltage rating of the motor, which in turn leads to an increased amount of current draw [40]. This in general leads to an increased heat generation in higher Kv motors, than lower Kv motors of the same size. This heating issue is even more evident in taller motors, due to their greater rotational speed [37].

Once again, when choosing a motor to pair with a propeller, it is important to achieve the desired thrust-to-weight ratio (of at least 2:1). But generally a rather low Kv rated motor seems to be appropriate for the relatively heavy lift use cases that the system will come to experience. It could be assumed that the system in question should be categorized as a "heavy lift", based on the previous narrative. However, after briefly looking at available COTS components, such as motors and corresponding propellers, it becomes evident that actual "heavy lift" cases refers to drones that requires thrust for much more than the projects required payload weight of 15 kg. This is of great importance, since blindly categorizing this as heavy lift drone could radically skew the choices of motors, and their corresponding parameters, from what is actually demanded and appropriate. Drone motors with very low Kv rating are not uncommonly recommended to be paired with propellers with diameters exceeding 1000 mm, which would not fit within the given dimensions. Therefore, this drone system should be classified as a semi-heavy lifting drone with a notable limitation in size.

Motor torque and Kv vs. torque constant (Kt)
Torque is depending on the stator volume, the materials (mainly magnets and copper windings) and the construction of the motor itself. Where the two latter differ rather insubstantiality between different motors. Therefore the torque of the motor can be quantified by the stator size, which can be simply calculated using the formula for the volume of a cylinder. A larger volume means a higher torque generation.

Previously, the Kv value was described as inversely proportional to the motors torque. However, the Kv does not directly affect the torque, but impacts something known as the torque constant (Kt). This constant is defined as the amount of current needed to produce a set amount of torque. In practice, higher Kv rated motors have a higher torque constant, drawing more current to achieve the same torque, which decreases its energy efficiency [37]. This is a result of additional energy losses in for example the ESC and wires. The higher current also results in an increased heat buildup in the motor, which as stated decreases its efficiency.

N and P ratings in motor
In addition to the motors size denotation, Kv and Kt value, the motors are also labeled with a N and P rating. This corresponds to the number of stator poles (N), and number of magnets (P), and is stated as e.g. 15N17P (15 stator poles, and 17 magnetic poles (magnets)). The motors in Figure 3.10 can be denoted with 6N8P. Since the motors are 3-phased, the number of stator poles are a multiple of 3 (like 6 or 15). As the number of stator poles increases, the precision of the motor control increases and the operation becomes smoother [41]. This is due to a more uniform magnetic field, and a more frequent magnetic switching, which enhances the drones responsiveness, and reduces the cogging torque (the resistance or irregular torque that occurs due to the interaction between the magnets and the slots in the stator, often when the rotor is stationary) [36]. There seem to be a divide in literature regarding if a lower or higher amount of poles increases the torque. However, there appears to be a misconception where the power output is mixed up with the torque

output, which is higher with a decreased amount of poles. The power output is a product of the torque and angular velocity, which can be higher even though the torque is lower, since the the RPM can have a larger increase than the experienced decrease in torque. So to conclude, there is an increase in the torque when the number of poles increase [36], [41]. It is also evident, as stated, that the RPM increases when the number of poles decreases. This is a direct effect of the motor mechanics and how it operates depending on the the number poles, since a 6-pole motor spins at twice the RPM of a 12-pole motor at the same input voltage. Since more poles increases the torque, the power output can also be higher with more poles at lower RPM. The number of permanent magnets (P) are often close to the number of poles, but not necessarily the same. It depends on the design of the motor, and if synchronous or asynchronous rotation is desired (if it is desired for the rotor to rotate at the same speed as the rotating magnetic field created by the stator, or not) [36].

Generally, a high pole count is suitable for large propellers, with higher torque, where heavier payloads and stable flight is required. Meanwhile, a low pole count is better suited for smaller drones, equipped with high-speed propellers, that require less torque [36]. The N and P rating can be said to not directly impact the motor performance, but it is deemed beneficial to have in mind when looking at motors, in order to understand their structure. Additionally, in practice, the N and P number is important when configuring a flight controller.

Motor winding

The motor winding directly influences the performance of a motor. The maximum current drawn by the motor is determined by the number of copper windings/turns (T) on each stator pole, denoted as e.g. 8T or 13T [41]. Additionally, the thickness of the wire affects the motors ability to handle different currents (without overheating) [40]. As the turn count, T, increases, the Kv value and the amount of current drawn decreases. The RPM also reduces, whilst their is an increase in torque. This is a consequence of an increased magnetic field on the stator pole [40]. In contrast, fewer turns decreases the resistance, and results in higher Kv values. However, the electromagnet fields are also reduced which decreases the torque output of the motor. Thick wires are able to handle a higher current, but the consequential reduction of the electromagnetic fields reduces the torque. Thinner wires creates stronger electromagnetic fields and therefore higher torques, but are not able to handle higher currents due to the internal resistance [37]. Therefore it is beneficial to opt for motors with thick wires and a high number of turns, T. Which unfortunately have a negative effect on the weight, and leads to a physically larger motor (since the stator size has to increase). As earlier stated, the semi-heavy payload carrying applications of the system leads to the demand of high torque, low Kv rating, and now a high number of turns, T, in the motors. The motor winding will not have to be considered specifically, but simply choosing a low Kv rated motor, that produces a high torque, will effectively already be a motor with a high number of turns on each coil.

Current and voltage relationship
There is an important relationship between the motors voltage and the current it draws. Higher motor voltage usually results in an increased current draw from the power source. The maximum current drawn is determined when the motor operates at its peak voltage, generating its maximum thrust. Each motor will be paired with an electronic speed controller (ESC). It is important to determine the maximum current drawn by the motor in order to chose a ESC that has a continuous current rating surpassing that of the motors maximum [37]. Having a small surplus provides additional safety against spikes in current demand, and problems relating to overheating, which contributes to the systems reliability. Usually, it is of importance to chose a drone motor that supports the voltage of the battery (which is usually denoted by a number of 'S':es, corresponding to the number of cells, and in turn the voltage, of the battery). However, in this case where the main power source is located on the ground, having its power fed through the tether, there is greater need to match the backup batteries voltage to the motors supported voltage. The voltage from the ground-based power source will through AC-to-DC, and DC-to-DC converters be transformed down to the demanded voltage of the motors, resulting in a greater flexibility when choosing the motors. Generally, motors utilizing higher voltage can deliver higher power outputs [36].

Cost
For the system to be considered a order winner, it is desired to deliver a competitive price relative to the provided performance. There area number of factors that influence the price of a drone motor. Generally, the motor type has a large influence of the price. For heavy lift applications, BLDC motors are more expensive than AC motors , which in turn is more expensive than brushed DC motors [37]. However, as previously discussed, this also influence their relative performance. In addition to this, the power rating of the motor have a direct tie to the price, where motors able to provide more thrust comes at a heftier price. The materials used and the build quality of the motors also have an influence. Some motors utilize special materials to endure harsh environments like a large temperature range, and moisture. This is something that is deemed relevant, since the considered system must be able to operate in and withstand harsh weather, and must be operable in a number of AECTP-230 zones, see the requirement specification in Appendix A, with an additional desire to be able to operate in even more.

3.2.3 Counter-rotating drone motor

One, more radically different, drone motor design is the counter-rotating drone motor, see Figure 3.11. This can appear similar to the coaxial motor configuration, but the difference is that the counter-rotating drone motor have two propellers powered by a single motor, compared to two separate motors. This setup is designed to enable the harness of energy from both the active and reactive forces that are generated by the rotating motor [37]. The energy from the reactive force is traditionally absorbed by the (stationary) stator, along with the drone body, but are in these motors utilized and redirected to drive a counter-rotating propeller. This means

that both the rotor and stator now rotates, in opposite direction, and therefore a slip ring mechanism is employed to electrify the motor [42].

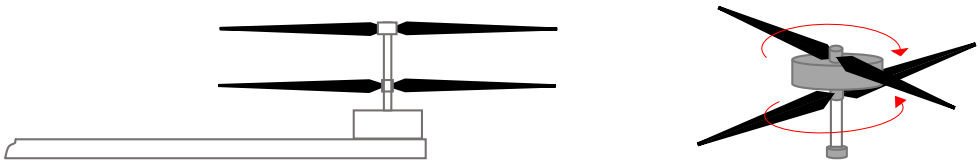

Figure 3.11: Counter-rotating drone motors, side and 3D view.

Compared to traditional motors, the counter-rotating motors achieve a greater overall energy efficiency. The extra forces harnessed can result in up to 50% higher energy efficiency (depending on motor size and configuration), than comparable motors on the market. This can contribute to improved thrust, which makes the especially suitable for applications requiring high payload capabilities [37], [42]. The company behind this innovation present a performance comparison chart themselves, see Figure 3.12, which compares the counter-rotating motor with a conventional electric motor. They also imply that the efficiency increase is up to 50%, which could lead to an up to 50% increased flight time (based on the thrust produced). Notable is that flight time is not directly determined by the system efficiency for a tethered drone, but opting for a efficient system is still very favorable. In the chart it can also be seen that the extra thrust provided can reach nearly 100%. One reason for this is that the motors spin up to 25% faster compared to conventional motors under the same current [43].

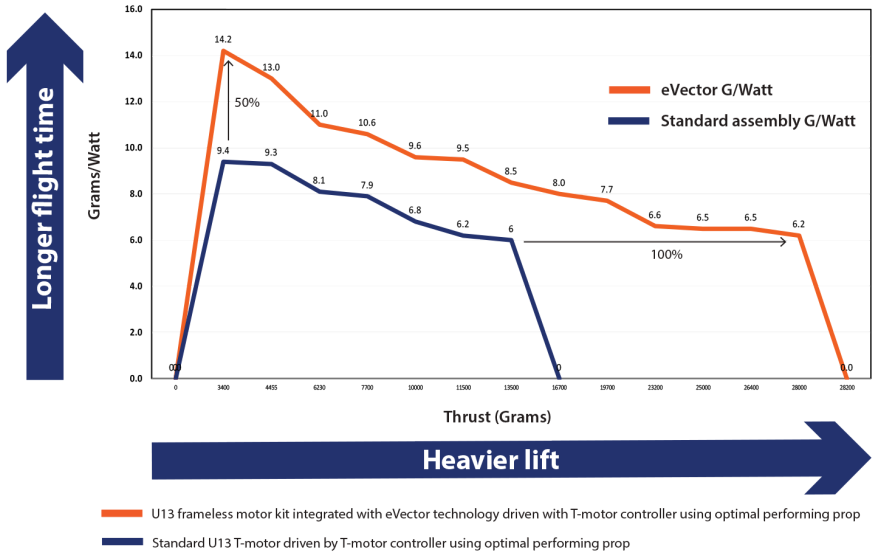

Figure 3.12: Performance comparison chart showing the operational thrust generated by the counter-rotating drone motor, compared over a range of amps to a conventional electric motor [44].

The company also suggest that the motors produce less noise, compared to non

counter-rotating motors [43]. They also state that their motors runs up to 50% cooler, which leads to a "much longer motor life" [45]. However, it must still be arguable that these motors have an increased complexity that could decrease their reliability and increase the required maintenance. Since they are patented by the company, strictly limiting the existing competition, there is a lower amount of available designs and less flexibility in being able to choose motors with specific performance metrics, appropriate for the system being developed. These motors seem to be available in various, but a limited amount of, thrust sizes. These seem to be 10, 20, 50 and 100 lbs of lift respectively [42]. These are also directly paired and sold with corresponding propellers, where the smallest propeller (for the 10 lbs motor) is 18 inches or ≈ 47 cm [46]. This is something that is larger than the available space for the majority of configurations and number of rotors. However, they state that they are able to develop custom configurations to suit specialized applications [42]. Although relevant, this would most definitely increase the price radically, and decrease the availability of the motors. Since there is a desire to utilize as many standardized, commercial off the shelf (COTS), components as possible. These counter-rotating motors will therefore only be deemed relevant if the specifications of the already available motors are suitable for the system. Either way, it is interesting to see how the availability of these develop in the future.

The counter-rotating drone motors have, as mentioned, similarities in appearance with the coaxial motor configuration. Since one counter-rotating drone motor drives two propellers, they are both lighter and more energy efficient, than the coaxial configuration [45]. Since both propellers are fitted to one motors, the difficulty associated with a double motor (per arm) rig, is also eliminated [43]. Compared to the coaxial configuration, these motors are also beneficial with regards to a minimization of the deployed footprint, since both propellers are mounted in a positive z-direction from the motor. Both propellers are for this reason also protected by the motor itself in negative z-direction (for example at landing). However, as discussed, the coaxial design offer a much higher availability and configurability, since it is not depending on a specially designed component, but instead levers the use of "any two motors" in a specific configuration.

3.2.4 Coaxial motor configuration

Previously, a coaxial configuration (recall Figure 3.8) has been investigated in terms of general thrust gain (or efficiency loss) and appropriate separation in the z-direction. However, the coaxial motor configurations impact on the choice of motors, and the associated parameters, is unknown.

With regards to motor choice for a coaxial configuration, it is proposed that reducing the upper rotor radius, and therefore increasing the induced power could lead to efficiency gains. This is a result of a larger portion of the lower rotor taking in "clean" air [47]. In a limited study, it is proposed that an 8% reduction in the radius of the upper motor produces the highest efficiency gain, see Figure 3.13. As previously discussed, reducing the radius of the upper rotor (having a smaller pro-

peller) would encourage the utilization of a motor with a higher Kv rating, spinning at a higher RPM (than the lower motor). However, the study's efficiency gains with the 8% radius reduction is, contrary to popular belief, in actuality obtained with matching RPM of the upper and lower motor. An efficiency gain is also obtained with matching propeller tip speed (higher RPM on the smaller upper propeller), although not as substantial. Which would lead to different upper and lower motors if they were chosen based on appropriate parameters, such as Kv rating.

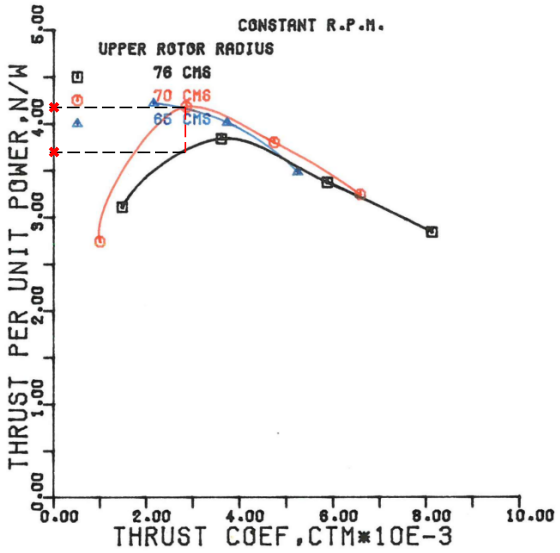

Figure 3.13: Efficiency with different upper rotor radii [47].

An estimate of the efficiency gain can be derived from the Figure, where the marked points on the y-axis correspond to approximately 3.7 and 4.2 N/W respectively. Which would relate to a efficiency gain of around 13.5%. However, it is noteworthy that the reduction in propeller radii used in the experiment, that achieves that maximum efficiency gain, is from 76 to 70 cm. If the analysis of the maximum radii and areas for different configurations, see 3.1.1.1, is observed, it is clear that both these propellers sizes (radii of 76 and 70 cm) are far larger than the available space for any configuration and for any amount of rotors. In Figure 3.13, it can also be seen that the efficiency gain effect is radically decreased when the rotor radius is instead reduced from 70 to 66 cm. Therefore, the argument could be made that this $\approx$ 13.5% efficiency gain will not be obtainable for the smaller rotor sizes that the system will utilize.

Another paper concludes that a variation of the upper propeller's size have an influence on the coaxial systems efficiency. Where an upper propeller with a smaller diameter than the lower, leads to an increased efficiency, and a upper propeller with a larger diameter results in a less efficient system [33]. The gain is also more significant when the input power, and therefore thrust, is increased. If different propeller sizes were used, it could be reasoned that the motors parameters would be affected. Since, as discussed, there is a relationship between propeller size (weight) and motor Kv rating. So a smaller upper propeller would reasonably be matched with a motor

with a higher Kv rating than that of the lower motor. It can also be recalled, from the previous Section 3.1.3, that an increased rotational speed of the upper propeller increases the total thrust "significantly". However, it was not recommended, due to the increased complexity of the control and the induced unbalanced torque in the coaxial rotor pairs [30].

3.2.5 Conclusion of motor section

To conclude, for this system experiencing its semi-heavy lifting applications, it would be beneficial to opt for brushless DC (BLDC) motors of the outrunner type. These should be rather wide, allowing for larger bearings and high torque, and give a thrust-to-weight ratio of at least 2:1, where a higher ratio leads to better acceleration. The Kv rating should be low-medium, and the Kt should be relatively low. This would result in the need for rather heavy propellers. The pole count and T-number (motor windings) should be relatively high. The electronic speed controller ESC should match the motor. There is also of great importance to chose a motor with materials that enables it to operate in the required (and desired) environments. A counter-rotating drone motor could be utilized to increase the efficiency/thrust, if the available sizes and thrust-ratings would be deemed relevant. If a coaxial motor configuration was adopted, an efficiency gain could be acquired if different motors were used on the upper and lower position (paired with appropriate propellers, of different sizes). However, this would most likely introduce further complexities, and it could be reasoned that this should only be further investigated if the coaxial setup came to be relevant, and additional thrust is needed.

3.3 Propellers

The drone's propellers are what converts the rotational energy outputted from the drone's motors into thrust, which enables the drone to lift, hover, and maneuver in space. These are usually designed in an airfoil shape, and generates the lift by the pressure difference they create, between their upper and lower surfaces. There are multiple things that influences the performance and choice of a propeller [48], like the overall propeller design, the number of propeller blades and their individual design. Additionally, things like a coaxial configuration could also influence the choice of the systems propellers. A couple of research questions have been formulated in order to guide the research related to the subsystem.

- How does the number of blades affect the performance of the propeller?
- How does the design of the individual blades affect the performance of the propeller, including parameters such as pitch, and diameter?
- How does the overall design of the propeller affect the performance, what differentiates classic propellers, from foldable ones, or propellers designed to be quiet (such as toroidal, or unevenly spaced blades)?
- How does the propeller material affect the performance, what is the optimal?
- How would a coaxial motor configuration impact the choice and design of propellers?
- How does a specific propeller get matched with a specific Kv-rated motor?

3.3.1 Number of blades on the propeller

The number of blades on each propeller have a great affect on the drones performance, and usually varies between two and six, see Figure 3.14, with exceptions in both directions.

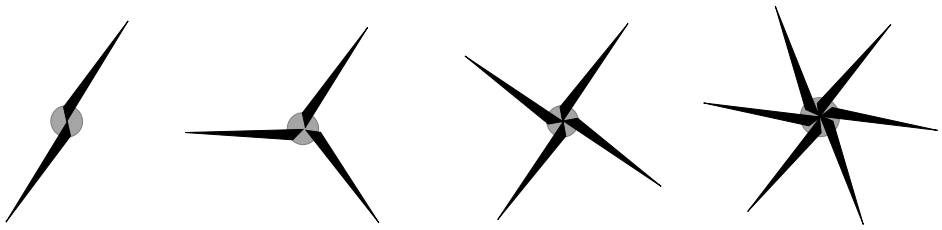

Figure 3.14: Different number of propeller blades. From left to right, two-, three-, four-, and six-bladed propeller.

Two-bladed propeller
Two-bladed, or dual propellers, are typically used on smaller drones. They are lightweight and offers a very high efficiency for a given power input, given their low drag [48]. Two-bladed propellers can also be spun at a higher RPM than higher-bladed counterparts [49], due to the smaller moment of inertia (due to the lower

weight). These propellers are also more durable at crashes, and the foldable version of them is easier and quicker to fold [49]. However, the two-bladed propeller produce less thrust for the same diameter compared to their higher-bladed counterparts. They can also be less stable then other propellers with higher blade-count, and are more strongly impacted by wind [49].

Three-bladed propeller
Three-bladed, or triple propellers, are typically used on larger drones due to the increased thrust that can be delivered within a given footprint [49]. Having the number of blades increased to three, also increases the stability and maneuverability of the drone [48]. Another benefit of the three-bladed propeller is that the balancing of the propeller does not have the same impact on the performance, as for two-bladed propellers where a perfect balance is needed in order to avoid unpleasant vibrations [49]. On the other hand, the efficiency of the three-bladed propellers are slightly lower than the two-bladed counterpart [48], but still remain in a good balance balance between thrust and efficiency. They are also inherently heavier, and are also more likely to be damaged in a collision.

Four- (or more) bladed propeller
Propellers with more than three blades, including quad-propellers, five-bladed propellers and hex-bladed propellers, have the ability to increase the thrust even more with the same propeller diameter, since more air can be displaced. Utilizing a higher blade count can also make the drone easier to control [48], and can improve the stability in wind, along with light-disc rotor loading conditions (something that otherwise worsens the flight stability) [50]. However, these propellers will have an even worse efficiency than the previously mentioned propellers, and also be even heavier and have a reduced durability.

It has been identified that it is of importance for the system to produce minimal noise whilst operating. Therefore it is relevant to also look specifically at the affect of the propeller blade-number on produced noise. One study investigates the aeroacoustics of two-, three-, and five-bladed propellers [51]. Both the narrow-band tonal noise and broadband noise components are studied. Tonal noise is discrete frequency components, where a high portion of energy are concentrated at a single frequency or within a narrow band of the spectrum. This noise is generated at the blade passage frequency and its harmonics. The broadband noise consists of a continuous spectrum of frequencies. Together they make up the overall sound pressure level (OASPL). The study concluded that two-bladed propellers produces the highest tonal noise levels, at the same tip speed, as the other (higher blade-numbered) propellers. The five-bladed propeller instead produces the highest broadband noise levels of the propellers [51]. It is important to note that the tonal noise is radiated mainly in the rotational plane, while the broadband noise mainly mitigates in the up- and downstream direction. The latter being a direction that can be argued to be more relevant for this tethered drone system, where the affected observers will mainly be located beneath the operating plane of the drone. However, because the system is designed to be very modular when it comes to application and payload,

the height of the drone and the location of the observers may vary. Additionally the total OASPL is still higher for a propeller with a lower blade number, when operating at the same thrust conditions. Since the total weight of the drone is not believed to be largely impacted merely by the number of propeller blades, the thrust that the drone needs to create can also be considered close to constant, regardless of the number of propeller blades. This renders the constant thrust condition between the number of propeller blades applicable. Another source also generally describes three-bladed propellers, compared to two-bladed propellers as much quieter [49].

In general, it can be stated that two (or one) blades are the most efficient. Whilst if the goal is to maximize the thrust within a given area, an increased number of blades, at a cost of lower efficiency can be utilized. In practice one-bladed propellers are not very practical, since they would need a counterweight in order to remain in balance. If this counterweight do not contribute with any additional thrust, the advantage of this blade-count would nullify [49]. It is stated that thrust gains of over 70% can be achieved with blade-counts exceeding two, compared to the dual-propeller configuration [50]. This without increasing the diameter of the propeller. The thrust gains do not increase linearly with the number of blades, as blade interference can decrease the efficiency of each blade's performance. For example, doubling the number of propeller blades, lets say from two to four, does not double the thrust produced. Adding more blades reduces the spacing between them, which can lead to higher drag and lower aerodynamic efficiency of the propeller. Therefore, the benefits also start to diminish, rendering a very high blade-number unsuitable. Increasing the number of blades, in addition to increased thrust also increases the stability of the drone, decreases the noise, and can increase the drones maneuverability. However simultaneously, in addition to decreased efficiency, the propellers gets increasingly more hard to fold and occupies a larger amount of space whilst folded, they become less durable, heavier, more expensive, and takes longer time to reach the same rotational speed, when increasing the blade count.

There are existing heavy lift drones that are utilizing only two-blades on their propellers, because of the efficiency that it brings. However, these studied examples are untethered, and therefore the efficiency of those systems corresponds directly to the flight-time. For a tethered system, this is not the case. The efficiency does also correspond to the flight-time, but is not as limited by it, since power can be continuously provided given that the power supply is repeatedly filled up with eg. fuel. Even though it is not as limited, it is still an aspiration to have a good efficiency, because of other benefits that this brings. This is things such as lighter components, smaller power supply, less heat development, less maintenance etc., in addition to a long continuous flight time without having to refuel the power supply. However, as the drones footprint is limited, it might be required to utilize more blades to produce the systems desired thrust.

3.3.2 Design of individual blades

As just discussed, if the propeller is studied as a whole, the number of propeller blades have a great impact on the propellers performance. If the focus is instead redirected to the individual propeller-blades design, the two specifications that largely determines the performance of the blade, and in turn the propeller, are the pitch and diameter. The pitch, or angle of attack of the blade, refers to the theoretical distance the propeller would move forward during one rotation, if there was no resistance [48], see Figure 3.15. The diameter of the blade relates to the tip-to-tip distance, or the diameter of the circular area that the propeller produces while rotating, which can also be seen in the figure.

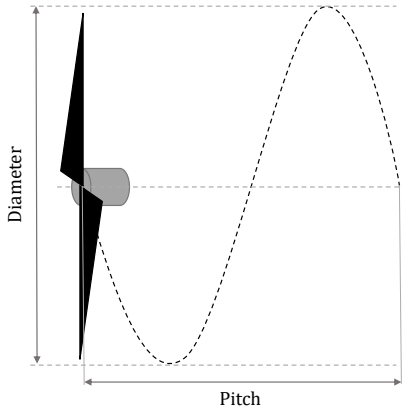

Figure 3.15: Pitch and diameter of a propeller blade. Figure illustrated with a dual-blade design, but the pitch and diameter is unrelated to the number of blades.

The diameter of the propeller is directly connected to the amount of air that the propeller displaces while rotating, which is what generates the thrust. Therefore, increasing the diameter of the propeller, also exponentially increases the thrust that it produces (due to the exponential relationship between a circles diameter and area), but requires a more powerful motor in order to produce the required torque to drive it due to increased drag [48]. The increased drag, and increased moment of inertia also leads to a increased response time when using larger propellers. Additionally, both acceleration and the ability to stop quickly suffers [52]. Increasing the diameter also increases the rotor area, without a too substantial increase in weight, which would generally lead to a lower disk-loading ratio. As previously discussed, the disk-loading ratio is the ratio between the weight and the total rotor disk area of the vehicle, usually standardized into N/m^2. Having a larger rotor disk area, by applying a larger propeller diameter, decreases the disk loading, which increases the total hover rotor and drone efficiency [53].

The blade's pitch is also connected to the thrust that is produced by the propeller. A higher pitch angle lets the blade move more air per revolution, which produces more thrust, and also higher top speeds [54]. This generally comes at a cost of a slightly reduced efficiency, compared to lower pitched blades, since additional torque is required to enable the movement of the additional air. More torque is also re-

quired in order to change RPM, which leads to a decrease in the responsiveness from the control inputs, making it harder to change directions of the drone. Even though more thrust is generated with an increased pitch angle, this is mainly at the high RPM, whilst less torque is produced in the low-end.

The diameter and pitch of a propeller blade is usually denoted with four numbers, XXYY or XX*YY, where the XX corresponds to the diameter in inches, and the YY is the screw pitch in Y.Y inches. Since increasing both the diameter and pitch increases the top (tip) speed, this also comes with the consequence of potentially higher noise emissions [51]. For this application, it would generally be beneficial to opt for the largest possible propeller diameter given the available area for the different configurations and number of rotors, as discussed in Section 3.1.1.1. The pitch would have to be optimized for the application in question, in order to balance the responsiveness and efficiency with the additional thrust. However, even though the system aims to be modular in its usage, the system can be considered to mainly be hovering. Therefore, choosing a propeller pitch suitable for very quick movement in the xy-plane is not too relevant, and a higher pitched blade can be considered reasonable. In practice, it is also hard to chose a propeller diameter and pitch-angle totally independently, since off the shelf propellers do not come in a large pitch range, given a diameter. If a propeller blade would come to be designed and produced, for the specific application, this would come to be more relevant.

3.3.2.1 Performance given specific propeller design

In order to more concretely evaluate the performance of a propeller there are a number of aerodynamic theories that could be used. These could be viewed as a progression of theories, each increasing in complexity and realism. Following will be a brief explanation of the concepts of Momentum theory (MT), Blade element theory (BET), and Blade element momentum theory (BEMT).

Momentum Theory (MT)
Momentum theory, also known as actuator disk theory or one-dimensional momentum theory, treats the entire rotor as a simple actuator disk that accelerates a stream of air, by creating an increase in pressure over the propeller plane [55]. In this theory no blade design is considered. Mainly, momentum theory is used to estimate the overall efficiency and thrust of a propeller in ideal conditions. The thrust can be seen as the change in the momentum of the fluid, as:

$$T = \rho u_A A_A (u_j - u_A)$$

Where:

- T = Thrust,
- ρ = Air density,
- A = Rotor disk area,
- u_A = Air velocity at the disk (induced velocity),
- u_j = Jet velocity in the far wake

If the goal is to solve for the thrust that a propeller produces, the velocity in the far wake, u_j, has to be derived, usually from CFD or experiments. Since this is not an option here, this theory provides little knowledge about how the design of the propeller affects the performance. However, it could be derived that, for a constant disk area A, and if both the induced velocity and jet velocity u_A and u_j are regarded as unchanged at constant RPM's, the thrust could be described as proportional to the air density ($T \propto \rho$). This relationship will be used in upcoming derivations.

Blade Element Theory (BET)
The blade element theory is somewhat more complicated, but still considered a relatively simple method of predicting propeller performance. It involves dividing the propeller blade into many independent elements along the length, and applying a force balance between the lift and drag, and the produced torque and thrust, of each element. The resulting individual contribution can be summed up to predict the overall propeller performance [56]. Inputs to the blade element theory include blade geometryand airfoil data such as the lift coefficient C_L and drag coefficient C_D. This theory ignores the secondary effects such as the induced velocity of the fluid due to the rotation of the propellers, something that the momentum theory considers. For this reason, the theory have been found to over-predict the thrust, whilst under-predicting the torque, when being compared to real propeller results. Either way, the theory is deemed useful for getting a first prediction of the thrust, torque and efficiency of a propeller.

Blade Element Momentum Theory (BEMT)
The blade element momentum theory combines the concepts of the momentum theory and the blade element theory, in order to offer a more accurate prediction of the propeller performance [57]. BEMT treats the rotor as a series of concentric rings (or blade elements), each with its own aerodynamic properties. The theory accounts for both the induced velocity of the flow, as in momentum theory, and the local aerodynamic forces on each element, as in blade element theory. Inputs to the theory include both blade geometry, such as its chord length, and blade twist, and aerodynamic properties such as data regarding the airfoil design. In BEMT, the thrust T is given by:

$$T = \int_0^R \frac{1}{2}\rho U^2 \left(C_L \cos\phi - C_D \sin\phi\right) c \, dr$$

Where:

- ρ = Air density,
- U = Relative velocity at the blade element,
- C_L = Lift coefficient at the blade element,
- C_D = Drag coefficient at the blade element,
- ϕ = Inflow angle at the blade element (angle between the relative wind and the rotor plane),
- c = Chord length of the blade at radius r,
- r = Radial position along the blade,
- R = Radius of the propeller blade

If all other factors, such as the blade geometry, lift and drag coefficients, and velocity etc. remains constant, the thrust can (just like in the momentum theory) be considered proportional to the air density ($T \propto \rho$).

By looking at all of the mentioned theories, and at both the previous discussed disk-loading ratio and thrust-to-weight ratio, it is deemed relevant to maximize the propeller diameter within given dimensions in order to maximize the thrust (to achieve a higher thrust-to-weight ratio) and the efficiency. For obvious reasons, this maximization in propeller diameter should include the gap between the propellers as discussed in Section 3.1.1.1. It is not always the case that the propeller pitch can be chosen independently of the propeller diameter, however this pitch could be increased if more thrust were to be needed, with the trade-off of decreased efficiency.

3.3.2.2 Application of blade theories

Both the BET, and the BEMT need a lot of specific parameters relating to the design of the propeller blade, such as blade geometry and airfoil data. This is something that is expected to be very hard to access for a chosen propeller, since manufacturers generally keep these parameters secret in order to protect their proprietary airfoil designs. In general, it could be stated that the mentioned theories, especially BET and BEMT, are more beneficial when it comes to designing a propeller rather than choosing an existing one. The reason is that when designing a propeller there are a lot of unknown parameters that need to be optimized for, whilst when choosing a preexisting propeller the empirical test data on performance data-sheets (containing things like thrust at different altitudes, and at specific currents and RPM values) are more useful. Detailed theoretical analysis might not be necessary, as long as it is not deemed relevant to perform significant modifications or optimizations of the blade or propeller design. A propeller theory, like the previously discussed, could be implemented, and the input parameters changed until the desired output is reached, as per that in the performance data-sheets. However, this would be meaningless, since the output parameters could instead be taken from the performance data-sheet directly. This would cause some problems to arise, mainly that some of the modularity in the model's code would be lost. However, the data related to the propeller could simply be changed based on the propellers specific performance data, meaning that this is not really a problem. However, one problem is that the effects of air density on the thrust and therefore current draw and power consumption would be lost. Something that these theories do include. However, this could be researched independently, and be based on the performance data-sheet of the chosen propellers and motors, and the effect could be added to the model.

It have been found that these performance data-sheets (that usually covers the performance of a specific propeller matched with a specific motor) include a thrust for both sea-level, and for a specified altitude, for a number of given RPM values. Upwards thrust of a propeller is assumed to be proportional to its rotational velocity squared as displayed in the upcoming Section 5.3.1.1. This relationship can be seen in (3.1), where k is the lift constant:

$$T = k\omega^2 \tag{3.1}$$

Given different thrusts at both sea-level and at a specified altitude, from specific RPM-values, a k-constant that changes based on the air density could be created. If the RPM is constant with a change in air density, the thrust could be written as proportional to the air density, and since the thrust is proportional to the air density (as described by MT and BEMT), the k-constant could be stated as proportional to the air density ($k \propto \rho$). For this reason, a value of k could be calculated at both sea-level and the specified altitude, and then interpolated in-between in order to get a value of k for any air density. Utilizing this, the air density effect is included in the output thrust calculation in the model.

There is also a need to calculate the air density effect on the current drawn, and power demand, based on a given angular velocity. In some performance data sheets a thrust at both a specified altitude, which is what the other parameters are evaluated for, and the thrust at sea-level can be found. The calculated thrust at sea-level is based on the given RPM, which means that the power requirements will vary from what is stated in the specification sheet. Therefore, there is a need to derive the current draw at sea level, at a given RPM, in order to be able to include this altitude effect on the current and power in the model later. The power required to drive a propeller is given by (3.2) [58]:

$$P_{\text{in}} = 2\pi\rho k_Q n^3 D^5 \tag{3.2}$$

Where:

- ρ = density of the fluid (air),
- k_Q = torque coefficient that is a mainly function of the propeller design,
- n = propeller speed (rev/s),
- D = diameter of the propeller

The coefficient k_Q is primarily considered a function of the propeller design, but is also affected by the Reynolds number (R_e), the mach number at the blade tips (M_{tip}), and the advance ratio (J) [58]. For this reason, k_Q can change slightly depending on the altitude that the drone operates in. However, for moderate altitude changes, and at tip speeds, where the propeller is considered as not experiencing compressibility effects (since it is likely outside of the mach regime), k_Q can be assumed constant. The system is restricted by the tether length, and is therefore directly limited to rather low altitude changes. However, the entire system could be used in environments of higher elevation, e.g on a mountain. Even so, the torque coefficient is still considered constant. This is since the altitude change is merely considered relevant if heights were to reach upwards of a couple thousand meters (≈ 5000) or more. At lower altitudes, the air is still dense enough for the flow to stay in a regime where propeller behavior doesn't shift drastically. Therefore, the input power can be considered proportional to the air density and the cube of the RPM:

$$P_{\text{in}} \propto \rho \cdot \text{RPM}^3$$

So for constant RPM's, the power scales linearly to the air density. Since the power is linear to the current (P=VI), and the drawn voltage is roughly constant, the current is considered linearly proportional to the air density:

$$I \propto \rho$$

Since the current is considered proportional to the air density, the current corresponding to the thrust at sea level can be approximated, for the different RPM values in the performance data. Since the relationship between angular velocity and current is exponential, the output current for a given angular velocity can not be calculated using interpolation. Instead a polynomial function can be fitted to both the current, based on different angular velocities, at sea-level, and at the specified altitude. This can later be used to get a current at both sea-level, and at the specified altitude for a input angular velocity. Since I $\propto \rho$, the actual current drawn, based on the present air density, can be estimated using interpolation between the current at sea-level and 3500 feet for the input angular velocity. This is performed for each motor separately, and a total current can be derived by summing the individual motor currents. Since the voltage is said to be constant, and is based on the motor voltage. The total and average power consumption for the motor-propeller combination can be derived.

3.3.3 Overall propeller design

Previously, the affect of the individual propeller blade's design on the performance of the system have been explored, by focusing on a conventional propeller design. However, there are several different propeller-designs, each aimed to accomplish different performance goals. Some propellers are designed to increase portability or thrust output, while some are aiming for efficiency, and others prioritize minimizing the noise emissions. Many of these propellers differ from the "classic" propeller, both when it comes to the design of the individual propeller blades, but also when it comes to the placement of these individual propeller blades. The following section explores a variety of alternative propeller designs, highlighting how they differ from the conventional propeller, and how their design could affect the system performance.

Conventional propeller
The conventional propeller could be considered a reference in this analysis. This propeller can be seen in Figure 3.16, image (a). The conventional propeller is fixed in shape and configuration, meaning that it is one solid part, independent of the blade-amount. The blades of this propeller are usually straight or slightly curved. The propeller is considered as reliable, and excels when it comes to efficiency and thrust generation [48]. Since these propellers are of the conventional design they render widely available in different sizes, number of propeller blades, and in different materials. For this reason, these propellers have been found to generally be the least costly out of the designs.

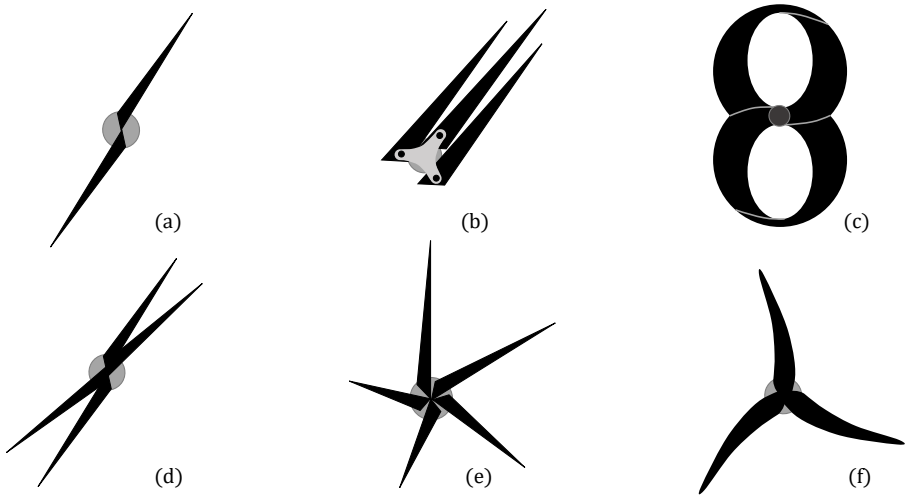

Figure 3.16: (a) Conventional propeller, (b) Foldable propeller (folded), (c) Toroidal propeller, (d) Unevenly spaced blades, (e) Blades of non-equal length, (f) Scimitar propeller. Note that these are for illustrative purposes. The number of propeller blades are not constant across all the displayed designs.

Foldable propeller

A propeller with collapsible blades, known as a foldable propeller can be seen in Figure 3.16, image (b). These propellers have blades that can fold against or over the drone's body, significantly reducing its footprint while landed or during transport [48]. This not only increases the ease of storage and the portability, but also largely increases the potential propeller size of the drone whilst being deployed as discussed in the area analysis in Section 3.1.1.1. This can, as also discussed, exponentially increase the produced thrust, whilst reducing the disk-loading-ratio, increasing the systems efficiency. Additionally, it can be recalled that the requirements that limit the drone's size only regards the size after landing (during transportation), and the drone size, disregarding the propellers, whilst landing (see Appendix A). This means that the drone, when landing is mainly limited by the motor-to-motor width, and not the total, propeller tip-to-tip width. A drawback that could be stated, relating to foldable propellers, is that the retraction time of the drone would increase. This is due to the fact that the propeller blades would have to be manually folded to within the base-dimensions after landing. Since the utilization of a propeller protection is also required, applying this to foldable propellers would mean that the protection would either have to be removed at landing, or in some-way folded together with the propeller blades. This is something that could also increase the total retraction time. However, it could be argued that in certain scenarios where the retraction time could be deemed very relevant, perhaps in applications related to natural disaster areas where danger could be quickly present, the protection could be removed pre-flight (if this is deemed more safe than the extra retraction time). One could theorize that extra time would be needed at deployment as well, for the exact same reason. However, these propellers usually unfold automatically due to the centrifugal force when the motor spins, meaning that the deployment time should not be affected. Another benefit of foldable blades, compared to conven-

tional fixed propeller blades, is a passive damping effect in lead-lag motion, due to the hinged design [50]. Lead-lag motion refers to the slight forward and backward movement of the propeller blades within their plane of rotation. This can increase the smoothness of the flight, and improve the overall flight stability, compared to a conventional propeller, where this motion can lead to vibrations and mechanical stress on the motor and propeller hub. In theory, due to the "free-moving" hinged propeller blades, the propeller cannot accelerate and decelerate as quickly as a fixed propeller. This is due to the blades own moment of inertia, which can cause a slight momentary mismatch in the angular velocity between the motor and the propeller. However, since the angular velocity and thus the centrifugal force is quite high, this mismatch could be reasoned to be very low, and should therefore not affect the flight performance noticeably.

Foldable propellers can be found with anywhere from two to six blades (with three blades in Figure 3.16, image (b)). The blades usually folds in the lateral direction, and as the number of blades exceed three, the blades usually fold in both the positive and negative local direction. This means that drone with a certain amount of rotors, in some configurations, would not allow for the propeller blades to be folded within the base dimensions, even though the motor could be located inside at landing. There are other foldable propellers that have their blades collapse either upwards or downwards, even though they are not nearly as common, these would counteract this problem. However, these propellers significantly increase the height of the drone whilst landed, but also eliminate the beneficial passive damping effect in lead-lag motion. It also counteracts the natural outwards-pushing centrifugal force experienced during rotation.

If a foldable propeller are compared to conventional propeller in terms of efficiency and thrust, it is reasoned to be a very small difference. The design of the individual propeller blades, and their length, does not require a significant change. The only differentiating factor is the mounting/hinge on the central hub. This mainly contribute with some, almost negligible, increase in drag, along with some additional weight. Therefore, it is reasoned that the small decrease in efficiency or thrust could also be neglected. This assumption has been confirmed when comparing performance data of commercially available propellers, combined with appropriate motors, and seeing only a very slight, if not, no difference in the performance. When looking at the availability of foldable propellers, they are deemed as largely available in different sizes. As the number of blades increase, the availability has been perceived as slightly decreasing. The foldable propeller do generally come at a higher cost, compared to the conventional fixed propellers, due to their increased complexity and the tolerances associated with the hinging mechanism.

Propellers designed to be silent

There a number of different propeller designs whereas the main aim is to reduce the noise emission. The means of doing this differs between designs.

The *toroidal propeller* have its blades looping together so that the tip of one blade curves back into the adjacent blade, see Figure 3.16, image (c). This closed-form structure minimizes the formation of vortices, that are otherwise mainly created at the tips of the blades [59]. Thanks to this design, the sound signals in the frequency range to which humans are most sensitive, are decreased. The propellers are also stiffer than the conventional ones, and also have a reduced risk of cutting or catching objects in the drones path. It is proposed that the thrust levels achieved are also "comparable" to that of a conventional propeller of the same size [59]. However, others suggests that the efficiency is almost reduced by 50% [60]. It must be stated that the latter tests included a propeller designed from scratch, since there are no readily available models online, unlike for traditional propellers. However, even if the propellers were estimated to have no reduction in efficiency and the decrease in noise were very beneficial, these would still be rather unsuitable for the system in question. The main reason being that propellers with this design cannot be made foldable. This largely limits their size and therefore thrust production. If a thrust is later required from the propellers, that requires the propellers to be foldable due to their size, these propeller cannot be utilized. Since the design is also (as of writing this) under patent protection, the availability of different materials and sizes are almost non-existent, leading to difficulties in acquiring the propellers either way.

The blades on a propeller are usually uniformly distributed around the central hub, and are of equal length. However, this is not essential. There are both propellers that have *unevenly spaced blades* and *blades of non-equal length*, see Figure 3.16, image (d) and (e) respectively. The reason for both of these design choices are the same. Traditionally, as the blades are evenly spaced, loud frequencies are created at the blade passing frequency and its harmonics [61]. By changing the spacing between the blades, or the length of the different blades, these frequencies are spread out over a larger number of tones, with the aim to reduce the overall perceived sound level. Some evidence does suggest that the noise is mainly reduced near the polar angels (in the plane of the propeller), whilst the noise is instead shifted away from the plane of the propeller. Therefore, this results in an significant increase in total acoustic intensity in the direction of the produced thrust, considering a propeller with uneven blade spacing [62]. These propellers could therefore be beneficial for fixed-wing aircrafts, where the plane of the propeller is perpendicular to the people below it. Since the considered tethered drone system will mainly be at hover and situated at xy-planes other than that of its observers, these propellers are deemed to have detrimental effects when it comes to noise emission. It can also be argued that, at least, propeller blades of non-equal length, would have an reduced efficiency and thrust, since they do not utilize the entire available space. Unevenly spaced blades would also be hard to design as foldable, since the centrifugal force would naturally want to spread the blades evenly.

Another propeller that benefits from reduced noise emission is the so called *scimitar propeller*, named after the resemblance to the curved scimitar sword. In some cases, this type of propeller design can also be found under the name "Polish propeller". This propeller have curved blades, see Figure 3.16, image (f), in order to

improve the propeller aerodynamics by mitigating the effects of compressibility, minimizing the effect of sonic shock wave formation. This increases the aerodynamic efficiency [48]. The sequent noise reduction due to this blade-sweep is in some cases seen as an incidental benefit [62]. This propeller design is primarily used in aircrafts and fixed-wing drones, but many standard multirotor drone propellers have also been seen adopting parts of this curved shape to achieve similar aerodynamic benefits. For this reason this propeller design can be considered merely a version of the conventional propeller, but with slightly lower noise emissions. From looking into available propellers, it could be said that there is usually no distinction made between the two, and therefore it might be hard to consciously chose just one or the other. However, for this reason they could also be considered as widely available.

To conclude, it could be argued that the conventional propeller design or the foldable propeller (perhaps with curved, scimitar shaped, blades) are the most appropriate for the system in question. This is both due to the fact that these designs indeed brings the most thrust and efficiency, together with the increased availability of these propellers in different sizes, with different number of propeller blades, and of different materials. Since the system is going to be modeled and simulated, it is also deemed beneficial to chose a propeller-design with high availability, in order to enable the extraction of various data from the performance data sheet (since higher availability of the propellers sequentially increases the availability of the performance data). The conventional propeller should be utilized over the foldable propeller, as long as the produced thrust is sufficient for the system. If more thrust is required, foldable propeller can be adopted, whilst sacrificing an almost negligible amount of efficiency and adding some time at retraction (due to the propeller having to be folded). If it is eventually discovered that a substantial margin in thrust or efficiency is available with the conventional propeller, it could become relevant to consider the utilization of propeller blades designed to be more silent. However, as discussed, most of these propellers rarely reduce the noise emission in the direction that can be expected for the observers (if this is considered to be anything other than near the polar angles of the rotors). Therefore, it is more probable that these performance margins could be used to increase the payload capacity, or flight height, among other things. It would also, as previously discussed, be rather hard to theoretically determine the produce thrust or efficiency of these alternate propellers. Without any existing performance data and with "classical" blade theories that don't apply to these designs (without performing significant modification), these designs could not be modeled.

3.3.4 Propeller material

The drone's propellers are available in a variety of materials, each offering their respective advantages and disadvantages. The most commonly used are *plastic propellers*, known for their low weight and cost-effectiveness. This not only makes them widely accessible for various applications, but also enables accessible and simplified replacement and repair [48]. However, this comes at the expense of lower durability and a tendency to deform under mechanical stress or high heat. As a result, plastic propellers are generally unsuitable for high-performance or heavy-lift drones.

On the other hand, there are *carbon fiber propellers*. These benefit from their low weight, just like the plastic propellers. However, they offer significantly greater strength-to-weight and stiffness. Additionally, carbon fiber propellers have an enhanced flight stability and aerodynamic performance, compared to plastic propellers. Some argues that they are also less prone to vibrations [48], perhaps because fo their increased aerodynamic performance. Although, others mean that it is instead plastic propellers that are less susceptible to vibrations, due to their lower rigidity (which also becomes beneficial in terms of shock absorption) [63]. Either way, carbon fiber propellers come at a much higher cost than plastic propellers, and are also more brittle, making them susceptible to cracking upon potential impact.

Either way, considering the requirements of a high-performance and heavy lifting drone that is being developed, where cost could be deemed a secondary concern, carbon fiber propellers are considered most suitable for this application. Their high strength-to-weight offer clear advantages in terms of performance, where additional weight instead could be utilized for heavier payloads or longer flight times, among other things. While carbon fiber is more brittle than plastic, and therefore prone to cracking upon impact, this drawback can be considered to be mostly mitigated since a propeller protection is required to be incorporated in the design.

3.3.5 Efficiency and performance of coaxial rotor variations

It can be recalled from Section 3.2.4 that there is literature that proposes that a reduction in the upper propeller radius could lead to efficiency gains. The lower rotor is working in the downwash of the upper, where a reduction in the upper rotor would allow for more "clean" air to enter the lower rotor [47], making it operate more efficiently. The efficiency gain was estimated to reach upwards of 13.5%, with a radius reduction from 76 to 70 cm. It was also determined that these efficiency gains was radically decreased if these propeller sizes were decreased. Since no configuration could allow for propellers with radii anywhere near 70-76 cm, the efficiency gain could also be estimated to be much lower than 13.5%. It is reasonable to also assume that while increasing the efficiency, the total thrust output is reduced.

Another paper proposes that changing the upper propeller's diameter had almost no influence when it comes to efficiency. Meanwhile increasing the lower propeller's diameter increased the efficiency, while decreasing it resulted in a lower system efficiency [33]. This is unfortunate due to the fact that the more space is in actuality available for the upper rotor compared to the lower rotor, given the payload blackbox dimensions. Therefore, no extra space that would allow for an increase of the lower rotor is available, since it is already desirable to opt for an maximization of the size of both propellers. Additionally, this paper further proposed that any variation in the upper propeller's pitch (compared to that of the lower) resulted in a decrease of the efficiency of the coaxial system. A reduction in the lower propeller pitch yielded the same result, meanwhile an increase in the lower propeller pitch actually increased the efficiency of the system. Increasing this pitch will as previously dis-

cussed induce a higher drag on the propeller, but also an increase in thrust, which must be proportionally higher than the increased power demand due to this drag. By changing the pitch of the propeller it could be argued that the 14-22% reduction in thrust as concluded in Section 3.1.3, instead could be considered as a somewhat smaller (than 14-22%) reduction in efficiency, while maintaining the same thrust.

If the lower propeller where to have a higher pitch than the upper, it would also be recommended to utilize motors of different Kv values. Since a higher pitch increases the drag, and therefore the torque needed to produce the same angular velocity, the lower motor should have a lower Kv value than that of the upper. This would introduce some further complexities. Different motors and propellers would most likely lead to a higher total cost, since the total number of different components increases. For this reason the ease of manufacturing, repairs and replacements would also be slightly hampered. This is extra important for a tethered system, since drone motors naturally have a limited life time and are usually designed and used by non-tethered drones. Therefore, this life-time could be reached more quickly when utilizing a tethered system, since individual flight times could reach up to an order of magnitude longer or more, compared to conventional battery limited flight. Clearly this flight time depends on the specific application in question, but if these motors would have to be changed at regular intervals, the entire supply chain would benefit from the employment of the same motor model up and down. It is not unreasonable to apply the same motor up and down, while using propellers of different sizes, however the effects related to the thrust/efficiency gain would likely not be as large (and would be hard to ascertain).

3.3.6 Propeller size selection

It has previously been discussed that a motor with certain Kv rating is generally chosen based on the propeller size, see Section 3.2.2. It can be recalled that the Kv rating is a number that corresponds to the RPM per volt, and is inversely proportional to the torque. Therefore, lower Kv ratings are suitable for heavier drones, that are equipped with larger and therefore heavier propellers [36]. However, what specific Kv rating that is suitable for what propeller size remains unknown.

Generally, when designing a drone system, the propellers are selected first, based on several factors. This is primarily determined by the available space, but also whether efficiency or agility is prioritized, could be considered. Usually after this, the motor is chosen and matched with the propellers based on factors such as the Kv rating. How this process in actually is performed can be considered rather fuzzy, an opinion many in the field seem to share. There are a number of look-up tables online, which covers different propeller sizes and battery voltages, and recommended motors respectively. However, these are generally for smaller, more entry-level drones with propeller sizes not exceeding 280 mm, see [64], [64].

Another method would be to utilize the relationship between Kv rating, RPM and voltage. It was previously stated that due to the relationship of $Kv = RPM/V$,

given the Kv rating of the motor, the RPM can be estimated by multiplying the Kv value with the voltage of the power source. However, this could also be used to form a upper limit of what Kv rating a motor could have. This comes from the fact that many propellers are specified with a maximum RPM value. Knowing the system voltage, the Kv can be estimated as RPM/V, since any higher Kv rating than that would produce a RPM higher than what the propeller could structurally handle. However, since this system is tethered the voltage utilized is also unknown, and will be subsequently chosen based on the motor requirements.

In practice, when one looks at a specific propeller, they have often been found to be matched with one (or several) recommended motor(s) by the manufacturer. This is especially true for high-performance and larger propellers, and aims to accomplish the optimal performance of the entire propeller-motor pair. For this reason, the problems relating to the choice of motor and its Kv rating, based on the propellers, are not particularly significant when merely choosing appropriate components used as performance references for a drone system. In contrast, such problems would become more noticeable if a motor were to be designed from scratch based on the specific system or propeller. Therefore, as the propellers and motors are generally not chosen independently there is an aim to utilize existing performance data that relates to specific propeller-motor combinations. It is, as many times previously discussed, beneficial for this drone system to employ a propeller of the largest possible size given the limiting dimension, in order to obtain the maximum efficiency and thrust. Therefore, a motor that is recommended for that specific propeller will sequentially be adopted.

3.4 Tether

The drone's tether serve multiple purposes when it comes to the functionality of the drone, and the drone itself. The tether is what carries the power from the ground station to the airborne system and its components, such as the motors, enabling any kind of flight. It also transfers data between the drone and potentially its payloads, and the ground station. Additionally, the tether functions as a fast and controlled means of landing, by utilizing a winch system to retract the drone. Keeping the tether under a constant tension also increases the stability of the drone. The following research questions have been formulated in order to guide the research related to the tether, and determine how the design of this relates and influences the performance of the system.

- What material components should be included in the tether, what are their purposes, and how do they affect the performance of the system?
- What components should be included in the onboard power conversion system (tether air module)?
- How does the voltage and power demand affect the the total size and weight of the tether and air module, how does this affect the performance of the system?

3.4.1 Tether material

The drone's tether is usually an optoelectronic composite cable, which combines optical fibers for data transmission, with electrical conductors for power transmission, within a single integrated structure. This cable can generally be considered as divided into four main components, something that can be seen in literature and in several COTS tethers [65], [66], [67]. These have their own material(s) and purposes which can satisfy different requirements of the system. These components are the conductor itself, a communication component, a insulation layer for the conductor, and a strengthening layer, all which can be seen in Figure 3.17. In addition to these, an outer most protective layer might also be present, to ensure weather resistance.

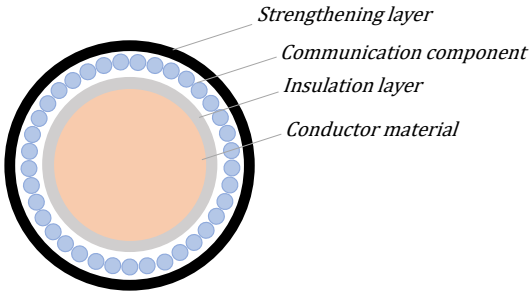

Figure 3.17: Cross-section of tether, with its different components. Note that this is only for illustrative purposes, and the size, shape, placement and amount of the components may differ from reality. For example, it can be reasoned that there would be dual conductor components, one for supplying power and one that acts as a ground, both with their individual insulation layer.

When analyzing which specific materials these components should be made up of, it would seem relevant to perform a material analysis, perhaps in Granta EduPack. However, the materials in the cable appear to be largely standardized for applications, and drone sizes, similar to the analyzed one [66], [67]. Therefore, reimagining this design would not only be unnecessary and time consuming, but would also complicate subsequent analyses. Utilizing a design similar to COTS tethers is beneficial, particularly when it comes to aspects such as weight estimation given specific power demands, tensile strength approximations, and also knowledge regarded that the tether is flexible enough be winded onto the tether drum without being damaged. A description of a cable, that frequently appears, is that it consists of an alloy lightweight high-temperature-resistant aviation wire, a composite fluoroplastic insulation layer, and a high-modulus tensile aviation-grade fiber woven layer. The following provides an overview of the tether's individual components, their respective functions, and an explanation behind the choice of the different materials.

Conductor - aluminium alloy

The conductor is a crucial component in the tether, responsible for transferring the power from the ground to the drone. It must strike a good balance between low weight and a high conductivity, in order to maximize the efficiency, through an minimization of energy losses. It must enable transferring of enough power,

for the drone to achieve at least its 2:1 thrust-to-weight ratio. To meet these demands, a lightweight high-temperature alloy aviation wire is used. This is typically an aluminium alloy which is usually used when the importance of the weight-to-conductivity ratio outweighs the pure conductivity [68]. Additionally, the high-temperature resistance ensures that the conductor can safely handle the continuous power transmission without risk of overheating or degradation, making it suitable for demanding operational environments, such as long-duration flights.

Communication component - fiber optics
The communication component is responsible for enabling high-speed data exchange between the drone and the ground station. To meet these requirements without significantly increasing the system's weight, single-mode fiber optics are used. Fiber optics are ideally suited for this application, as they support rapid transmission of large volumes of data [69]. Additionally, they secure the data output through an increased immunity to electromagnetic interference and jamming, all while being significantly lighter than traditional copper-based solutions [70]. This makes them an optimal choice for tethered airborne systems, where both communication reliability and weight efficiency are critical.

Insulation layer - composite fluoroplastic
The insulation layer serves multiple purposes aimed at enhancing the safety of the tethered drone system This layer is typically made from a composite fluoroplastic material. Exactly what this material is, is deemed rather unrelevant, but it provides electrical insulation, prevents short circuits, leakage currents, and protects the system from exposure to high voltages. A fluoroplastic material is also chosen for its thermal resistance, and chemical stability, which also help prevent heat buildup within the cable during operation. Despite these protective qualities, the insulation layer remains lightweight, maintaining the overall weight efficiency of the system.

Strengthening layer - fiber woven layer
The strengthening layer increases the tensile strength of the tether, ensuring that the tether can be kept under constant tension without it snapping, in order to increase the stability of the drone. It also enables the retraction of the drone, through the usage of the tether winch. Typically, this is composed of a high-modulus tensile aviation-grade fiber woven layer, often made from materials like Kevlar, which provides the mechanical strength necessary. Additionally, it protects the internal components of the cable from dynamic loads, such as tension impulses caused by wind or the drone's retraction process while also minimizing additional weight.

Although the cable is composed of materials with a relatively high Young's modulus, such as high strength fibers and alloys, it clearly remains flexible enough to be wound up and retracted efficiently. Meanwhile, the stiffness of the cable ensures structural integrity and prevents excessive deformation under tension. This balance between stiffness and flexibility is critical for both maintaining stability during operation and enabling retraction and convenient storage.

It must be specifically ensured that the tensile strength of such a tether is sufficient for this application. An estimation of the drone weight, looking at drones with similar payload weights, has an upper boundary anywhere between 30-40 kg. Utilizing the highest value of 40 kg and an thrust-to-weight ratio of 2:1, the drone would inherently be able to produce 80 kg of thrust. It can therefore be reasoned that the tensile strength must be at least equals to the difference between the maximum amount of thrust that can be produced, and the weight of the drone (without payload of upwards of 15 kg, therefore 25 kg), meaning 55 kg. Looking at the tethers that have previously been used as references for this design, they have a tensile strength of ≥ 300 and ≥ 200 kg respectively [66], [67]. This would therefore enable a safety factor of around 5.5 and 3.6. This safety factor is deemed sufficient when it comes to the management of impulses in the tensile load. Additionally, this is deemed as a sufficient tensile strength for retracting the drone with the cable.

3.4.2 Airborne tether components

In preexisting drone tether system solutions, there is often a system referred to as the *tether air module* [66], [67]. The tether air module, is the part of the tether system that is situated on the drone itself. This module mainly acts as an onboard power conversion system, and therefore includes a DC-to-DC converter that enables safe and efficient conversion of high-voltage power supplied from the ground, and also associated active heat dissipation mechanisms. Additionally, the module serves other purposes such as power distribution to different onboard components, and provides system monitoring and diagnostics capabilities.

Not all of these mentioned functions are included in the functional description of this system, see Section 2.5.1. The active cooling of the DC-to-DC converter can be considered as a necessary subsystem of the converter itself, that enables it to function over extended periods. This is particularly critical when stepping down from high supply voltages to usable voltage level, especially when handling high power levels that this system will certainly have to do. This can be assumed, since even though a converter with a high efficiency (e.g 95%) would be utilized, a significant amount of energy would still be dissipate as heat. Therefore, effective thermal management is necessary to not only maintain performance and reliability, but also to reduce the concentration of heat generation within the system. On the contrary, functions such as system monitoring and diagnostics are surely beneficial, but have not previously been considered for this system. It is still believed that the weight and performance of this system can, once again, be approximated by looking at preexisting systems. Even though not all of these functions are totally necessary, these do provide an extra margin when it comes to the weight of this systems *tether air module*. This is especially beneficial if the power demand of this drone exceeds that of the reference systems previously examined, since the weight of the converter generally increases with higher power levels, even when the supply voltage remains the same.

In addition to the components in the tether air module, other airborne components relating to the tether are required. Mainly it has been identified that there

needs to be something that enables rotation of the drone with respect to the tether. Either rotations of accidental nature, such as caused by the environment, or that the drone equipped with some payloads might benefit from performing full rotations, perhaps several or continuously. This is in order to prevent torsional shear stresses caused by excessive twisting of the cable. Something that could lead to a torsional load exceeding the sheer strength of the material, which could result in torsional shear failure. This needs to be prevented in order to ensure reliability of the system.

One potential solution would be to incorporate the usage of a slip-ring between the tether and the tether air module. However, a traditional slip-ring only enables continuous electrical transmission. It must be recalled that the tether consists of several components, where the fiber optical communication component also needs to function, regardless of the relative tether and drone yaw-angle. There are also something called a fiber optic rotary joint (FORJ), which is the optical equivalent of a slip ring, and allows for continuous rotation while maintaining the integrity of the optical signal. Thus, the core challenge remains, where a slip ring cannot be used for power transmission and a FORJ for optical communication at the same time. Both components require placement along the central axis of the tether. This creates a design conflict, as the tether would need to carry both power and data while allowing for free rotation, which traditional slip rings and FORJs cannot achieve together. Possible solutions to this problem could be to transform the optical signal into an electrical signal before the slip ring with an transceiver, and transforming it back to an optical signal afterwards if required. However, this would drastically increase the complexity and could lead to unwanted signal degradation and latency in the system. Another solution could be to utilize wireless transmission for the data signal. However, this compromises the security of the data being transferred, which is unacceptable. Lastly, there are some available hybrid rotary joints, which combines a slip ring (for power) and a FORJ (for fiber optics) into a single rotating assembly. These are available for high-voltage and high power transmissions, along with continuous fiber-optic communication, while allowing unlimited rotation without twisting the cable [71].

Looking at existing hybrid rotary joints, it is evident that these would have no problem to cover the power and voltage requirements of the system. It must however be noted that this would introduce additional weight and complexity to the system, but is regardlessly deemed necessary for the modular function, and reliability, of the drone. In addition to the extra weight, this hybrid rotary joint would introduce the need for some further considerations. Since the hybrid rotary joint is not designed to withstand tensile loads, there would need to be decoupled systems that manages the the rotational and tensile load at the attachment point of the tether. This tension management system would need to account for the continuous tether tension, as well as the increased tension during the drone's retraction. While the design of this dedicated system falls outside the scope of the current project, it is essential that it allows for yaw rotation, while managing the tensile load through another suitable structural arrangement, something that would in turn also contribute to the total system weight.

3.4.3 Voltage, power demand and tether weight

What voltage that is most beneficial to feed through the tether, what power demand will be present, and how this affects the tether weight needs to be analyzed. A literature review analyzed data from 182 publications related to tethered drones. It found that high-voltage DC energy transfer was generally the preferred energy transfer solution [2]. However, the review noted that the specific approach used in these studies was not explicitly described. The few publications that actually described their energy transfer techniques mostly used DC voltages over 100 V to minimize the losses due to the Joule effect in the tether. The Joule effect is a physical effect where current flow through a conductor generates heat [72]. How much larger than 100 Vdc is however unclear. The drone's total power demand can be mainly associated with the power demand of the motors, since these are by far the greatest power consumer. This power demand something that is unknown at this point, but formulating a relationship between power demand and tether weight is important.

It is, as discussed, of great importance to minimize the weight of the tether (as per D6.2 in the requirement specification, see Appendix A) without compromising it's performance. One way to reduce the tether weight is to increase the supply voltage. Since power is given by $P = VI$, a higher voltage allows the same power to be transmitted with lower current. While this does reduce the energy loses due to the Joule effect in the tether, the primary benefit is not the loss reduction itself, but rather the ability to utilize a thinner cable. Therefore, reducing the current leads to a smaller cross-sectional area in order to maintain a constant amount of (acceptable) losses. Something that directly translates into a lighter tether. However, increasing the supply voltage also increases the demands on the onboard power conversion system, or the DC-to-DC converter. Due to a higher voltage, the DC-to-DC converter itself have been seen to generally increase in both size and weight. Additionally, solutions relating to thermal management also seem to increase in complexity, size and weight.

Another approach is to reduce the supply voltage and increase the current. This would result in an increase of the tether thickness, in order to decrease the resistance, and thereby maintain the same acceptable power loss level. This would reduce the demands on the onboard power conversion system, resulting in, what would be reasonable to assume to be, a lighter and less complex DC-to-DC converter and thermal management system. This can be considered a trade-off, and it is unknown which approach would yield the lowest total weight, and highest general benefits.

If the tether length, power consumption, power loss, and resistivity are assumed to be unchanged between the different approaches. A relationship between the different voltages, and cross-sectional areas (which directly determines the weight given the constant length) can be derived as:

$$A_2 = A_1 \cdot \left(\frac{V_1}{V_2}\right)^2$$

Therefore reducing the voltage by lets say a factor of 4 in order to reduce the weight of the onboard power conversion system, increases the cross-sectional area, and thereby the weight of the tether by a factor of 16.

Looking at preexisting tether systems for drones of similar sizes [67], it can be concluded that a tether with an supply voltage of around 800 Vdc, inputs around 715 Vdc to the drone's power conversion system. This utilizes a tether weighing around 2900 g per 100 meters. Therefore, if this supply voltage were reduced from 800 to 200 Vdc, the cable weight would based on the mentioned relationship increase to 46400 g per 100 meters ($2900 \cdot 16 = 46400$). This would clearly not be recouped with any lighter power conversion system, making such a reduction in voltage practically unfeasible. Additionally, increasing the cross-sectional area to maintain a acceptable power loss level, would also increase the drag on the tether, since the diameter would increase linearly with the decrease in voltage. Therefore, a factor 4 reduction in voltage would also lead to 4 times the drag-force on the tether.

In practical tether design, it might not be reasonable to maintain the same power loss over different voltages and current, specifically due to this quadratic increase in cross-sectional area and weight. However, even though the power loss is allowed to increase, and the cross sectional area is instead assumed to scale linearly with current, a 200 Vdc system would still result in a tether weight of 11600 g per 100 meters ($2900 * 4 = 11600$). This is clearly still not recouped with any lighter power conversion system, since this system for available tethered systems and 800 Vdc tethers weighs no more than 4300 g [66].

If the cross-sectional area, and therefore tether weight, is linearly scaled with current, this means that the weight can also be linearly scaled with power demand, given a constant voltage. However, looking at existing tether cables of (12Kw, 2900g/100m) [66] and (6Kw, 2100g/100m) [67] a nonlinear relationship can be seen between power demand and weight. Even though this appears strange, it must be recalled that the tether includes other components than merely the conductive part (which is the part that do scale with power demand). Things such as the fiber optics, the shielding etc. that also makes up portions of the weight, does not have to be significantly scaled with an increase in power. Therefore, an assumption that the entire tether weight is considered to be linearly scaled with power demand, could be considered conservative, since the actual tether weight would be lower. This would instead allow for extra margins that could for example account for some of the extra power losses that appears with an increase in power demand, and therefore deemed as a beneficial assumption.

It is also interesting to define the relationship between tether length and weight. Does this scale relatively linear, where extra power losses due to the increased length can be considered negligible? In practice, the resistance, and therefore power loss scales linear with the length of the tether, since $P_{loss} = I^2R$ and $R = \rho * L/A$. Therefore increasing the length with a factor of 2, while keeping the same power loss, would require a doubling of the cross-sectional area of the tether, and therefore

double the weight. However, as previously discussed, the tether will be based on a preexisting reference tether. As long as this reference is of equal or greater length, than this final tether, this serves as a conservative assumption, suggesting that the actual power loss and weight of the final tether will be equal to or less than those of the reference.

Therefore to conclude, it is clearly better to utilize a higher voltage in terms of total tether and air module weight. Looking at preexisting systems many of them seem to operate in the $\approx$ 600-1000 Vdc range [66], [67], [73], rendering the 800 Vdc mentioned above as a rather reasonable voltage level. It can be reasoned that the motivation for not using even higher voltage levels, to further reduce losses, is that the current loss levels are considered acceptable within the system, and are balanced against factors such as safety, weight, and system complexity. Ensuring a thin cable and low weight not only increases the efficiency of the system, since the system needs to carry less dead weight (tether), but also counteracts the excessive drag-forces that would emerge, and ensures a low space, which enables efficient storage. Keeping the tether at a low weight is also beneficial in terms of the system responsiveness and maneuverability, since the moment of inertia is clearly decreased with a lower weight. All of this is achieved while keeping the power outside of the high-voltage territory ($\leq$ 1500 Vdc), which allows for the avoidance of complex safety and compliance requirements as stipulated by Swedish law [74]. Furthermore, it seems both reasonable and beneficial, to assume a linear relationship between the power consumption and total tether weight, as well as between tether length and tether weight.

3.5 Other subsystems

The subsystems that have been deemed as the most important have been researched, but many systems still remain largely unexplored. Instead of formulating specific research questions for these, this investigation focuses on broader considerations related to each subsystem. While many additional questions could be explored, the scope and limitations of the project necessitate a more focused approach. As such, the investigation is merely concerned with identifying what is required to estimate the weight of various components and to assess their general affect, or lack thereof, on the overall system performance, together with compatibility with the other subsystems.

3.5.1 Power supply

The power supply system produces the electrical power that is delivered to the drone via the tether. The power supply is a limiting factor in the design of the drone, since this needs to be able to supply the required power to the drone system (including the peak power at 100% motor throttle, and the continuous power demand of the drone). This power supply would, for this application, most probably be a portable gasoline generator. The size of this generally increases with an increase in power output, and is ultimately limited by the base dimensions of 1100 $\times$ 1500 mm, as

seen in the requirement specification. It would be beneficial to maximize the power output of the generator, in order to maximize the opportunities that this brings to the design and function of the drone, in terms of both extra payload weight, or longer continuous flight-times. The largest available portable generator (in terms of output power) that could be found, that fits inside the base dimensions, could supply a continuous power of 19 kW, with peak power of 22 kW [75]. The dimensions of this generator is roughly $1092 \times 733 \times 733$ mm. It could be argued that it would be beneficial to utilize two smaller generators with a collective power output that corresponds to the power output of the single generator, in terms of redundancy. Since if one stopped working, the other one could theoretically sustain a hovering of the drone, since the thrust-to-weight ratio is at minimum 2:1. Therefore, the drone should be able to hover at half throttle or less, where even less power would be needed, since the efficiency (g/W) increases with decreased throttle.

It could be believed that the utilization of two generator units would produce a higher noise level, something which is advantageous to reduce at the base of the system. Looking at the previous cited generator, it can be seen that the 19 kW generator produces a (weighted) sound level of 79 dBA (which generally corresponds to a even higher dB level). A 9.5 kW generator (half of the 19 kW power) produces a sound level of 74 dB [76]. However, sound levels in decibels are measured on a logarithmic scale, meaning that two sources producing 74 dB achieves a combined sound level of approximately 77 dB. This is still below the 79 dBA produced by the single 19 kW generator. Therefore, from a noise perspective, using two smaller generators may actually result in a slightly lower overall sound emission.

However, as previously stated, the size of the generator(s) are limited by the base dimensions. Looking at the generator that produces 9.5 kW (half of the 19 kW power), the size is roughly $737 \times 762 \times 660$ mm. Therefore, two of these would theoretically fit inside the 1100×1500 mm base dimensions and occupy $1472 \times 762 \times 660$ mm (depending on orientation). In spite of this, it must be recalled that other systems such as the tether winch mechanism, the landing platform, the control station must also fit inside of the base. Therefore, it is assumed that in practice only one power supply, of roughly these dimensions, could fit within the base. Utilizing one generator unit would also bring other benefits, such as a decreased complexity with only one fuel tank, one set of start buttons, which could contribute to a shorter deployment- and retraction time. Furthermore, the redundancy that could theoretically be achieved by the usage of two smaller generators could instead be achieved with, the already incorporated, backup battery.

This generator achieves an 8-hour runtime at 50% load, which can be assumed to be the most common operating condition, given the 2:1 thrust-to-weight ratio and the drone primarily remaining stationary in hover. This runtime could be increased (from the generator standpoint) by simply refueling the tank every 8-hours (or as needed) in order to achieve a continuous deployment of the drone system.

3.5.2 Backup battery

The drone's battery aims to serve as a backup in case of failure of the supplying of power, with the aim to still enable landing. This can be either the power supply that stops running, or any type of tether failure that would hinder the supply of power, such as a complete snapping of the tether. Therefore, mainly the battery capacity and weight of this backup battery has to be determined, based on a given backup flight duration, system voltage levels, and the current draw of the motors. Looking at existing batteries, specifically designed for drones, specific battery sizes C_{ref}, weights W_{ref} and operating voltage levels V_{ref} can be determined. It would be beneficial if this data could be used in order to determine the weight of the systems backup battery, $W_{battery}$. Firstly the battery capacity needed to fly for a specified duration t_{flight} (min), with a set number of motors N_{motors}, and their current draw I_{motor}, would have to be determined. The battery capacity (in mAh) that is required for the system, $C_{battery}$ is provided by (3.3).

$$C_{\text{battery}} = \frac{I_{\text{motor}} \cdot t_{\text{flight}} \cdot N_{\text{motors}} \cdot 1000}{60} \tag{3.3}$$

The battery capacity is calculated based on the current draw at hover and the desired untethered flight time. Since the drone is expected to primarily operate in hover, the current at hover is used to calculate the required battery capacity. As the battery is designed as a backup, it's important to note that during landing, the current required will in fact likely be lower, as the drone mainly descends, drawing less power compared to at hover.

In order to then determine the weight of the battery, several assumptions are made. Firstly, it is assumed that the reference battery and the required battery have the same energy density and that the performance characteristics are consistent across both systems. This implies that the weight of the battery will scale linearly with its energy capacity. Additionally, it is assumed that voltage is adjusted linearly by changing the number of cells in series to meet the required voltage of the system, and then also scaled linearly by this reference-to-required voltage ratio. It is also assumed that the increase in weight due to these parameters will not result in disproportionately larger packaging or structural weight.

Utilizing these assumptions, (3.3) and data from the reference battery, the weight of the battery, $W_{battery}$, can be determined by (3.4).

$$W_{\text{battery}} = W_{\text{ref}} \cdot \left(1 + \frac{C_{\text{battery}} - C_{ref}}{C_{\text{ref}}}\right) \cdot \left(1 + \left(\frac{V_{\text{system}} - V_{\text{ref}}}{V_{\text{ref}}}\right)\right) \tag{3.4}$$

These equations can be used regardless of the desired untethered flight time. However, it could be noted that the battery weight is calculated using the battery capacity with the current at hover, which is in actuality influenced by the drone's total weight (which the battery weight is a part of). For this reason, an iterative update

of the current, based on the battery weight, would have to be performed. Furthermore, what the desired flight time is can be considered based on the application in question, since it might be beneficial to equip the drone with a larger backup battery in more demanding environments, or a smaller battery if there is instead a desire to have payloads of higher weight. Regardless, it is believed that a minimum of five minutes of battery-driven flight would be needed regardless of application in order to enable an emergency landing.

3.5.3 ESC

The electronic speed controllers (ESCs) are vital components in the drone's propulsion system. they control the speed of the motors by regulating the power delivered, responding to instructions from the flight controller. When choosing an ESC, it is essential to ensure compatibility with both the system's voltage (which is the voltage output from the tether air module or the voltage of the backup battery), and the current draw of the motor-propeller combination when operating at full throttle [77]. ESCs have two current ratings, continuous and burst/peak. The continuous rating indicates the amount of current the ESC can handle over extended periods, while the burst or peak current rating represents the maximum current for short durations (around 5 seconds). It is important to choose an ESC with a current rating that exceeds this peak current of the system, in order to ensure safe and reliable performance under various operating conditions.

3.5.4 IMU and flight controller

The IMU and flight controller are key components of the drone's control system. The IMU measures motion and orientation (using accelerometers and gyroscopes), while the flight controller processes this data to stabilize and control the drone, through inputs to the ESCs [78]. It is essential for the flight controller, and the IMU in turn, to support the voltage level of the system. For this tethered drone, GPS compatibility is not required, but redundancy is essential to maintain control in case of component failure. This could be achieved by incorporating multiple IMUs on the drone. Many modern flight controllers come with one or several built-in IMUs, to provide this redundancy. The power demands of these components are considered minimal, compared to the total system consumption, and can therefore be neglected.

3.5.5 Propeller protection

Protection of the propellers is required in the xy-plane of the drone, in order to ensure safe usage of the product. This is both for the safety of the drone itself, while it is deployed, and for the safety of the user and its surroundings whilst being retracted. The propeller protection is assumed to have no direct affect on the performance of the propeller-motor combination. Instead, the protection is only considered to affect the system in terms of weight, together with drag in the x- and y-directions. The reason for neglecting its influence on performance is that the propeller protection is merely aimed to cover the propellers in the xy-plane. Therefore, their height will

only be determined by the minimum height required in order to ensure their structural integrity. This height is regarded as rather low, especially if the protections were to be produced in carbon fiber. Additionally, looking at commercially available propeller protections, which are mainly adopted for smaller drones, these appear to have a very small height [79]. If these protections are linearly scaled based on the radius, and their weight being multiplied by a factor of 2 for extra sturdiness, the height of the protections would still be relatively low. For this reason, these are conclusively deemed to have no affect on the aerodynamics of the propellers.

Due to multiple potential configurations of this system that utilize foldable propellers, as discussed in Section 3.1.1.1, some extra design considerations have to be made with regards to the propeller protection. One benefit of using foldable propellers, over for example foldable arms (as a means of increasing propeller size and thrust) is that foldable propeller does not need to be unfolded manually before deployment, contrary to foldable arms. This reduces the total deployment time of the drone. However, if propeller protection were to be added, these would have to be added in place manually before deployment. At landing, the foldable propeller could be simply rotated over the respective arms, to enable transportation within the given dimensions. However, prior to this, the propeller protections would have to be removed, since they would extend outside of the usable area of the landed drone. Therefore, it would be beneficial to design these protection in such a way that they could also be rotated over the respective arms, together with the propeller blades. This would remove some of the extra time associated with adding the protection before deployment, and the majority of the extra time required after landing. This would require the individual protections to rotate around shared rotational axes with the propellers (i.e. the rotor rotational axis).

3.5.6 Converters

As seen in the functional description, two converters are included in the system. The first one is an AC-to-DC power converter that converts the power from the power supply from AC to the DC before it is supplied to the tether. Subsequently, a DC-to-DC converter is present, as a part of the tether air module, that converts the voltage down to an appropriate and usable level for the system. As previously discussed, the weight of these are said to increase with increased power demand. This is mainly relevant for the onboard converter, something that has already been discussed in Section 3.4.2. Beyond the weight of the converters, their conversion efficiency also influences the performance of the system, mainly with regards to the power that is needed to be outputted from the power supply compared to the actual required power of the drone. The efficiency is clearly beneficial to maximize, in order to increase performance and reduce the heat development in the system. The efficiency of a converter is negatively influenced by the converters internal resistance, something that increases with higher currents [80]. For higher voltage systems, which must be considered in this case, the efficiency of both the AC-to-DC and DC-to-DC converters is assumed to reach upwards of 95%, based on existing available converters and literature [81], [82].

4

Concept generation and evaluation

Previously, several subsystems have been investigated with regards to a number of research question, in order to determine how different design choices would affect the performance of the system. Several of these choices can be made independently of the rest of the design. However, some of these need to be evaluated together on a system level. The following chapter presents a process where concepts are created, compared, evaluated, and eliminated, resulting in a final concept.

4.1 Concepts

To enables this evaluation, several *concepts* are constructed through the combination of a number of (what could be considered as) sub-solutions. This is the combination of the following. Firstly, the number of rotors is included, where the options being a quadcopter, hexacopter, or octocopter. Additionally, the different configurations discussed in the area analysis (see Section 3.1.1.1) are included. This relates to if the propellers are foldable or non-foldable, and if the drone should be designed to land in any yaw-angle or is limited by a specific yaw-angle. Lastly, if the drone is utilizing a non-coaxial or coaxial setup is included, thus if there are one motor on each arm, or two motors acting in the same rotational axis. Initially all these concepts are utilizing a 2-bladed conventional propellers, either foldable or non-foldable, since this offers the highest efficiency. This combination of rotor count (3 options), configurations (foldable/non-foldable), yaw constraints (specific/any), rotor arrangement (coaxial/non-coaxial), and a fixed 2-bladed conventional propeller results in a total of 24 design concepts ($3 \times 2 \times 2 \times 2 \times 1 = 24$).

However, before initiating any type of comparison and evaluation between these concepts, some concepts are excluded as they do not satisfy the system requirements. The non-coaxial quadcopter is eliminated, since it has been found to lack redundancy (see Section 3.1.1.1). A key requirement of the system is that the drone must be operable in the event of a single motor failure, a criterion this concept does not fulfill. Additionally, all the concepts that are associated with landing in a specific yaw-angle are eliminated due to practical constraints in complexity, time and reliability. It is deemed unrealistic to design and model a drone system that would be able to handle this landing repeatedly, especially while subjected to harsh environments such as strong winds, and where there is a great importance to maximize the retraction velocity. Landing in any yaw angle would require less rotational control over the drone at landing, which would result in the ability to retract the

drone by simply initiating the winch, while maintaining a certain tensile resistance. Furthermore, as seen in the area analysis in Section 3.1.1.1, no area were lost by enabling landing in any yaw-direction, except for the quadcopter.

Following these eliminations, 10 concepts continue to be considered for evaluation and comparison. These can bee seen in Table 4.1, where they are structured according to the previously mentioned parameters that these concepts are composed of. It should be recalled that *Configuration 2* refers to foldable propellers and landing in any yaw-angle, while *Configuration 4* refers to non-foldable propellers and landing in any yaw-angle.

	Configuration 2			**Configuration 4**		
	Quad	**Hexa**	**Octo**	**Quad**	**Hexa**	**Octo**
Non-coaxial	*	Yes	Yes	*	Yes	Yes
Coaxial	Yes	Yes	Yes	Yes	Yes	Yes

Table 4.1: Concepts prior to iterative process. *) Non-coaxial quadcopter, which is not considered due to lack of redundancy.

In order to arrive at a final concept, the remaining alternatives must be eliminated through some kind of performance-based comparisons. A number of general drone metrics could be recalled, which could be used for this comparison. This could be the *disk-loading ratio*, which relates the drones weight to its total rotor area, $Disk - loading\ ratio = W/A_{rotor}$. A lower disk loading is generally equivalent to a higher efficiency. The concepts could also be compared in terms of their maximum *thrust-to-weight ratio*. This relates the total thrust output to the drones weight, $TtW\ Ratio = T/W$. It is recommended to opt for a ratio of at least 2:1, where an even higher ratio would be beneficial in terms of additional acceleration and extra thrust for stability and redundancy. Furthermore, the concepts could also be compared in terms of their *power consumption*, where the lowest power consumption for the set payload weight could be considered the most efficient solution. This power consumption depends on the motors that are utilized, together with their efficiency, and is therefore indirectly dependent on the weight of the airborne system. Therefore, regardless of the method of comparison, it is necessary to derive the weight of the different concepts. This is reasonable, since many aspects of the design of any drone system are closely associated with the systems weight.

It should be noted that the concepts could also be compared based on factors such as their overall complexity, level of redundancy, stability, noise emission, together with their general retraction and deployment capabilities (primarily in terms of complexity and time required for operation). However, the reason why these factors are not used as primary comparison and evaluation criteria, is because these are only deemed relevant for the concepts that actually does produce the required thrust-to-weight ratio, and that have a power requirement which does not exceed the power that is available from the power supply.

4.2 Weight estimation

As stated, it is of great importance to derive an estimate of each individual concepts weight. In order to obtain this total weight of each individual concept, the weight is divided into two parts, a fixed weight component and a variable weight component. The fixed weight component is the weight that is regarded as independent of the concept, this is things such as the payload weight or the weight of some onboard electronics, which remains constant. The variable weight components is the weight that is dependent on the concept. The concept in turn determines parameters used to determine this weight, with addition to factors such as maximum flight altitude (tether length), and the non-tethered flight duration.

4.2.1 Fixed weight

The fixed weight components are regarded as the payload, tether air module, IMU, flight controller, frame (excluding arms), and additional weight. Firstly, the total maximum weight of the payload is given in the objectives of the project, where the upper and lower payload should have a combined weight upwards of 15000 g.

The weight of the tether air module is estimated by looking at preexisting systems. The weight of one tether air module, for a tether that outputs 12 kW, is 4300 g [66]. This system could require a power demand that is exceeding 12 kW, but as previously discussed, there are functions in the reference tether air module that are not considered for this system, such as different types of system monitoring and diagnostics. Therefore, considering a weight of 4300 g for the system provides extra margins that could account for a potential higher power demand, and therefore a heavier onboard converter.

The weight of the IMU and flight controller is also regarded as fixed. Looking at commercially available components, the IMU typically range from 3-55 g. Since this system will utilize higher voltage levels for its larger motors, the upper range will have to be used. Due to the requirement of redundancy, a conservative assumption of an IMU weight of 150 g will be utilized (since then multiple could be incorporated). The weight of the flight-controller seem to range anywhere from 9-75 g. The heaviest of these support up to 11 motor outputs. Additionally, it includes a IMU. Since the weight of the IMU is estimated separately, an approximated weight of 75 g will be used for the flight controller.

The weight of the frame is also regarded as fixed. To achieve a sufficient estimation, an existing hexacopter frame will be used as reference, since that utilizes the average number of arms regarded in the concepts. The reference frame should be designed for take-off weights similar to those of these concepts, which can be roughly estimated to anywhere from around 25-45 kg. One hexacopter frame weighing around 2 kg, has a diameter of 1300 mm, and is designed for a take-off weight upwards of 33 kg [83]. Since the drone is limited by a 1500 mm wide base, and considering the previous estimated take-off weight, this seems very reasonable. This frame's arms

are stated to be carbon fiber tubes, with an outer diameter of 30 mm, an inner diameter of 28 mm, and a length of 420 mm. This yields a material volume of around 38.26 cm^3. Utilizing a carbon fiber density of 2.00 g/cm^3, the weight of each arm can be estimated to around 76.52 g/arm. This means that the base excluding the arms weigh approximately 1541 g ($2000 - 76.52 \cdot 6 \approx 1541$). The reason for excluding the weight of the arms in this fixed weight, is since this can instead be considered as a variable weight depending on the number of arms, among other factors.

The additional weight is estimated as 2000 g. This aims to include the weight of fasteners, additional cables, damping, the hybrid rotary joint and its associated tensile load management system, among other things. This could be considered as a percentage of the other total weight, but is here considered as fixed for simplicity.

A summary of the different components that are considered to have a fixed weight, along with their respective weight can be seen in Table 4.2.

Weight of component	**Weight (g)**
Payload	15000
Tether air module	4300
IMU	150
Flight controller	75
Frame (base chassis, feet)	1541
Additional weight	2000
Total	23066

Table 4.2: Fixed weight components and their associated weight, together with the total fixed weight.

4.2.2 Variable weight

The variable weight components are regarded as the tether, propeller protection, arms, propellers, motors, ESCs and the backup battery.

One of the existing tethers that have previously been used as a reference had a weight of 2900 g/100 m, and had a power output of 12 kW. As discussed there, it is conservative to assume a linear relationship between weight and power demand based on this reference, but beneficial to account for extra power losses that arise with an increase in power. Utilizing this gives an average tether weight of 241.67 g/(100m·1kW). This can be used for the individual concepts to estimate their tether weight, since the power consumption between these will also vary, since they drive propellers of different sizes, utilizing different motors. Additionally, this can be used to analyze the change in tether weight, and in turn the total weight, based on the altitude of operation (i.e. the tether length).

When estimating the weight of the propeller protection, it is evident that this depends on both the radius of the rotors and the total number of rotors. Looking at

a commercially available propeller protection the weight is stated as 21.125 g/rotor [79]. This is for a rotor with a relatively low diameter of 239 mm. The weight of this protection is linearly scaled with the radius, and multiplied with a factor of 2 for the extra sturdiness required for the increased size. This results in a weight of approximately 0.34 g/(1 mm rotor radius). To get the total propeller protection weight of the system, this is then multiplied by the number of rotors. Furthermore, a coaxial configuration is assumed to have double the amount of propeller protections, and therefore double the weight.

As stated, the weight of the arms in the reference are estimated to 76.52 g/arm. In addition to being dependent on the number of arms, this weight can also be considered to be influenced by the concept. More specifically, if the concept in questions utilizes foldable propellers, it can be argued that the arm itself will be longer, since the motor will be placed closer to the edge of the base. Therefore, if the entire width of the base were to be utilized, the length of the individual arms would increase upwards of 100 mm, or an additional 23.8 g/arm. This results in a arm-weight of 100.33 g/arm, and in the same way, it could be argued that non-foldable propeller would result in an even shorter arm. These are therefore approximated to weigh 23.8 g less instead, or a total of 52.71 g/arm. Additionally, for concepts that are utilizing a coaxial configuration, the arms will hold a greater weight, and be exposed to a greater torque (nearly 2 times higher), therefore an extra 50% weight will be added to the individual arm weight if the concept is coaxial, to account for the additional strength required. In practice, a higher number of arms would also result in less thrust per arm, and therefore the need for thinner, and lighter, arms. However, since this is merely a rough estimate, such a consideration will not be regarded.

The weight of the propeller is mainly associated with its size, which is beneficial to maximize, which makes the available space the limiting factor. The motors are chosen based on the propeller, and the ESC is then chosen based on the peak current of the motor. For each iteration, the propellers, the motors and the ESCs, should be chosen from the same supplier respectively, in order to enable comparability between the concepts.

As discussed in Section 3.5.2, the weight of the backup battery is estimated by (3.4), and therefore approximated by the usage of a reference battery, and dependent on the desired untethered flight-time, the current of the motor during hover, the number of motors, and the voltage level of the system. The reference battery is a 16000 mAh, 21.6 V, Lipo battery [84]. This provides a high power and is specifically designed for drone usage, rendering the assumption of a constant energy density and consistent performance characteristics reasonable. A summary of the different components that are considered to have a variable weight between concepts, and what their weight depends on can be seen in Table 4.3.

Weight of component	Weight depends on
Tether	Flight altitude, power consumption
Propeller protection	Radius of rotors, number of rotors
Arm	Non-foldable/foldable propellers, non-coaxial/coaxial
Propeller	Available space
Motor	Propeller
ESC	Peak current (of motor)
Battery	Non-tethered flight-time, current at hover

Table 4.3: Variable weight components and what their weight depends on.

4.3 Iterative weight derivation and concept evaluation

The weight of these variable weight components have to be derived. Therefore, an iterative process is performed that not only combines the calculation of the weight of the separate concepts, with analysis of thrust sufficiency, and power requirement associated with available space for power supply. It also looks at different motor-propeller combinations from different suppliers, with their associated performance-data, and also analyses the impact of a change in the number of propeller blades. A simplified illustration of this iterative process can be seen in Figure 4.1.

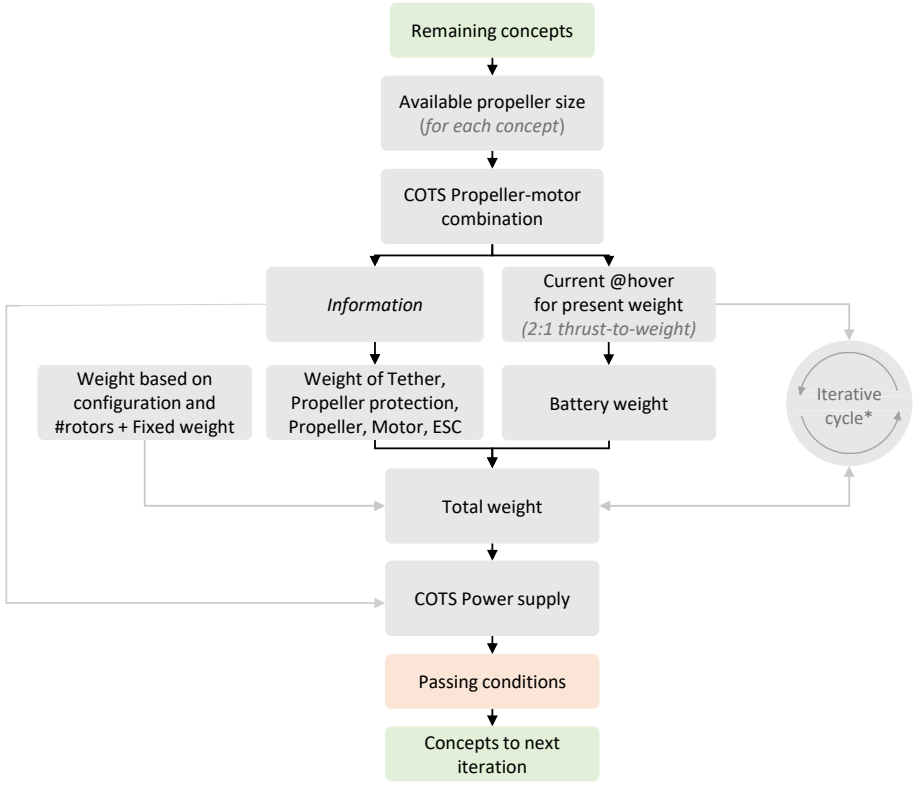

Figure 4.1: Simplification of the iterative process flow. *) Iterative current-weight cycle, see Figure 4.2.

As seen in the figure, the process consists of several steps carried out both subsequently, and, at times, simultaneously. Each iteration uses the remaining concepts as input, and results in all, some, or none of the concepts advancing to the next iteration, based on a set of iteration-specific passing conditions. Each iteration is also characterized by a unique focus. The first iteration considers propellers and motors from one supplier. To assess sensitivity, the second iteration utilizes propellers and motors from a different supplier. Finally, the third iteration looks at three-bladed propellers (recall that all concepts initially utilizes two-bladed propellers) and their associated motors, which are then compared with their two-bladed counterparts.

The process itself starts by choosing the largest available propeller for each remaining concept, utilizing the required propeller gap, as calculated in the area analysis (see Section 3.1.1.1). This is beneficial in terms of both thrust production and efficiency. This means that the propeller will be foldable for some concepts, while non-foldable for others, and will not change based on if the concept is coaxial or not. This propeller is combined with a brushless DC (BLDC) outrunner motor. More specifically, the highest thrust-producing BLDC outrunner motor that is recommended by the specific supplier, but with a voltage level kept at maximum 50.4V (12S) for efficiency. From the performance data associated with these propeller-motor combinations a lot of information can be derived, such as the maximum current and voltage level, together with the thrust, efficiency and current at different throttle-levels or RPM's (in reality these are in some cases estimated based on available data related to other altitudes than of what is used in the iterative process. All values in the process are intended to correspond to sea-level). The given thrust is reduced by 22% for all the concepts with a coaxial design, as discussed in Section 3.1.3. Additionally, the weight of the propellers and motors themselves can be derived, together with the weight of a propeller adapter (which connects the blades of the foldable propellers). The propeller size is also used to derive the weight of the propeller protection for each concept. Furthermore, ESCs can be chosen for each concept, with a current rating that exceed the peak current of the motors, and its weight can be derived. By knowing both the thrust and efficiency (in g/W) of the motors, the power demand of the motors can be calculated. Other components than the motors also need power, such as certain payload or onboard electronics, but these are deemed as insignificant and are disregarded. Therefore, this power demand can be used to estimate the tether weight of each concept assuming a certain tether length (which is initially set to 70 m).

In the figure, the battery weight is also derived from the current at hover for the present weight. This weight, together with the previous mentioned weights, the weight that is derived based on the configuration, and the fixed weight gives each concept its total weight. However, it must be recalled that the weight of the backup battery is estimated based on the assumption that the drone will produce thrust for a desired untethered flight time at hover (initially 5 min, with a 2:1 thrust-to-weight ratio). Therefore, this weight is dependent on the weight at hover, which in turn is associated with a specific amount of thrust at different motor current levels. However, complexities arise since this thrust at hover is in turn determined by the weight

of the backup battery. Therefore, an iterative cycle between current at hover and total weight have to be performed. This cycle have been illustrated in Figure 4.2.

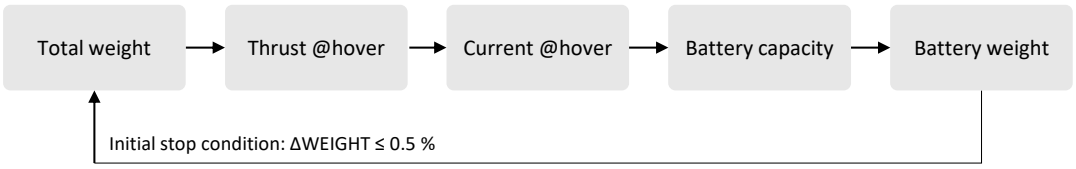

Figure 4.2: Iterative current-weight cycle.

Looking at this figure, it is evident that there are recursive dependencies between the components of the cycle. The total weight affects the thrust required to hover, which in turn determines the current at this hover thrust. This current dictates the necessary battery capacity, and consequently, the battery weight. This battery weight in turn contributes to the total weight of the drone. Due to this interdependency, the process must be resolved iteratively, where a stop condition is created that terminates the loop when the change in total weight between iteration falls below a defined threshold. This threshold is initially set to 0.5%, but increased when increased design accuracy is required.

Once the total weight has been derived, the final power demand of the system (i.e. the motors) becomes known. Therefore, a commercially available power supply (or multiple power supplies) can be considered for each concept, that provides power exceeding the systems power demand. Thereafter, different passing conditions are considered that allow certain concepts to proceed to the next iteration. These passing conditions mainly relate to thrust sufficiency, for the 2:1 thrust-to-weight ratio, and if the power demand is low enough for the power supply to physically fit within the base dimensions. However, in some iterations extra margins are added to reduce the risk for viable concepts to be prematurely excluded due to the limitations of a certain supplier, among other variables. The following provides a brief explanation of each specific iteration, highlighting its defining focus, the corresponding passing conditions, and the concepts that remain afterward.

Iteration 1
In the first iteration, all 10 concepts that can be seen in table 4.1 are considered. For each individual concept, a propeller and motor combination is chosen from the same supplier, to enable comparability between the concepts. Eventually, the total weight of each concepts, and the maximum thrust they can produce is derived. Additionally, the power demand of the concepts are derived, and COTS power supplies are chosen. For the first iteration, the passing conditions, which will all have to be fulfilled, are set as:

- Thrust sufficient OR extra thrust required $< 50\%$
- Maximum power required at the power supply ≤ 28 kW

The passing conditions are formulated in this manner to account for potential improvements. Firstly, it can be argued that it might be plausible for a concept to achieve 50% extra thrust if another propeller-motor combination is chosen, from another supplier. Furthermore, as discussed in Section 3.5.1, the largest commercially available power supply that could be found had a peak power of 22 kW. It was also argued that it is not reasonable to use more than a single power supply. Therefore, an extra margin has been set to account for potential efficiency gains that a new propeller-motor combination, from another supplier, could achieve. The remaining concepts after this first iteration with these passing conditions can be seen in Table 4.4.

	Configuration 2			**Configuration 4**		
	Quad	**Hexa**	**Octo**	**Quad**	**Hexa**	**Octo**
Non-coaxial	*	Yes	Yes	*	No	No
Coaxial	No	No	Yes	No	No	No

Table 4.4: Remaining concepts after first iteration. Configuration 2 refers to foldable propellers and landing in any yaw-angle. Configuration 4 refers to non-foldable propellers and landing in any yaw-angle. *) Non-coaxial quadcopter, which is not considered due to lack of redundancy.

Iteration 2 - New propeller-motor supplier
In the second iteration, a new motor and propeller combination is selected for each of the 3 remaining concept. These propellers and motors are chosen from another supplier in order to determine if these have a better chance of meeting the required thrust-to-weight ratio, along with the sufficiently low power demand. For this iteration, other passing conditions are formulated:

- Thrust sufficient OR extra thrust required $< 50\%$
- Maximum power required at the power supply ≤ 22 kW

In this iteration, the 50% extra thrust margin is no longer associated with potential thrust gains from other propeller and motor supplier, but instead related to the potential thrust gains that can be achieved with a three-bladed propeller. It can be recalled from Section 3.3.1 that thrust gains up to 70% can be achieved with the same propeller area, when increasing the number of propeller blades from two. However, since this 70% increase is for more blades than three, a 50% thrust margin is set for this transition from two to three blades. Since the efficiency of the propeller reduces when the number of blades increases, it is no longer deemed reasonable to also reduce the power required at the power supply for the next iteration. Especially when the power demand already have exceeded the available capacity with propellers and motors from two separate suppliers. Therefore, a passing condition of 22 kW at the power supply is now set. The remaining concepts can be seen in Table 4.5.

	Configuration 2			Configuration 4		
	Quad	**Hexa**	**Octo**	**Quad**	**Hexa**	**Octo**
Non-coaxial	*	Yes	Yes	*	No	No
Coaxial	No	No	No	No	No	No

Table 4.5: Remaining concepts after second iteration. *) Non-coaxial quadcopter, which is not considered due to lack of redundancy.

Iteration 3 - Three-bladed propeller
For the third, and final iteration, three-bladed propellers are utilized for the 2 remaining concepts. It is immediately evident that the thrust increases while the efficiency decreases slightly. For this iteration, the passing conditions are simple and formulated as:

- Thrust sufficient
- Maximum power required at the power supply $\leq$ 22 kW

If the additional thrust that is produced is not sufficient when it comes to achieving the desired 2:1 thrust-to-weight ratio, the concept is eliminated. It is at this point deemed unrealistic to further increase the thrust without compromising on other aspects of the performance. Once again, the power demand must also be able to be supplied from the power supply. It can be noted that even though the power supply can supply a peak power of 22 kW, the power demand of the drone itself must be lower to account for the losses associated with the converter efficiencies. Following this analysis, only 1 concept remains. This is the non-coaxial hexacopter with configuration 2 (foldable propellers, and landing in any yaw-angle), see Table 4.6.

	Configuration 2			Configuration 4		
	Quad	**Hexa**	**Octo**	**Quad**	**Hexa**	**Octo**
Non-coaxial	*	Yes	No	*	No	No
Coaxial	No	No	No	No	No	No

Table 4.6: Remaining concepts after third (final) iteration. *) Non-coaxial quadcopter, which is not considered due to lack of redundancy.

When considering the general reasons for elimination of the different concepts, a pattern emerges. Primarily, it becomes evident that the concepts that utilizes a coaxial setup and foldable propellers have a power requirement that exceed what can supplied, while also being accommodated within the base. The concepts with non-foldable propellers, even though much lighter than the other concepts, did not produce a sufficient amount of thrust to achieve a thrust-to-weight ratio of at least 2. Lastly, the non-coaxial octocopter, with foldable propellers also produced an insufficient amount of thrust.

Even though only one concept remains, the final design and therefore weight is still unknown. Since this concept already met the thrust and power demand requirements without added margins when using the two-bladed propeller, this concept

must now be evaluated using both two- and three-bladed propellers for comparison. The two-bladed propeller and motor combination that was used in the second iteration will be used for this comparison, since its performance data is deemed as more favorable, and also since that results in the same supplier being used for both the two-bladed and three-bladed propeller in the comparison.

4.4 Two- and three-bladed propeller comparison

In order to eliminate the inferior solution, a performance-based comparison is conducted between the two-bladed and the three-bladed foldable propeller, for the non-coaxial hexacopter. This comparison is made with the previously mentioned minimum disk-loading ratio, the maximum thrust-to-weight ratio, and the minimum power consumption. In addition to this, other metrics that have previously served as variable input in the iterative process are evaluated based on their limits. For example, a payload weight of 15 kg was given, however this could be very beneficial to increase in order to further broaden the options when it comes to choice of payload and application. What is the upper limit for this payload weight while maintaining a 2:1 thrust-to-weight ratio for the different number of propeller blades? Furthermore, the tether length and the untethered flight time could also be of interest to increase.

Some general parameters, such as the respective total weights, the thrust production and demand, and the disk loading when the maximum thrust is used, are also used to get a sense of the difference between the solutions, and can be seen in Table 4.7.

Parameter	**2-bladed**	**3-bladed**
Weight (incl. tether and 15 kg payload) [kg]	35.388	36.444
Thrust produced [kg/rotor]	12.053	13.939
Thrust demand [kg/rotor]	11.796	12.148
Disk loading [N/m^2]	190.232	195.909

Table 4.7: Drone weight, thrust production and demand, and disk loading for a non-coaxial hexacopter with 2-bladed and 3-bladed foldable propellers.

It is evident that as a result of an increased number of propeller blades, the total weight of the 3-bladed solution is slightly higher. As expected, this also results in a higher thrust production per rotor with the same propeller diameter, but also leads to a higher disk-loading ratio, which generally corresponds to a lower efficiency. The mentioned performance limits used for the actual comparison can bee seen in Table 4.8. The limits are increased to their respective maximum one at a time, meaning that these upper limits can not be applied simultaneously.

Limit (not simultaneously)	**2-bladed**	**3-bladed**
Max. tether length [m]	91.00	182.00
Max. payload weight [kg]	15.80	20.37
Max. untethered flight time [min]	6.70	17.30
Max. thrust-to-weight ratio [:1]	2.04	2.29
Max. efficiency [g/W]	4.81	4.54
Min. power req. at power supply [kW]	14.68	16.12
Max. continuous flight-time* [h]	10.35	9.43
Min. disk loading [N/m^2]	189.86	192.48

Table 4.8: Comparison of performance limitations between 2-bladed and 3-bladed propellers for a non-coaxial hexacopter with foldable propellers. Yellow highlights the cell corresponding to the value which is deemed most beneficial.

For the calculation of the limits in this table, the same parameter values used as input to the iterative process, are used (if the particular limit is not being directly investigated). These values are a payload weight of 15 kg, tether length of 70 m, thrust-to-weight ratio of 2:1, untethered flight time of 5 min, and converter efficiencies of 95%. As seen in the table, due to the increased thrust produced with the 3-bladed propellers, the tether and therefore flight altitude could be increased to 182 m, compared to *merely* 91 m with the 2-bladed propeller. As a result of the same increase in thrust, the maximum payload weight could also be further increased, or the extra thrust could be used to incorporate a backup battery with a higher capacity that would allow for a longer untethered flight time. Note that the additional space this would occupy is not considered. Furthermore, the additional thrust production could be kept as an increased thrust-to-weight ratio to allow for higher acceleration. On the other hand, as already mentioned, the 2-bladed propeller benefits from a higher efficiency than the 3-bladed. This can also be translated to a lower power requirement at the power supply with the same payload weight and thrust-to-weight ratio. This can also be expressed as a higher maximum continuous flight time using one fuel tank (*) with 19 kW power supply, one fuel tank, assuming 50% power supply load corresponds to 50% thrust). This is extremely conservative as efficiency increases with reduced thrust, which means that the actual maximum continuous flight-time on one fuel tank is in fact higher than what is stated in the table.

By analyzing these performance limitations it becomes clear that just as expected, the two-bladed propeller is more beneficial when it comes to increased efficiency, whilst the three-bladed propeller triumphs in all aspects that are related to additional thrust. The 2-bladed propeller main benefit of additional efficiency is not deemed as the most important factor, due to the system actually being tethered, and there is expected that the tank is able to be filled up at regular intervals, of every 9 hours or so, rendering this benefit mostly obsolete. This ties back to the main benefit of any tethered drone system, which is the nearly continuous flight-time, due to the ability to continuously feed power to the drone. On the contrary, the extra thrust margins that the three-bladed propeller brings are deemed as much more beneficial. This not only makes the system less sensitive to un-included weight that might be present, but also increases the flexibility when it comes to application.

This flexibility leads to increased performance that would allow for either heavier payloads, higher altitudes, higher acceleration (faster deployment and retraction), longer untethered flight time, or a combination of the mentioned. Additionally, the cost of the different propellers is roughly the same, and as previously discussed, the noise emitted is also reduced when transitioning from two-bladed to three-bladed propellers. For the mentioned reasons, the two-bladed hexacopter solution is eliminated, and the three-bladed hexacopter emerges as the most favorable solution.

4.5 Final concept - three-bladed hexacopter

The three-bladed hexacopter is the only solution remaining. An illustration of this solution, aiming to convey the size of the drone, can be seen in Figure 4.3, alongside a human reference (an average-height Swedish woman).

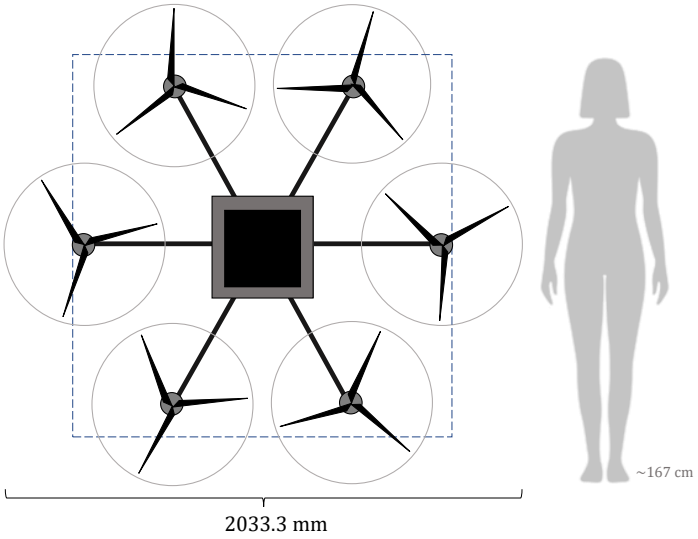

Figure 4.3: Simplified illustration of the remaining concept consisting of a non-coaxial hexacopter with 3-bladed foldable propeller. The black and dark gray squares represents the upper and lower payload. The blue dashed rectangle corresponds to the base dimensions. Additionally, a human reference corresponding to an average-height Swedish woman of 167 cm.

As seen in the figure, the hexacopter has a tip-to-tip distance of 2033.3 mm in its deployed state, while all the motors are positioned within the base dimensions during landing, and all the propellers are contained within the base after being folded. This distance is calculated by utilizing the known base width of 1500 mm, together with the motor dimeter of 89 mm, and rotor radius of 311.15 mm, $(1500 + 311.15 \cdot 2 - 2 \cdot (89/2) = 2033.3$ mm).

As previously discussed in Section 3.1.1.1, a gap between the propellers was necessary in order to ensure safety and keep air-flow interference down. An illustration of this gap for this specific hexacopter, and the associated propeller sizes can be seen

in Figure 4.4. It was analyzed and concluded that a 1/7th reduction of the different configurations radii was beneficial, in order to ensure a gap corresponding to 1/3 of the propeller diameter. However, this 1/7th gap was also meant to "cover the actual size of the, previously assumed infinitely thin, motors". Therefore, by ensuring that all the motors are positioned within the base dimensions during landing, this true gap distance might actually be a bit smaller. In this case, the 311.15 mm propeller equals a $\approx$ 13.3 % reduction from the theoretical maximum area, which is a bit less than the 1/7th reduction of $\approx$ 14.3%. This reduction in propeller size is considered close enough, even though this does not offer any extra margins in width when the hexacopter lands in a very specific yaw-angle. Therefore, in practice, this would likely not pose any major issue, but to be safe, additional margin could be added by slightly reducing the gap.

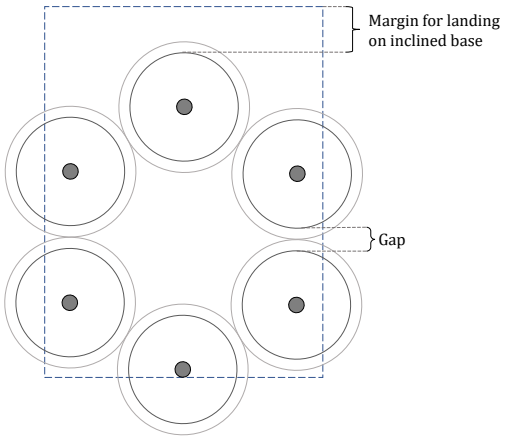

Figure 4.4: Illustration of gap between the propellers, where the dark gray circles represents the actual size of the rotors, and the light gray circles represent the maximum rotor size while keeping the motors within the base. Additionally, the illustration shows the available margin for landing on an inclined base.

It is also a requirement to be able to deploy from and land on uneven terrain, or a non-leveled surface, as per R12.2 in Appendix A. This requirement relates to an inclined-angle through a rotation along the width of the base. Since the drone will descend with a horizontal orientation, the inclined base will, from the drone's perspective, be shorten than the given length of 2000 mm. This manageable incline angle is therefore associated with the available margin between the drone and the upper side of the base, as also seen in Figure 4.4. Using the size of the drone, the length of the base dimension, and the radius of a motor (to enable landing in any yaw) a minimum margin of 188.85 mm is obtained (when using the yaw-angle that corresponds to the smallest margin). Using trigonometry, a corresponding maximum allowed inclined angle of $\approx 25°$ can be derived. This is considered more than enough, since it is in practice unreasonable to utilize the system in any environment with that incline angle. Since the final propellers are foldable, the desire D14.1, relating to a minimization of the drone deployed footprint, see requirement specification in Appendix A, is ultimately considered as not fulfilled.

The third iteration that resulted in the final non-coaxial hexacopter with foldable propellers can be seen in Appendix B, together with the used weights for the different components (some have been updated after the iterations. The most recent and most accurate weights can be seen in the appendix), with addition to the input parameters. All the used reference components also have their product names stated. Furthermore, the associated iterative current-weight cycle can also be seen in Appendix B. In this cycle, the stop condition for the difference in weight is set to 0.05%, compared to the initial 0.5%, for increased accuracy.

By changing the input parameters, which do not need to remain constant, a flexibility in application is achieved. For example, the payload weight could be either decreased or increased from 15 kg, if another thrust-to-weight ratio is deemed necessary or sufficient for the use case in question. It has been repeatedly emphasized that a thrust-to-weight ratio of 2:1 is required for the system. However, a ratio as low as 1.5:1 could theoretically still permit the drone the operate, although with a reduced acceleration and resistance against wind and other disturbances, if additional payload weight was instead prioritized. On the other hand, if the payload would weigh less than 15 kg, a higher thrust-to-weight ratio could be exploited in term of additional acceleration. The non-linear relationship between the thrust-to-weight ratio and payload weight is derived from iterative weight analysis process, and is presented in Figure 4.5. In this table, the tether length is set constant to 70 m.

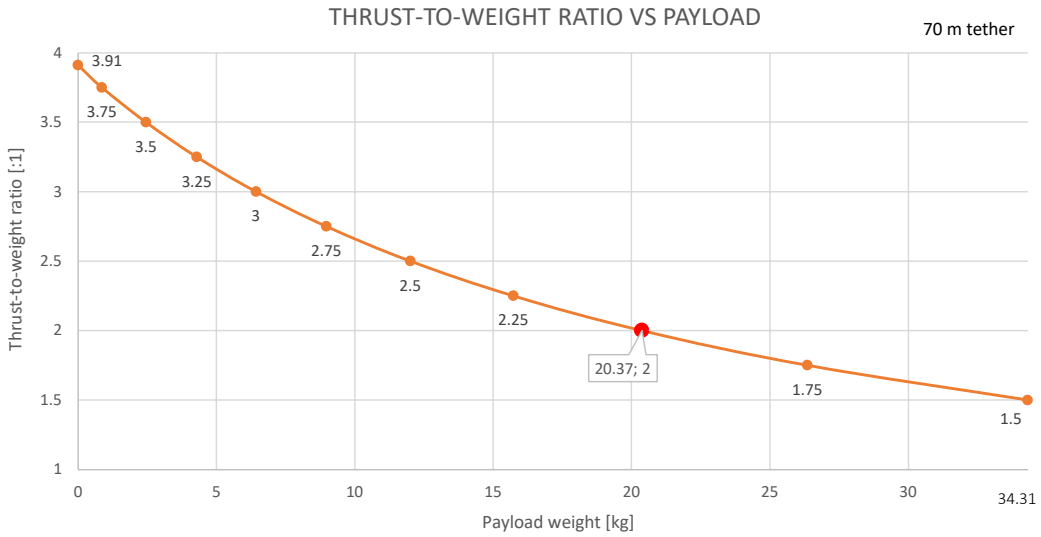

Figure 4.5: Relationship between thrust-to-weight ratio and payload weight, given a 70 m tether.

The payload weight that corresponds to the required 2:1 thrust-to-weight ratio, is marked in the graph. The corresponding payload weight of 20.37 kg could also be seen in Table 4.8. The highest thrust-to-weight ratio, with a payload weight of zero, is 3.91:1. In contrast, reducing this ratio to 1.5:1 would allow for a payload weight upwards of 34.31 kg. Due to the drone's ability to achieve a thrust-to-weight ratio exceeding 2:1, while carrying a payload of 15 kg, it is considered to possess the great maneuverability in the z-direction, that enables the fulfillment of requirement R2.6 (see the requirement specification in Appendix A).

Another relationship that can be created that could be beneficial to utilize, is the relationship between the payload weight and the tether length. Previously it has been discovered that a maximum tether length of 182 m could be achieved, while maintaining a payload weight of 15 kg. However, in some cases, it might be beneficial to increase this length even further, whilst equipping the drone with a slightly lighter payload. Alternatively, a specific application could require flight altitude lower than the existing tether length, where the reel-out length could be limited, and a heavier payload could be applied. The relationship between the payload weight and the tether length is also derived from the previous iterative process and is presented in Figure 4.6. Since the reference tether system is equipped with a 220 m tether, this limits the tether length in the graph. Additionally, a constant thrust-to-weight ratio of 2:1 is set.

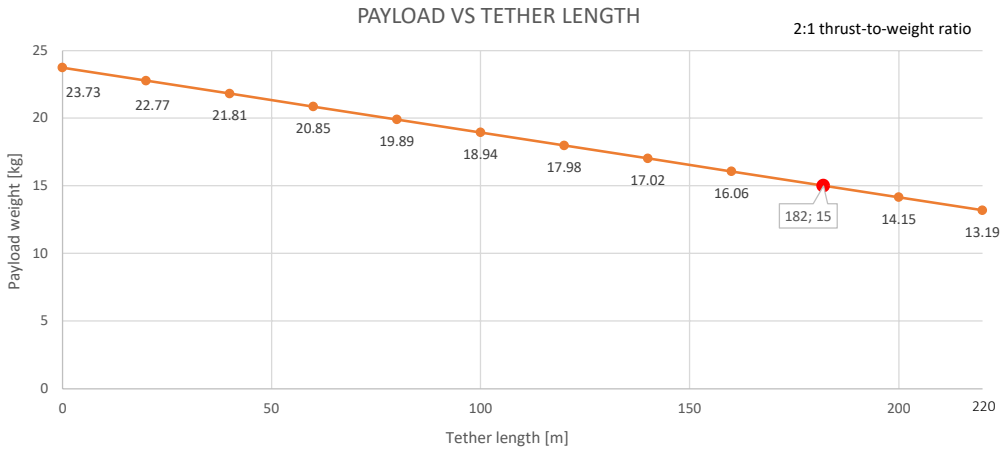

Figure 4.6: Relationship between payload weight and tether length, given a 2:1 thrust-to-weight ratio.

The linear relationship observed in the figure arises from the assumption that the tether weight scales linearly with the tether length. The base input of 15 kg payload is marked in the graphs, which corresponds to an 182 m tether, which have previously been seen in Table 4.8. It can be derived that using the maximum tether length of the reference system allows for a payload of 13.19 kg, whereas the payload capacity increases to approximately 23.73 kg as the tether length approaches zero.

4.5.1 Sensitivity analysis

A sensitivity analysis is conducted to evaluate how sensitive the results of the final concept are to changes in key parameters, and assumptions made. For the calculation of the values in this table, the same parameter values, used as input to the iterative process, are used (if the particular parameter is not being directly investigated). These values are a payload weight of 15 kg, tether length of 70 m, thrust-to-weight ratio of 2:1, untethered flight time of 5 min, and converter efficiencies of 95%. The analysis can be seen in Table 4.9.

Parameter	**Value**
Total extra weight margin [kg]	5.37
Additional weight [kg] $\leq$	7.37
Thrust [%] $\geq$	87.2
Tether weight [g/(100m*1kW)] $\leq$	628.3
Total fixed weight [kg] $\leq$	28.44
Converter efficiency* [%] $\geq$	95

Table 4.9: Key system parameters and performance constraints related to weight, efficiency, and thrust. *) Either the AC-to-DC converter or the DC-to-DC converter.

In this table it can seen that due to the high thrust production relative to the thrust demand, there are a lot of margins when it comes to the assumption of weight. In total, the additional weight could reach upwards of 7.37 kg (contrary to the estimated 2 kg) whilst still maintaining the required 2:1 thrust-to-weight ratio. Also the tether weight, estimated per 100 m and 1 kW, could be much higher without compromising the result. This can also be translated into the fact that the thrust could be merely 87.2% of what was stated in the performance data-sheet from the supplier, and still meet the other requirements. The most critical factor that can be derived from this sensitivity analysis is the converter efficiency. This is initially set to 95% for both converters. If either of these efficiencies were to decrease slightly, the power supply's peak power could fall below the power required by the drone system at full thrust. Although there is a thrust margin, meaning the 2:1 thrust-to-weight ratio would still be maintained, the motors and propellers would no longer be utilized to their full potential. One possible solution to this issue is to slightly decrease the propeller blade pitch angle. As previously discussed, reducing the pitch angle increases efficiency at the expense of thrust. However, due to the resulting reduction in thrust, the outcome would be similar to simply lowering the motor throttle. Something that would be more beneficial since it would still allow for the full utilization of the motors performance.

For this reason, the hexacopter is considered largely insensitive to most changes in input parameters. Moreover, the one parameter to which it is sensitive does not compromise the overall functionality of the system due to the existing margins in thrust.

4.5.2 Cost analysis

It is of interest to perform a cost analysis of the hexacopter system, since it is desired to ensure a competitive price of the system, as per D4.2 as seen in Appendix A. The cost analysis will mainly cover the components where a commercial off the shelf (COTS) component have been used as reference in either the weight estimation, or in other parts of the iterative process, that resulted in the hexacopter concept. Other components that are important for the system, but where a COTS component is not available will have its price roughly estimated. This is things such as the propeller protection, together with a rough estimate of the cost of the systems additional components. Subsystems such as the ground control station and landing platform are completely excluded due to limitations in the project scope. Additionally, the cost of the payload is omitted for clear reasons. An estimated cost breakdown, separated into COTS and non-COTS components, is presented in Table 4.10. The table includes a reference column which will be used to reference different components, in order to motivate their respective estimated price.

Component	**Price ($)**	**Amount**	**Total ($)**	**Ref.**
COTS:				
Motor	710	6	4314	(1)
Propeller	380	6	2280	(2)
Propeller adapter	35	6	210	(3)
ESC	235	6	1410	(4)
Flight controller	66.63	2	133.26	(5)
Backup battery	291.53	2	583.06	(6)
Chassis (incl. arms, legs)	1639	1	1639	(7)
Tether system	27599	1	27599	(8)
Power supply	8090	1	8090	(9)
Non-COTS:				
Propeller protection	100	6	600	(10)
Tensile load management	500	1	500	(11)
Hybrid rotary joint	5000	1	5000	(12)
Additional	5000	1	5000	(13)
Total (USD)			**57304.32**	
Total (SEK)*			**550121.47**	

Table 4.10: Cost estimation breakdown of COTS and non-COTS components for the drone system, together with a total cost in USD and SEK. Prices are incl. VAT. Additionally, a reference ID is given to each component for upcoming motivation of respective estimated price. *) Utilizing a conversion rate of 9.60 SEK/USD.

For the majority of the COTS components the price is directly taken from the suppliers listed price. This is for components such as the motor (1) [85], propeller (2) [86], propeller adapter (3) [87], ESC (4) [88] and power supply (9) [75]. The price of the flight controller (5) is based on an existing flight controller [89], which includes one IMU. For this reason the price of the IMU is not added separately. The cost of two flight controller are added to the analysis to achieve redundancy. The backup

battery (6) is based on a existing Lipo battery [84], which has a voltage rating half of what this system is using. Therefore, two of these are added to be able to connect them in series in order to achieve the requested voltage level. This can be considered as a conservative cost estimation, since the hexacopter requires a lower battery capacity than the reference battery provides (if the system provides 5 minutes of untethered flight). The cost of the entire chassis (7) is not separated into the cost of the individual components such as the arms, legs, or central frame. Instead, it is based on an existing hexacopter frame that supports a similar take-off weight, while being approximately the same size as this hexacopter [83]. Similarly, the tether system (8) is not divided into its components such as the tether cable itself, the base power station including the AC-to-DC converter and winding mechanism, and the tether air module. Instead, this is based on an existing tether system [66], that already includes all of the mentioned components. The reference system does not handle the same power as what is required for this system. However, the tether cable related to the stated price is 220 m long, which make the the price seems like a reasonable estimation regardless. Additionally, this COTS tether system has a real-in tension of maximum 20 N, which is a lot less than what is required for this system in order to maintain a continuous tether-tension, and a sufficient retraction tension. This system can be estimated to require a maximum tension of roughly 643 N, which is the difference between the maximum thrust produced and the minimum weight of the airborne system (excl. payload and tether weight). However, the reference tether cable is rated with tensile strength that allows it to handle up to 300 kg or 2943 N. Therefore, it is reasoned that an additional, stronger, winch incorporated into this system would not increase the total tether system price (of 27599 USD) substantially.

The cost of the propeller protection (10) is estimated by looking at an existing propeller protection used for a much smaller drone [79]. The reference protection costs 49 USD, which includes protection for four propellers with a radius of 119.5 mm each. Since this systems propellers are substantially larger, with a radius of 311.15 mm each, the price of the associated protection is estimated to be slightly more than double of what the reference protection costs, but for each individual propeller. The costs of the tensile load management system (11) and the fiber optic rotary joint (12) are rough estimates. The tensile load management system cost is based on general pricing for simple carbon fiber structures, while the price of the hybrid rotary joint is derived from existing hybrid rotary joint prices. The key difference is that this hybrid FORJ needs to accommodate a significantly higher power requirement, which would likely increase the overall price rather substantially. Lastly, an additional cost is included to account for the price of all supplementary cables, fasteners, joints, damping materials, and other components, not explicitly mentioned.

It would be beneficial to compare the estimated cost of this tethered drone system to that of an existing system, in order to assess whether the analysis is reasonable and whether the price is truly competitive. However, it is challenging to find a publicly available price of an existing tethered drone system that is of comparable

size and payload capacity. Luckily, this wont be necessary, as the cost estimation for the current system already incorporates the price of a commercially available tether system. Therefore, the cost comparison can focus solely on the drone platform itself, which is more feasible given the broader availability of drones with comparable payload capabilities.

Freefly's Alta X is a quadcopter that accomplishes around a 2:1 thrust-to-weight ratio with payload weight of 15 kg [90]. This drone is sold as a bundle, with a price of around 36040 USD. To enable a reasonable comparison between the current system and this reference drone, the components related to the tether would have to be excluding. This is things such as the entire tether system, power supply, tensile load management system, together with the fiber optic rotary joint. Furthermore, 1/4th of the additional costs are disregarded, since these are deemed associated with the tethered system. The total cost of this hexacopter would therefore be estimated to around 14865 USD. This price does not include any overhead, R&D costs, costs associated with assembly, cost relating to the manufacturing of certain components, or any incorporated profit margin. Since the system is mainly consisting of, and based on existing COTS components, some R&D, manufacturing and overhead expenses are inherently included in the listed prices. Nevertheless, while it is difficult to conclusively determine whether the price is lower than that of the reference drone, it may still be considered competitive.

Furthermore, a differentiating factor can be found in the hexacopter compared to the reference system. Since the reference drone is a quadcopter, it could be considered to lack the redundancy that the hexacopter possess. It is however inconclusive if this differentiating factor exists compared to all available tethered drone system. Nonetheless, this hexacopter is uniquely designed to fit within given dimensional constraints, which distinguishes it from other systems for this specific usage.

4.5.3 Lifespan and service interval

While already examining the constituent components, it is also beneficial to consider the system's expected lifespan or required service intervals, as per R5.2, that the drone must have sparse maintenance, see Appendix A. Firstly, this is difficult to determine, since this data is not available for all the COTS components, and an estimation of lifespan is complicated to give for the non-COTS components. Many of the components, such as the motors, propellers and adapters, and ESCs are all from the same supplier. This supplier do provide some information related to the lifespan of the components [91]. The motors, and especially their bearings can be considered the most limiting factor. These bearing have a rated lifespan of 200 hours. Replacement bearings are available from the same supplier, along with corresponding installation instructions. Therefore, these components could be replaced relatively easily, eliminating the need to replace the entire motor, which is something that would reduce the long-term maintenance cost of the system. Furthermore, it must be noted, that this is also impacted by the environmental operating conditions, such as temperature, humidity, vibrations, etc. Many customers have however reported

that they have run the motors for over 1000 hours without performing maintenance. The ESC should be replaced after 4000 hours of operation or every 15 years, whichever comes first. The propellers does not have a set lifespan, instead this is mainly dependent on how they are stored. It is however recommended to perform inspections to ensure the overall condition of the propeller's airworthiness, and replace them if cracks are found.

Generally, it is deemed beneficial in terms of both reduced maintenance and repair time, complexity and cost, that the system is based on several existing components, as per D5.1 in the requirement specification, see Appendix A. Additionally, components such as the chosen propellers are described as dynamically-balanced, and provided in matched-sets. Which simplifies installation of the blades, without any need for secondary balancing. This contributes to the fulfillment of R5.1, that the system must in most cases be maintainable on site. Furthermore, due to the use of carbon fiber components and a gasoline-powered power supply, desire D10.1, stating that renewable and environmentally friendly materials should be used, is considered as not fulfilled.

4.5.4 Base dimensions and constituent components

All the subsystems contained within the base has to be able to fit within the given dimensions, as per requirement R1.2, see Appendix A. Even though the total base height is optional, recall Figure 1.3 in Section 1.2.3, it is deemed beneficial to place the sub-systems within the lower part of the base, which is 1100×1500 mm. The COTS-systems that have been used as reference, and which are housed within the base, includes the power supply and the tether ground system (responsible for tether storage and winching). The power demand of the hexacopter exceeds the output of the referenced tether ground system. However, since the referenced system uses a longer cable than what is expected for the hexacopter, the overall size is assumed to be roughly comparable. The dimensions of the tether ground station is $640 \times 550 \times 350$ mm and the power supply is $732.8 \times 1092.2 \times 732.8$ mm (length$\times$width$\times$height).

A key limitation regarding the placement of these systems is that, to enable retraction of the drone by initiating the winching of the tether, the tether, which exits along the width of the tether ground station, must be aligned with the center of the drone's intended landing position. Since the length of the tether station (645 mm) is less than half the width of the base station (750 mm), it can be positioned in such a way that the tether maintains a central alignment with the drone's landing position. Since the length of the power supply (1092.2 mm) is slightly less than the length of the base (1100 mm), and its width (732.8 mm) is also less than half the width of the base station, it can also be accommodated within the base and without interfering with the tether station. This leaves an additional available space of 525×767.5 mm that can be used to house the control station, and potential storage of additional fuel for the power supply. Moreover, this additional space could be used to partially house the extra space associated with a stronger winch. Since the development of a

ground control station is outside the scope of the project, its exact size will not be determined, but is assumed to fit within the base, given this available space. The base containing the tether station, power supply and additional space for the control station and additional fuel, can bee seen in Figure 4.7.

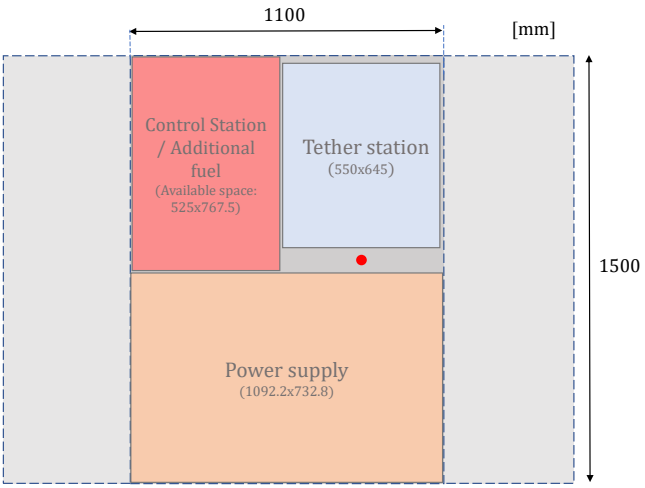

Figure 4.7: Base containing the tether station, power supply, and additional space for the control station and additional fuel. Dimensions are displayed in the respective rectangles. Red dot represent the center position of the drone.

The red dot, representing the center position of the drone, aligns with the exit point of the tether on the tether station. The light gray rectangle represents the entire (2000×1500 mm) base dimensions, which will accommodate the landing platform. This landing platform would have to be designed in a way that enables the landing of the hexacopter, regardless of yaw-angle. This could, for example, be achieved by adding a groove in a circular shape, with a diameter matching the furthest distance between the drone's legs, and a centrally placed hole through which the tether is fed. This is entirely feasible, and for that reason, all components intended to be housed within the base are deemed to fit, and the requirement R2.1 is considered fulfilled.

4.5.5 Supplementary requirement fulfillment

The requirement specification have been referenced multiple times, both during the research of the different subsystems, but also in connection to the resulting hexacopter design. However, some requirements demand a separate evaluation regarding their fulfillment. The following section consists of brief motivations for whether some requirements and desires have been fulfilled or not, or if the fulfillment is deemed inconclusive. The verdict regarding the fulfillment of these requirements, with addition to all the other requirements, can ultimately be seen in Appendix H. In this appendix, a reference is added to each requirement, pointing to the respective section(s) where its fulfillment, or lack thereof, is discussed or can be inferred.

Environment and weather resistance
The systems ability to operate in different AECTP-230 zones i captured in R8.2 and D8.2, see the requirement specification in Appendix A. In practice, this corresponds to specified temperate- and relative humidity ranges that the system should or is desired to be able to operate in. This is partially assessable based on the available data for COTS components in the system. Temperature specifications are available for most components, with the ESC having the narrowest identified range of -25°C to 95°C, together with the Lipo batteries with a minimum discharge temperature of around -20°C. As a result, it can directly be concluded that D8.2 is not fulfilled, since this would require operability in the extended temperature range of -46°C to 49°C. On the other hand, Requirement R8.2, which specifies a range of -19°C to 39°C, falls within the ESCs stated operating limits and the batteries discharge temperature, and is therefore considered fulfilled from a temperature perspective. However, the situation is less clear regarding humidity. Most components do not provide explicit ratings for allowable relative humidity. The COTS tether system used as a reference indicates operational tolerance between 10–80% relative humidity and storage tolerance of 5–90%. These tolerances falls outside the relative humidity ranges associated with the zones in R8.2. However, since the tether system is merely a reference system, together with the lack of definitive data for the other COTS- and non-COTS components, the the humidity aspect of R8.2 is deemed inconclusive. Consequently, R8.2 is considered inconclusive as a whole.

Furthermore, the majority of the reference COTS components are in general specifically designed for drone applications, which inherently suggests the use of weather-resistant materials and construction. No information has been found that contradicts this assumption. Based on this, Requirement R10.1 is considered fulfilled.

Heat development and harmfulness to users
There is a need to minimize heat development within the system and to ensure that the product poses no harm to the user(s). These considerations are addressed in requirements R3.4, R3.5, and desire D16.1, as detailed in the requirement specification in Appendix A. Reference components have generally been selected based on their ability to operate at low temperatures, mainly since this is commonly associated with higher efficiencies. For instance, the reference motor features an integrated centrifugal fan that promotes cool running temperatures [85]. The tether includes an insulation layer providing thermal resistance, and the ESC is housed in an all-aluminum case designed for *cool-running* temperatures [88]. Therefore, heat development in the system is considered minimized. Furthermore, with the inclusion of the system's propeller protection, backup battery for emergency landing, and motor redundancy, combined with minimized heat development, the requirement related to ensuring no harm to users, and thus all the aforementioned requirements, are considered fulfilled.

Payload obstruction and noise emission
It is desired to minimize noise emission from the system, and it is required that no parts of the system obstruct the mounted payload to a higher degree. See D8.1 and R16.1 in the requirement specification, Appendix A. The efforts to minimize

the noise have been several, but ultimately rather limited, since improvements often come at the expense of reduced efficiency or thrust production, something that is deemed as more important for this system. Three-bladed propellers tend to produce comparatively lower noise emissions than, for example, two-bladed propellers. However, since the chosen propellers were not specifically designed for noise reduction, D8.1 is ultimately considered as not fulfilled.

The main potential obstruction for the payloads concerns the bottom-mounted payload and primarily stems from the inclusion of the legs. However, these legs are relatively thin, which would reduce this obstruction. The payload can also be mounted in a way that further minimizes the obstruction. Additionally, the incorporation of the hybrid rotary joint reduces the need for the payload to rotate independently, thereby largely mitigating obstruction concerns. As a result, requirement R16.1 is considered fulfilled.

5
Hexacopter modeling

The hexacopter is the first system to be modeled and arguably the most important component of the tethered drone solution. The model is important as it will serve as the basis for future simulations aimed at validating and evaluating the overall system performance under various operational conditions. The hexacopter dynamics are modeled using the Euler–Lagrange equations of motion and are symbolically derived in Matlab. The Newton–Euler formulation is also a common modeling approach presented in the literature but it has been shown that the Euler Lagrange approach is beneficial for modeling of the tether and will thus be used for modeling of all systems in this project.

The chapter starts by presenting the model description as well as the chosen coordinate system configuration. Thereafter, the models assumptions and limitations are discussed. The models equations of motions are then derived using the Euler–Lagrange approach, where a particular focus has been put on external forces acting on the system to make the model as realistic as possible. Lastly, the model parameters are derived from the hexacopter CAD model, specifications of COTS components, and relevant literature sources.

5.1 Model assumptions and limitations

The hexacopter's mathematical model is constructed to accurately capture real-world physics, resulting in a high-fidelity representation of the system dynamics. A few assumptions and limitations are however made to decrease model complexity and ensure that the model is completed within the given time-frame. In this chapter, the main assumptions in the derivation of the drone model are presented and discussed. The list below outlines general assumptions commonly made in drone modeling, while project-specific assumptions are detailed in the following sections.

- *Rigid body assumption*
  The hexacopter body is assumed to be rigid, meaning that all parts of the hexacopter's structure is also assumed to be rigid and at a fixed distance from one another during drone movement. The rigid body assumption implies that no structural deformation or bending occurs. The assumption also neglects vibrations, which have a negligible effect on the overall flight dynamics but can significantly influence the drone's durability, as prolonged vibrations may lead to mechanical wear or components loosening over time.

- *Drone symmetry assumption*
  The hexacopter is assumed to be symmetrical around its vertical axis which passes through its center of mass and is perpendicular to the plane of the rotors. This assumption implies that the distribution of mass, the moment of inertia and the aerodynamic properties of the drone are uniform across the horizontal plane. This means that the drone is balanced, if the payloads center of mass is also placed on the same vertical axis.

- *Rotor thrust and torque*
  For the hexacopters rotors, a simplifying assumption is made that both the thrust and torque produced are proportional to the squared rotational velocity. This relation is thus empirically derived for a certain propeller geometry. The assumption is commonly made in the literature if the exact propeller geometry is not known. Since the propellers used in this project are based on commercial off-the-shelf (COTS) components with unknown exact geometry, this approximation is considered appropriate for the model. The implication of using this assumption is that higher-order aerodynamic effects, such as wake interactions and induced flow variations, are neglected. These effects could be captured using blade element theory, as previously discussed, given that the exact propeller geometry was known.

- *Simplified body aerodynamic modeling*
  The project is limited from use of computational fluid dynamics (CFD) simulations for calculations of drag coefficients and forces applied to the hexacopter. The coefficients are instead calculated by means of superposition of aerodynamic elements. This assumption yields a level of uncertainty when it comes to the impact of wind disturbances. The size of the aerodynamic elements are however chosen conservatively, meaning that drag forces are overestimated. The assumption is thus considered acceptable for the purposes of this thesis.

- *Flat earth assumption*
  The flat earth assumption is a simplification of the environment which the drone/system operates in. The assumption implies that the earth is flat, non rotating and has a constant gravitational pull. Coriolis and centrifugal forces due to the earths rotation is thus neglected. The assumption is made according to the framework CADAC (Computer Aided Design Of Aerospace Concepts) where it is recommended to apply the flat earth assumption for small UAV:s [92].

- *Laminar flow assumption*
  The airflow surrounding the hexacopter is assumed to remain predominantly laminar. This is because during tethered operation the tether is intended to remain nearly vertical, thereby limiting significant lateral displacement of the hexacopter. Although turbulence may arise from wind disturbances or rotor interactions, such effects are deemed negligible under the expected operating

conditions. This assumption will also be applied in the calculation of aerodynamic effects on the tether in Section 6.4.1.2.

- *Ground effect limitation*
  The ground effect is a phenomenon which increases lift and reduces aerodynamic drag when the rotor is within one rotor diameter of the ground. This occurs due to the rotors induced velocity being reduced as the wake is limited by the ground, which in turn increases the rotors lift. The phenomenon decreases exponentially as the rotor gains altitude or starts moving vertically. The ground effect is excluded from the hexacopter model, both to maintain model simplicity and because it depends on ground geometry, which is assumed to be unknown.

5.1.1 Forward flight theory

The drone is assumed to have constant altitude during operation, with no significant vertical velocity. The impact of wind will however induce several forces and torques which are described by forward flight theory. These effects arise from the relative airflow generated by oncoming winds and can be described by splitting the drones rotors into two half regions; an advancing side and a retreating side [93]. Stationary flight is shown for reference in Figure 5.1, image (a), while the two regions for a rotor with relative airspeed are illustrated in image (b). It is shown that the advancing side experiences a higher relative air velocity than the propellers rotational speed, and the retreating side experiences a lower relative velocity. A reverse flow region may also occur on the retreating side of the disk, where the relative airflow is in reverse direction which generates a negative thrust. A dissymmetry of lift will thus occur as the advancing region produces more lift compared to the retreating side. This will thus produce a rolling moment. The asymmetry of lift creates a time varying periodic load every revolution, which in turn leads to a dynamic response of the blade which causes the blade to bend upwards. This effect is called 'blade flapping', where the flapping motion of the blade acts to reduce the lift asymmetry across the rotor disk. Full-size helicopters deliberately utilize this phenomenon by allowing the rotor blades to flap, enabling more stable and controlled forward flight.

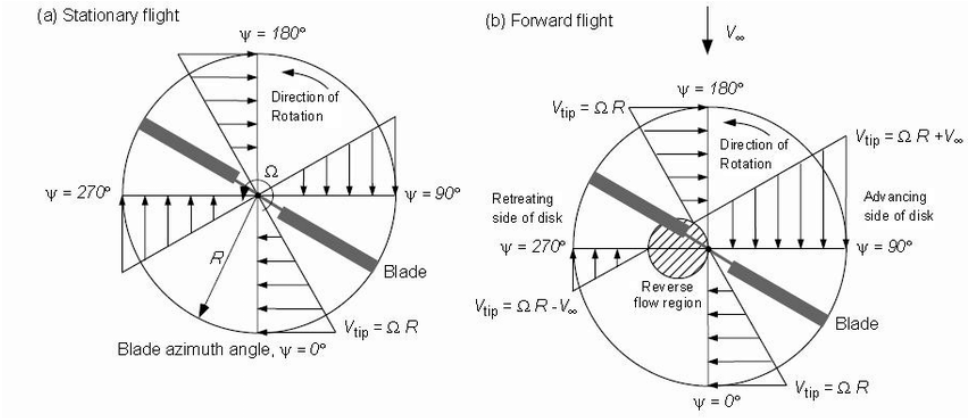

Figure 5.1: Rotor relative airspeeds, reverse flow region and dissymmetry of lift [94].

A different approach is usually taken when modeling and designing multi-rotor UAVs. The drone's propellers are usually assumed rigid, which is a reasonable assumption given the design choice of carbon fiber propellers described in Section 3.3.4. The blade flapping phenomenon will thus not aid in reducing dissymmetry of lift. The dissymmetry is however less significant in multi-rotors, in comparison to helicopters, since the use of counter-rotating rotors tend to largely cancel out this effect. The use of counter-rotating rotors are described in greater detail in Section 5.2.1. Given that dissymmetry of lift is mainly canceled out for multi-rotors, the effect will be omitted and not included in the drone model.

5.1.2 Rotor flow states

There are four distinct rotor flow states that describe how the rotor interacts with the surrounding air: normal working state, vortex ring state, turbulent wake state, and windmill brake state. These states are defined within the scope of momentum theory, under the assumption that airflow is uniform in the slipstream. The flow state of the rotor is highly dependent on its flight regime – whether it is climbing, hovering, or descending. The states can be described by using the vertical climb velocity of the rotor V_c, and the induced flow or inflow velocity v_h at the rotor disk during hover. The ratio between these two variables are denoted as the climb velocity ratio V_c/v_h. Below is a short description of each rotor flow state [93], as well as an illustration of each state shown in Figure 5.2 below.

- *Normal working state*
  The rotor is in a normal working state during hover and ascent which implies the condition ($V_c/v_h \geq 0$). Hover is theoretically the lower boundary of the state, but it has been shown that momentum theory for the normal working state provide reasonable results for a slow descent as well (up to $V_c/v_h > -\frac{1}{2}$). The assumption that the rotor torque is proportional to the rotational velocity squared, only holds for the normal working state. This state, illustrated in Figure 5.2, image (a), is characterized by downward airflow through the rotor and a corresponding downward-moving slipstream beneath it.

- *Vortex ring state*
  The vortex ring state occurs when the rotor is in a slight descent ($-1 \leq V_c/v_c < 0$). Due to the rotor descending, a definite slipstream will not exist as the flow within the slipstream changes direction at a certain point below the rotor. The air with a velocity opposite to the rotors descent will thus be recirculated into the rotor and cause a high degree of turbulence. This in turn leads to a loss of rotor thrust, which also can be insensitive to an increase in motor torque due to the recirculation. The vortex ring state is illustrated below in Figure 5.2, image (b).

- *Turbulent wake state*
  When the rotor descends even faster ($-2 \leq V_c/v_c < -1$) it is in the turbulent wake state. For the upper interval of the state, the rotor can be characterized by no airflow through the rotor. The rotor can be considered a solid circular disk, with an upward vertical airflow generating a turbulent wake beneath it. For the lower interval of the state, turbulent airflow will move upwards through the rotor, which will be the cause of autorotation. This occurs for a climb velocity ratio of $V_c/v_h \approx -1.75$ if the rotor is assumed to have no losses, implying an ideal autorotation. In reality, the autorotation is approximated to occur for a climb velocity ratio of ($-1.8 \leq V_c/v_c < -1.85$). Autorotation is the phenomenon where the rotors rotation is solely power by the upward airstream, which in turn slows the rate of descent. The effect of autorotation is what allows helicopters to land during motor failure and could be something to consider for catastrophic failure of all the drones rotors. The turbulent wake state is visualized in Figure 5.2, image (c).

- *Windmill brake state*
  For even higher rates of descent ($V_c/v_h < -2$) the rotor is in the windmill brake state as shown in Figure 5.2, image (d). The state is characterized by a smooth airflow with a definite slip stream moving upwards through the rotor.

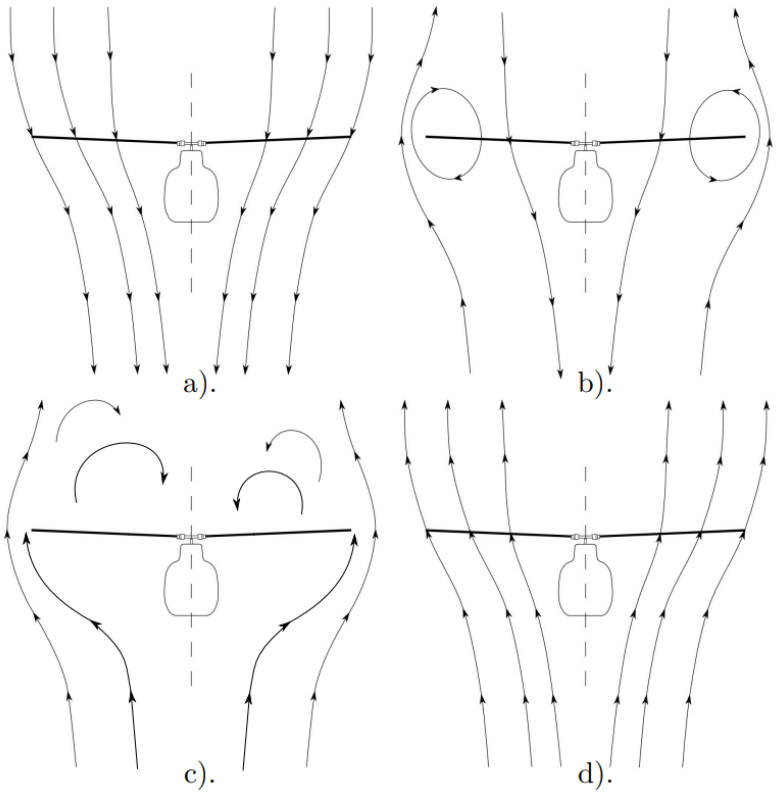

Figure 5.2: Rotor flow states: a) Normal working state b) Vortex ring state c) Turbulent wake state d) Windmill brake state [22].

In Figure 5.3 below, the four rotor states are plotted in relation to the climb velocity ratio as well as the rotor torque ratio, which is the ratio between the rotors instantaneous torque Q and the rotors torque produced at hover Q_h. It is shown that the normal working state is in the region of ascent, while the remaining states are in the region of descent. The point of ideal autorotation is also indicated, occurring at a rotor torque ratio of zero, meaning no motor torque is required. Additionally, it is illustrated in the figure that the torque curve is derived by measurements for the vortex ring state and turbulent wake state. This is due to the influence of turbulence and an absence of a uniform slipstream, which makes it necessary to determine the curve empirically [94]. This is the basis for assuming that the rotor is in a normal working state at all times in the model, while allowing for a descent of ($-\frac{1}{2} \leq V_c/v_h < 0$) to be included in the state. The theoretical framework used is thus assumed valid up to a maximum descent rate of $V_c = -v_h/2$. Exceeding this rate is however inadvisable, as it results in diminished performance and compromised stability due to the emergence of vortex rings.

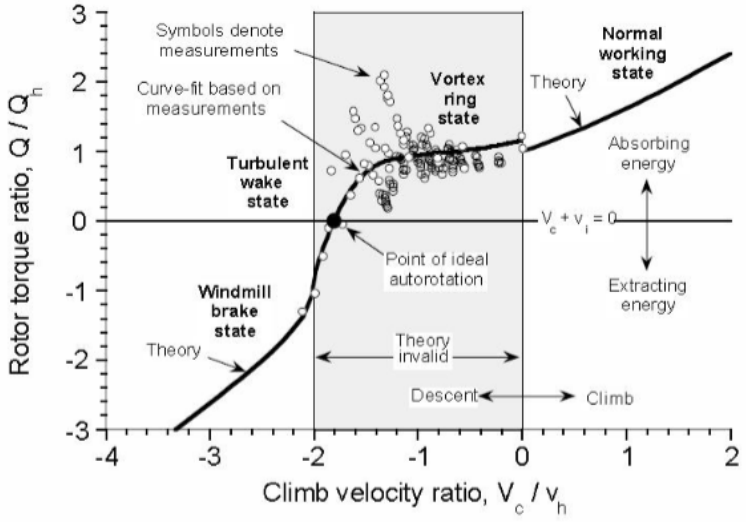

Figure 5.3: Rotor flow states – torque curve for rotor in vertical climb or descent [94].

Calculating the maximum rate of descent, the induced inflow velocity at hover v_h is first calculated using momentum theory as shown below, where T is the rotor's produced thrust, A is the rotor area and ρ is the air density.

$$v_h = \sqrt{\frac{T}{2\rho A}}$$

Assuming that the drone is close to sea-level, and that the area is derived from the final concept proposed in Section 4.5, the maximum descent rate v_h is calculated to be 4.3 m/s. As previously mentioned, such a descent rate leads the rotor into a vortex ring state, characterized by diminished aerodynamic efficiency and reduced stability due to turbulence. A conservative descent rate of 2 m/s is thus deemed appropriate.

5.2 Model description

This section introduces the foundational components of the hexacopter's physical and mathematical framework, beginning with the coordinate systems that describe its orientation and movement relative to the environment world frame. The hexacopter's body and payloads are defined with respect to these frames, and their combined influence on the system's mass distribution and inertia are derived. Furthermore, the kinematic relationships that enable transformation between coordinate systems are established using Euler angles. Together, these elements form the basis for deriving the equations of motion and control strategies presented in later chapters.

5.2.1 Hexacopter coordinate system configuration

As shown in Figure 5.4, the system consists of two different coordinate frames: an inertial world coordinate frame $\{W\} = \{x_W, y_W, z_W\}$ and a hexacopter body-fixed coordinate frame $\{B\} = \{x_B, y_B, z_B\}$. The body frames origin is selected to coincide with the hexacopters center of mass (CoM). The frame is oriented as shown in Figure 5.4 below, where x_B points in the direction of the first motor $M1$. The body frames origin also coincides with the drones geometric center in the xy-plane as it is assumed that the drone is symmetric around its z-axis. Both the world frame and body frame are orthogonal Cartesian coordinate systems, with the world frame considered stationary due to the flat earth assumption. The two coordinate frames are related using the Euler angles ϕ (roll), θ (pitch) and ψ (yaw) which are described in greater detail in Section 5.2.3.

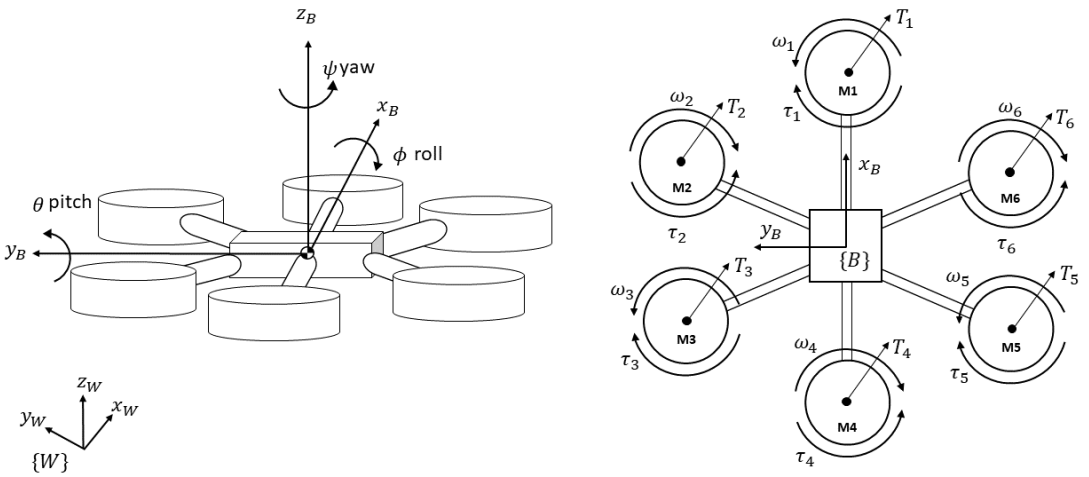

Figure 5.4: Hexacopter coordinate system configuration with visualization of torques, thrusts, and rotational velocities.

The hexacopter has six degrees of freedom – linear motion in all three axes (forward/backward, left/right, up/down) and rotational motion around these axes, described by the Euler angles roll, pitch, and yaw. These DOFs are selected as the hexacopters system states. Control is achieved through six control inputs corresponding to the individual thrusts T_i, which are generated by adjusting the angular velocity ω_i of the rotors. Only four of the control inputs are however linearly independent system variables which can be used to independently influence the systems state, which means that the system is under-actuated, causing some states to be indirectly influenced by the control inputs. This characteristic will be discussed in more detail in Chapter 7.1. It is also worth noting that each rotor produces a torque τ_i around its rotational axis as a result of its angular velocity ω_i. To counteract the individual yaw torques produced by each rotor, the direction of rotation is alternated between adjacent rotors. This configuration enables the opposing torques to cancel

each other out in steady flight, while yaw control can still be achieved by adjusting the ratio between clockwise and counterclockwise rotor speeds. The control inputs T_i as well as the alternating rotational velocities ω_i and torques τ_i can be seen in Figure 5.4 above.

5.2.2 Payload description

The payloads, which have been previously presented in Section 1.2.2, are also included in the hexacopter model. In Figure 5.5 below, The hexacopter is shown with the upper and lower payload attached. For illustrative purposes, motor $M4$ has been intentionally omitted to improve visibility. Furthermore, the size of the respective payloads in the figure are not to scale. The upper and lower payloads are associated with the coordinate systems $\{U\}$ and $\{L\}$, which are positioned at the CoM of their respective payloads. Both payloads are assumed to be geometrically symmetric about their local z-axis and are mounted along the drone's z-axis.

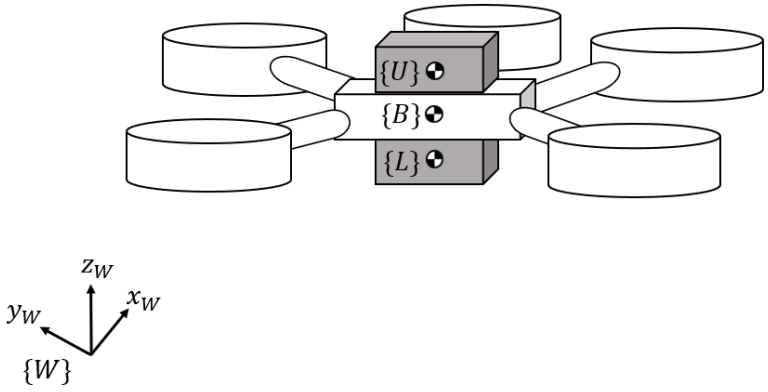

Figure 5.5: Hexacopter payload configuration.

To relate the payload coordinate frames to the drones body frame, two position vectors are defined in $\{B\}$. $\mathbf{r}_{U,B}$ describes the position of the upper payload and $\mathbf{r}_{L,B}$ describes the position of the lower payload. The vectors are shown below, where z_U and z_L are the absolute position between a payloads CoM and the drones CoM.

$$\mathbf{r}_{U,B} = \begin{bmatrix} 0 \\ 0 \\ z_U \end{bmatrix}, \quad \mathbf{r}_{L,B} = \begin{bmatrix} 0 \\ 0 \\ -z_L \end{bmatrix} \tag{5.1}$$

The physical properties of the payloads and hexacopter considered in the model include their masses, centers of mass (CoM), moments of inertia, and aerodynamic drag. To simplify the later derived equations of motion, the hexacopter body and payloads will be treated as a single rigid body for calculations regarding masses and moments of inertia. They will however be regarded as separate for aerodynamic calculations due to their complexity. The combined system will be referred to as H, representing the entire hexacopter assembly. The total mass and CoM position of

the hexacopters assembly defined in the body coordinate frame is thus defined as shown below.

$$m_H = m_B + m_L + m_U \tag{5.2}$$

$$\mathbf{r}_{H,B} = \frac{\mathbf{r}_{B,B}m_B + \mathbf{r}_{L,B}m_L + \mathbf{r}_{U,B}m_U}{m_B + m_L + m_U} = \begin{bmatrix} 0 \\ 0 \\ \frac{m_U z_U - m_L z_L}{m_Q} \end{bmatrix}_B$$

The inertia tensor for H will be calculated relative to the body frame $\{B\}$. Since the inertia tensors of the upper and lower payloads are defined relative to their own centers of mass, they must be shifted to the body frame using the parallel axis theorem, as shown below.

$$\begin{cases} \mathbf{I}_{U,B} = \mathbf{I}_{U,U} + m_U \left[(\|\mathbf{r}_{U,B}\|^2)\mathbf{I} - \mathbf{r}_{U,B}(\mathbf{r}_{U,B})^T \right] \\ \mathbf{I}_{L,B} = \mathbf{I}_{L,L} + m_L \left[(\|\mathbf{r}_{L,B}\|^2)\mathbf{I} - \mathbf{r}_{L,B}(\mathbf{r}_{L,B})^T \right] \end{cases} \tag{5.3}$$

The total inertia tensor of the hexacopter assembly can then be obtained by summing the individual inertia tensors of the hexacopter body and the payloads, each expressed relative to the body frame.

$$I_{H,B} = I_{B,B} + I_{U,B} + I_{L,B} \tag{5.4}$$

5.2.3 Kinematics

A kinematic relation is needed to transform coordinates from the body frame $\{B\}$ to the world frame $\{W\}$. Tait-Bryan angles are commonly used to describe such transformations, and in this case, the 3-2-1 Euler rotation matrix (Yaw ψ, Pitch θ, Roll ϕ) is chosen. The elementary rotation matrices and the multiplication of these are shown below. For notation simplicity, the sine and cosine functions are abbreviated as s and c.

$$R_z = \begin{bmatrix} c(\psi) & -s(\psi) & 0 \\ s(\psi) & c(\psi) & 0 \\ 0 & 0 & 1 \end{bmatrix} R_y = \begin{bmatrix} c(\theta) & 0 & s(\theta) \\ 0 & 1 & 0 \\ -s(\theta) & 0 & c(\theta) \end{bmatrix} R_x = \begin{bmatrix} 1 & 0 & 0 \\ 0 & c(\phi) & -s(\phi) \\ 0 & s(\phi) & c(\phi) \end{bmatrix}$$

$$\overset{B}{R}_W = R_z(\psi)R_y(\theta)R_x(\phi)$$

Where $R_z(\psi)$ represents the yaw rotation around the world axis z_W, $R_y(\theta)$ represents the pitch rotation around the intermediate axis y_1, and $R(\phi)$ represents the roll rotation around the body axis x_B. The resulting rotation matrix which transforms body coordinates into world coordinates is shown below.

$$\overset{B}{R}_W = \begin{bmatrix} c(\psi)c(\theta) & c(\psi)s(\phi)s(\theta) - c(\phi)s(\psi) & s(\phi)s(\psi) + c(\phi)c(\psi)s(\theta) \\ c(\theta)s(\psi) & c(\phi)c(\psi) + s(\phi)s(\psi)s(\theta) & c(\phi)s(\psi)s(\theta) - c(\psi)s(\phi) \\ -s(\theta) & c(\theta)s(\phi) & c(\phi)c(\theta) \end{bmatrix} \tag{5.5}$$

One aspect of Euler angles that must be considered is the gimbal lock phenomenon, which occurs when two of the three rotational axes become aligned, resulting in the loss of one degree of freedom. This singularity occurs for the chosen 321 Tait-Bryan angles when $\theta = \pm 90deg$. The singularity is deemed acceptable as the hexacopters pitch will be close to zero. The rotation matrix that transforms coordinates from the world frame to the body frame is obtained by performing the transpose of the matrix above, as shown below.

$$\overset{W}{R}_B = \left(\overset{B}{R}_W\right)^T \tag{5.6}$$

In the hexacopters body frame $\{B\}$ the linear velocities are expressed as v_{Bx}, v_{By}, v_{Bz} and the rotational velocities are expressed as $\omega_{Bx}, \omega_{By}, \omega_{Bz}$. As rotational velocities are defined in the body frame, they will differ from the Euler angles, which are defined for intermediate coordinate frames. An expression between the rotational velocities and the Euler angle derivatives is derived using the elementary rotation matrices from the 3-2-1 Euler convention.

$$\boldsymbol{\omega_B} = \begin{bmatrix} \omega_{B_x} \\ \omega_{B_y} \\ \omega_{B_z} \end{bmatrix} = \begin{bmatrix} \dot{\phi} \\ 0 \\ 0 \end{bmatrix} + R_x(\phi) \begin{bmatrix} 0 \\ \dot{\theta} \\ 0 \end{bmatrix} + R_x(\phi)R_y(\theta) \begin{bmatrix} 0 \\ 0 \\ \dot{\psi} \end{bmatrix}$$

The relation can be simplified and also inverted as shown below, where tan is abbreviated as t. The resulting matrix T can only be inverted for $\theta \neq \pm 90deg$. It should be noted that the matrix T reduces to the identity matrix for small Euler angles. However, this step cannot be omitted, as the UAV may experience large angle displacements.

$$\boldsymbol{\omega_B} = \underbrace{\begin{bmatrix} 1 & 0 & -s(\theta) \\ 0 & c(\phi) & c(\theta)s(\phi) \\ 0 & -s(\phi) & c(\theta)c(\phi) \end{bmatrix}}_{T} \begin{bmatrix} \dot{\phi} \\ \dot{\theta} \\ \dot{\psi} \end{bmatrix}, \quad \begin{bmatrix} \dot{\phi} \\ \dot{\theta} \\ \dot{\psi} \end{bmatrix} = \underbrace{\begin{bmatrix} 1 & s(\psi)t(\theta) & c(\phi)t(\theta) \\ 0 & c(\phi) & -s(\phi) \\ 0 & s(\phi)/c(\theta) & c(\phi)/c(\theta) \end{bmatrix}}_{T^{-1}} \boldsymbol{\omega_B} \tag{5.7}$$

5.3 Euler–Lagrange formulation

The generalized coordinates q_h are chosen to reflect the systems DOF:s. For the hexacopter, the linear position in all three axes as well as the hexacopters Euler angles are chosen as shown below. The generalized coordinates can thus be considered as the hexacopters system states, which are described in the world frame $\{W\}$.

$$\mathbf{q}_h = \begin{bmatrix} x_W & y_W & z_W & \phi & \theta & \psi \end{bmatrix}^T \tag{5.8}$$

5.3.1 External forces

To derive the equations of motion using the Euler–Lagrange formulation, all external forces acting on the hexacopter have to be accounted for. The external forces

which are considered in the model are thrust and torque generated by the rotors, aerodynamics, and gyroscopic progression. The total external force is thus obtained by summing the contributions from the previously mentioned effects as shown below.

$$\mathbf{Q}_h = \mathbf{Q}_{rotor} + \mathbf{Q}_{gyro} + \mathbf{Q}_{aero}$$

It is important to note that the external forces act on the system states defined in (5.8). The "external forces" $\mathbf{Q}$ are thus both linear forces and rotational torques, structured as shown below. If an effect cannot be explicitly expressed in terms of external forces, the principle of virtual work is applied to account for its influence on the system dynamics, as detailed in Section 5.3.1.4.

$$\mathbf{Q}_h = \begin{bmatrix} Q_x & Q_y & Q_z & Q_\phi & Q_\theta & Q_\psi \end{bmatrix}^T \tag{5.9}$$

5.3.1.1 Rotor thrust and torque generation

The equations describing the thrust and torque exerted by the rotors on the hexacopter is, as stated in Section 5.1, assumed to be proportional to the rotational velocity squared. The relation for the thrust produced by a rotor is shown below, where k is the lift constant.

$$T_i = k\omega_i^2 \quad \rightarrow \quad \omega_i = \sqrt{T_i/k} \tag{5.10}$$

The second relation corresponds to the torque generated by the rotors drag, acting along its axis of rotation. The relation is shown below, where b is the rotors drag constant. In literature, the rotor inertia term $I_R\dot{\omega}$ is often included to represent the dynamic resistance to variations in rotational speed. This term is however omitted to reduce model complexity, and the resulting lag due to dynamic resistance will instead be captured within the system's overall lag dynamics.

$$\tau_i = b\omega_i^2 \tag{5.11}$$

The contributions of rotor thrusts and torques are to be incorporated into the generalized force vector $\mathbf{Q}_{rotor}$. The net thrusts are calculated as shown below, where it is illustrated that the combined thrust from all rotors results in a total force acting along the z-axis of the local body frame $\{B\}$.

$$T_B = \begin{bmatrix} 0 \\ 0 \\ T_z \end{bmatrix}_B, \quad T_z = \sum_{i=1}^{6} T_i \tag{5.12}$$

The net thrust can then be transformed to the world frame $\{W\}$ by using the transformation matrix derived in (5.5).

$$T_W = \overset{B}{R}_W T_B = T_z \begin{bmatrix} -s(\theta) \\ s(\phi)c(\theta) \\ c(\phi)c(\theta) \end{bmatrix}$$

The individual rotor thrusts and torques also contribute to a net moment acting on the hexacopter's body frame. Thrust imbalances between opposing rotors induce

torques around the roll (ϕ) and pitch (θ) axes, while the individual rotor torques result in a net torque around the yaw (ψ) axis. The final expression describing the net torques acting on the hexacopter in the body frame is shown below, where d is the length from the hexacopters CoM to the rotor-axes in the xy-plane in $\{B\}$.

$$\tau_B = \begin{bmatrix} d \cdot cos(\pi/6) \cdot (T2 + T3 - T5 - T6) \\ d \cdot (T_4 - T_1) + d \cdot sin(\pi/6) \cdot (T_3 + T_5 - T_2 - T_6) \\ -\tau_1 + \tau_2 - \tau_3 + \tau_4 - \tau_5 + \tau_6 \end{bmatrix} \tag{5.13}$$

The rotor thrusts and torques, expressed in terms of the external force vector, can thus be written as:

$$\mathbf{Q}_{rotor} = \begin{bmatrix} T_W \\ \tau_B \end{bmatrix}$$

By expressing the rotor torques τ_i in terms of the rotor thrusts T_i, through substitution of ω_i from (5.10) into (5.11), the rotor torques τ_i can be expressed directly in terms of the rotor thrusts T_i, resulting in the following relation:

$$\tau_i = T_i \frac{b}{k} \tag{5.14}$$

When substituting τ_i from (5.14) into (5.13), and combining the result with the thrust expression from (5.13), a matrix which relates rotor torque inputs to net forces and torques applied to the hexacopter's body frame is obtained. This is known as the inverse of the motor mixing matrix MM. It is trivially seen that the motor mixing matrix inverse is equal to $\mathbf{Q}_{rotor}$ but written in terms of the rotor thrusts using matrix-vector notation.

$$\begin{bmatrix} T_z \\ \tau_\phi \\ \tau_\theta \\ \tau_\psi \end{bmatrix} = \underbrace{\begin{bmatrix} 1 & 1 & 1 & 1 & 1 & 1 \\ 0 & d\frac{\sqrt{3}}{2} & d\frac{\sqrt{3}}{2} & 0 & -d\frac{\sqrt{3}}{2} & -d\frac{\sqrt{3}}{2} \\ -d & -d\frac{1}{2} & d\frac{1}{2} & d & d\frac{1}{2} & -d\frac{1}{2} \\ -\frac{b}{k} & \frac{b}{k} & -\frac{b}{k} & \frac{b}{k} & -\frac{b}{k} & \frac{b}{k} \end{bmatrix}}_{MM^{-1}} \begin{bmatrix} T_1 \\ T_2 \\ T_3 \\ T_4 \\ T_5 \\ T_6 \end{bmatrix} \tag{5.15}$$

The motor mixing matrix is subsequently derived by computing the pseudo inverse of (7.5) above, since MM^{-1} is not square and therefore not directly invertible. As shown in the equations below, the matrix MM provides an explicit mapping from the desired total thrust and body-frame torques to the individual rotor thrusts required to produce them. The matrix will be used in Section 7.4 for the development of the control algorithm; it is not applied in the modeling itself but is presented here for context.

$$MM = \left(MM^{-1}\right)^{\dagger}$$

$$\begin{bmatrix} T_1 \\ T_2 \\ T_3 \\ T_4 \\ T_5 \\ T_6 \end{bmatrix} = \underbrace{\begin{bmatrix} \frac{1}{6} & 0 & -\frac{1}{3d} & -\frac{k}{6b} \\ \frac{1}{6} & \frac{\sqrt{3}}{6d} & -\frac{1}{6d} & \frac{k}{6b} \\ \frac{1}{6} & \frac{\sqrt{3}}{6d} & \frac{1}{6d} & -\frac{k}{6b} \\ \frac{1}{6} & 0 & \frac{1}{3d} & \frac{k}{6b} \\ \frac{1}{6} & -\frac{\sqrt{3}}{6d} & \frac{1}{6d} & -\frac{k}{6b} \\ \frac{1}{6} & -\frac{\sqrt{3}}{6d} & -\frac{1}{6d} & \frac{k}{6b} \end{bmatrix}}_{MM} \begin{bmatrix} T_{tot} \\ \tau_\phi \\ \tau_\theta \\ \tau_\psi \end{bmatrix} \tag{5.16}$$

5.3.1.2 Rotor Gyroscopic force

Due to the inertia of the spinning rotors, the gyroscopic effect will take place when the hexacopter turns in pitch (ϕ) or roll (θ). The inertia vector is aligned with the z-axis of the local body frame $\{B\}$. Assuming the hexacopter's rotors experience constant precession around the x- or y-axis of the body frame, the resulting gyroscopic torque is perpendicular to both the inertia vector and the precession vector, and its direction is derived using the right-hand rule. An example of this is shown in Figure 5.6, where the inertia vector points along the z-axis and the rotor undergoes a rotation around the x-axis with angular velocity ω_ϕ, resulting in the gyroscopic torque τ_θ around the y-axis.

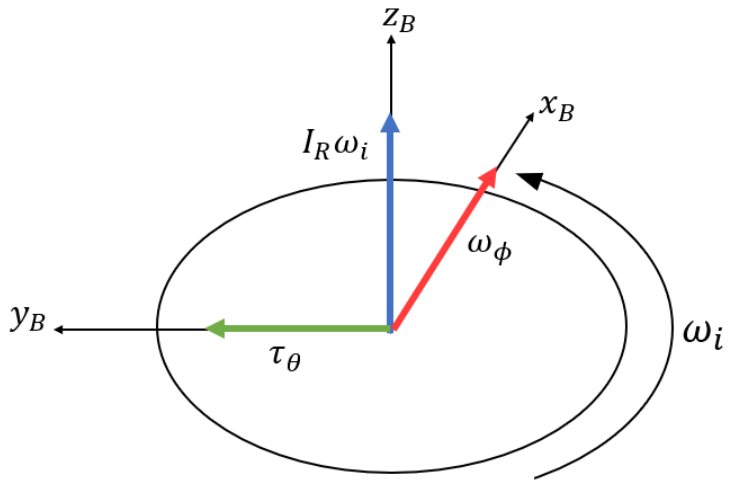

Figure 5.6: Illustration of rotor gyroscopic effect.

The gyroscopic torque can thus be computed as the cross product of the inertia vector and the precession vector. The precession vector represents the angular velocity components corresponding to the rotation of the rotor about the x- or y-axis of the body frame.

$$\tau_g = I_r\omega_r \times \omega_p$$

This relationship can be explicitly expressed using the individual rotor angular velocities and the precession angular velocities, as shown below.

$$\tau_g = \begin{bmatrix} I_r\omega_y(\omega_1 - \omega_2 + \omega_3 - \omega_4) \\ I_r\omega_x(-\omega_1 + \omega_2 - \omega_3 + \omega_4) \\ 0 \end{bmatrix}$$

As shown below, the external forces can be expressed directly in terms of the gyroscopic torques.

$$\mathbf{Q}_{\text{gyro}} = \begin{bmatrix} 0_{1\times 3} & \tau_g \end{bmatrix}^T$$

5.3.1.3 Wind disturbance definition

Before analyzing the impact of aerodynamic drag on the hexacopter, it's important to first characterize the wind disturbances that define the surrounding fluid flow. In particular, specifying the altitude at which wind speed is measured is crucial when determining the conditions the model will be exposed to. The standard practice for wind forecast measurements is to record wind speeds at a height of 10 meters above the ground. Therefore, any wind disturbances applied to the model will be related to wind speed measurements performed at this height. To relate the measured wind speeds at 10 meters, to the wind speed at the UAV altitude, the wind profile power law is used.

$$V_2 = V_1 \left(\frac{z_2}{z_1}\right)^{\alpha} \tag{5.17}$$

The relation is shown above, where the wind speed V_2 at height z_2 is estimated based on a known wind speed V_1 at the reference height z_1. The coefficient α is the wind shear exponent, which is an empirically derived constant that is dependent on the characteristics of the underlying terrain. The table below illustrates the wind shear exponent for several different terrain types.

Terrain description	α
Smooth, hard ground, lake or ocean	0.1
Short grass on untilled ground	0.14
Level country with foot-high grass, occasional tree	0.16
Tall row crops, hedges, a few trees	0.2
Many trees and occasional buildings	0.22-0.24
Wooded country - small town and suburbs	0.28-0.3
Urban areas with tall buildings	0.4

Table 5.1: Wind profile power law for different terrains [95].

For simplicity, the equation can be expressed as shown below, where V_{10} represents the measured wind speed at 10 meters, and V_H denotes the wind speed at the hexacopter's altitude z_h.

$$V_h(z_h, t) = V_{10}(t) \left(\frac{z_h}{10}\right)^{\alpha} \tag{5.18}$$

Wind speeds at 10 meters altitude can either be sourced from real-world measurement data or approximated using a model. The modeling approach has been selected, as it offers the advantage of flexibility and the ability to account for varying conditions. Complex wind models, such as the Dryden Wind Turbulence Model, simulates wind turbulence by using stochastic processes to represent random fluctuations in wind speed [96]. However, a more simplistic approach is preferred to keep the overall model simple, which will still be sufficient given the relatively low altitudes at which the drone will operate (≤ 1 km). A simpler approach is proposed by Stull [97], where the wind is approximated as the superposition of three different types of flow, which are described below.

- *Mean wind* – Relatively constant but varying slowly over the course of hours
- *Wind waves* – Regular linear oscillations of wind, often with periods of ten minutes or longer
- *Turbulence* – Irregular, quasi-random, non-linear variations or gusts, with durations of seconds to minutes

The simulation duration is discussed in greater detail in Section 8.1.1, however it can already be noted that the system will be simulated for approximately a few minutes. Given this relatively short time frame, the flow type known as wind waves, characterized by oscillations on the order of ten minutes or longer, will have limited influence and is therefore excluded from the model. Instead, this flow type is effectively accounted for within the mean wind flow, with a greater focus placed on turbulence, which is more relevant to the time scale under consideration. To better capture the effects of turbulence, it is divided into two components: a low-frequency part and a high-frequency part. The low-frequency turbulence, varying over the span of minutes, represents larger-scale gusts or gradual changes in wind speed. These gusts are modeled by a sine wave, and scaled by the mean wind speed and a gust-factor. In contrast, high-frequency turbulence, with variations occurring over seconds, captures the rapid, smaller-scale wind fluctuations. The high frequency turbulence part is modeled by use of white noise passed through a first-order high-pass filter, which follows a method similarly implemented by Li [98], where first-order filters and white noise is used to describe both low- and high-frequency components. This results in the equations below, where $V_{10}(t)$, describes the wind speeds at 10 meters, and $v_{HF}(t)$ describes the high frequency turbulence component created by passing white gaussian noise through a first-order low-pass filter.

$$\begin{cases} V_{10}(t) = V_{mean}\left(1 + K_G \sin(\omega_s t) + v_{HF}(t)\right) \\ v_{HF}(t) = \mathcal{L}^{-1}\left\{\frac{s}{s+\omega_c} WGN(0, I)\right\} \end{cases} \tag{5.19}$$

The parameters defined above may be adjusted to simulate a variety of wind conditions. However, baseline values are specified here based on Stulls approach [97] and established standards related to wind environmental testing. Given that the low-frequency turbulence typically fluctuates over time scales on the order of minutes,

Variable	Description
V_{mean}	Mean wind speeds at 10 m altitude
K_G	Wind gust scaling coefficient
ω_s	Sinusoidal gust signal frequency
ω_c	Cutoff frequency of the high-pass filter
I	Intensity of the white Gaussian noise (WGN)

a sine wave period of 60 seconds is chosen as a conservative approximation. This period corresponds to the sine wave frequency being $\omega_s = 0.1$ rad/s. The cutoff frequency ω_c of the high-pass filter is also set to 0.1 rad/s, ensuring that higher-frequency fluctuations, beyond those captured by the sine wave, are represented for the high-frequency turbulence. The baseline value for the intensity I of the white gaussian noise is chosen as 0.01, but can be altered to change the intensity of turbulence.

The amplitude of the sine wave is determined by a gust coefficient which is defined by the MIL STD 810 G military standard for environmental testing [99]. In the standard it is proposed that a gust must have a duration such that its size is eight times the downwind dimension of an object in order for it to produce a force on the structure commensurate with the gust speed. The gust coefficient is thus dependent on the size of the hexacopter, and is determined to be $K_G = 1.47$, for the given hexacopter size defined in Section 4.5. This result is further supported by the STANAG 2895 standard, which suggests a comparable gust coefficient of $K_G = 1.54$ [100].

To categorize the amplitude of the mean wind speed V_{mean}, the Beaufort wind scale is used [101]. The scale divides the wind speed conditions into 12 levels, ranging from *calm* (Force 0) to *hurricane* (Force 12). Each level corresponds to specific wind speed intervals and an associated impact on the environment (both for land and at sea). The scale is commonly applied in meteorology and engineering to assess wind conditions, and can be seen in the Appendix E. The scale offers a practical framework for classifying the wind conditions that the hexacopter is capable of operating in.

Wind speeds which are applied to the hexacopter are thus modeled by selecting a wind force level on the Beaufort wind scale, which defines a corresponding mean wind speed V_{mean}. Gusts and turbulence are then included in accordance to (5.19) and then related to the height of the drone using the wind profile power law (5.18). The wind speed, as defined above, is also given a direction, which can be altered within the model. The wind disturbance $V_h(z_h)$ is assumed to act within the global XY-plane, with an angle of attack γ relative to the world X-axis. There is thus no wind applied in the global z-axis. The wind speed vector can thus be defined by the following equation.

$$\mathbf{V}_h = \begin{bmatrix} cos(\gamma) \cdot V_H(z_h, t) \\ sin(\gamma) \cdot V_H(z_h, t) \\ 0 \end{bmatrix} \tag{5.20}$$

The wind disturbance relative to the drone and world frame is shown in Figure 5.7 below.

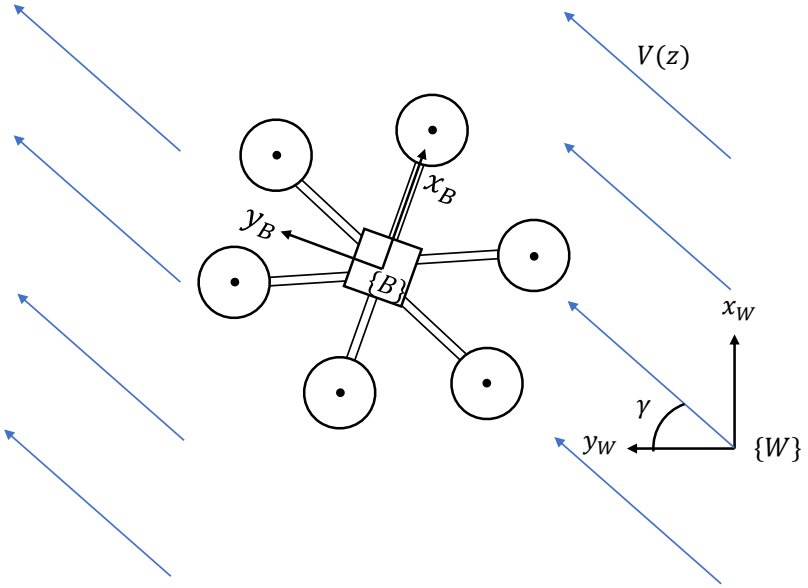

Figure 5.7: Wind disturbance relative to world frame $\{W\}$.

5.3.1.4 Aerodynamic drag

When a rigid body moves relative to the fluid it is immersed in, it experiences a force that opposes the relative motion, known as drag. The rigid body's drag is dependent on its relative speed, size and shape, as well as the properties of the fluid which surrounds it. For this analysis, it is assumed that the winds acting on the hexacopter and its payloads are incompressible and laminar. These assumptions are reasonable because the hexacopter assembly will be tethered and operate at low speeds. Further justification for these assumptions is provided in Section 5.1. The drag force acting on an object submerged in a fluid with relative fluid flow is calculated using the formula shown below.

$$F_D = C_D A \frac{\rho V_{rel}^2}{2} \tag{5.21}$$

Variable	Description
F_D	Drag force
C_D	Drag coefficient
A	Reference area
ρ	Air density.
V_{rel}	Flow velocity relative to object

Equation (5.21) is used to compute the aerodynamic drag on the hexacopter and its payloads in all translational degrees of freedom in the hexacopters body frame $\{B\}$. The aerodynamic drag of the hexacopter frame is first calculated. The relative

fluid flow velocity $V_{Hrel,W}$ is defined as the wind velocity minus by the hexacopter's velocity in the world frame, as shown in the equation below.

$$V_{h,rel,W} = \begin{bmatrix} V_{h,x} - v_x \\ V_{h,y} - v_y \\ -v_z \end{bmatrix} \tag{5.22}$$

The relative velocity is then transformed to the body frame by means of the rotation matrix (5.6), as seen below.

$$V_{h,rel,B} = \overset{W}{R}_B V_{h,rel,W}$$

The hexacopter drag force is then calculated as shown below, with the reference area and drag coefficient adjusted for each local coordinate direction. As previously stated, the hexacopter is assumed to be symmetric about its local z-axis. Therefore, the same reference area and drag coefficient are used for the local x- and y-axis.

$$F_{h,D,B} = -\frac{1}{2}\rho \begin{bmatrix} C_{D,xy} A_{xy} V_{h,relx,B}^2 \\ C_{D,xy} A_{xy} V_{h,rely,B}^2 \\ C_{D,z} A_z V_{h,relz,B}^2 \end{bmatrix} \tag{5.23}$$

The drag forces which are defined in the body frame above are transformed in the world frame by use of (5.5) so that it can later be applied to the model as an external force.

$$F_{h,D,W} = \overset{B}{R}_W F_{h,D,B} \tag{5.24}$$

As stated in Section 5.2.2, the payload drag forces are excluded from the hexacopter's drag calculation in (5.23) above. This is due to the complexity involved in accurately determining the aerodynamic drag coefficients, as well as the fact that the payloads may experience different velocities relative to the hexacopter due to its rotational velocity. To account for this, a skew-symmetric matrix is used to incorporate the rotational velocity of the entire hexacopter assembly when calculating the velocity of the payloads. Since the calculations for both the upper and lower payloads are identical, the derivation below will solely present the lower payload derivations. To calculate the lower payload velocity in the world frame $v_{L,W}$, the position vector from (6.8) will be transformed to the world frame as shown below.

$$r_{L,W} = \overset{B}{R}_W r_{L,B}$$

Differentiating the position vector in the world frame yields the following.

$$\dot{r}_{L,W} = \frac{d\overset{B}{R}_W}{dt} r_{L,B} + \overset{B}{R}_W \frac{dr_{L,B}}{dt} = \frac{d\overset{B}{R}_W}{dt} r_{L,B}$$

The skew-symmetric matrix Ω can then be used to express the rotation matrix derivative.

$$\dot{R} = \Omega R, \quad \Omega = \begin{bmatrix} 0 & -\omega_z(t) & \omega_y(t) \\ \omega_z(t) & 0 & -\omega_x(t) \\ -\omega_y(t) & \omega_x(t) & 0 \end{bmatrix}$$

$$\dot{r}_{L,W} = \frac{d\overset{B}{R}_W}{dt} r_{L,B} = \Omega \overset{B}{R}_W r_{L,B}$$

The translational velocity of the payloads is expressed as the sum of the translational velocity of the hexacopter and the additional velocity induced by its rotational motion.

$$v_{L,W} = v_{B,W} + \dot{r}_{L,W} = v_{B,W} + \Omega_B \overset{B}{R}_W r_{L,B}$$

The aerodynamic drag is then calculated in a similar manner to that of the hexacopter. It is however assumed that the wind velocity applied to the hexacopter, as defined in (5.20), is also applied to the payloads even though there may be slight variations in altitude and wind speeds.

$$V_{L,rel,W} = \begin{bmatrix} V_{h,x} - v_{L,x,W} \\ V_{h,y} - v_{L,y,W} \\ -v_{L,z,W} \end{bmatrix}$$

The relative velocity is then transformed to the body frame.

$$V_{L,rel,B} = \overset{W}{R}_B V_{,Lrel,W}$$

This results in the forces applied to both the upper and lower payload due to aerodynamic drag. It is important to note that the drag forces due to the payloads are not considered in the local z-direction. This is because, from the perspective of the z-axis, the payloads do not introduce additional area compared to the hexacopter frame, and therefore do not contribute to any further drag forces in this direction.

$$F_{U,D,B} = -\frac{1}{2}\rho \begin{bmatrix} C_{U,D,xy} A_{U,xy} V^2_{h,relx,B} \\ C_{U,D,xy} A_{U,xy} V^2_{h,rely,B} \\ 0 \end{bmatrix}, \quad F_{L,D,B} = -\frac{1}{2}\rho \begin{bmatrix} C_{L,D,xy} A_{L,xy} V^2_{h,relx,B} \\ C_{L,D,xy} A_{L,xy} V^2_{h,rely,B} \\ 0 \end{bmatrix} \tag{5.25}$$

The drag forces acting on the hexacopter frame can be directly applied as external forces, as they are defined to align with the directions of the generalized coordinates. The drag forces acting on the payloads are however displaced from the body coordinate system $\{B\}$ and will thus contribute with both a force and a torque applied to $\{B\}$. As a result, the previously calculated drag forces on the payloads must also be expressed as equivalent torques with respect to $\{B\}$. This is achieved using the principle of virtual work, which is extensively detailed in [102] and will be briefly summarized here. The principle of virtual work states that the total virtual work performed by a force F_w due to a virtual displacement $\delta\xi$ of an object, is as shown below.

$$\delta W = F_w^T \delta\xi$$

In the equation above, ξ represents the position of the payloads in the world frame and is equivalent to $P_{L,W}$ and $P_{U,W}$. The positions are calculated as follows.

$$P_{L,W} = \begin{bmatrix} x \\ y \\ z \end{bmatrix} + {}^{B}_{W}R\,\mathbf{r}_{L,B}, \quad P_{U,W} = \begin{bmatrix} x \\ y \\ z \end{bmatrix} + {}^{B}_{W}R\,\mathbf{r}_{U,B} \tag{5.26}$$

The virtual displacements of the hexacopter's position can be expressed in terms of the system's generalized coordinates as:

$$\delta\xi = \frac{\partial\xi}{\partial q}\delta q$$

This yields the virtual work expressed in terms of generalized coordinates.

$$\delta W = \left(F_w^T \frac{\partial\xi}{\partial q}\right)\delta q \tag{5.27}$$

According to d'Alembert's principle, the virtual work can be written in a general form as shown below [102].

$$\delta W = Q\delta q$$

Given the two relations above, the external forces Q can thus be derived as:

$$Q = F_W^T \frac{\partial\xi}{\partial q} \tag{5.28}$$

The payload drag forces calculated in (5.25) and the payload position calculated in (5.26) are then substituted into (5.28) to give the final external forces expression for the payloads drag. Note that the drag forces are expressed in the world frame, where they have been transformed using the rotation matrix similarly to (5.24).

$$Q_{U,D} = F_{U,D,W}^T \frac{\partial P_{U,W}}{\partial q}, \quad Q_{L,D} = F_{L,D,W}^T \frac{\partial P_{L,W}}{\partial q}$$

The combined affect of the drag forces applied to the hexacopter frame, as well as its payloads, are summarized below.

$$\mathbf{Q}_{aero} = \begin{bmatrix} F_{h,D,W} \\ 0_{3\times1} \end{bmatrix} + Q_{U,D} + Q_{L,D}$$

5.3.2 Euler–Lagrange equations of motion

Both the kinetic and potential energy is needed to formulate the Euler Lagrange equations. These calculations are simplified as the hexacopter is treated as one single rigid body in regard to its mass and inertia. The hexacopter assembly will have the total mass m_H which is located at a distance $\mathbf{r}_{H,B}$ from the body frame $\{B\}$. Additionally, the hexacopter assembly possesses an inertia tensor $I_{H,B}$, which describes its rotational inertia with respect to the body frame.

When defining the kinetic energy of the hexacopter, the rotational velocity is expressed in the body frame, as the hexacopter's rotation occurs relative to this frame. This is also the reason why the inertia tensor is defined in the body frame. The

translational velocity will however be expressed in the world frame due to the choice of generalized coordinates. The kinetic energy of the system is thus calculated as shown below, where the rotational velocities are derived using the Euler angle derivatives derived in (5.7) and the hexacopter speed V_W is the derivative of the systems global position states in the world frame.

$$T_h = \frac{1}{2} m_h V_W^T V_W + \frac{1}{2} \omega_B^T I_i \omega_B$$

To calculate the potential energy of the hexacopter assembly, the position of its center of mass must first be determined, as shown below.

$$P_{h,W} = \begin{bmatrix} x \\ y \\ z \end{bmatrix} + \overset{B}{R}_W \mathbf{r}_{h,B}$$

The systems potential energy can then be calculated as:

$$V_h = m_h g P_{h,W}^T \begin{bmatrix} 0 \\ 0 \\ 1 \end{bmatrix}$$

Given the kinetic and potential energy calculated above, the Lagrangian can then be defined as shown below.

$$L_h(q, \dot{q}, z) = T_h(q, \dot{q}) - V_h(q)$$

The Euler Lagrange equations of motion is then derived as:

$$EL: \quad \frac{d}{dt}\left(\frac{\partial L_h}{\partial \dot{q}_h}\right) - \frac{\partial L_h}{\partial q_h} = Q_h$$

Where the time derivative is expanded as:

$$\frac{d}{dt}\left(\frac{\partial L_h}{\partial \dot{q}_h}\right) = \frac{\partial}{\partial q_h}\left(\frac{\partial L_h}{\partial \dot{q}_h}\right)\dot{q}_h + \frac{\partial}{\partial \dot{q}_h}\left(\frac{\partial L_h}{\partial \dot{q}_h}\right)\ddot{q}_h$$

This will yield a second order differential equation, which can be written in the form shown below.

$$W\ddot{q}_h + \frac{\partial}{\partial q}(W(q_h)\dot{q}_h)\dot{q}_h - \nabla_{q_h} T_h + \nabla_{q_h} V_h = Q_h \tag{5.29}$$

The matrix denoted as $W(q_h)$ above is known as the weight matrix and is derived by computing the partial derivative of the hexacopter mass position with respect to the generalized coordinates as shown below.

$$W(q_h) = m_h \frac{\partial P_h}{\partial q_h}^T \frac{\partial P_h}{\partial q_h}$$

Given the second-order differential equation in (5.29), an integrator is implemented to yield a system of first order differential equations (ODE:s). The subscript h is omitted in the equation below for clarity.

$$\begin{bmatrix} 0 & I \\ W(q) & 0 \end{bmatrix} \begin{bmatrix} \dot{X} \\ \dot{q} \end{bmatrix} = \begin{bmatrix} X \\ Q - \frac{\partial}{\partial q}(W(q)\dot{q})\dot{q} - \nabla_q T - \nabla_q V \end{bmatrix} \tag{5.30}$$

The ODE above represents the system's dynamics and serves as the mathematical model of the hexacopter. To complete the model, actuator lag dynamics will be introduced in the following section.

5.3.3 Complete hexacopter model with actuator lag dynamics

The hexacopter will exhibit lag dynamics, meaning it has a delay between receiving a control input and responding to it. The lag dynamics have been shown to be sufficiently described by a first order transfer function, which is applied to the rotor thrusts as shown below [22].

$$\dot{T}_i = -\frac{1}{\tau_a} T_i + \frac{1}{\tau_a} T_{R,i} \tag{5.31}$$

The variable T_i is the motor thrusts, $T_{R,i}$ is the reference value of the motor thrusts and τ_a is the actuator lag dynamics time constant. The time constant encapsulates actuator lag, but is also a lumped value and includes lag due to battery dynamics, ESC commands, and other system delays. The time constant τ_a has to be empirically derived by measuring the system delay which occurs when applying a rotor torque reference. Due to the theoretical nature of this project, the time constant can not be derived by physical tests of the proposed hexacopter. A measurement is therefore taken from a similar tethered drone system presented in [22], where the time constant was determined to be 5 ms. As a conservative estimate, the time constant is set to $\tau_a = 10$ ms, due to the hexacopter being slightly larger than the one presented in the reference.

The lag dynamics is implemented by including the first order differential equations (5.31) into the drones system of equations (5.30). A total of six lag dynamic equations are included, corresponding to the six rotors of the hexacopter. These equations are presented in vector form and integrated into the overall system as shown below. The subscript h is omitted in the equation for clarity.

$$\begin{bmatrix} 0 & I & 0_{1\times 6} \\ W(q) & 0 & 0_{1\times 6} \\ 0_{6\times 1} & 0_{6\times 1} & I_{6\times 6} \end{bmatrix} \begin{bmatrix} \dot{X} \\ \dot{q} \\ \dot{\mathbf{T}} \end{bmatrix} = \begin{bmatrix} X \\ Q - \frac{\partial}{\partial q}(W(q)\dot{q})\dot{q} - \nabla_q T - \nabla_q V \\ -\frac{1}{\tau_a}\mathbf{T} + \frac{1}{\tau_a}\mathbf{T}_R \end{bmatrix} \tag{5.32}$$

The ODE shown above represents the complete hexacopter model with actuator delay included. Although the left-hand side matrix can be inverted to express the system in its explicit form, this step is typically avoided due to the complexity of the symbolically derived weight matrix $W(q)$. Furthermore, the system cannot be solved analytically because of nonlinearities arising from centrifugal forces, relative wind speeds that depend on the hexacopter's velocity, and the nonlinear effects of gravity. Instead, the system of equations is solved numerically using an implicit solver, as described in more detail in Section 8.1.1.

5.4 Hexacopter parameter derivation

In this section, all of the hexacopter and payload parameters are derived, except for the configuration and dimensions of the drone which is presented in Section 4.5. These parameters are used in the previously derived hexacopter model and are chosen to ensure the highest possible model accuracy. The parameters are derived from COTS data-sheets, a CAD model of the hexacopter, reference literature, and established formulas for inertia and drag coefficients.

5.4.1 Rotor coefficients

The coefficients needed to define the rotor forces and torques are the rotor lift coefficient k, the drag coefficient b and the rotor-propeller inertia. The lift coefficient is first determined using the performance data-sheet of the reference propeller-motor combination, which is shown in Appendix C. The data-sheet includes both the thrust at 3500 feet, and at sea-level, along with RPM values corresponding to those thrust-values. The lift coefficient k is thus calculated using (5.10) at both sea-level and at 3500 feet for each RPM. The resulting coefficients are shown below.

$$\begin{cases} k_{sea-level} = 4.3365E-04 \\ k_{3500feet} = 3.9541E-04 \end{cases}$$

By interpolating between these values based on the input air density, the rotor lift coefficient k can be adjusted to account for the effect of air density on the model's output thrust. In the interpolation, the air density at sea level with a temperature of 20°C and a relative humidity of 40% is given as $\rho_{sea-level} = 1.225\ Kg/m^3$. Based on these conditions the air pressure at 3500 is approximated to be $\rho_{3500feet} \approx 1.0586\ Kg/m^3$. Given the lift coefficient and air density values, the lift coefficient is expressed as a function of air density by means of interpolation, as shown below.

$$k(\rho) = k_{3500-feet} + \frac{\rho - \rho_{3500-feet}}{\rho_{sea-level} - \rho_{3500-feet}} * (k_{sea-level} - k_{3500feet}) \tag{5.33}$$

Given that the lift coefficient $k(\rho)$ has been calculated as shown above, the next step is to compute the drag coefficient $b(\rho)$. While a drag coefficient typically characterizes the aerodynamic drag force acting on an airfoil, in this case it describes the drag torque resulting from this force. This relationship is captured by the empirical expression presented in (5.11). The drag coefficient will be approximated by

establishing a linear relationship between the lift and drag coefficients. This ratio, referred to as the lift-to-drag-torque (L/DT) ratio, is conceptually similar to the lift-to-drag (L/D) ratio, which is typically used when drag is represented as a force instead of a torque. Both of these ratios are strongly influenced by the rotor geometry and surface characteristics and they are generally not constant with respect to the incoming airflow. However, in this case, the ratio will be assumed constant relative to the airflow (or rotor RPM), as both the drag and lift coefficients are considered constant when the rotor is operating under normal working conditions, as described in Section 5.1.

The L/DT ratio can therefore be estimated either by comparing it to projects that assume a normal working flow state, or by calculating it based on empirical data when the rotor operates at an RPM corresponding to this state. In the table below, several L/DT ratios are presented under the assumption that both the lift and drag coefficients are constant.

Lift constant: k	**Drag constant:** b	L/DT	**Source**
$4.70E-3$	$2.28E-4$	20.6	[103]
$2.98E-6$	$1.14E-7$	26.14	[104]
$3.13E-5$	$7.5E-7$	41.73	[105]

Table 5.2: Lift and drag coefficients for various rotors reported in the literature.

The lift-to-drag coefficient ratio has also been analyzed for different oncoming airspeeds corresponding to the rotor's normal working state [106]. The cited work shows that the lift-to-drag-torque (L/DT) ratio, when in the normal operating state, is within the range of 35 to 45. It is important to note that the source originally presents the lift-to-drag (L/D) ratio, which has been converted into the examined lift-to-drag-torque (L/DT) ratio by calculating the torque based on the rotor's effective radius. The effective radius depends on the rotor geometry and is approximated using the equation shown below.

$$r_{eff} = \frac{2}{3}R$$

Summarizing the results from both the literature and empirical analysis, the L/DT ratio is estimated to lie within the range of 20 to 45. Based on this range, a value of 35 is selected, as it provides a conservative estimate of the ratio's average. The drag coefficient, dependent on the air density, is thus calculated as:

$$b(\rho) = 35 \cdot k(\rho) \tag{5.34}$$

The rotor-propeller moment of inertia $I_{R,zz}$ is also to be calculated. It is calculated by summing the moment of inertia of the rotor with the propeller. The moment of inertia of the motor rotor is obtained from the reference product datasheet provided in Appendix C. The inertia of the propeller blades is approximated by modeling each blade as a thin rod, leading to the expression below. The values used are based on reference propeller specifications provided in Appendix C. Summing the rotor and calculated propeller inertia gives us the final value $I_{R,zz} = 5 \cdot 10^{-4}\ Kgm^2$.

5.4.2 Hexacopter inertia

To estimate the moment of inertia of the hexacopter, both the mass, size and position of the different subsystems are required. Even though the design of this hexacopter has not been developed to a high level of detail, the sizes of the majority of the subsystems are still known. For all the subsystems, the mass is either known, have been approximated, or is considered a part of the additional weight of the hexacopter. To approximate the moment of inertia, the masses of the different components are lumped together into different basic geometric shapes, represented as individual CAD-parts. Which components that are lumped together is based on their usual position in available systems, and their estimated position for this specific system. The dimension of the components of unknown sizes have been approximated based on existing reference systems, and limiting dimensions of the hexacopter. For example, when dimensioning the central-chassis, the sizes of the payload black-boxes are utilized, and an extra margin is added. This is then compared to existing systems in order to confirm reasonability. The density of the different CAD-parts are then changed in order to get the desired weight within the given volume, and then assembled together, in order to obtain a simplified CAD -assembly of the entire hexacopter, excluding the tether and payload, see Figure 5.8.

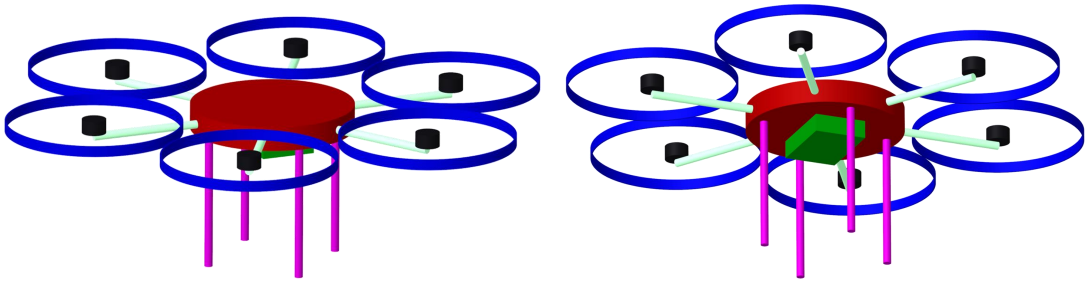

Figure 5.8: CAD-model consisting of basic geometrical shapes that contains the lumped masses of the different subsystems.

The subsystems that are geometrically grouped, along with their mass, quantity, and the color that they have in the CAD-model, can be seen in Table 5.3.

Component(s)	**Color**	**Total mass [g]**	**Quantity**
Chassis + Electronics* + Additional	Red	5738	1
Motor + Propeller	Black	979.7	6
Arm + ESC	Mint	214.33	6
Leg	Pink	65	4
Tether air module	Green	4300	1
Propeller protection	Blue	104.8	6

Table 5.3: Geometrically grouped subsystems, their color in the CAD-model, total weight, and the quantity of these grouped subsystems. *) Electronics = Battery + IMU + Flight controller.

From this model, the moment of inertia in the different directions, I_{xx}, I_{yy}, and I_{zz}, can be calculated. Since the hexacopter is assumed to be symmetrical in the x and y direction, an average of the inertia tensors in xx and yy are taken in order to get an approximation of the moment of inertia as:

$$I_{xx} \approx I_{yy} = 2.098 \ kg * m^2$$

And a moment of inertia in zz of:

$$I_{zz} = 4.004 \ kg * m^2$$

5.4.3 Hexacopter projected area

Utilizing the same CAD-model consisting of the basic geometrical shapes, as described in the derivation of the moment of inertia, and seen in Figure 5.8, the area projected onto the different planes can be estimated. This area is not the actual area, but rather a simplified area consisting of basic 2D shapes, which in this case are multiple rectangles of different sizes, aimed to cover the components from different directions. Furthermore, the area projected in the x- and y-directions are assumed to be identical. These areas will later be used, together with the aerodynamic drag coefficients, to calculate the drag forces in the different directions.

The rectangles that are used in order to estimate the area projected in the x or y direction can be seen in Figure 5.9.

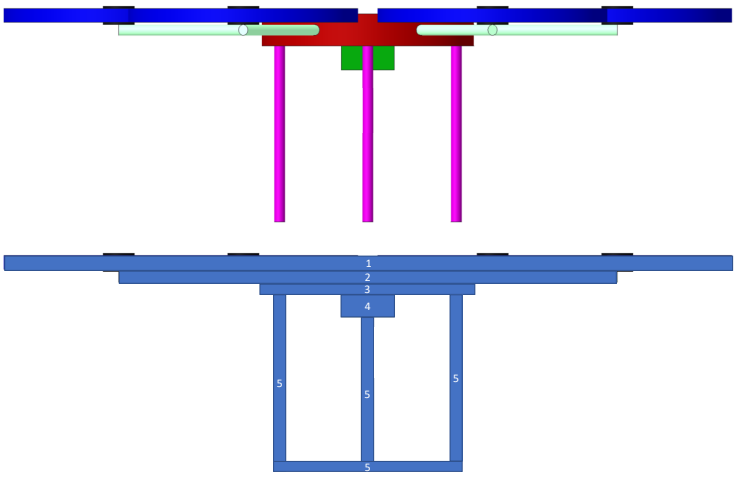

Figure 5.9: The basic 2D shapes utilized to approximate the area projected in the x- or y-direction.

This results in a total projected area in the x- or y-direction, A_{xy}, which can be seen below. The calculations associated with this area estimation can be found in Appendix D.

$$A_{xy} \approx 0.2185 \text{ m}^2$$

In the same way, the area projected in the z-direction is estimated, but with the basic 2D shapes being a combination of circles and rectangles, see Figure 5.10. Here, the propeller protection is completely neglected, since it is assumed to not contribute to the area projected in z, and therefore drag in the z-direction.

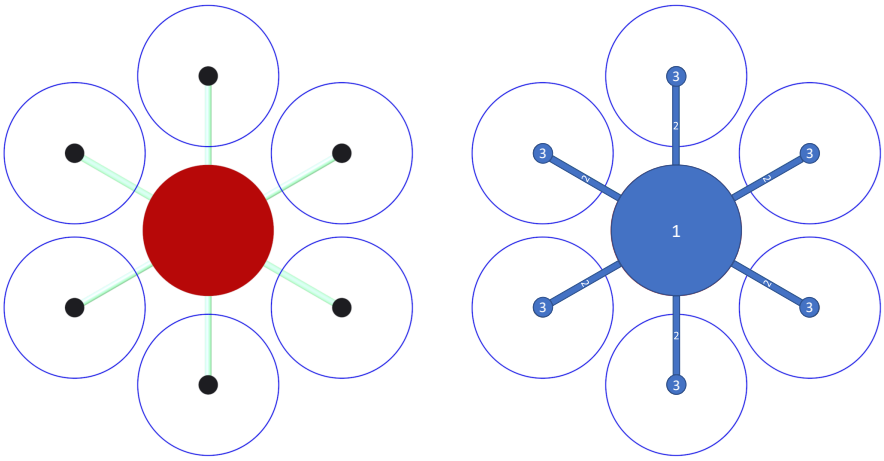

Figure 5.10: The basic 2D shapes utilized to approximate the area projected in the z-direction. (Note that this numbering is not associated with the previous seen in the estimation of x- or y-direction projected area.)

This results in a total projected area in the z-direction, A_z, which can be seen below. The calculations associated with this area estimation can be found in Appendix D.

$$A_z \approx 0.3930 \text{ m}^2$$

5.4.4 Hexacopter aerodynamic coefficients

When estimating the aerodynamic drag coefficients for the different body-axis directions of the hexacopter, the same simplified geometries (as for the approximation of the projected areas) are used, see Figures 5.9 and 5.10. In this case, the different 2D shapes are instead considered as 3D cylinders and cubes. The area of each individual 2D shape is used as a reference area, A_i when calculating the total drag coefficient in a specific direction. The drag coefficients in the x- and y-directions are considered equal. To determine a total drag force in each direction, the method of superposition is utilized, where the individual components of the hexacopter are analyzed independently, in terms of reference area (which is already given in the previous section) and drag coefficient. This is then combined using (5.35), to obtain an estimate of the total drag coefficient.

$$C_{D_{total}} = \frac{\sum_{D,i}^{n} C_{D,i} A_i}{A_{total}} \tag{5.35}$$

The drag coefficients for various common 3D geometries are widely available, since they have been experimentally determined. These coefficients are dependent on the Reynolds number, which varies substantially between different flow regimes. In this case, as previously discussed, external laminar flow is assumed ($Re < 5E{+}05$) [107].

The drag coefficient for long cylinders, oriented perpendicular to the flow, are determined through interpolation based on the aspect ratio between the length and diameter of the cylinder, see Figure 5.11. This gives drag coefficients in the range of 0.85-0.88 for different bodies of the hexacopter. Some cylinders are considered short, since L $\ll$ D. The drag coefficient for these short cylinders oriented perpendicular to the flow is assumed to be around 1.1. A drag coefficient of 1.1 is considered a reasonable estimate for a short cylinder perpendicular to flow, as such bluff bodies typically produce strong pressure drag, with empirical values commonly ranging between 1.0 and 1.2. Short cylinders that are instead aligned with the flow normally have a drag coefficient of around 1.15. The tether air module, labeled number 4 in Figure 5.9, is determined to have a drag coefficient of 1.05, since it is assumed to have a similar drag coefficient to that of a cube.

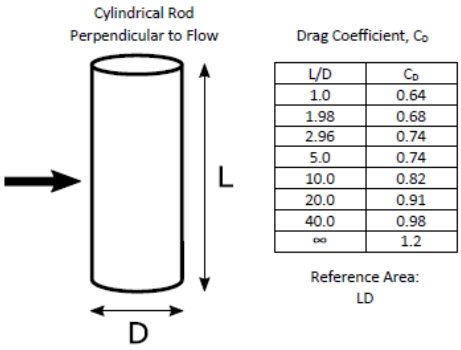

Figure 5.11: Cylindrical rod perpendicular to flow, with variation in cylinder normal drag coefficient with aspect ratio [108].

Combining these different drag coefficients with their respective reference areas, and the total area in each direction as per (5.35), the total drag coefficients in the xy-, and z-directions are estimated as:

$$\begin{cases} C_{D,xy} \approx 1.028 \\ C_{D,z} \approx 1.100 \end{cases}$$

5.4.5 Tether anchor point

The anchor point position of the tether with respect to the drone center of mass is beneficial to minimize. This point is limited by the length of the legs, along with half the thickness of the chassis, see Figure 5.12, image (a). The length of the legs are limited by the height of the lower payload black-box (400 mm), the height of the tether air module (68 mm), along with an additional leg diameter (30 mm) as discussed in the projected area calculation in the x- or y-direction. Half the thickness of the chassis is 45 mm. This equals a total length of 543 mm.

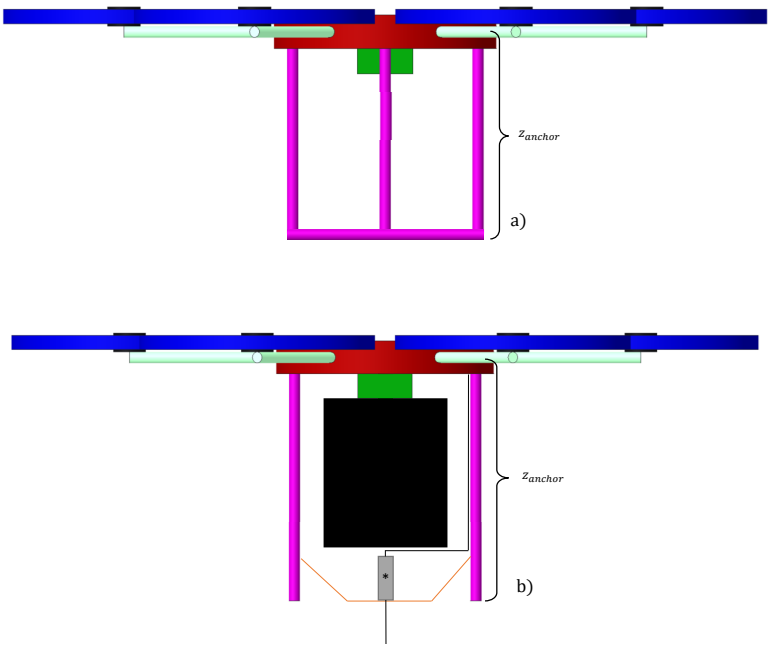

Figure 5.12: (a) Anchor point without the incorporation of the rotary joint and tension management system (this is not used), (b) Anchor point with the incorporation of the *) rotary joint, and tension management system (this anchor point is used in the model).

Additionally, as discussed in Section 3.4.2, the incorporation of a hybrid rotary joint between the tether and the tether air module is necessary in order to avoid torsional shear failure. Since this joint is not designed to withstand tensile loads, a separate decoupled system that handles the tensile load would also have to be incorporated at the attachment point of the tether. Therefore, the length of the rotary joint would also contribute to the position of the tether anchor point. An illustration of the incorporation of this rotary joint and tension management system can be seen in Figure 5.12, image (b). Since the size of this joint is unknown, an extra margin to the previously mentioned distance is therefore added in order to include the size of this joint and the tension management system. The anchor point is therefore approximated as:

$$z_{anchor} \approx 0.700 \text{ m} \tag{5.36}$$

5.4.6 Payload inertia and aerodynamic coefficients

The payload's moment of inertia is calculated using the standard formula for the moment of inertia of a rectangular box, where the payload black-box dimensions are presented in Section 1.2.2. The moments of inertia along the three principal axes, relative to the center of mass of the payload, are calculated in (5.37). These moments of inertia are then shifted to the body frame coordinate system $\{B\}$ by means of the parallel axis theorem, presented in (5.3).

$$\begin{cases} I_{xx} = \frac{1}{12} m_i (w^2 + h^2) \\ I_{yy} = \frac{1}{12} m_i (d^2 + h^2) \\ I_{zz} = \frac{1}{12} m_i (w^2 + d^2) \end{cases} \tag{5.37}$$

To calculate the payload's aerodynamic coefficients, the payload is approximated as an upright cylinder rather than a rectangular box. This simplification ensures that the drag force is uniform in all directions. As previously stated, the payloads will not contribute to any drag force in the local z-direction, as this is already accounted for in the hexacopter drag equations. The payload cross-section area for the payload black-boxes, around the z-axis is thus calculated as shown below.

$$A_{P,xy} = W \cdot H \tag{5.38}$$

The payload drag coefficient $C_{DP,xy}$, is then similarly to the hexacopter parameter derivations, calculated by interpolating the table shown in Figure 5.11.

5.4.7 Summary of parameters

A summary of all hexacopter parameters used in the model is presented in the table below. All derived parameters are considered constant, except for the rotor coefficients, which vary with the surrounding air density and thus depend on the hexacopter's operating altitude and atmospheric conditions.

Variable	Simulation Parameter	Value	Unit	Derivation
m_h	Mass	18.091	$[kg]$	(5.2)
d	Arm length	0.706	$[m]$	CAD
$I_{xx} = I_{yy}$	Moment of inertia	2.098	$[kg \cdot m^2]$	CAD
I_{zz}	Moment of inertia	4.004	$[kg \cdot m^2]$	CAD
$I_{R,zz}$	Rotor moment of inertia	5E-3	$[kg \cdot m^2]$	(**??**)
$k(\rho)$	Rotor lift constant	*function*	$\frac{N \cdot s^2}{rad^2}$	(5.33)
$b(\rho)$	Rotor drag constant	*function*	$[\frac{Nm \cdot s^2}{rad^2}]$	(5.34)
A_{xy}	Area projected in x or y direction	0.2185	$[m^2]$	App. D
A_z	Area projected in z direction	0.393	$[m^2]$	App. D
$C_{D,xy}$	Drag coefficient for x & y direction	1.028	$[\ -\ ]$	Fig 5.11
$C_{D,z}$	Drag coefficient for z direction	1.100	$[\ -\ ]$	Fig 5.11
τ_a	Actuator lag coefficient	0.01	$[s]$	Sec 5.3.3
z_{anchor}	Anchor-point position	0.700	$[m]$	(5.36)
ω_{max}	Maximum rotor speed	5400	$[RPM]$	App. C

Table 5.4: Hexacopter parameters.

All payload parameters considered in the model are presented in the table below. Their respective values are not explicitly presented in the table, as all parameters are to be updated for different simulation cases. A simulation case will later be configured by adjusting the variable parameters, after which the remaining parameters will be computed using the equations presented in the table.

Variable	Simulation Parameter	Unit	Derivation
m_U	Upper payload mass	$[Kg]$	*Variable*
m_L	Lower payload mass	$[Kg]$	*Variable*
z_U	Upper payload position	$[m]$	*Variable*
z_L	Lower payload position	$[m]$	*Variable*
$[L, W, H]_U$	Upper payload dimensions	$[m]$	Sec 1.2.2
$[L, W, H]_L$	Lower payload dimensions	$[m]$	Sec 1.2.2
$[I_{xx}, I_{yy}, I_z]_U$	Upper payload moment of inertia	$[Kg \cdot m^2]$	(5.37)
$[I_{xx}, I_{yy}, I_z]_L$	Lower payload moment of inertia	$[Kg \cdot m^2]$	(5.37)
$A_{U,xy}$	Upper payload cross-section area	$[m^2]$	(5.38)
$A_{L,xy}$	Lower payload cross-section area	$[m^2]$	(5.38)
$C_{D,U,xy}$	Upper payload drag coefficient around z	$[\ -\ ]$	Fig 5.11
$C_{D,L,xy}$	Lower payload drag coefficient around z	$[\ -\ ]$	Fig 5.11

Table 5.5: Payload parameters.

5.4.8 Model power output

Additionally, to estimate the motor power consumption under varying conditions, the relationship between angular velocity and current draw is evaluated. This allows altitude effects to be captured via changes in air density, enabling more accurate power predictions during flight. Since the current is considered proportional to the air density, the current corresponding to the thrust at sea level can be approximated, for the different RPM values in the performance data for the reference motor-propeller combination. Since the relationship between angular velocity and current is exponential, the output current for a given angular velocity can not be sufficiently estimated using interpolation. Instead a polynomial function is fitted to both the current based on different angular velocities at sea-level, and at 3500 feet, given in the data-sheet. This relationship between current drawn and angular velocity of the propeller, for both sea-level and a reference altitude of 3500 feet can be seen in Figure 5.13.

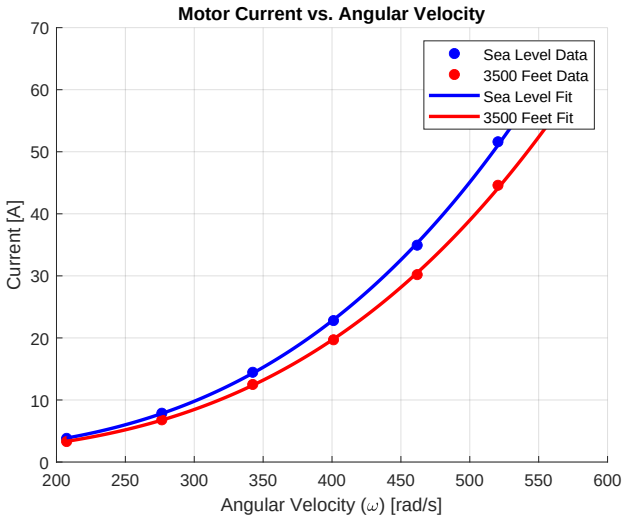

Figure 5.13: Relationship between angular velocity and current at sea-level and 3500 feet, by fitting a polynomial function to the performance data.

These polynomial functions can be used to get a current at both sea-level, and at 3500 feet for an input angular velocity. Since $I \propto \rho$, the actual current drawn, based on the present air density, can be calculated using interpolation between the current at sea-level and 3500 feet for the input angular velocity. This is performed for each motor separately, and a total current is derived by summing the individual motor currents. Since the voltage is said to be constant, and is based on the motor voltage. The total and average power consumption of the motor-propeller combination can be derived.

6
Tether modeling

As the tether is expected to significantly affect the drone's flight performance and stability, accurately modeling its dynamics is essential for a realistic representation of the tethered hexacopter system. The coupled system is required for evaluating and validating overall performance, as well as for computing key metrics such as torques, forces, and rotational velocities, which are critical for system design. It can also be used for analyzing the stability of the drone and the power consumption of the system. This chapter initially outlines the impact of the tether on system performance and identifies key system characteristics that influence stability. A mathematical model of the tether is then derived by first examining several tether modeling approaches, ultimately selecting the lumped mass model (LMM) enhanced with torsional springs and dampers. Additional effects incorporated into the LMM include wind disturbances, as defined in Section 5.3.1.3, and constraint conditions that couple the tether and hexacopter models, resulting in the combined tether-drone system. Both the tether model and the coupled tether-drone system are derived using the Euler—Lagrange formulation, as this method is well-suited for modeling the LMM and effectively handling constraint conditions.

6.1 Tether influence on flight dynamics and stability

The most prominent effect of the tether on the hexacopter is the positional constraint imposed by its total length, $L_{t,tot}$, which limits the maximum distance the hexacopter can travel. The tethers total length is defined as the distance between the tether winch, which coincides with the world frame $\{W\}$, and the tether anchor point, located at the bottom of the hexacopter. In addition to imposing a position constraint on the hexacopter, the tether will also have a direct impact on the hexacopter's stability. The primary source of instability in the system arises when the tether transitions rapidly from a slack to a taut state, resulting in a sudden increase in tether tension. The rapid transition from a slack to a taut tether results in an impulse force in the tether and may occur for several reasons, such as wind disturbances pushing the hexacopter upward or laterally, overly aggressive hexacopter movement upward, or excessive winching of the tether downward. This impulse force results in an impulse moment because the tether is not connected to the drone's CoM. The tether is instead connected to the drones anchor point which is located at a distance z_{anchor} below the drones CoM, as described in Section 5.4.5. The resulting impulse moment induces abrupt roll and pitch torques on the drone,

which are the main contributors to its instability.

To prevent impulse moments and the resulting instability, it is therefore essential to maintain the tether in a taut state at all times during operation to ensure stable flight. This does increase the power requirements of the system but the positive tether tension will also act as a stabilizing force that damps external disturbances and restricts excessive movement, particularly in response to gusts of wind or turbulence. The tether will thus act as a destabilizing disturbance when it is in a loose state, but will instead act as a stabilizing element for positive tether tension. The tether tension can be regulated through coordinated control of the hexacopter and the tether winch.

6.2 Modeling approaches

The need for accurate cable/tether modeling is found in many different industries and has mainly been researched for maritime vessels, aerial towing and space applications [109]. The primary methods for modeling a cable presented in the literature is the finite element method (FEM) and the lumped mass model. Both methods discretizes the cable into small elements. The finite element method accurately solves for deformation, capturing bending, stretching, and torsion with high precision. The method uses computationally expensive and complex elements but typically requires fewer elements than the lumped mass model to achieve comparable accuracy [110]. The lumped mass model (LMM) works by discretizing the model into a series of point masses connected by a set of tether elements. The elements can contain springs, dampeners or other mechanical components to accurately model the tether [111]. The disadvantages of the LMM is the need for more elements compared to the FEM. The advantages of the LMM is that the model elements are less computationally complex and the model is highly adjustable for external forces. The LMM is therefore selected as the tether modeling method, combined with the Euler–Lagrange formalism.

Additional methods proposed in the literature for modeling and simulating a tethered UAV system is by modeling the tether as a rigid link and assuming that it is taught at all times [112]. This method is a special case of the LMM, where there is only one link element which is completely rigid. The method fails to capture the tether's dynamics and becomes inaccurate when the tether lacks positive tension. It has however been shown to be a useful method when developing advanced control algorithms such as MPC and non-linear control. Another method involves using the catenary equations under a quasi-static assumption [22]. The catenary equations captures the static tether geometry and forces, when the tether is lacking of positive tension, in comparison to the rigid body approximation.

6.3 Model description

As mentioned earlier, the lumped mass model will be used, and there are multiple approaches to modeling the tether elements. One common modeling approach is to consider longitudinal strains by means of springs and dampeners. This will however not be considered as the longitudinal strains will be negligible compared to other factors influencing the system's dynamics. This is due to the tether being extremely stiff in the longitudinal direction, as it is composed of fiber-optic cables, an aluminum alloy aviation wire, a high-modulus tensile fiber woven layer, and a composite fluoroplastic insulation layer, as described in greater detail in Section 3.4.1. The tether element will however include torsion springs and dampers, as this has been recommended in [113] to improve the model accuracy. This is also recommended and implemented in [114] where both springs and dampeners are implemented in bending, as well as longitudinally. The springs provide resistance to angular displacement between tether elements which prohibit sharp acute angles. The dampers introduce energy dissipation, improving simulation stability and model accuracy by capturing the energy losses a real tether experiences due to the internal material damping, friction, and resistance from the surrounding environment. Three torsional springs and three dampers are thus arranged in parallel between adjacent tether elements.

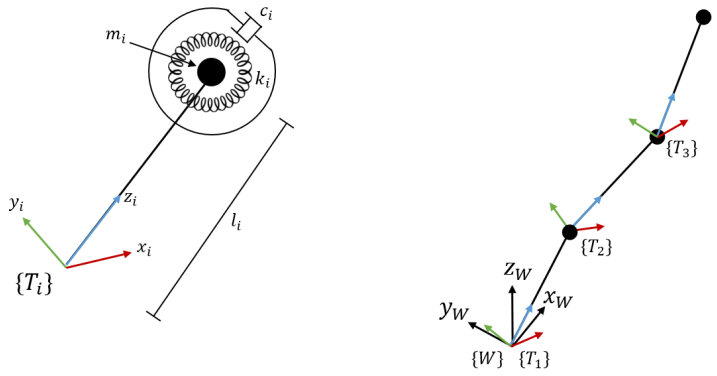

Figure 6.1: Tether element with torsion spring, torsion damper and point mass to the left. Assembly of multiple tether elements to the right.

The chosen tether element is shown in Figure 6.1 above to the left where m_i is the element mass, l_i is the element length and $\{T_i\}$ is the local element coordinate system. The damper constant is denoted as c_i and the spring constant is denoted by k_i. In Figure 6.1, to the right, the assembly of several tether elements is also shown, where the spring and damper symbols have been omitted for the simplicity of the figure. In the actual implementation, the tether is constructed from an assembly of N_t tether elements. As the tether will be mostly vertical when the tUAV is operational, the tethers position is initialized as vertical. This means that each tether element coordinate frame $\{T_i\}$ is perfectly aligned withe the previous coordinate frame but shifted with the vector $(0, 0, l_i)$. The first tether element coordinate

frame $\{T_1\}$ coincides exactly with the world coordinate frame $\{W\}$.

A rigid body in 3D space has six degrees of freedom: three translational and three rotational. The model's constraint implementation is detailed in Section 6.4.2, but to summarize, a tether element's translational motion is fully constrained by its connection to either the world coordinate frame $\{W\}$ or a preceding tether element $\{T_i\}$. This implies that a tether element only has three degrees of freedom and its pose is fully defined by its rotation which will be defined by the Euler angles $(\phi_i, \theta_i, \psi_i)$. The Euler angles are thus the three successive rotations which describe the tether element's rotation in relation to the world frame $\{W\}$. Similarly to the drone model implementation, the 3-2-1 Euler rotation matrix will be used which is shown in (5.5). The Euler angles are chosen as the tether models system variables, meaning that the system has a total of $3N_t$ states. These states are assembled into a single vector, representing the generalized coordinates of the tether model, as shown below.

$$q_t = \begin{bmatrix} \phi_1 \\ \theta_1 \\ \psi_1 \\ . \\ . \\ . \\ \phi_N \\ \theta_N \\ \psi_N \end{bmatrix}, \quad \dot{q}_t = \begin{bmatrix} \dot{\phi}_1 \\ \dot{\theta}_1 \\ \dot{\psi}_1 \\ . \\ . \\ . \\ \dot{\phi}_N \\ \dot{\theta}_N \\ \dot{\psi}_N \end{bmatrix}$$

For future derivations, the generalized coordinates are also partitioned for each corresponding tether element, as shown below.

$$q_{t,i} = \begin{bmatrix} \phi_i \\ \theta_i \\ \psi_i \end{bmatrix}, \quad \dot{q}_{t,i} = \begin{bmatrix} \dot{\phi}_i \\ \dot{\theta}_i \\ \dot{\psi}_i \end{bmatrix}$$

The translational position and velocity of the tether elements mass will later be needed for the Euler–Lagrange formulation. The tether elements mass is as stated located at $(0, 0, l_i)$ in the tether elements local coordinate frame. The translational position in the world frame is then calculated by means of the generalized coordinates and the 3-2-1 rotation matrix from (5.5) as shown below.

$$P_{t,i} = \begin{bmatrix} x_i \\ y_i \\ z_i \end{bmatrix} = \sum_{j=1}^{i} {}^{B}R_W(\phi_j, \theta_j, \psi_j) \begin{bmatrix} 0 \\ 0 \\ l_j \end{bmatrix} = \sum_{j=1}^{i} l_j \begin{bmatrix} s(\phi_j)s(\psi_j) + c(\phi_j)c(\psi_j)s(\theta_j) \\ c(\phi_j)s(\psi_j)s(\theta_j) - c(\psi_j)s(\phi_j) \\ c(\phi_j)c(\theta_j) \end{bmatrix} \tag{6.1}$$

The translational velocities of the tether elements mass is calculated by differentiating the position shown above.

$$
\begin{aligned}
\dot{x}_i = \sum_{j=1}^{i} l_j \Big(& \dot{\phi}_j c(\phi_j) s(\psi_j) + \dot{\psi}_j c(\psi_j) s(\phi_j) + \dot{\theta}_j c(\phi_j) c(\psi_j) c(\theta_j) \\
& - \dot{\phi}_j c(\psi_j) s(\phi_j) s(\theta_j) - \dot{\psi}_j c(\phi_j) s(\psi_j) s(\theta_j) \Big) \\
\dot{y}_i = \sum_{j=1}^{i} l_j \Big(& \dot{\psi}_j s(\phi_j) s(\psi_j) - \dot{\phi}_j c(\phi_j) c(\psi_j) \\
& + \dot{\psi}_j c(\phi_j) c(\psi_j) s(\theta_j) + \dot{\theta}_j c(\phi_j) c(\theta_j) s(\psi_j) - \dot{\phi}_j s(\phi_j) s(\psi_j) s(\theta_j) \Big) \\
\dot{z}_i = \sum_{j=1}^{i} l_j \Big(& - \dot{\phi}_j c(\theta_j) s(\phi_j) - \dot{\theta}_j c(\phi_j) s(\theta_j) \Big)
\end{aligned}
$$

As motivated and derived for the hexacopter model in Section 5.2.3, the Euler angle derivatives are not equal to the coordinate systems rotational velocities. The rotational velocities are derived using the equation below.

$$
\begin{bmatrix} \omega_{x,i} \\ \omega_{y,i} \\ \omega_{z,i} \end{bmatrix} = \underbrace{\begin{bmatrix} 1 & 0 & -s(\theta_i) \\ 0 & c(\phi_i) & c(\theta_i) s(\phi_i) \\ 0 & -s(\phi_i) & c(\theta_i) c(\phi_i) \end{bmatrix}}_{T} \begin{bmatrix} \dot{\phi}_i \\ \dot{\theta}_i \\ \dot{\psi}_i \end{bmatrix} \tag{6.2}
$$

6.4 Euler–Lagrange formulation

In this section, the Euler—Lagrange equations of motion are derived for both the tether model and the coupled tether–drone model. The generalized coordinates for the tether, earlier introduced as q_t, captures the tethers translational and rotational states and form the bases for deriving the systems equations of motion.

6.4.1 External forces

The two external forces considered in the model are the aerodynamic forces and dampening forces between tether elements. In the Euler–Lagrange formulation for the tether system, damping forces are included in the external forces as they are non-conservative forces that dissipate energy. Aerodynamic forces are considered non-conservative as they introduce slight resistance when the tether moves. However, their primary effect comes from wind disturbances, which have a more significant influence on the tether's motion and dynamics. The sum of the external forces are expressed as shown below.

$$
\mathbf{Q}_t = \mathbf{Q}_{t,damp} + \mathbf{Q}_{t,aero}
$$

It is also important to note that the "external forces" in this case are actually torques rather than forces, since the generalized coordinates are defined as Euler angles. The external forces vector will thus have the form:

$$
\mathbf{Q}_t = \begin{bmatrix} \tau_{\phi,1} & \tau_{\theta,1} & \tau_{\psi,1} & \tau_{\phi,2} & \tau_{\theta,2} & \tau_{\psi,2} & \dots & \tau_{\phi,N} & \tau_{\theta,N} & \tau_{\psi,N} \end{bmatrix}^T
$$

6.4.1.1 Rotational damping

The rotational damping acts as resistive torques that oppose relative rotational motion between adjacent tether elements. Each pair of adjacent tether elements is connected by three dampers, one for each Euler angle, providing resistance to rotation about all three axes. For model simplicity, the damping constant c_t is assumed to be identical for all rotational degrees of freedom. To compute the damping torques the Rayleigh dissipation function $\mathcal{R}(\dot{q})$ is used, which describes energy dissipation due to non-conservative forces such as friction or damping. When writing it in its general form, for a set of particles that travel at the velocity v_i, the function is written as shown below [115].

$$\mathcal{R}(v) = \frac{1}{2}\sum_{i=1}^{N} c_i v_i^2$$

Expanding this to the tether element masses in the LMM, the following expression is obtained. The first term is excluded from the summation, as it represents the damping between the first tether element and the world frame.

$$\mathcal{R}(\dot{q}) = \frac{1}{2}(c_\phi \dot{\phi}_1^2 + c_\theta \dot{\theta}_1^2 + c_\psi \dot{\psi}_1^2) + \frac{1}{2}\sum_{i=1}^{N-1}(c_\phi(\dot{\phi}_{i+1} - \dot{\phi}_i)^2 + c_\theta(\dot{\theta}_{i+1} - \dot{\theta}_i)^2 + c_\psi(\dot{\psi}_{i+1} - \dot{\psi}_i)^2)$$

The damping torques are obtained by computing the Jacobian of the Rayleigh dissipation function with respect to the time derivatives of the generalized coordinates, as shown below.

$$\mathbf{Q}_{t,damp} = -\nabla_q \mathcal{R}(\dot{q})$$

6.4.1.2 Aerodynamic drag

The tether model is subjected to aerodynamic drag, similar to the hexacopter model. One main difference is however that the tether elements can not be assumed to be completely vertical, while the hexacopter is assumed to be close to horizontal at all times. The drag forces applied to the tether is thus dependent on the tethers attitude. The aerodynamic drag is highly dependent on the wind disturbances present in the simulation environment. These wind disturbances are defined in Section 5.3.1.3. The only adjustment made to the wind disturbance model for the LMM is that the wind turbulence function at 10 m above sea level, $V_{10}(t)$, defined in (5.19), is applied at the midpoint of each tether element rather than at the height of the hexacopter. To calculate the midpoint position of each tether element, (6.1) is adjusted to the following.

$$P_{mid,i} = \begin{bmatrix} x_{mid,i} \\ y_{mid,i} \\ z_{mid,i} \end{bmatrix} = \sum_{j=1}^{i-1} {}^{B}_{W}R(\phi_j, \theta_j, \psi_j) \begin{bmatrix} 0 \\ 0 \\ l_j \end{bmatrix} + {}^{B}_{W}R(\phi_i, \theta_i, \psi_i) \begin{bmatrix} 0 \\ 0 \\ \frac{1}{2}l_i \end{bmatrix} \tag{6.3}$$

The wind turbulence function can then be related, using the wind profile power law, for each tether element as shown below.

$$V_i(z_{mid,i}, t) = V_{10}(t) \left(\frac{z_{mid,i}}{10} \right)^{\alpha} \tag{6.4}$$

The relative fluid flow velocity vector is then defined for each tether element similarly to the implementation used for the hexacopter in (6.5). The relative flow is evaluated at the midpoint of each tether element, meaning that the velocity at this midpoint is used. This velocity is obtained by differentiating the translational midpoint position, as shown in (6.3), following the same approach used for the tether element endpoint.

$$V_{rel,W,i} = \begin{bmatrix} V_{x,i} - \dot{x}_{mid,i} \\ V_{y,i} - \dot{y}_{mid,i} \\ -\dot{z}_{mid,i} \end{bmatrix} \tag{6.5}$$

To calculate the impact of the relative fluid flow on the tether elements, Hoerner's cross flow principle for a slender cylinder in uniform and subcritical flow will be used [116]. The cross flow principle accounts for both drag and lift forces, applying them based on the orientation of each tether element relative to the flow direction. The principle is applied in the plane defined by the relative fluid flow vector and the tether element vector shown below.

$$d_i = \overset{B}{R}_W(\phi_i, \theta_i, \psi_i) \begin{bmatrix} 0 \\ 0 \\ l_i \end{bmatrix}$$

The relative fluid flow, the tether element and the resulting drag and lift forces are illustrated in Figure 6.2. The angle β_i is the angle between these two vectors, where the fluid flow $V_{rel,W,i}$ is applied uniformly to the tether element.

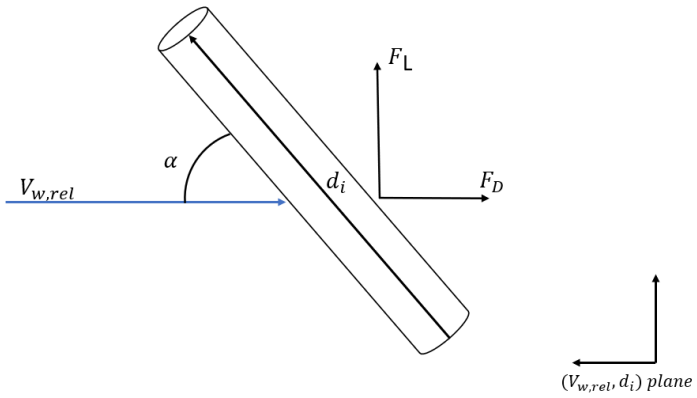

Figure 6.2: Tether element effected by wind in ($V_{rel,W,i}$, d_i) plane.

The angle between the vector $V_{rel,W,i}$ and d_i is calculated using the dot product formula.

$$\beta_i = cos^{-1} \left(\frac{V_{rel,W,i} \cdot d_i}{||V_{rel,W,i}||\ ||d_i||} \right)$$

Where the lift force $F_{L,i}$ and drag force $F_{D,i}$, as shown in Figure 6.2, is calculated using the cross flow principle as shown below [116].

$$\begin{cases} F_{L,i} = \frac{1}{2}\rho D l_i |V_{rel,W,i}|^2 C_{L,i} \\ F_{D,i} = \frac{1}{2}\rho D l_i |V_{rel,W,i}|^2 C_{D,i} \end{cases}$$

Where $C_{D,i}$ and $C_{L,i}$ is the tether elements drag and lift coefficients which are dependent on the angle β_i. They are calculated as shown below using the skin friction constant C_f and the basic drag constant $C_{d,basic}$. The coefficients C_f and $C_{d,basic}$ are dependent on the Reynolds number, the tethers geometry and surface roughness. These coefficients are derived in Section 6.5.

$$\begin{cases} C_{D,i} = C_{D,basic}\ sin^3(\beta_i) + \pi C_f \\ C_{L,i} = C_{D,basic}\ sin^2(\beta_i) cos(\beta_i) \end{cases}$$

The drag and lift forces are subsequently converted into parallel and perpendicular components of d_i. The parallel component is calculated by projecting the lift and drag forces on the normalized tether element vector $\hat{d}_i$, while the perpendicular component is calculated by subtracting the parallel component from the sum of drag and lift forces as shown below. The parallel force is aligned with the tether element's z-axis, expressed in the world frame $\{W\}$. The parallel force will thus correspond to the component of the force acting along this axis in the world frame, denoted as $F_{z,W,i}$.

$$\begin{cases} \hat{d}_i = \frac{d_i}{|d_i|} \\ F_{\parallel,i} = (F_{L,i} \cdot \hat{d}_i)\hat{d}_i + (F_{D,i} \cdot \hat{d}_i)\hat{d}_i = F_{z,W,i} \\ F_{\perp,i} = F_{L,i} + F_{D,i} - F_{\parallel,i} \end{cases}$$

To calculate the forces along the tether element's x- and y-axes, the corresponding unit vectors expressed in the world frame are required and are derived below.

$$\hat{x}_{W,i} = \overset{B}{R}_W(\phi_i, \theta_i, \psi_i) \begin{bmatrix} 1 \\ 0 \\ 0 \end{bmatrix}, \quad \hat{y}_{W,i} = \overset{B}{R}_W(\phi_i, \theta_i, \psi_i) \begin{bmatrix} 0 \\ 1 \\ 0 \end{bmatrix} \tag{6.6}$$

The forces applied to the tether elements x- and y-axes expressed in the world frame are then calculated by projecting the perpendicular component on the unit vectors derived in 6.6 above.

$$\begin{cases} F_{x,W,i} = (F_\perp \cdot \hat{x}_{i_W})\hat{x}_{i,w} \\ F_{y,W,i} = (F_\perp \cdot \hat{y}_{i_w})\hat{y}_{i,w} \end{cases}$$

This results in the complete aerodynamic force vector for a tether element, expressed in the world frame, as shown below.

$$F_{W,i} = \begin{bmatrix} F_{x,W,i} \\ F_{y,W,i} \\ F_{z,W,i} \end{bmatrix}$$

Since the external forces are defined as torques, the aerodynamic force vector has to be converted into an equivalent torque representation. This is done using the principle of virtual work. The principle was previously introduced and applied to the hexacopter model in Section 5.3.1.4, and is here adapted for the tether elements. In the equation below, the resulting external forces for a tether element is calculated, where $P_{mid,i}$ denotes the translational motion of the element's midpoint and $q_{t,i}$ is the corresponding generalized coordinates.

$$Q_{aero,i} = F_{W,i} \frac{\partial P_{mid,i}}{q_{t,i}}$$

The final external force expression due to aerodynamic drag is thus calculated as:

$$\mathbf{Q}_{aero} = \begin{bmatrix} F_{W,1} \frac{\partial P_{mid,1}}{q_{t,1}} & F_{W,2} \frac{\partial P_{mid,1}}{q_{t,2}} & \dots & F_{W,N_t} \frac{\partial P_{mid,N_t}}{q_{t,N_t}} \end{bmatrix}^T$$

6.4.2 Constraints

Before deriving the tether model, a constraint is defined to attach the tether to the world frame. This section also introduces an additional constraint that links the tether to the hexacopter model from Section 6.4.3, thereby forming the coupled tether-drone system. Both of the constraints are holonomic distance constraints, where the tether-to-world constraint specifically links the first tether element to the world frame $\{W\}$. This link corresponds to the difference vector shown below.

$$\delta_{\text{world}} = P_{1,W} - \begin{bmatrix} 0 \\ 0 \\ 0 \end{bmatrix}$$

The constraint is thus given by:

$$\sqrt{(\delta_{\text{world}}^T \delta_{\text{world}})} - l = 0$$

The preceding expression is then restructured to obtain the final tether-to-world constraint equation presented below.

$$c_{\text{world}}(q) = \frac{1}{2}(\delta_{\text{world}}^T \delta_{\text{world}} - l^2) = 0 \tag{6.7}$$

The tether-to-drone constraint is applied between the tether's final point mass and the hexacopter's anchor point, which is connected via a spherical joint allowing free rotational motion around the anchor. The holonomic distance constraint maintains a fixed separation of length l between the tether's end mass and the hexacopter's anchor point, effectively linking the two subsystems. To fully define this constraint, the positions of both connection points must be specified. The anchor-point position is defined in the hexacopter's body frame as shown below.

$$\mathbf{r}_{U,B} = \begin{bmatrix} 0 \\ 0 \\ -z_A \end{bmatrix} \tag{6.8}$$

The position of the anchor point in the world frame is thus defined as shown below, where the position vector describes the hexacopters translational motion in the world frame.

$$P_{A,W} = \begin{bmatrix} x \\ y \\ z \end{bmatrix} + \overset{B}{R}_W \mathbf{r}_{U,B} \tag{6.9}$$

The position of the final (N:th) point mass in the tether is denoted as $P_{N,W}$. The difference in position is thus defined as:

$$\delta_{\text{drone}} = P_{A,W} - P_{N,W}$$

The distance constraint is then written as:

$$\sqrt{(\delta_{\text{drone}}^T \delta_{\text{drone}})} - l = 0$$

The expression above is reformulated to derive the final constraint equation, as shown below.

$$c_{\text{drone}}(q) = \frac{1}{2}(\delta_{\text{drone}}^T \delta_{\text{drone}} - l^2) = 0 \tag{6.10}$$

With the two necessary constraints now defined, their application across the different models can be summarized. The standalone hexacopter model does not incorporate any constraints, as it is assumed to move freely. The constraint c_{world} is used to attach the tether to the world frame and is therefore included in the standalone tether model. For the coupled tether–hexacopter system, both c_{world} and c_{drone} are required to ensure that the tether is connected both to the world frame and to the hexacopter. The combined constraint equation for the tether–hexacopter system is expressed as shown below.

$$c(q) = \begin{bmatrix} c_{\text{world}}(q) \\ c_{\text{drone}}(q) \end{bmatrix} = \mathbf{0} \tag{6.11}$$

The constraints introduced above will be incorporated into the respective models as they are derived in the following sections, but the physical meaning of the constraint implementations is briefly discussed here. The constraints are incorporated through the Euler–Lagrange formulation, using Lagrange multipliers λ to enforce the constraint equations $c(q) = 0$. Physically, λ can be interpreted as the generalized force required to satisfy the constraint. In the case of a holonomic constraint, such as the distance constraints described earlier, λ corresponds to the magnitude of the force acting along the direction that enforces the constraint. More specifically, λ_{drone}, which enforces the constraint c_{drone}, can be interpreted as the magnitude of the tension force exerted by the tether on the drone. The tether tension force is a valuable model output that will be used for subsequent analysis and integrated into the control loop to regulate tether tension. It is derived by means of the Lagrange Multiplier λ_{drone} and the translational position of the hexacopters anchor-point $P_{A,W}$ as defined in (6.9). The derivation of the tether tension is shown in the equation below.

$$F_t = \left(\frac{\partial c_{\text{drone}}}{\partial P_{A,W}}\right)^T \lambda_{\text{drone}} \tag{6.12}$$

6.4.3 Euler–Lagrange equations of motion

To derive the Euler–Lagrange equations of motion, the kinetic and potential energy of the tether system are first expressed. The potential energy of the system is composed of both the tether element springs potential energy and the potential energy contribution of the gravitational field. There are three torsion springs between all adjacent tether elements and between the first tether element and the world frame. The spring potential energy is expressed as shown below, where the angles corresponding to the world frame ($i = 0$) are zero.

$$V_{spring} = \frac{1}{2}\sum_{i=0}^{N} k_\phi(\phi_{i+1} - \phi_i)^2 + k_\theta(\theta_{i+1} - \theta_i)^2 + k_\psi(\psi_{i+1} - \psi_i)^2$$

The potential energy due to the gravitational field of the earth is expressed using the lumped mass position vectors defined in (6.1).

$$V_g = \sum_{i=1}^{N} m_t g \begin{bmatrix} 0 & 0 & 1 \end{bmatrix} P_i$$

Which yields the total potential energy of the LMM:

$$V_t = V_{spring} + V_g$$

The system's kinetic energy consists of contributions from translational and rotational motion. Where the kinetic energy due to translational motion is defined using the derivative of the tether element position vector.

$$T_{trans} = \sum_{i=1}^{N} \frac{1}{2} m_t P_i^T P_i$$

The kinetic energy due to rotational motion is computed using the angular velocity of each tether element, expressed in its respective body frame $\{T_i\}$, as previously derived in (6.2).

$$T_{rot} = \sum_{i=1}^{N} \frac{1}{2} \omega_{T_i}^T I_t \omega_{T_i}$$

Where the total LMM kinetic energy is expressed as:

$$T_t = T_{trans} + T_{rot}$$

Given the derived potential and the kinetic energy of the tether system, the equations of motion are derived using the Euler–Lagrange formulation which is applied in a similar manner as in Section 5.3.2, but with the added constraint c_{world}. The tether systems Lagrangian is thus defined as:

$$L_t(q_t, \dot{q}_t, z) = T_t(q_t, \dot{q}_t) - V_t(q_t) - \lambda_{\text{world}}^T c_{\text{world}}(q)$$

Which yields the following Euler–Lagrange equations of motion:

$$EL: \quad \frac{d}{dt}\left(\frac{\partial L_t}{\partial \dot{q}_t}\right) - \frac{\partial L_t}{\partial q_t} = Q_t, \quad c_{\text{world}}(q_t) = 0$$

The expression above can then be expanded and expressed in terms of the systems weight matrix $W(q)$, where the constraint equation $c(q)$ is added to fully define the system:

$$\begin{cases} W(q_t)\ddot{q}_t + \frac{\partial}{\partial q_t}(W(q_t)\dot{q}_t)\dot{q}_t - \nabla_{q_t} T_t + \nabla_{q_t} V_t + \nabla_{q_t} c_{\text{world}} \cdot \lambda_{\text{world}} = Q_t \\ c_{\text{world}}(q_t) = 0 \end{cases} \tag{6.13}$$

The system of equations (6.13) includes both differential and algebraic components, with the constraint equation representing the algebraic part. This structure classifies the system as a differential-algebraic equation (DAE) system. It is however trivially seen that the Lagrange multiplier λ_{world} cannot be directly computed from the constraint equation, as it does not explicitly contain it. This issue arises because the resulting differential algebraic equation (DAE) system has a differential index of 3, which can not be explicitly solved and is not suitable for standard numerical solvers. To build intuition for this, consider that the equations of motion are defined in terms of generalized accelerations $\ddot{q}$, while the constraint equations specify constraints on the systems position q_t. As a result, the constraint forces, appearing in the equations of motion as $\nabla_q c(q) \cdot \lambda$, cannot be solved for by the position constraints. In order to relate the position constraints to the systems accelerations, the constraint equation is thus differentiated twice, so that the DAE is reduced to the differential index 1. The derivative of the constraint equation is shown below. The implemented constraint corresponds to the world constraint in (6.7), and all Euler-–Lagrange terms refer to the tether, but explicit subscripts are omitted in the following equations for clarity.

$$\dot{c}(q, \dot{q}) = \frac{\partial c}{\partial q}\dot{q} = 0$$

$$\ddot{c}(q, \dot{q}, \ddot{q}) = \frac{\partial c}{\partial q}\ddot{q} + \frac{\partial}{\partial q}\left(\frac{\partial c}{\partial q}\dot{q}\right)\dot{q} = 0$$

When using the second order derivative of the constraint equation, the system of equations become solvable and is shown below.

$$\begin{bmatrix} W(q) & \nabla_q c \\ \nabla_q c^T & 0 \end{bmatrix} \begin{bmatrix} \ddot{q} \\ \lambda \end{bmatrix} = \begin{bmatrix} Q - \frac{\partial}{\partial q}(W(q)\dot{q})\dot{q} - \nabla_q T - \nabla_q V \\ -\frac{\partial}{\partial q}\left(\frac{\partial c}{\partial q}\dot{q}\right)\dot{q} \end{bmatrix}$$

Similarly to the hexacopter model derivation, an integrator is applied to transform the second-order differential equation into ODE:s, as shown below.

$$\begin{bmatrix} 0 & I & 0 \\ W(q) & 0 & \nabla_q c \\ \nabla_q c^T & 0 & 0 \end{bmatrix} \begin{bmatrix} \dot{X} \\ \dot{q} \\ \lambda \end{bmatrix} = \begin{bmatrix} X \\ Q - \frac{\partial}{\partial q}(W(q)\dot{q})\dot{q} - \nabla_q T - \nabla_q V \\ -\frac{\partial}{\partial q}\left(\frac{\partial c}{\partial q}\dot{q}\right)\dot{q} \end{bmatrix} \tag{6.14}$$

The equations of motion presented in (6.14) are referred to as the tether model, and is a system of DAE:s. The simulation methodology is described in detail in Section 8.1.1 while key characteristics of the system, when coupled with the hexacopter model, are outlined in the following Section 6.4.4.

6.4.4 Tether–hexacopter coupled model

Given that the hexacopter and tether model are derived in Sections 5.3.2 and 6.4.3 respectively, the next step is to derive the coupled tether–drone system model. This derivation follows the established Euler–Lagrange methodology by summing the energy contributions of each system and combining their generalized coordinates and external forces. The energies of the coupled system are thus written as:

$$\begin{cases} T = T_t + T_h \\ V = V_t + V_h \end{cases}$$

The generalized coordinates, external forces, constraints and Lagrange multipliers are combined as shown below. Note that the tether-to-drone constraint is also added to the existing tether-to-world constraint, in accordance to (6.11). This also implies that there are two system Lagrange multipliers as shown below.

$$q = \begin{bmatrix} q_h \\ q_t \end{bmatrix}, \quad \mathbf{Q} = \begin{bmatrix} Q_h \\ Q_t \end{bmatrix}, \quad c(q) = \begin{bmatrix} c_{\text{drone}}(q) \\ c_{\text{world}}(q) \end{bmatrix}, \quad \lambda = \begin{bmatrix} \lambda_{\text{drone}} \\ \lambda_{\text{world}} \end{bmatrix}$$

The equations of motion are then derived following the same procedure used for the tether in Section 6.4.3, as this system similarly contains constraint equations. Lag dynamics are also added to the model, as detailed in 5.3.3, which yields the coupled tether-drone model with lag dynamics as shown below.

$$\begin{bmatrix} 0 & I & 0 & 0 \\ W(q) & 0 & \nabla_q c & 0 \\ \nabla_q c^\top & 0 & 0 & 0 \\ 0 & 0 & 0 & I \end{bmatrix} \begin{bmatrix} \dot{X} \\ \dot{q} \\ \lambda \\ \dot{T} \end{bmatrix} = \begin{bmatrix} X \\ Q - \frac{\partial}{\partial q}(W(q)\dot{q})\dot{q} - \nabla_q T - \nabla_q V \\ -\frac{\partial}{\partial q}\left(\frac{\partial c}{\partial q}\dot{q}\right)\dot{q} \\ -\frac{1}{\tau_a}T + \frac{1}{\tau_a}T_R \end{bmatrix}$$

While the simulation methodology is described in detail in Section 8.1.1, understanding the size and characteristics of the model is crucial for evaluating simulation performance and determining the appropriate simulation approach. The number of system states grows linearly with the number of tether elements in the LMM. The hexacopter dynamics, constraints, and lag components contribute a total of 20 system states, while each additional tether element introduces 6 more states. This implies that the size of the system matrix grows quadratically with the number of tether elements, as shown below:

$$n_{\text{matrix\_elements}} = (20 + 6N_t)^2 = 400 + 240N + 36N_t^2$$

Furthermore, due to the interconnected nature of the tether, where the position and orientation of each element are functions of all preceding elements, the system exhibits strong coupling. This coupling leads to increased computational complexity and a denser system structure as N_t increases. In addition to this, the equations governing the dynamics are highly nonlinear due to the trigonometric relations present in the rotational kinematics and the constraint forces introduced via Lagrange multipliers.

6.5 Tether parameter derivation

In this section, parameters are derived for the tether elements, which discretize the tether into N_t equal parts. The tethers parameters are derived by means of reference literature, established formulas for inertia and drag, and comparisons to COTS components. Since the tether is divided into discrete elements, the properties of each element are dependent on the chosen number of segments, N_t. More specifically, the length of each tether element depends on the number of segments N_t, which also affects the corresponding mass and inertia. The element length is calculated as shown below.

$$L_t = \frac{L_{t,tot}}{N_t}$$

The diameter of the tether is estimated using the assumed linear relationship between power consumption and weight, as described in Section 3.4.3. The chosen COTS tether, used as a reference, has an outer diameter of 5 mm and an output of 12 kW [66]. Given the system's maximum power demand of approximately 19.82 kW, the required diameter is determined by linearly scaling the cross-sectional area, yielding the final tether diameter shown below.

$$D_t \approx 6.42\ mm \tag{6.15}$$

The tether linear mass density, λ_t, is derived by dividing the total tether mass with the total tether length. The final hexacopter concept is initially designed to have a tether length of 70 m, which has been derived to have a mass of approximately 3.35 Kg. This results in the following linear mass density, λ_t.

$$\lambda_t \approx \frac{3.3528}{70} \approx 4.79 \times 10^{-2}\ Kg/m \tag{6.16}$$

Given the previously calculated linear mass density of the tether, the mass of each tether element can now be calculated as shown below.

$$m_t = \lambda_t L_t$$

It is approximated that each tether element is shaped as a cylinder. The inertia is thus calculated using standard formulas for a solid cylinder, as shown in the

equations below. The inertia is calculated in reference to each tether elements coordinate frame $\{T_i\}$, which is positioned at the bottom end of each tether element.

$$\begin{cases} I_{xy,t} = \frac{1}{12} m_t L_t \\ I_{zz,t} = \frac{1}{2} m_t R_t \end{cases} \tag{6.17}$$

6.5.1 Aerodynamic coefficients

The first aerodynamic coefficient considered is the basic drag coefficient, $C_{D,basic,t}$. This coefficient is determined specifically for the tether elements and therefore depends on the length of each tether segment. The value of the drag coefficient is obtained by interpolating data from the previously presented table in Figure 5.11, with the tether element diameter D_t and length L_t presented above.

The skin friction coefficient depends on the object's geometry, surface roughness and the Reynolds number. In accordance to previous assumptions, the flow regime is assumed to be laminar. The tether element is as previously stated, modeled as a cylinder which does not have a simple analytical solution for the skin friction coefficient c_f. This is due to the surface curvature of the cylinder which affects the pressure gradient around the cylinder and the boundary layer development. Therefore, the tether element is approximated as a flat surface for the purpose of calculating the friction drag coefficient, which is an approach shown to yield comparable results in [117]. The skin friction coefficient is thus derived from the Blasius boundary layer solution, which assumes a thin boundary layer, constant pressure across the layer, and fluid flow along a flat plate. This yields the relation shown below [118].

$$C_f = \frac{0.664}{\sqrt{Re_x}} \tag{6.18}$$

The friction drag coefficient, is as shown above, dependent on the Reynolds number. To simplify the complexity and calculation of the friction drag coefficient, the Reynolds number is assumed to be constant and set at the upper limit of the laminar flow regime ($Re_x \approx 5 \times 10^5$). This assumption reflects a conservative approach, as the system is most susceptible to failure under high wind speeds, which correspond to high Reynolds numbers. Based on the assumptions outlined above, the friction drag coefficient for the tether element is determined to be $C_f = 0.001$.

6.5.2 Spring and damper coefficients

The torsional springs and dampeners between each adjacent tether element, the hexacopter anchor-point and the world frame were added to improve model accuracy, as recommended in [113], [114]. It is however a highly complex task to derive the spring and damping coefficients, as noted in the literature. This complexity is further compounded by the tether being a composite structure made of multiple materials with differing mechanical properties, as described in Section 3.4.1.

Additionally, the spring and damping coefficients are influenced by the tether's discretization, specifically the number of segments N_t used in the model. Given the aforementioned challenges in estimating the spring and damping coefficients, it is concluded that these parameters must be empirically determined through physical testing of the actual tether. This conclusion is further supported by the absence of any established definitions for these coefficients based on material properties or discretization level in existing LMM:s.

Since there are no analytical solutions for these parameters, and physical testing is out of scope for the thesis, the parameters are to be manually tuned in accordance to their functionality. As described in Section 6.3, the springs resist angular displacement between tether elements, preventing sharp acute angles, while the dampers dissipate energy, enhancing simulation stability and accuracy by accounting for internal damping, friction, and environmental resistance. The tuning of the tether coefficients is performed when solely simulating the tether model, where the effects of the coefficients on the system's behavior can be clearly observed and adjusted accordingly. While this approach introduces some degree of uncertainty to the model, the inclusion of these elements is still valuable as it allows the simulation to account for physical effects that would otherwise be neglected.

6.5.3 Summary of parameters

A summary of the tether parameters are presented in Table 6.1 below, where the parameters are specifically derived for the tether elements. As stated, the tether element parameters are greatly influenced by the level of discretization of the cable, meaning that a majority of the parameters are a function of N_t. While N_t can be freely chosen, it is closely linked to the simulation time and will be discussed further in Section 8.1.1. It is also important to note that, similar to the hexacopter and payload parameters, the tether parameters can be adjusted as needed by modifying the primary tether characteristics: total length, diameter, and linear mass density.

Variable	Simulation Parameter	Value	Unit	Derivation
λ_t	Tether linear mass density	4.790E-02	$[Kg/m]$	(6.16)
$L_{t,tot}$	Tether length	70	$[m]$	App. A
D_t	Diameter	6.42E-03	$[m]$	(6.15)
N_t	Tether elements	*Variable*	$[m]$	–
k_t	TE spring coefficient	*Manually tuned*	$[N/m]$	–
c_t	TE damping coefficient	*Manually tuned*	$[Ns/m]$	–
$C_{f,t}$	TE skin friction coefficient	0.001	[–]	(6.18)
$C_{D,basic,t}$	TE basic drag coefficient	*Interpolate*	[–]	Fig 5.11
$I_{xy,t}(N_t)$	TE Moment of inertia	*Function*	$[Kg \cdot m^2]$	(6.17)
$I_{z,t}(N_t)$	TE Moment of inertia	*Function*	$[Kg \cdot m^2]$	(6.17)

Table 6.1: Tether parameters.

7

Control system design

This chapter presents the design and implementation of a control system for a tethered hexacopter, based on a cascaded PID architecture. The primary objective is not to develop an optimal controller, but to establish a performance baseline with PID control. Control systems are designed for altitude, attitude, and tether tension control. Additionally, the control architecture is adapted to account for potential rotor failure scenarios. A basic feedback loop, shown in Figure 7.1, outlines the core components of the control system: the controller, the system model (commonly referred to as the plant), and the feedback path. It is important to note that these components are interchangeable depending on the specific control objective. In this work, the previously derived tether model, hexacopter model, and the coupled tether-hexacopter model are each used as the plant in different control and simulation scenarios.

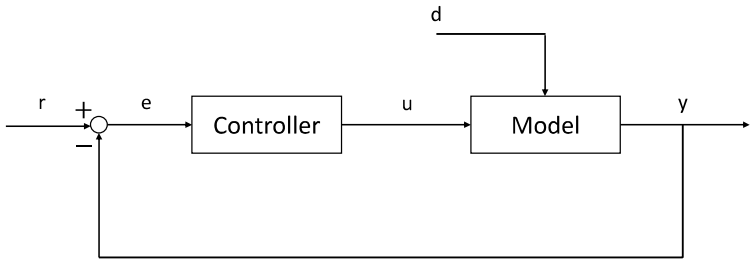

Figure 7.1: Basic feedback control loop. r is the reference input, e is the tracking error, u is the control input, d is the disturbance, and y is the system output.

7.1 The control problem

As explained in Section 5.2.1, the hexacopter has a total of six degrees of freedom: translational motion along the x, y, and z axes in the world frame $\{W\}$, and rotational motion (attitude) relative to $\{W\}$, described by the Euler angles ϕ (roll), θ (pitch), and ψ (yaw). The hexacopter has a total of six control inputs which are the thrust forces generated by the rotors. It is however important to note that the rotor thrusts are not all independently usable for controlling the system's DOF:s. Due to the symmetry and placement of the hexacopters rotors, only four "virtual" control inputs can be effectively used. The independent control inputs are:

1. The total thrust T_{tot} in the body-fixed frame $\{B\}$, primarily affecting vertical motion
2. Roll torque τ_ϕ, due to rotor thrust imbalances around the local x-axis
3. Pitch torque τ_θ, due to rotor thrust imbalances around the local y-axis
4. Yaw torque τ_ψ, resulting from asymmetric rotor torque generation

As a result of the hexacopter operating in a 6-DoF space while having only four virtual control inputs, the system is classified as underactuated. Despite this, the system remains controllable when appropriate control strategies are employed. To explore this in greater detail, the system's state variables are classified as independent or dependent. The variables that can be controlled directly is the z-position, as well as the three hexacopter rotations described by the Euler angles. These are considered as independent variables. The remaining state variables, which is the x and y position in $\{W\}$, are thus considered dependent state variables. The x position is dependent on the pitch angle (ϕ) and is indirectly controlled by pitching forward or backwards. Similarly, the y position is dependent on the roll angle (ϕ).

Given that the hexacopter's underactuated nature has been determined, with state variables classified as either dependent or independent, it is essential to analyze the relationship between the virtual control inputs (defined in the list above) and the six corresponding rotor thrust control inputs. This relationship is governed by the motor mixing matrix, originally derived in (5.16). This matrix provides the necessary mapping from the desired net thrust and body-frame torques to the corresponding rotor thrusts. Since it plays a central role in the control strategy discussed in this chapter, the matrix is restated here:

$$\begin{bmatrix} T_1 \\ T_2 \\ T_3 \\ T_4 \\ T_5 \\ T_6 \end{bmatrix} = \begin{bmatrix} \frac{1}{6} & 0 & -\frac{1}{3d} & -\frac{k}{6b} \\ \frac{1}{6} & \frac{\sqrt{3}}{6d} & -\frac{1}{6d} & \frac{k}{6b} \\ \frac{1}{6} & \frac{\sqrt{3}}{6d} & \frac{1}{6d} & -\frac{k}{6b} \\ \frac{1}{6} & 0 & \frac{1}{3d} & \frac{k}{6b} \\ \frac{1}{6} & -\frac{\sqrt{3}}{6d} & \frac{1}{6d} & -\frac{k}{6b} \\ \frac{1}{6} & -\frac{\sqrt{3}}{6d} & -\frac{1}{6d} & \frac{k}{6b} \end{bmatrix} \begin{bmatrix} T_{tot} \\ \tau_\phi \\ \tau_\theta \\ \tau_\psi \end{bmatrix}$$

7.2 Controller selection and comparison

As previously presented, the hexacopter system is highly nonlinear, multivariable and underactuated with coupled system states. This complexity is further compounded by the constraints imposed by the tether within the hexacopter-tether system. The control problem does not have a unique solution, meaning that a multitude of different controllers and control architectures could be implemented, each offering distinct trade-offs in performance, robustness, and implementation complexity. A summary of two comparative studies evaluating controllers for multirotor UAVs is presented in Table 7.1 [119], [120]. In the table, FSC refers to Full-state control which describes the controller's ability to regulate all system states within a single control loop.

Control Method	Control Type	FSC	Advantages	Disadvantages
PID	Linear	No	Simple to implement, systematic tuning, possible zero steady state error, does not require model	Struggles with coupling and nonlinearities, limited multivariable handling, poor robustness
LQR	Linear	Yes	Simple to implement, Optimal performance for linear systems, fast dynamics	Requires accurate linear model, not robust to strong nonlinearities, may fail to overcome steady-state errors
MPC	Either	Yes	Handles constraints, predicts future behavior, robust	Computationally intensive, complex to tune, may exhibit slow response
Feedback Linearization	Nonlinear	Yes	Cancels nonlinearities, enables linear control of nonlinear systems	Requires full nonlinear model, sensitive to model inaccuracies
Backstepping	Nonlinear	Yes	Effective for underactuated systems, good robustness against disturbances	Low robustness for system uncertainty
Sliding Mode Control (SMC)	Nonlinear	Yes	Robust to disturbances and model uncertainties	Can cause chattering, may require high-frequency control

Table 7.1: Comparison of control methods for multirotor UAVs.

Given that the tether-hexacopter system is constrained, with the position of the hexacopter's anchor point limited by the tether length, Model Predictive Control (MPC) proves to be a suitable control strategy [121]. MPC is particularly favorable because it can explicitly handle both state and input constraints, such as tether length, tether tension, and rotor thrust limits. Unlike the other conventional controllers presented in Table 7.1, MPC optimizes the control inputs (rotor thrusts) while explicitly accounting for constraints imposed by the tether, ensuring that the system operates safely within its physical limits. MPC is considered a suitable control strategy, given its viability for future physical implementation. It is however not implemented in this project, as the primary objective is to evaluate the system's performance through simulation rather than to develop a real-time control solution. Given its implementation complexity and tuning effort, MPC is thus less suited for the intended simulation loop compared to simpler alternatives.

Due to the simulation-oriented scope of the thesis, PID control was selected to reduce controller design complexity while still achieving satisfactory system performance. By choosing PID control, a controller is obtained that is easy to tune for various scenarios and requires minimal computational resources, making it well-suited for system analysis through simulation. Given this, it is unlikely that PID is the most optimal controller or that the controller will be optimally tuned for the tether-hexacopter system within the scope of this thesis. As a result, rather than deriving the most optimal controller, the PID controller serves to establish a lower boundary for the systems performance.

7.3 Methodology for PID controller tuning

Several PID tuning methods exist, including empirical approaches such as the Ziegler-Nichols method and model-based techniques such as pole placement. While these methods offer a systematic solution for PID tuning, manual tuning remains a widely adopted approach in UAV applications due to its simplicity. For this reason, manual tuning is adopted for the hexacopter's PID controllers. The process of manual PID tuning is well-established in the litterature [122], and follows a structured methodology as shown in the list below.

1. Set K_P, K_I, and K_D to zero.
2. Increase K_P until oscillations are sustained or nearly sustained (use a long simulation time, e.g., 100s).
3. Increase K_D slightly to reduce oscillations to one period (use a shorter simulation time, e.g., 10s).
4. Increase K_I until the steady-state is near the setpoint and oscillations stabilize around it.
5. Additional tuning: Increase K_P to eliminate steady-state error, K_I to reduce error, and K_D to minimize overshoot for a smooth output.

The tuning steps outlined above are applied to each PID controller, with the process involving step-response tests on the nonlinear hexacopter model presented in Section 5.3.3. After tuning each PID controller individually on the standalone hexacopter model, they are further fine-tuned using the complete coupled nonlinear tether–hexacopter model, with adjustments made based on performance under wind disturbance conditions.

7.4 Controller architecture

As shown in Table 7.1, a majority of the control strategies are capable of regulating the full system state within a single control loop. Despite this, a two-loop (cascaded) control architecture is commonly adopted for multirotor UAVs as it allows for the separation of the dynamic response into fast and slow components. The two-loop cascaded architecture used in this work is inspired by the approach presented in [123], although alternative architectures are also commonly implemented.

For example, the four-loop cascaded architecture described in [22] introduces two additional control loops for velocity and angular rate control. While this structure can enhance free-flight performance, it is not considered necessary for the more constrained dynamics of tethered flight. For the chosen controller architecture, the inner loop controls the system's attitude (ϕ, θ, ψ) and is tuned for a fast dynamic response, while the outer loop controls translational position and is tuned for slower dynamics. This separation of time scales improves system stability, simplifies the tuning process and ensures that the dependent variables (x, y) are controlled before adjusting the underlying independent variables (ϕ, θ) that influence them. This implies that the outer-loop controller, which regulates the position (x, y), generates reference commands for the attitude angles (ϕ, θ), which in turn directly affect the position dynamics. A simplified schematic of the controller architecture is shown in Figure 7.2 below. Note that the wind disturbance previously derived in Section 5.3.1.3 is also an input to the model.

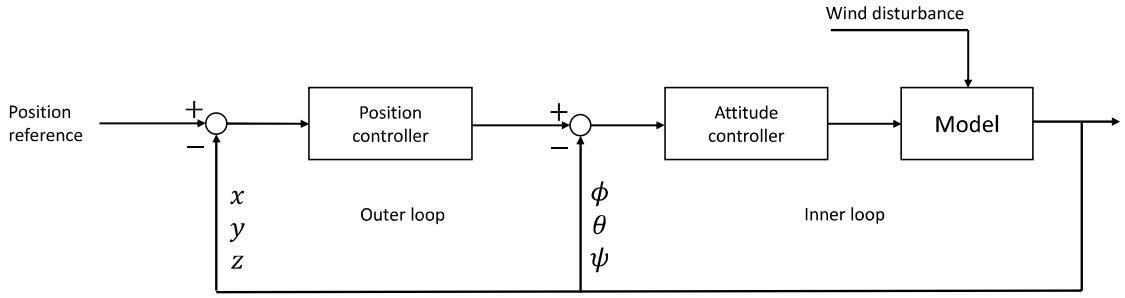

Figure 7.2: Simplified schematic of hexacopter controller. The inner loop controller regulates attitude and the outer loop controller regulates position.

Given the cascaded control architecture, any of the controllers listed in Table 7.1 could be used for both the inner and outer loops. However, as previously discussed in Section 7.2, PID control is preferred and is therefore selected for both loops. The fully defined controller architecture is shown in the figure below, where there are a total of six PID controllers, one for each hexacopter state variable. Observe that the wind disturbance input is generated by feeding the hexacopter's vertical z-position back into the wind model (5.20), which then outputs the corresponding wind speeds acting on the hexacopter. This applies when the hexacopter-only model is selected. Alternatively, if the coupled tether-hexacopter model is used, the vertical positions of each tether element midpoint are also fed back into the wind model (6.4), which calculates the wind speed at each respective height. The complete control architecture, including all PID controllers, is shown in Figure 7.3 below.

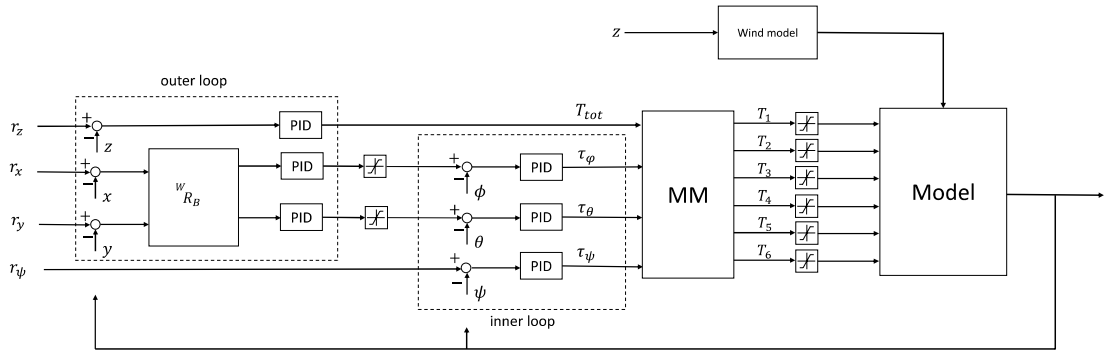

Figure 7.3: Block diagram of the complete cascaded controller architecture for hexacopter control.

Two matrix transformations have been implemented in the control loop shown above: the world to body rotation matrix defined in (5.6) and the motor mixing matrix defined in (5.16). The position reference (r_x, r_y, r_z) is defined in the world frame $\{W\}$, while the hexacopter acts within its local body frame $\{B\}$. Since the hexacopter may be arbitrarily rotated during flight, it cannot directly use the world frame reference positions to determine its required motion to reach the reference. The world frame position error for (x, y) is therefore transformed into the hexacopter's body frame by applying the rotation matrix. Note that the vertical z-position is typically treated as invariant to rotation, even if it is slightly influenced by roll and pitch, and is thus directly referenced in the world frame without requiring transformation. The motor mixing matrix is applied after both the outer and inner control loops. It converts the virtual control inputs, described in Section 7.1, into the individual rotor thrust commands, which are then fed into the hexacopter model.

A total of eight saturation blocks are incorporated into the controller: two of these limit the pitch and roll commands, while the remaining six enforce the physical thrust limits of the individual rotors, as determined by their hardware constraints. The saturation limits for roll and pitch are tuned to prevent the outer loop from sending excessively large angle references to the inner loop, which could make the hexacopter unstable and thus causing it to flip over. Based on simulation testing of the system, a roll and pitch limit of 30 degrees was determined to be appropriate.

The PID controllers are manually tuned in accordance to the method presented in Section 7.3. The inner loop controllers are tuned first, followed by the tuning of the outer-loop controllers. This sequence is important as effective control of the translational positions (x, y) relies on the accurate control of the hexacopters roll and pitch (ϕ, θ). All PID controller gains, tuned for the final hexacopter and tether system with parameters listed in Tables 5.4 and 6.1, are summarized in Table 7.2 below. Note that, although outer-loop controllers are typically tuned for slower dynamics than the inner loop, the vertical position controller for z requires significantly higher gains. This is primarily because it must continuously counteract gravity. Additionally, the yaw controller is assigned lower gains compared to the roll and pitch

controllers. This is because yaw regulation is less critical for overall stability and position control. This also implies that excessively high yaw gains may degrade the effectiveness of the roll and pitch controllers, thus reducing flight stability.

Loop / Variable	K_p	K_i	K_d
Outer Loop (Position Control)			
x	0.5	0.08	0.3
y	0.5	0.08	0.3
z	140	20	250
Inner Loop (Attitude Control)			
ϕ (Roll)	150	25	80
θ (Pitch)	150	25	80
ψ (Yaw)	80	5	20

Table 7.2: PID gains for inner and outer loop hexacopter controllers.

Lastly, the control reference for the system needs to be determined. For the coupled tether-hexacopter model, this reference should correspond to a vertical hexacopter position with zero yaw, representing a fully upright orientation. This reference reflects the desired steady-state configuration of the entire tethered hexacopter system under nominal operating conditions, as defined in the equation below. It should be noted that alternative references are used when performing step response tests for the standalone hexacopter model during controller tuning.

$$\begin{bmatrix} r_x \\ r_y \\ r_z \\ r_\psi \end{bmatrix} = \begin{bmatrix} 0 \\ 0 \\ L_{t,tot} + z_{anchor} \\ 0 \end{bmatrix}$$

7.5 Tether tension control

As motivated in Section 6.1, a certain level of tether tension is necessary for flight stability. The hexacopter controller, presented in Section 7.4, generates tether tension indirectly when there is a vertical z-position error, as it responds by increasing upwards thrust to reduce the error. This is however deemed insufficient because it depends solely on the presence of a position error to produce tension. In practice, a sustained tether tension is also required when there is no position error to enhance disturbance rejection and maintain system stability. This mechanism could theoretically be introduced by the position controller by increasing the vertical position reference r_z. This approach is however deemed impractical as it creates an unattainable reference, leading to controller integrator windup over time. To address this, a dedicated tether tension controller is needed to ensure continuous tension.

To achieve this, two different options are considered: an open–loop controller and a closed–loop controller with tether tension feedback. Both options introduce a degree of control redundancy as they act on the same control input T_{tot}, alongside the existing z-position controller. This is however a deliberate design choice as tether tension will now be guaranteed at all times and independently of the vertical position error, while the existing position controller remains responsible for correcting z-position errors. The open-loop tether tension control is implemented by adding the tension reference directly to the vertical thrust command generated by the z-position controller, as shown in Figure 7.4.

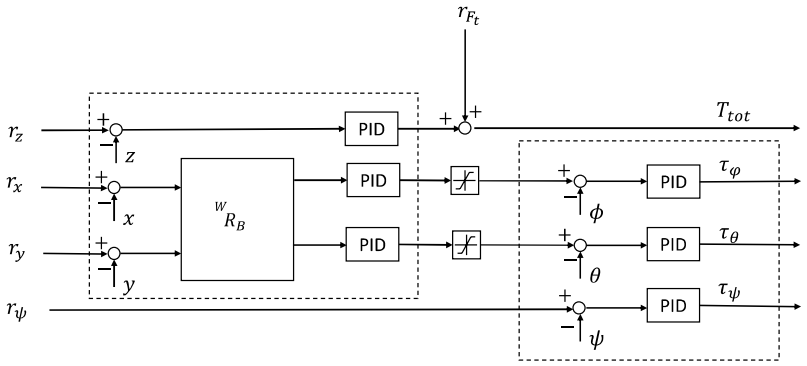

Figure 7.4: Block diagram of closed-loop tether tension control added to existing architecture.

For the closed loop configuration shown in Figure 7.5, the tether tension is actively controlled using feedback from the tether tension defined in (6.12). Implementing this controller in a real-world scenario would require accurate and reliable tether tension measurements, typically obtained through a dedicated force sensor. By implementing both the open- and closed-loop configurations, the trade-offs between simplicity and performance can be evaluated, providing insight into whether the added sensor is justified.

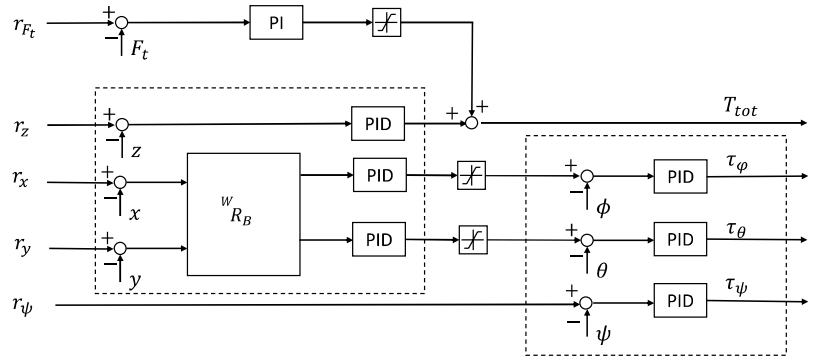

Figure 7.5: Block diagram of open-loop tether tension control added to existing architecture.

The closed-loop tether tension controller is implemented as shown in the figure above, where a PI controller is used in combination with a saturation block to ensure that only positive tension values are applied. Several different controllers where tested for the tether tension control, where it was shown that introducing the derivative term in a PID controller would cause high-frequency oscillations and large control inputs. This is due to there being a high frequency wind disturbance applied to the hexacopter and tether. Similarly, high values of the proportional gain led to an undesirable oscillatory behavior. The resulting PI controller design, which relies primarily on the integral term, is well-suited for the application as it eliminates steady-state error while producing a smooth control signal that avoids abrupt changes or oscillations in the tether tension. The PI controller gains were set to $K_p = 2.5$ and $K_I = 40$.

For simplicity, the tether tension reference is defined as a percentage of the remaining available thrust beyond what is required to maintain hover. A tension level of x% represents the fraction of available thrust beyond what is required to maintain hover, and is calculated in (7.1) below. The appropriate value for the tether tension reference depends on the expected level of wind disturbances, as further examined in Section 8.2. In principle, the reference could be dynamically adjusted using an additional open-loop controller based on wind measurements. However, accurate and reliable wind sensing is considered challenging and impractical in this context, and is therefore deemed out of scope for this work.

$$r_{F_t} = \frac{x}{100}(\text{thrust-to-weight} - 1) \cdot mg \tag{7.1}$$

7.6 Control during rotor failure

A critical case in evaluating the hexacopter's performance is its behavior during rotor failure. The resulting hexacopter concept is partially motivated by its ability to provide a degree of redundancy, allowing continued flight even after the loss of a rotor. The primary challenge however, lies in understanding how control can be maintained under such failure conditions and how overall performance is affected.

In the event of a rotor failure, the hexacopter must satisfy two key equilibrium conditions to maintain stability. The first is torque equilibrium around the yaw axis: rotors spinning in the opposite direction of the failed rotor must reduce their rotational speed to compensate for the resulting imbalance in reactive torque. The second is a attitude torque equilibrium in roll and pitch: thrust from rotors on the side opposite the failure must be reduced to prevent the generation of unbalanced torques that could cause the hexacopter to flip. The generally accepted approach to satisfy both of these conditions is to turn of the rotor adjacent to the failed one, as stated in [124]. The approach is shown in Figure 7.6, where it is assumed that rotor 1 fails and rotor 4 is subsequently turned off. The immediate impact of this is the reduction of the thrust-to-weight ratio, where the new value is calculated to be 1.53:1. The ability to generate torque within the body frame is also further reduced,

since the loss of two rotors eliminates a key lever arm for producing torque about the axis perpendicular to the line between them, which is in this scenario the y-axis.

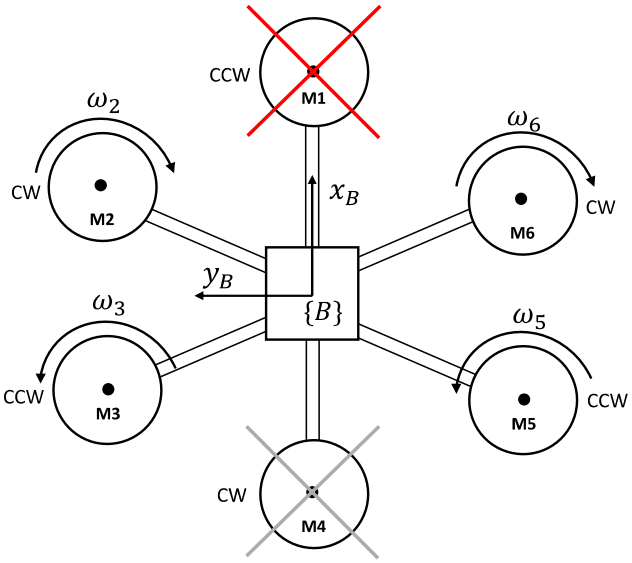

Figure 7.6: Proposed approach for addressing Rotor 1 failure for hexacopter.

When updating the controller following a rotor failure, the PID gains do not need to be changed, as they only generate the virtual control variables described in Section 7.1, which are subsequently mapped to motor commands via the motor mixing matrix. The mixing matrix must however be adjusted to correspond to the changed actuator arrangement. If it is assumed that rotor 1 fails, as shown in Figure 7.6, then the MM inverse is derived as follows.

$$\begin{bmatrix} T_z \\ \tau_\phi \\ \tau_\theta \\ \tau_\psi \end{bmatrix} = \underbrace{\begin{bmatrix} 0 & 1 & 1 & 0 & 1 & 1 \\ 0 & d\frac{\sqrt{3}}{2} & d\frac{\sqrt{3}}{2} & 0 & -d\frac{\sqrt{3}}{2} & -d\frac{\sqrt{3}}{2} \\ 0 & -d\frac{1}{2} & d\frac{1}{2} & 0 & d\frac{1}{2} & -d\frac{1}{2} \\ 0 & \frac{b}{k} & -\frac{b}{k} & 0 & -\frac{b}{k} & \frac{b}{k} \end{bmatrix}}_{M^{-1}} \begin{bmatrix} T_1 \\ T_2 \\ T_3 \\ T_4 \\ T_5 \\ T_6 \end{bmatrix} \tag{7.2}$$

Which simplifies to:

$$\begin{bmatrix} T_z \\ \tau_\phi \\ \tau_\theta \\ \tau_\psi \end{bmatrix} = \underbrace{\begin{bmatrix} 1 & 1 & 1 & 1 \\ d\frac{\sqrt{3}}{2} & d\frac{\sqrt{3}}{2} & -d\frac{\sqrt{3}}{2} & -d\frac{\sqrt{3}}{2} \\ -d\frac{1}{2} & d\frac{1}{2} & d\frac{1}{2} & -d\frac{1}{2} \\ \frac{b}{k} & -\frac{b}{k} & -\frac{b}{k} & \frac{b}{k} \end{bmatrix}}_{MM^{-1}} \begin{bmatrix} T_2 \\ T_3 \\ T_5 \\ T_6 \end{bmatrix} \tag{7.3}$$

Reducing the matrix MM^{-1} to its row reduced echelon form yields the matrix shown below. From this, it is trivially concluded that the mixing matrix loses rank and is thus rank deficient. More specifically, it is shown that independent yaw control is lost and the yaw row is linearly dependent on the pitch and roll rows. This implies

that the system is no longer fully controllable in yaw, meaning that any attempt to generate yaw torque must come at the expense of pitch and/or roll control.

$$\begin{bmatrix} T_z \\ \tau_\phi \\ \tau_\theta \\ \tau_\psi \end{bmatrix} = \underbrace{\begin{bmatrix} 1 & 0 & 0 & 1 \\ 0 & 1 & 0 & -1 \\ 0 & 0 & 1 & 1 \\ 0 & 0 & 0 & 0 \end{bmatrix}}_{MM^{-1}} \begin{bmatrix} T_2 \\ T_3 \\ T_5 \\ T_6 \end{bmatrix} \tag{7.4}$$

To quickly address why a hexacopter missing two adjacent rotors loses yaw controllability, while a quadcopter with the same number of rotors remains controllable, it is necessary to examine the rotor spin directions shown in Figure 7.6. The figure illustrates that the remaining rotors no longer alternate their spin directions as rotors 2 and 6 spin CW, while rotors 3 and 5 spin CCW. This arrangement causes any torque generated for pitch control to simultaneously produce a torque around the yaw axis, coupling the two. For this specific rotor failure, roll control is not coupled to yaw but this is not the case if any of the diagonal rotors fails.

Several solutions and trade-offs exist for managing the loss or coupling of yaw control. A commonly accepted approach, as noted in [124], is to disregard yaw control entirely, allowing the hexacopter to drift about the yaw axis. Alternative strategies involve sacrificing control authority in roll or pitch, which will worsen system stability. The most viable solution is considered to be the intentional loss of yaw control, preserving roll and pitch stability. This is particularly appropriate during emergency procedures, such as a winched descent, where maintaining stability is critical. This further underscores the importance of designing the system to be capable of landing safely in any yaw orientation, as discussed in Section 4.1. The resulting MM inverse is thus calculated to be the following.

$$\begin{bmatrix} T_z \\ \tau_\phi \\ \tau_\theta \end{bmatrix} = \underbrace{\begin{bmatrix} 1 & 0 & 0 & 1 \\ 0 & 1 & 0 & -1 \\ 0 & 0 & 1 & 1 \end{bmatrix}}_{MM^{-1}} \begin{bmatrix} T_2 \\ T_3 \\ T_5 \\ T_6 \end{bmatrix} \tag{7.5}$$

The actual mixing matrix used to convert control inputs into individual motor thrusts is then obtained by computing the pseudo inverse of the matrix above:

$$\begin{bmatrix} T_2 \\ T_3 \\ T_5 \\ T_6 \end{bmatrix} = \begin{bmatrix} \frac{1}{4} & \frac{\sqrt{3}}{6d} & -\frac{1}{2d} \\ \frac{1}{4} & \frac{\sqrt{3}}{6d} & \frac{1}{2d} \\ \frac{1}{4} & -\frac{\sqrt{3}}{6d} & \frac{1}{2d} \\ \frac{1}{4} & -\frac{\sqrt{3}}{6d} & -\frac{1}{2d} \end{bmatrix} \begin{bmatrix} T_{\text{tot}} \\ \tau_\phi \\ \tau_\theta \end{bmatrix}$$

8

Tethered drone simulations

The primary aim of simulating the tether–drone model, configured with the designed controllers and subjected to environmental factors such as wind disturbances, is to evaluate the performance and limitations of the complete system. More specifically, the simulation results represent a conservative lower bound for system performance as the system has been continuously modeled with conservative assumptions, and the controller is not guaranteed to yield optimal performance under all conditions. Nevertheless, the performance remains a realistic estimate, making this lower bound a reliable benchmark for assessing the product feasibility for future development. The simulation objectives considered in this study are presented in the list below.

1. Evaluate system performance and power consumption
2. Analyze hexacopter stability under varying weather conditions
3. Analyze hexacopter stability for varying payload configurations
4. Determine appropriate tether tension levels
5. Assess safety in scenarios involving rotor failure
6. Estimate landing and take-off durations

By addressing the simulation objectives listed above, the results can also serve to validate the system design by comparing its performance against the requirement specifications outlined in Appendix A. The system validation provides quantitative evidence to support design decisions, highlight potential risks, and pinpoint areas for future research and development.

8.1 Simulation setup and evaluation

There are a total of three models that are simulated: the tether model, which is used to tune the torsion and dampener coefficients, the hexacopter model, which is used to optimize its controller, and the coupled tether-drone model, which evaluates the overall performance and limitations of the system. In addition to the hexacopter and tether model parameters derived in Sections 5.4 and 6.5, a set of environment parameters remain configurable. The baseline values of the environment parameters are presented in Table 8.1 below, and will later be modified to simulate the system under varying conditions, such as different wind speeds. Other parameters which can be varied are the payload masses and their center of mass positions relative the hexacopter body frame as presented in Table 8.4.

Variable	Simulation Parameter	Value	Unit
ρ	Air density	1.225	$[Kg/m^3]$
γ	Wind angle of attack	0	$[rad]$
α	Hellman's exponent	0.2	$[\,-\,]$
V_{wind}	Operational wind speed	Force 2	$[m/s]$

Table 8.1: Baseline environment parameters.

8.1.1 Simulation methodology

As outlined in the Hexacopter and Tether Modeling, Chapters 5 and 6, the hexacopter and tether models are described as systems of ordinary differential equations (ODEs), while the coupled system is modeled as a DAE with a differential index of 1. It is thus suitable to choose a simulation solver capable of handling both types of systems, simplifying the process by avoiding the need to switch between different solvers. The solver chosen for the Simulink simulation is the implicit method ode23s, which is based on a modified Rosenbrock method. The solver is primarily designed to solve index-1 DAEs, which is beneficial as the majority of simulations will be done with the coupled tether-drone system. The ode23s solver is also capable of handling stiff systems as it is variable step and implicit, which is suitable for handling systems which have both fast and slow dynamics. The previously derived tether-drone system is a mildly stiff DAE as the tether tension responds quickly compared to the hexacopters motion. There may also be fast oscillations in the LMM tether if there is a high degree of wind disturbance with a lot of noise.

The following solver settings, shown in Table 8.2 below, were used to ensure efficient and accurate simulation of the system. These parameters were carefully selected to balance computational speed with the precision required for modeling the coupled tether-drone system. The following solver settings are used in all simulations presented in this chapter unless stated otherwise. The simulations were run on a computer equipped with a 13th Gen i9 processor (2.2 GHz) with 65.5 GB of RAM memory.

Solver Setting	Value
Max Step Size	0.01
Min Step Size	0.001
Relative Tolerance	$1e-5$
Absolute Tolerance	$1e-7$

Table 8.2: Solver settings used in simulations.

With the solver and its settings defined, a set of initial conditions are now required to initiate the simulation. The required initial conditions are the system states which are defined to be the generalized coordinates q, their time derivatives $\dot{q}$ and the rotor thrusts $\mathbf{T}$. Unless stated otherwise, the coupled system is initialized with

a fully vertical tether at rest, and rotor thrusts set to match the hexacopter's trim conditions. This yields the following initial conditions.

$$q = \mathbf{0}, \quad \dot{q} = \mathbf{0}, \quad \mathbf{T} = \mathbf{1}_{6\times 1} \cdot g(m_H + m_L + M_U)/6$$

8.1.2 Simulation times and tether discretization

One key factor influencing the accuracy of the simulation and the systems representation of real-world behavior, is the degree to which the tether is discretized with the parameter N_t. A higher level of discretization yields a more accurate result but also increases simulation times. As stated in Section 6.4.4, the size of the system matrix is proportional to N_t^2. Additionally, the coupled nature of the tether, where the position and velocity of each element depend on all preceding elements, results in a strongly coupled and densely structured system. The symbolic derivation of the model further contributes to this complexity, as the use of trigonometric relationships results in large, nonlinear expressions for each element. All previously presented factors contribute to a rapid increase in simulation time as N_t grows. It is thus essential to choose a value of N_t, which allows for feasible simulations, given the thesis time-frame.

An analysis of simulation times and model size as a function of N_t is presented in Table 8.3 below. Three different time metrics are considered: the write time, which refers to the time required to symbolically derive the system equations and export them to a .txt file; the compile time representing the duration needed for Simulink to compile the system model; and the simulation time which reflects the time taken to run the actual simulation for 10 seconds with an applied wind disturbance. The model size is also presented, which corresponds to the size of the .txt file containing the system of equations, which is not equivalent to the size of the compiled Simulink model.

N_t	**Write (s)**	**Compile (min)**	**Simulate (min)**	**Model size (kB)**
1	7.9	1:20	6:28	192
2	17.9	4:04	8:41	490
3	28.2	12:05	15:32	932
4	42.6	35:08	60:54	1,522
5	75.4	107:22	135:05	2,516

Table 8.3: System simulation timing metrics and model size as a function of N_t.

In the table above, it is shown that all system timing metrics increase exponentially, which is to be expected as previously motivated. The maximum compilation and simulation times are for ($N_t = 5$) and add up to a total of roughly four hours. It is thus shown that simulations with ($N_t \geq 5$) are not feasible given the thesis time-frame and computational resources, and are therefore not to be considered for future simulation. This limitation implies that achieving a high level of tether discretization is not possible, which may have an effect on the models accuracy, especially for

capturing complex dynamics such as tether oscillations and curvature.

Given the limitation on tether discretization, it is essential to assess the impact that this discretization has on the system's states and outputs. To analyze this, the system was simulated for different values of N_t, with a small wind disturbance (Force level 2) added to examine the systems dynamics while ensuring that the system remains stable. The simulations resulted in state and output mean values as well as the root mean square error (RMSE) of $(1 \leq N_t \leq 3)$ relative to the reference model $(N_t = 4)$, where the result is shown in Appendix F. The system outputs considered is the sum of all rotor thrusts $\sum T$, the tether tension F_t and the system power consumption P_{sys}.

The simulation results indicate that the discretization parameter N_t has a negligible effect on the mean values of both system states and outputs, with the hexacopter's x and y positions showing only marginal deviations across varying discretization levels. The RMSE analysis shows that the system outputs start to converge for $(N_t \geq 2)$, while the system states vary. The varying RMSE of system states is to be expected as comparing two different simulations with different N_t values imposes different kinematic and dynamic constraints, which result in different trajectory deviations rather than model inaccuracy. Given this, it is concluded that a value of $(N_t = 3)$ is an appropriate level of discretization for achieving feasible simulation times yet accurate results. Although this level of discretization may not fully capture complex tether dynamics such as oscillations, it represents the most viable compromise between computational feasibility and model accuracy within the constraints of this thesis.

8.2 Stability and performance analysis

The main objective of the stability analysis is to determine the weather conditions under which the tethered hexacopter system remains stable and operational. As discussed in Section 6.1, tether tension plays a critical role in the system's stability. Therefore, this analysis also examines the appropriate levels of tether tension for various weather scenarios and how these requirements affect power consumption. To conduct the analysis, the system is simulated across a range of wind conditions and tether tension levels to evaluate its performance and stability. Each simulation is run for 30 seconds to ensure consistent evaluation across conditions. Since higher tether tension increases stability, the tether-hexacopter system is initially simulated at the lowest thrust level (corresponding to the lowest tension). If the system is stable at this level, it can be assumed to remain stable for all higher tether tension levels under the same wind conditions. It is also reasonable to assume that if the system is unstable at a given tether tension and wind speed, it will remain unstable at higher wind speeds for the same tension level. The wind speeds are defined in accordance to the Beaufort wind scale, which is shown in Appendix E.

Each simulation is classified based on the system's response: Stable (S) indicates that the hexacopter maintains a consistent altitude with minimal variation, and Unstable

(U) describes cases where the altitude or other state variables grow unbounded or exceed operational limits. The system is simulated using the baseline environmental parameters (excluding wind speed), and a set of baseline payload parameters as defined in the table below. The values in the table assume that each payload's CoM is located at the center of its corresponding black box.

Variable	Value	Unit
m_U	5	$[Kg]$
m_L	10	$[Kg]$
z_U	0.295	$[m]$
z_L	0.313	$[m]$

Table 8.4: Baseline payload parameters.

8.2.1 Tether tension controller comparison

In this section, the nonlinear tethered drone system is simulated under both open-loop and closed-loop tether tension control strategies to assess their suitability. By comparing these two configurations, the trade-offs between control simplicity and system performance can be evaluated. The simulations are conducted under baseline environmental and payload conditions, presented in Table 8.1 and 8.4, to determine the system's power consumption and identify its operational limitations in terms of stability and performance. These simulations are carried out across a range of wind conditions defined by the Beaufort wind scale, and with tether tension reference levels specified as percentages of the available thrust above the hexacopter's trim state. The simulations are first conducted using the open-loop tether tension controller, with the results summarized in Table 8.5 below. The parameter $V_{h,mean}$ represents the mean wind speed at the operating height of the hexacopter, which is approximately 70 meters.

Beaufort	$V_{h,mean}$	0%	1%	2.5%	5%	10%	15%	20%	25%
f0	0.61	U	S	S	S	S	S	S	S
f1	1.97	U	S	S	S	S	S	S	S
f2	4.55	U	S	S	S	S	S	S	S
f3	6.82	U	S	S	S	S	S	S	S
f4	10.91	U	S	S	S	S	S	S	S
f5	14.54	U	U	U	U	U	U	S	S
f6–f12	19.99–45.45	U	U	U	U	U	U	U	U

Table 8.5: Stability analysis of the tethered drone system under baseline conditions using open-loop tether tension control.

For the closed-loop solution, it is evident that a certain level of tether tension is required, as previously discussed in Section 6.1. It can also be seen that the system handles mean wind speeds up to roughly 11 m/s (at hexacopter height) with a very low degree of tether tension. The maximum mean wind speeds that the system

can manage is roughly $14,5\ m/s$, which corresponds to 52 km/h, and considering the gust factor K_G, this corresponds to peak wind speeds of up to 77 km/h. For reference, these wind speeds align with level 5 on the Beaufort scale, categorized as a "fresh breeze," which causes small branches to sway (assuming $\alpha = 0.2$). To maintain stability under these conditions, the closed-loop tension controller is set to a reference value of 20% of the maximum tether tension, corresponding to a force of 92 N. If the hexacopter experiences wind speeds beyond this limit, the system becomes unstable and ultimately crashes, regardless of the chosen tether tension reference. Simulation results also indicate that excessively high tether tension is undesirable, as increased tension does not necessarily improve system stability. This is because the tension controller consumes a significant portion of the available thrust to maintain tether tension, thereby limiting the capacity of the altitude and attitude controllers to effectively stabilize the system. As a result, system stability cannot be guaranteed for all tether tension levels above 25%. To compare the open-loop and closed-loop controllers equivalent simulations have been conducted, with the results summarized in Table 8.6 below.

Beaufort	$V_{h,mean}$	**0%**	**1%**	**2.5%**	**5%**	**10%**	**15%**	**20%**	**25%**
f0	0.61	U	S	S	S	S	S	S	S
f1	1.97	U	S	S	S	S	S	S	S
f2	4.55	U	S	S	S	S	S	S	S
f3	6.82	U	U	S	S	S	S	S	S
f4	10.91	U	U	U	S	S	S	S	S
f5	14.54	U	U	U	U	U	U	U	S
f6–f12	19.99–45.45	U	U	U	U	U	U	U	U

Table 8.6: Stability analysis of the tethered drone system under baseline conditions using closed-loop tether tension control.

For the closed–loop solution, the upper wind speed limit the system can withstand is shown to be equivalent to that of the open–loop solution which corresponds to a Beaufort force level of 5, or a mean wind speed of approximately 14.5 m/s at hexacopter height. It is however shown that the closed-loop controller requires a generally higher tether tension level compared to the open–loop solution. An example of this being that the closed–loop solution requires a 25 % tether tension reference to maintain stability under wind force level f5, whereas the closed-loop controller achieves stability with only 20 %. This behavior is expected due to the control redundancy between the closed–loop tether tension controller and the attitude controller. Specifically, when an z-position error occurs, the altitude controller contributes to the tether tension, prompting the tether tension controller to reduce its input. As a result, a higher initial tension reference is necessary to maintain overall system performance. This coupled controller behavior is absent in the open-loop configuration, as the tether tension controller operates independently of the altitude controller in this case. Due to the differing behaviors caused by a given reference in the two controllers, they are compared based on mean system power consumption and the hexacopter's z-position relative to the reference height. The

simulations used for this comparison correspond to the lowest tether tension that maintains stability for each tested mean wind speed. These results are summarized in Table 8.7 below and illustrated as graphs in Appendix G.

Beaufort	$V_{h,\mathbf{mean}}$	**Power (W)**		e_z **(mm)**	
		Open-loop	**Closed-loop**	**Open-loop**	**Closed-loop**
f0	0.61	5599.9	5600.0	0.00	0.00
f1	1.97	5600.0	5601.0	0.01	0.01
f2	4.55	5602.1	5605.4	0.23	0.22
f3	6.82	5611.4	5774.6	1.17	0.82
f4	10.91	5798.8	6076.5	3.54	3.07
f5	14.54	7894.4	8622.4	5.67	8.19

Table 8.7: Mean power consumption and z-position error e_z, for lowest tether tension that maintains system stability for each wind-speed.

The table above shows that the open-loop simulation requires less power to maintain stability across all tested wind speeds. It is also shown that the closed–loop approach achieves lower z-position errors at lower wind speeds, while the open-loop solution yields better position accuracy at the highest wind speed tested. A closer inspection of the position error, shown in Figure G.1, reveals that the closed-loop system generally maintains low errors but is highly sensitive to large disturbances, resulting in sharp error spikes.

As shown in Figure G.2, the closed-loop tether tension closely follows its reference value, as intended. However, since it does not aim to exceed this reference, the system may lose stability for large wind disturbances where greater tether tension levels would be required. For these large wind disturbance conditions the closed-loop tether tension controller and altitude controller exhibit counteracting control objectives, and thus degrading overall system performance. This is due to the closed–loop controller redundancy previously mentioned. This explains why the closed-loop solution can generally maintain stability at lower tether tension reference levels, as the altitude controller is given greater flexibility to compensate for large z-position errors.

The closed-loop controller has therefore demonstrated effective tracking of the tension reference but exhibits poor disturbance rejection and higher power consumption compared to the open-loop solution. While neither controller can manage a wind force level of f6, the open–loop controller has been shown to be an effective control option, due to its low power consumption and ability to reject large wind disturbances. The open–loop controller is therefore selected as the control architecture for future tests involving tether tension control. Nonetheless, potential improvements to the closed-loop controller remain an area for future work, as discussed in more detail in Section 10.7.

8.2.2 Environmental variation

The tethered drone system has previously been tested across a range of wind speeds. However, the influence of the wind profile power law, as defined in Equation (5.18), has not yet been examined. To clarify, the wind profile power law is used to scale wind speed measurements taken at a reference height of 10 meters to the altitude of the hexacopter and tether elements. For a given set of wind speeds at the hexacopter and tether heights, the system behavior remains unchanged, but the corresponding wind speeds measured at 10 meters will vary depending on environmental conditions. The previously conducted simulations, presented in Table 8.5, can thus be used to analyze how the wind shear exponent α affects the wind speeds measured at 10 meters. The results of this analysis are presented in Figure 8.1, where the wind shear exponent α is varied for different mean wind speeds at the hexacopter height.

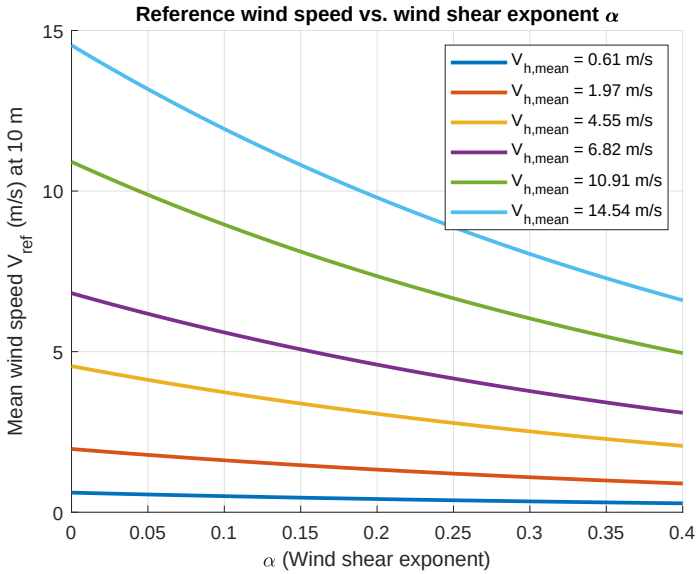

Figure 8.1: Wind shear exponent α effect on wind speeds measured at 10 meters.

The figure above shows that as the wind shear exponent α increases, the wind speed measured at 10 meters required to produce a given wind speed at the hexacopter height decreases. This behavior is expected, as a high wind shear exponent α indicates greater surface roughness or environmental obstruction at 10 meters (as defined in Table 5.1), which causes the wind speed to increase more rapidly with altitude, resulting in higher wind speeds at the hexacopter height.

As shown in Section 8.2.1, the hexacopter remains stable for mean wind speeds up to approximately 14.5 m/s at its operating height. Based on this analysis, the corresponding ground-level mean wind speeds, measured at 10 meters, are indicated by the highest light blue curve in Figure 8.1. These values represent the tested upper limit for which stability has been confirmed for ground level mean wind measurements. Ground-level wind speeds exceeding this curve, under the given environmental conditions, may therefore pose a risk to system stability. This implies that stability cannot be guaranteed for ground-level wind speeds exceeding 12 m/s when

operating in environments characterized by smooth hard ground, lakes, or oceans ($\alpha = 0.1$). Similarly, stability cannot be assured for ground-level wind speeds above 6 m/s in environments such as urban areas with tall buildings ($\alpha = 0.4$).

8.2.3 Payload variation

To evaluate the impact of an alternative payload configuration compared to that listed in Table 8.4, a worst–case scenario is simulated. In terms of hexacopter stability, the system becomes most unstable when the entire payload is concentrated in the top payload black-box. Therefore, the simulation is conducted using the payload parameters specified in Table 8.8 below. For these simulations the baseline environmental parameters are used with the open–loop tether tension controller.

Variable	Value	Unit
m_U	15	$[Kg]$
m_L	0	$[Kg]$
z_U	0.295	$[m]$
z_L	0	$[m]$

Table 8.8: Payload parameters for the worst-case configuration, where the entire payload mass is located in the upper payload black-box.

The tether-drone system is therefore simulated across a range of wind speeds, following the same procedure used in Section 8.2.1. The simulation results show that the worst-case payload configuration does not significantly affect the system's stability. Stability performance remains consistent with that of the baseline payload configuration presented in Table 8.5, indicating that the worst-case configuration can also withstand mean wind speeds of up to approximately 14.5 m/s. Additionally, the system maintains stability with only a 1% tether tension reference at mean wind speeds up to around 11 m/s. A summary of the mean power consumption and hexacopter z-position for the system under baseline and worst-case payload configurations is presented in Table 8.9 below.

Beaufort	$V_{h,\mathbf{mean}}$	Power (W)		e_z (mm)	
		Baseline	Worst–case	Baseline	Worst–case
f0	0.61	5599.9	5599.9	0.00	0.00
f1	1.97	5600.0	5600.0	0.01	0.01
f2	4.55	5602.1	5602.1	0.23	0.23
f3	6.82	5611.4	5611.4	1.17	1.17
f4	10.91	5798.8	5822.7	3.54	4.93
f5	14.54	7894.4	7921.8	5.67	8.89

Table 8.9: Comparison of mean power consumption and z-position error (e_z) for the baseline and worst-case payload configurations across different wind speeds.

The results show that at low wind speeds ($\leq$ 7 m/s), the worst-case payload configuration exhibits minimal differences in power consumption and z-position error compared to the baseline. A slight increase in power consumption and z-position error for the worst–case configuration is however noticeable for higher wind speeds. This behavior is expected, as the primary sources of power consumption ordered by significance are: lift generation, maintaining tether tension, and torque production to resist wind disturbances. The impact of torque production to resist aerodynamic drag forces are thus only prominent for higher wind speeds.

8.3 Safety analysis for rotor failure

Simulations were performed to evaluate the impact of a rotor failure on system stability and performance. These simulations were conducted using the baseline environmental and payload parameters. The hexacopter's control strategy was modified as described in Section 7.6, where the failure scenario results in the loss of yaw control and the intentional deactivation of the motor adjacent to the failed one. It is thus assumed for these simulations, that motor 1 has lost all power and that motor 4 is subsequently turned off. The loss of yaw control could inherently be considered a source of instability, as uncontrolled yaw could introduce a continuous rotational motion that would not be corrected. In this analysis, stability is thus evaluated with respect to pitch, roll, and the positional control of the hexacopter. The results of the simulations are summarized in Table 8.10 below.

Beaufort	$V_{h,mean}$	**0%**	**1%**	**2.5%**	**5%**	**10%**	**15%**	**20%**	**25%**
f0	0.61	U	S	S	S	S	S	S	S
f1	1.97	U	S	S	S	S	S	S	S
f2	4.55	U	S	S	S	S	S	S	S
f3	6.82	U	S	S	S	S	S	S	S
f4	10.91	U	S	S	S	S	S	S	S
f5	14.54	U	U	U	U	U	U	U	U
f6–f12	19.99–45.45	U	U	U	U	U	U	U	U

Table 8.10: Stability analysis of the tethered drone system under baseline conditions using open-loop tether tension control.

The results show that the stability performance of the hexacopter under a rotor failure condition remains comparable to that of the fully functional system. The system is however no longer capable of maintaining stability at a wind speed of 14.5 m/s at the hexacopter's operational altitude. This result is somewhat expected, given the reduction in thrust-to-weight ratio from 2.29:1 to 1.53:1, as discussed in Section 7.6. With the reduced thrust capacity, the system can no longer simultaneously sustain the 20% tether tension reference required for stability, as outlined in Section 8.2.1, and maintain sufficient power for effective attitude control. Stability is thus only guaranteed for 10.9 m/s mean wind speeds at the hexacopter height of 70 meters.

Since the preceding analysis does not account for yaw stability, it is important to examine the yaw behavior observed in the different simulation scenarios. The results show that all stable cases exhibit a total yaw deviation of less than 1°, whereas unstable simulations demonstrate more pronounced yaw motion. There are however limitations in the current model that constrain the ability to fully assess this effect. Specifically, the hexacopter is modeled as a symmetric system, with aerodynamic drag forces applied uniformly across all components. As a result, asymmetric drag, an important factor in yaw instability, is not represented in the simulation. As a result, the precise impact and extent of yaw deviation remain inconclusive within the scope of this analysis. An additional observation is that the mean power consumption in the rotor failure case increases to approximately 7 kW, compared to around 5 kW for the fully operational system. The increase is mainly due to the extra load each remaining rotor has to carry to make up for the failed one, along with reduced efficiency at the higher RPMs needed to generate the sufficient thrust.

8.4 Deployment and retraction time analysis

Since the tether winch mechanism, or any other method for altering the tether element lengths has not been modeled in this thesis, the deployment and retraction times are instead derived by simulating the standalone hexacopter model. This has been performed by adding the total tether weight to the weight of the hexacopter. The weight corresponding to 1% tether tension is also added to the hexacopter body, as this has been shown to be necessary for stability in Section 8.2.1. The hexacopter system is then simulated with baseline payload and environmental parameters which are presented in Table 8.4 and 8.1. It should be noted that the deployment and retraction times do not account for docking procedures, folding of the propeller blades, or any modifications to the propeller guards. They only reflect the time required to move the hexacopter between the base station and its operating altitude.

Deployment and retraction times are calculated for movement between the base station (0 m) and the operating altitude of 70 m. The simulations were conducted without wind disturbances, representing ideal conditions. However, the absence of wind is not expected to significantly affect the results, as tether tension is accounted for in the model. Given this, the deployment time for the system to the height of 70 m, was shown to be 5.1 s. This time accounts for the full range of motion, including both acceleration and deceleration, ensuring the hexacopter comes to a complete stop at the operational altitude. The short deployment time is largely attributed to the system's thrust-to-weight ratio of 2.29:1. This would however be reduced if a greater tether tension force would be applied. The total deployment time may also be influenced by the design of the tether winch and any start-up procedures required at the control station. With that said, the deployment time is still considered to be low.

The derivation and simulation of the retraction time is more complex than the deployment time due to the aerodynamic effects present during descent. While the hexacopter operates in the *normal working state* during hover or ascent, as described in Section 5.1.2, descent causes the hexacopter rotors to transition into one of the alternate flow states. These states are characterized with reduced performance and in the worst-case scenario, can lead to the *windmill brake state*, which implies that the hexacopter is in a free fall. For both safety and optimal performance, the aim is to maintain the rotors within the *vortex ring state* during descent. The performance in this state must be determined empirically and depends on specific design factors such as the geometry of the hexacopter and the presence of propeller guards.

Given the uncertainties involved and the inability to derive this empirical relationship within the scope of this thesis, the retraction performance is assumed to be similar to that of the *normal working state*. This assumption holds under the condition ($-\frac{1}{2} \leq V_c/v_h < 0$), as detailed in Section 5.1.2, which corresponds to a maximum allowable descent velocity of 4.3 m/s. To enforce the velocity constraint and achieve the desired performance, a velocity controller was implemented within the control architecture described in Section 7.4. The simulation of the descent from 70 m to the ground station at 0 m yields a retraction time of 18.5 s. Similar to the deployment time, this retraction time includes deceleration to a complete stop but excludes other factors such as docking procedures or the folding of propellers and propeller guards. This retraction time is considered the upper limit of what qualifies as a safe descent. Shorter retraction times are certainly feasible, as the hexacopter is capable of descending more quickly, but at the cost of propeller efficiency and hexacopter stability. Furthermore, the system is also simulated for the even more conservative velocity constraint of 2 m/s, which yields a retraction time of 37.5 s

9
Conclusion

The results presented in this report are indicative of the drone's performance, as supported by both theoretical derivations and simulation outcomes. The proposed hexacopter system, equipped with foldable propellers, enables safe landing regardless of yaw-angle. The drone manages to achieve a thrust-to-weight ratio exceeding 2:1, while allowing power to be continuously supplied from a ground-based commercial of the shelf (COTS) power supply. An evaluation of the requirement specification, detailed in Appendix H, indicates that all requirements have been fulfilled or have a result that is deemed as inconclusive. Some desires remain unmet due to trade-offs made in favor of more essential design requirements, while others were not evaluated at all. Overall, the system has been successfully designed to accommodate a modular payload capacity exceeding the desired 15 kg, whilst allowing for a flight altitude above 70 m, enabling usage in numerous applications and fields. This performance can be achieved while staying within the dimensional constraints of the base, drone, and payload. Additionally, the design incorporates the essential motor redundancy and additional backup systems, enhancing the system's robustness and operational safety. Furthermore, measures have been implemented to mitigate potential harm to users, in accordance with relevant safety considerations. The resulting system is competitive in terms of cost, and the drone architecture emphasizes low maintenance and operational reliability. The tethered system reliably supplies both the adequate power and high speed, disturbance free, and secure communication to and from the drone, further contributing to the overall robustness and performance of the design. Moreover, the system has proven to offer both fast and reliable means of deployment and retraction, enabling effective operation.

Therefore, it can be stated that the principal objectives of the project, examining the capabilities and limitations of a tethered, payload-carrying drone, have been thoroughly investigated. This was achieved through the systematic formulation and investigation of research questions targeting the drone's various subsystems. The resulting hexacopter design, developed through the iterative concept generation and evaluation phase, was further validated through Euler–Lagrange modeling and system simulations, which proved effective. The simulations also examined the capabilities of the system in order to formulate additional results. The system meets the derived customer needs and fulfills the majority of the formulated requirements, demonstrating the feasibility of the concept and highlighting the advantages a tethered system can offer over traditional untethered drones in a range of applications.

10

Discussion and recommendations

The development and evaluation of the tethered hexacopter system has yielded valuable insights, not only into the technical feasibility of the proposed design, but also into the broader considerations that influence system performance and applicability. This chapter reflects on key design choices made throughout the project, highlights their implications, identifies potential areas for improvement, and proposes recommendations for future development. Where relevant, alternative designs and extended functionality are also discussed, based on the findings and constraints identified throughout the project.

10.1 Hybrid power system

The benefits of a coaxial rotor setup have been considered extensively throughout the subsystem research in Chapter 3. These benefits mainly include higher thrust production within limited drone dimensions. Additionally, the increased level of redundancy for a hexacopter and octocopter, and the introduction of the required redundancy for the quadcopter, is a considerable benefit. The quadcopter features the largest total rotor area (in the majority of the configurations), and the largest rotor diameter among all configurations, rendering it beneficial to adopt if the coaxial setup could be utilized. However, despite these advantages, all coaxial concepts that incorporated foldable propellers were ultimately eliminated due to their power demand exceeding what could be supplied by the power supply, while being incorporated within the base dimensions. Coaxial configurations using non-foldable propellers were also deemed unsuitable, as they failed to achieve the required thrust-to-weight ratio.

Nevertheless, future iterations could revisit coaxial concepts by introducing a hybrid power system. Such a system could utilize the onboard backup battery not only for emergency scenarios as currently, but also to supplement power delivery during high-demand phases, such as takeoff or harsh weather conditions. When the power draw drops below the supply power of the generator, such as during steady hover when the full 2:1 thrust-to-weight ratio is not utilized, the battery could be recharged via the tether. This would be feasible as long as the total power requirement is below half of what could be provided by the power supply. This dynamic power management approach may allow coaxial setups to be viable in future designs without exceeding the base system's power limitations, whilst introducing further functions for the onboard battery. One important drawback of using the backup

battery as a supplemental power source is the risk of, partially or fully, draining it during standard operation. In the event of an emergency, such as a tether failure or loss of power from the base, the battery may not be sufficiently charged to support an untethered return or safe landing. This would compromise one of its primary functions, which is providing redundancy and ensuring operational safety. To mitigate this risk, future designs could exploit the additional thrust margin, that a coaxial concept would bring, to accommodate a larger battery. This would enable temporary power supply during peak loads while still retaining enough capacity and flight time for emergency scenarios.

Furthermore, beyond the potential coaxial setup, the current hexacopter could also benefit from the integration of a hybrid power system. Previously, it was assumed that components other than the motors had a negligible power demand, and were therefore disregarded in the total power requirement. However, in practice, the cumulative power consumption of various onboard subsystems, although individually small, can become significant. This is particularly true given the virtually non-existing margin between the system's total power requirement and the maximum power output of the power supply. Additionally, the power demand of the payload has not been accounted for in the current analysis, which may be considerable depending on the application. For this reason, a similar hybrid power system could be employed, where the backup battery supplies power to non-propulsion systems and potential payloads, during periods where the motors requires the full capacity of the power supply (or when the remaining available power is simply not sufficient for the other systems). Thereafter, when the power demand of the motors decrease, such as during hovering, the battery could be recharged using the surplus power from the power supply. This approach would help ensure that the motors can operate at maximum throttle during short periods of peak demand, while still maintaining the power delivery to other subsystems and potential payloads.

10.2 Interchangeable propellers

The final hexacopter design utilizes three-bladed propellers, primarily due to their higher thrust production and the direct benefits associated with it, such as increased payload capacity and greater flight altitude. Additionally, three-bladed propellers offer secondary advantages, including decreased noise emissions. However, these benefits come at the trade-off of slightly reduced efficiency.

That said, the number of propeller blades does not necessarily need to remain fixed. Depending on the specific application, it could be feasible to implement a system that allows for interchangeable propellers with different blade counts, while using the same motors. Since the motors and propellers are usually selected as matched pairs, this would not always be feasible as it may compromise compatibility. However, in the case of this specific hexacopter, the same motor was used in both the two-bladed and three-bladed propeller analysis. Therefore, two-bladed propellers could, for instance, be employed in scenarios where improved efficiency is prioritized over the maximum thrust, such as operations where refueling is not available, and

maximizing continuous flight time is prioritized. This approach converts the inherent trade-off between thrust production and efficiency into a time-based separation, allowing each to be chosen based on the current need. Moreover, the propeller could also be changed to a propeller design focused specifically on noise reduction, such as the toroidal propeller, if the resulting trade-off in reduction of thrust and efficiency is deemed acceptable. However, this could put even more demand on the motor choice in terms of compatibility. Nonetheless, it could be argued that a slight mismatch would be tolerable, given the already existing performance compromises. In such cases, prioritizing a lighter propeller over a heavier one would be beneficial, as it would reduce the risk of potential damage to components due to an excessive current draw, as discussed in Section 3.2.2. This adaptability in propellers would enable greater flexibility across varied use cases, allowing users to optimize the system slightly based on application-specific requirements.

10.3 INS for precision applications

The current hexacopter is equipped with inertial measurement units (IMUs) that provide acceleration and angular velocity data used for basic stabilization and control. While this is sufficient for most applications, certain use cases or payloads may require more precise orientation or motion tracking than the IMU alone can offer. In such cases, an inertial navigation system (INS), which fuses IMU data over time to estimate position and orientation with greater accuracy [125], may be necessary. However, an INS would contribute to the total weight of the hexacopter significantly, and also take up a lot of physical space. For this reason, it could be argued that the implementation of the INS could be considered merely a modular addition, integrated as part of the payload when needed. This would help minimizing the system weight, size, and complexity when the INS is not required, while still allowing for improved accuracy when demanded by a certain payload or application.

10.4 Features disregarded due to complexity

Several design features were ultimately excluded from the current hexacopter system due to increased mechanical complexity, and challenges relating to modeling. However, these features are promising for future development and could offer significant performance benefits if properly implemented.

One such feature is the use of foldable arms. Incorporating foldable arms introduces several previously discussed challenges, such as precise structural alignment during deployment, increased mechanical complexity and wear, longer retraction and deployment times, and potentially reduced reliability. Moreover, when deployed, the increased footprint in the air may affect maneuverability since the moment of inertia would increase. It would also place greater demands on control accuracy, especially for landing at constrained yaw angles. If these challenges were addressed, foldable arms would allow for larger propellers, beyond the fixed constraints of the base. This could significantly improve thrust production, enhancing payload capacity and

broadening the drone's range of applications. Foldable arms would also support increased arm lengths for better flight stability, and could contribute to improved transportability and compact storage. A potential future solution could involve a landing platform that automates the folding and storage process post-landing, helping mitigate some of these challenges and ensuring a secure transition between flight and storage.

Additionally, the use of counter-rotating propellers, or unevenly lengthened arms, represents other opportunities for performance optimization. These configurations may yield gains in overall thrust production, without exceeding base dimensions, though they would likewise increase design and control complexity. Further exploring these design alternatives in future work could lead to a more high-performing tethered drone system, especially in scenarios where enhanced lift capability is a priority.

10.5 Hexacopter model accuracy

To begin evaluating the accuracy of the hexacopter model, it is important to note that all primary governing effects have been incorporated. These include gyroscopic precession, actuator lag dynamics, inertial effects of payloads, and aerodynamic forces such as lift and drag due to relative fluid flow. It should also be noted that the hexacopter parameters were conservatively estimated, implying that the actual system performance is likely to exceed the predicted performance by the model. The hexacopter model assumes laminar flow however, which introduces the main source of uncertainty, as turbulent effects are likely to occur around the hexacopter body under high wind conditions. To address this, it would be beneficial to perform CFD simulations or conduct experimental flight tests across a range of wind conditions. This is essential because the aerodynamic effects of wind on the hexacopter are highly dependent on its geometry, and there is no literature that directly supports or validates this unique hexacopter design. Experimental testing or CFD simulations would provide a more accurate understanding of how wind disturbances influence the hexacopter through aerodynamic forces such as drag and lift.

Furthermore, the propellers are assumed to operate in the *normal working state*. This assumption is accurate for the hexacopter's typical operational use, such as when hovering in place. During descent however, the assumption becomes less valid. To maintain its applicability, an upper limit on the descent speed is imposed, as detailed in Section 5.1.2. To reduce the uncertainty associated with this assumption, it would again be beneficial to perform experimental studies or CFD simulations. These analyses would help to better characterize the hexacopter's aerodynamic performance during descent and determine a more accurate maximum descent speed. Additionally, the investigations would be necessary to determine how the propeller guards effects rotor performance in the different rotor flow states.

10.6 Tether model accuracy

As detailed in Section 6.2, there are several different approaches proposed in the litterature to model a tether/cable. The chosen method was to implement an LMM, which was shown to to be computationally demanding due to the strong coupling and nonlinear behavior of the tether elements. Considerable effort was made to reduce this computational load during the thesis. Given the imposed constraints on time and computational resources however, the tether discretization was limited to ($N_t = 3$), which is considered to be a low value. As a consequence, additional oversight was required during simulation to ensure that tether tension remained non-negative, as negative tension would correspond to compressive forces within the tether, which are physically unrealistic given that cables cannot support compression. Furthermore, certain higher-order effects such as tether oscillations may not be fully captured or accurately represented by the LMM. These effects are however expected to be minimal in a well-functioning system, where maintaining tether tension is a control objective that keeps the tether nearly straight. Nonetheless, they may become more pronounced in near-failure scenarios or under extreme disturbances.

Despite the previously mentioned modeling uncertainties, it should be noted that the LMM sufficiently captures the primary forces acting on the hexacopter, including the constraining effects of the tether and the load distribution resulting from aerodynamic forces along the tether. Nevertheless, it may be valuable to explore alternative modeling approaches, such as FEM, which is based on element displacements and can incorporate more detailed material properties. Another promising approach, proposed by Professor Emanuel Dean from Chalmers, involves using a neural network to model the tether. This method could offer a highly effective way to capture complex high-order dynamics and material behavior, but it would require empirical data of the coupled tether-drone system. While the neural network would not provide a visual representation of tether motion during simulation, it would accurately predict the forces exerted on the hexacopter which is ultimately most relevant for control and system behavior.

10.7 Tether tension control

It was shown from the system simulation that the open–loop tether tension control was a better approach compared to the closed–loop approach. The open-loop controller maintained stability while achieving lower power consumption and reduced altitude error, particularly under high wind conditions. The limitations of the closed-loop controller arise from the interaction between the tether tension and altitude controllers. In high wind scenarios, the closed-loop tether tension controller can oppose the actions of the altitude controller, leading to undesired control behavior. As a result, a generally higher tether tension level is required to compensate this coupled behavior, which reduces overall system efficiency. In contrast, the open-loop approach applies a constant, independent tether tension force that contributes directly to the total upward thrust without interfering with altitude control.

While the results might initially imply that a closed-loop tether tension control strategy is ineffective, this is more reflective of the current implementation rather than a fundamental limitation of the approach itself. In fact, evidence shows that the closed-loop controller maintains more consistent tether tension levels (see Appendix G), which is advantageous for minimizing component wear and ensuring system stability. The main performance issues arise from the previously discussed coupling between the altitude and tension controllers, as well as the use of a constant tension reference. Addressing either of these issues, through decoupling strategies or adaptive reference generation, could lead to significant performance improvements in the closed-loop control approach.

The coupling between altitude and tether tension control can be resolved by introducing an additional control input, thus making the system fully actuated. This could appropriately be achieved by implementing a tether winch actuator model in the coupled tether–drone model. This would allow the winch to control hexacopter altitude while the hexacopter's total upward thrust controls tether tension, or vice versa. To address the limitations of a constant tether tension reference, a more adaptive approach involves making the reference dependent on the magnitude of wind disturbances. This can be implemented via an open-loop feedforward controller that determines the reference tension as a function of measured wind speed. The computed reference is then supplied to the existing closed-loop tension controller. There are several ways to measure or estimate the wind speeds, where four proposed options are outlined in the list below.

- The system operator can estimate wind speeds at ground level using the Beaufort wind scale.
- Measurements can be obtained from live meteorological data.
- Wind speeds can be measured directly at the ground station.
- Wind speeds can be measured onboard the hexacopter.

Bibliography

[1] Elistair. "Khronos". (n.d.), [Online]. Available: https://elistair.com/solutions/tethered-dronebox-khronos/. (accessed: 12.05.2025).

[2] M. N. Marques, S. A. Magalhães, F. N. Dos Santos, and H. S. Mendonça, "Tethered unmanned aerial vehicles—-a systematic review", *Robotics*, vol. 12, no. 4, 2023, ISSN: 2218-6581. DOI: 10.3390/robotics12040117. [Online]. Available: https://www.mdpi.com/2218-6581/12/4/117.

[3] A. Saif, K. Dimyati, K. A. Noordin, N. S. M. Shah, S. H. Alsamhi, and Q. Abdullah, "Energy-efficient tethered uav deployment in b5g for smart environments and disaster recovery", in *2021 1st International Conference on Emerging Smart Technologies and Applications (eSmarTA)*, 2021, pp. 1–5. DOI: 10.1109/eSmarTA52612.2021.9515754.

[4] M. Mozaffari, W. Saad, M. Bennis, Y.-H. Nam, and M. Debbah, "A tutorial on uavs for wireless networks: Applications, challenges, and open problems", *IEEE Communications Surveys & Tutorials*, vol. 21, no. 3, pp. 2334–2360, 2019. DOI: 10.1109/COMST.2019.2902862.

[5] A. Fotouhi, H. Qiang, M. Ding, *et al.*, "Survey on uav cellular communications: Practical aspects, standardization advancements, regulation, and security challenges", *IEEE Communications Surveys & Tutorials*, vol. 21, no. 4, pp. 3417–3442, 2019. DOI: 10.1109/COMST.2019.2906228.

[6] M. A. Kishk, A. Bader, and M. Alouini, "Capacity and coverage enhancement using long-endurance tethered airborne base stations", *CoRR*, vol. abs/1906.11559, 2019. arXiv: 1906.11559. [Online]. Available: http://arxiv.org/abs/1906.11559.

[7] O. Bushnaq, M. Kishk, A. Çelik, M.-S. Alouini, and T. Al-Naffouri, *Optimal deployment of tethered drones for maximum cellular coverage in user clusters*, Nov. 2020. DOI: 10.48550/arXiv.2003.00713.

[8] Elistair. "Event security: Using drones for public surveillance". (n.d.), [Online]. Available: https://elistair.com/event-security/. (accessed: 4.02.2025).

[9] Elistair. "Monitoring traffic: Managing crowds with drones". (n.d.), [Online]. Available: https://elistair.com/monitoring-traffic-drone/. (accessed: 4.02.2025).

[10] Advexure. “Event security: Using drones for public surveillance”. (2024), [Online]. Available: https://advexure.com/blogs/news/continuous-overwatch-tethered-drones-for-extended-public-safety-operations. (accessed: 4.02.2025).

[11] sea-machines. “Event security: Using drones for public surveillance”. (2024), [Online]. Available: https://sea-machines.com/combining-small-unmanned-surface-vehicles-susv-and-tethered-drones/. (accessed: 4.02.2025).

[12] S. Pugh, “Total design: Integrated methods for successful product engineering”, *Addison-Wesley*, 1991.

[13] A. Saxena. “Essential drone parts: A comprehensive guide”. (2024), [Online]. Available: https://evelta.com/blog/essential-drone-parts-a-comprehensive-guide/?srsltid=AfmBOori3Q3KCSYRbcL9WcPz1CpZr5wNV5f1ncn5kaWk0gljSzbtCjL0. (accessed: 7.02.2025).

[14] UMILES. “What are the parts of a drone? full list”. (2023), [Online]. Available: https://umilesgroup.com/en/what-are-the-parts-of-a-drone-full-list/. (accessed: 7.02.2025).

[15] Dronefly. “Anatomy of a drone - what’s inside a dji phantom drone”. (n.d.), [Online]. Available: https://www.dronefly.com/pages/anatomy-of-a-drone-whats-inside-a-dji-phantom-drone?srsltid=AfmBOoo5m8hWxNUBxCGF8ytYnGoWimdTpwQS5RwU_VT07cPzoJ9osM3k. (accessed: 7.02.2025).

[16] W. Walendziuk, D. Oldziej, and M. Slowik, “Power supply system analysis for tethered drones application”, in *2020 International Conference Mechatronic Systems and Materials (MSM)*, 2020, pp. 1–6. DOI: 10.1109/MSM49833.2020.9202196.

[17] J. Malmqvist, “Improved function-means trees by inclusion of design history information”, *Journal of Engineering Design, Vol. 8, No. 2*, 1997.

[18] Grepow. “Quadcopter vs multirotor vs hexacopter vs octocopter: What’s the difference?” (2024), [Online]. Available: https://www.grepow.com/blog/quadcopter-vs-multirotor-vs-hexacopter-vs-octocopter.html. (accessed: 11.02.2025).

[19] A. Pennington. “Why octocopters are better than quadcopters”. (2015), [Online]. Available: https://www.thebroadcastbridge.com/content/entry/1180/why-octocopters-are-better-than-quadcopters. (accessed: 14.02.2025).

[20] Pilot Institute. “Is a drone with more rotors better?” (2021), [Online]. Available: https://pilotinstitute.com/more-rotors-better/. (accessed: 11.02.2025).

[21] K. Singh, “Modelling and controls of a hexacopter”, M.S. thesis, Texas A&M University - Kingsville, 2018.

[22] I. P. Graziano, "The design, modelling and control of an autonomous tethered multirotor UAV", M.S. thesis, Stellenbosch University, 2017.

[23] J. Schmitt. "The best coaxial design for drones 2025". (2025), [Online]. Available: https://www.tytorobotics.com/blogs/articles/best-coaxial-rotor-design-for-uavs?srsltid=AfmBOorCAVGzUI4Bh2x9cC9SDTXarwGsQHz-NmTbt718wUuPQVEyuQQn. (accessed: 11.02.2025).

[24] A. stack exchange, *How much distance do i need between quadcopter propellers to avoid issues?*, Online forum post, 2017. [Online]. Available: https://aviation.stackexchange.com/questions/22269/how-much-distance-do-i-need-between-quadcopter-propellers-to-avoid-issues, (accessed: 15.06.2025).

[25] pravesh736, *Effect of gap between to propellers in multi rotor*, Online forum post, 2013. [Online]. Available: https://www.rcindia.org/multirotors/effect-of-gap-between-to-propellers-in-multi-rotor/, (accessed: 15.06.2025).

[26] I. Penkov and D. Aleksandrov, "Analysis and study of the influence of the geometrical parameters of mini unmanned quad-rotor helicopters to optimise energy saving", *INTERNATIONAL JOURNAL OF AUTOMOTIVE AND MECHANICAL ENGINEERING*, vol. 14, pp. 4730–4746, Dec. 2017. DOI: 10.15282/ijame.14.4.2017.11.0372.

[27] H. Albedran and J. Károly, "Evolutionary control system of asymmetric quadcopter", *International Review of Applied Sciences and Engineering*, vol. 14, pp. 374–382, Mar. 2023. DOI: https://doi.org/10.1556/1848.2022.00584.

[28] J. Lim. "Non-symmetric non-planar quadrotor". (2015), [Online]. Available: https://404warehouse.net/2015/09/22/symmetric-non-planar-quadrotor/. (accessed: 20.02.2025).

[29] R. Bennett, *Do mounting motors at different height each other has any impact on performances?*, Online forum post, 2022. [Online]. Available: https://drones.stackexchange.com/questions/2488/do-mounting-motors-at-different-height-each-other-has-any-impact-on-performances, (accessed: 15.06.2025).

[30] C. Umar and M. F. Zulkafli, "Distance and rotational speed analysis of coaxial rotors for uthm c-drone", *Progress in Aerospace and Aviation Technology*, vol. 1, Dec. 2021. DOI: 10.30880/paat.2021.01.01.006.

[31] A. Bondyra, S. Gardecki, P. Gąsior, and W. Giernacki, "Performance of coaxial propulsion in design of multi-rotor uavs", in Mar. 2016, vol. 440, pp. 523–531, ISBN: Print ISBN: 978-3-319-29356-1, Online ISBN: 978-3-319-29357-8. DOI: 10.1007/978-3-319-29357-8_46.

[32] M. Brazinskas, S. D. Prior, and J. P. Scanlan, "An empirical study of overlapping rotor interference for a small unmanned aircraft propulsion system", *Aerospace*, vol. 3, no. 4, 2016, ISSN: 2226-4310. DOI: 10.3390/aerospace3040032. [Online]. Available: https://www.mdpi.com/2226-4310/3/4/32.

[33] M. Simões, "Optimizing a coaxial propulsion system to a quadcopter cédric", 2014. [Online]. Available: https://api.semanticscholar.org/CorpusID:10956021.

[34] M. Nahon, I. Sharf, A. Harmat, *et al.*, "Ground effect experiments and model validation with draganflyer x8 rotorcraft", May 2014. DOI: 10.1109/ICUAS.2014.6842370.

[35] OscarLiang. "Brushed motors vs brushless motors for quadcopter". (2024), [Online]. Available: https://oscarliang.com/brushed-vs-brushless-motor/. (accessed: 26.02.2025).

[36] Grepow. "An in-depth guide to drone motors". (2024), [Online]. Available: https://www.grepow.com/blog/an-in-depth-guide-to-drone-motors.html. (accessed: 26.02.2025).

[37] JOUAV. "The ultimate guide to heavy lift drone motors". (2024), [Online]. Available: https://www.jouav.com/blog/heavy-lift-drone-motors.html. (accessed: 25.02.2025).

[38] T. Robotics. "Comparing AC vs DC vs BLDC motor efficiency". (n.d.), [Online]. Available: https://www.unmannedsystemstechnology.com/feature/comparing-ac-vs-dc-vs-bldc-motor-efficiency/?srsltid=AfmBOoqP8lV_6GRLATalfKJGlQG1_U-KvFS_3mGEV6PfVUD9zWh7ZgaF#ruffruff-table-of-contents-item-1. (accessed: 26.02.2025).

[39] Ryan. "Brushless inrunner vs outrunner motor?" (2018), [Online]. Available: https://www.radiocontrolinfo.com/brushless-inrunner-vs-outrunner-motor/. (accessed: 26.02.2025).

[40] OscarLiang. "How to choose fpv drone motors – considerations and best motor recommendations". (2024), [Online]. Available: https://oscarliang.com/motors/#Brushless-vs-Brushed-Motors. (accessed: 26.02.2025).

[41] Lammotor. "11 common drone motor parameters". (2025), [Online]. Available: https://lammotor.com/11-drone-motor-parameters/. (accessed: 27.02.2025).

[42] M. Ball. "Cr flight develops revolutionary heavy-lift motors for uavs". (2020), [Online]. Available: https://www.unmannedsystemstechnology.com/2020/04/cr-flight-develops-revolutionary-heavy-lift-motors-for-uavs/. (accessed: 28.02.2025).

[43] crflight. "Evector from cr flight". (2019), [Online]. Available: https://www.crflight.com/. (accessed: 28.02.2025).

[44] crflight. "Operational thrust comparison". (n.d.), [Online]. Available: https://www.crflight.com/evector-2/. (accessed: 28.02.2025).

[45] expouav. “Cr flight”. (2019), [Online]. Available: https://www.expouav.com/exhibitor-news/cr-flight/. (accessed: 28.02.2025).

[46] crflight. “Evp-10 electric propulsion system with evector technology”. (n.d.), [Online]. Available: https://www.crflight.com/evp10/. (accessed: 05.04.2025).

[47] M. J. Andrew, “Coaxial contrarotating twin rotor aerodynamics”, Ph.D. dissertation, University of Southampton, 1981.

[48] Grepow. “How to choose the right drone propeller?” (2024), [Online]. Available: https://www.grepow.com/blog/how-to-choose-the-right-drone-propeller.html. (accessed: 10.02.2025).

[49] Gisdrones. “2 blade vs 3 blade prop quadcopter: Which is good for inspection drone?” (2022), [Online]. Available: https://gisdrones.com/2-blade-vs-3-blade-prop-quadcopter-which-is-good-for-inspection-drone/. (accessed: 31.03.2025).

[50] KDEDirect. “Everything you need to know about kde direct folding propellers”. (2018), [Online]. Available: https://www.kdedirect.com/blogs/news/kde-direct-folding-propellers. (accessed: 10.02.2025).

[51] K. Baskaran, N. S. Jamaluddin, A. Celik, D. Rezgui, and M. Azarpeyvand, “Effects of number of blades on propeller noise”, *Journal of Sound and Vibration*, vol. 572, p. 118 176, 2024. [Online]. Available: https://www.sciencedirect.com/science/article/pii/S0022460X23006259.

[52] Robocraze. “All about drone propellers”. (n.d.), [Online]. Available: https://robocraze.com/blogs/post/all-about-drone-propellers. (accessed: 31.03.2025).

[53] Krossblade. “Disc loading and hover efficiency”. (n.d.), [Online]. Available: https://www.krossblade.com/disc-loading-and-hover-efficiency. (accessed: 10.02.2025).

[54] OscarLiang. “How to choose the best propellers for your fpv drone: Beginner’s guide and recommendations”. (n.d.), [Online]. Available: https://oscarliang.com/propellers/. (accessed: 31.03.2025).

[55] V. Bertram, “Chapter 2 - propellers”, in *Practical Ship Hydrodynamics (Second Edition)*, V. Bertram, Ed., Second Edition, Oxford: Butterworth-Heinemann, 2012, pp. 41–72, ISBN: 978-0-08-097150-6. [Online]. Available: https://www.sciencedirect.com/science/article/pii/B9780080971506100028.

[56] Aerodynamics4studens. “Blade element theory for propellers”. (n.d.), [Online]. Available: https://www.aerodynamics4students.com/propulsion/blade-element-propeller-theory.php. (accessed: 11.04.2025).

[57] M. K. Rwigema, “Propeller blade element momentum theory with vortex wake deflection”, *27th international congress of the aeronautical sciences*, 2010.

[58] P. Z. S. Spakovszky, *Thermodynamics and propulsion, 11.7 performance of propellers*, https://web.mit.edu/course/16/16.unified/www/SPRING/thermodynamics/notes/node86.html, Lecture Notes, Massachusetts Institute of Technology, 1993.

[59] M. L. Laboratory, *Toroidal propeller*, Innovation Highlight, Technology in Support of National Security, Lincoln Laboratory, Massachusetts Institute of Technology, Available at: https://www.ll.mit.edu/sites/default/files/other/doc/2022-09/TVO_Technology_Highlight_41_Toroidal_Propeller.pdf, 2022.

[60] OscarLiang. "Toroidal propellers: A quieter future for fpv drones?" (n.d.), [Online]. Available: https://oscarliang.com/toroidal-propellers/. (accessed: 14.04.2025).

[61] H. Kastelloo. "How do the zipline silent propellers work?" (2023), [Online]. Available: https://dronexl.co/2023/05/04/how-do-zipline-silent-propellers-work/. (accessed: 14.04.2025).

[62] T. Y. Kim, "Reduction of tonal propeller noise by means of uneven blade spacing", M.S. thesis, University of California, 2016.

[63] yangjulia. "Exploring different materials for drone propellers and selecting the right blades for your drone motor". (n.d.), [Online]. Available: https://store.mad-motor.com/blogs/learn/exploring-different-materials-for-drone-propellers-and-selecting-the-right-blades-for-your-drone-%20motor#:~:text=Plastic%20Composite%3A%20Plastic%20composite%20propeller%20blades%2C%20typically%20made,making%20them%20suitable%20for%20beginner%20and%20recreational%20drones.. (accessed: 20.04.2025).

[64] O. Liang. "Lookup table: Motor & prop sizes, kv, battery cell count, and weight for fpv drone builds". (n.d.), [Online]. Available: https://oscarliang.com/table-prop-motor-lipo-weight/. (accessed: 21.04.2025).

[65] GORE, *Understanding and maximizing tethered drone cable performance in harsh operating conditions*, 2019. [Online]. Available: https://www.gore.com/system/files/2021-04/GORE-Tethered-Drone-Cables-WhitePaper_031319.pdf.

[66] [Online]. Available: https://rosefinch-technology.en.made-in-china.com/product/BAKpYVOdLUkM/China-Drone-Accessories-12000W-Multifunctional-Drone-Tether-Power-Station.html, (accessed: 24.04.2025).

[67] [Online]. Available: https://rosefinch-technology.en.made-in-china.com/product/vORAFZwckLTr/China-Multifunctional-Tethered-Uav-Unmanned-Aerial-Vehicle-Drone-Tether-Power-Station.html, (accessed: 24.04.2025).

[68] P. wire. “Wires in aerospace and aviation: A comprehensive study”. (2024), [Online]. Available: https://pelicanwire.com/2024/11/wires-in-aerospace-and-aviation-a-comprehensive-study/.

[69] U. systems and L. solutions. “Understanding the power and data capabilities of tethered drones”. (n.d.), [Online]. Available: https://www.unmannedsas.com/post/understanding-the-power-and-data-capabilities-of-tethered-drones. (accessed: 24.04.2025).

[70] FS. “The advantages and disadvantages of optical fiber”. (n.d.), [Online]. Available: https://www.fs.com/blog/the-advantages-and-disadvantages-of-optical-fiber-2721.html. (accessed: 24.04.2025).

[71] MOOG. [Online]. Available: https://www.moog.com/products/fiber-optic-rotary-joints/hybrid-forj.html, (accessed: 25.04.2025).

[72] Simscale. “What is joule heating?” (n.d.), [Online]. Available: https://www.simscale.com/docs/simwiki/heat-transfer-thermal-analysis/what-is-joule-heating/. (accessed: 22.04.2025).

[73] drone-payload. [Online]. Available: https://www.drone-payload.com/product/heavy-lift-high-power-optical-fiber-tethered-drone-system/, (accessed: 24.04.2025).

[74] *Starkströmsförordning (2009:22)*, 2009. [Online]. Available: https://www.riksdagen.se/sv/dokument-lagar/dokument/svensk-forfattningssamling/lag-200922-om-fardplaner-for-fornybar-energi_sfs-2009-22.

[75] Winco. [Online]. Available: https://apelectric.com/winco-wl22000ve-19000w-electric-start-portable-generator-with-anderson-plug/, (accessed: 29.04.2025).

[76] DuroMax. [Online]. Available: https://www.amazon.com/DuroMax-XP12000EH-000-Watt-Portable-Generator/dp/B01M0N8256?th=1, (accessed: 29.04.2025).

[77] O. Liang. “Understanding escs for fpv drones: How to choose the best electronic speed controller”. (), [Online]. Available: https://oscarliang.com/esc/#How-to-Choose-ESC. (accessed: 29.04.2025).

[78] O. Liang. “Flight controller explained: How to choose the best fc for fpv drone”. (n.d.), [Online]. Available: https://oscarliang.com/flight-controller/#How-to-Choose. (accessed: 29.04.2025).

[79] DJI. [Online]. Available: https://store.dji.com/product/dji-mavic-3-propeller-guard?set_region=US&from=site-nav&_gl=1%2A18xnuf8%2A_up%2AMQ..%2A_ga%2ANjQwMzEwMDE0LjE3NDU5MzYzMjU.%2A_ga_HXRDE344GS%2AMTc0NTkzNjMyNS4xLjAuMTc0NTkzNjMyNS4wLjAuMA..&vid=110061, (accessed: 29.04.2025).

[80] T. said energy. “Dc-dc power converters: Efficiency calculations?” (n.d.), [Online]. Available: https://thundersaidenergy.com/downloads/dc-dc-power-converters-efficiency-calculations/. (accessed: 29.04.2025).

[81] O. Kreutzer, M. Billmann, and M. Maerz, *A passively cooled 15 kw, 800 v dc-dc converter with a peak efficiency of 99.7%*, https://publica.fraunhofer.de/handle/publica/401967, (accessed: 29.04.2025), 2017.

[82] G. Roos. "Dc/dc converters deliver higher efficiency and greater flexibility". (n.d.), [Online]. Available: https://www.electronicproducts.com/dc-dc-converters-deliver-higher-efficiency-and-greater-flexibility/. (accessed: 29.04.2025).

[83] RJXHOBBY. [Online]. Available: https://rcdrone.top/products/rjx-1300mm-hexacopter-frame?currency=USD&variant=46196354515168&utm_source=google&utm_medium=cpc&utm_campaign=Google%20Shopping&stkn=677f40c1dee9&gad_source=1&gclid=EAIaIQobChMI6OG81Mj_iwMVyhiiAx1wiDrPEAQYASABEgIKN_D_BwE, (accessed: 2.05.2025).

[84] HobbyDrone. [Online]. Available: https://www.hobbydrone.cz/en/battery-pilotix-lipo-6s-16000mah-60c-xt90/, (accessed: 2.05.2025).

[85] KDEDirect. [Online]. Available: https://www.kdedirect.com/collections/uas-multi-rotor-brushless-motors/products/kde8218xf-120, (accessed: 7.05.2025).

[86] KDEDirect. [Online]. Available: https://www.kdedirect.com/collections/multi-rotor-propeller-blades/products/kde-cf245-tp, (accessed: 7.05.2025).

[87] KDEDirect. [Online]. Available: https://www.kdedirect.com/collections/multi-rotor-propeller-blade-adapters/products/kde-tpahl-ml, (accessed: 7.05.2025).

[88] KDEDirect. [Online]. Available: https://www.kdedirect.com/collections/uas-multi-rotor-electronics/products/kde-uas95hvc, (accessed: 7.05.2025).

[89] Unmannedtechshop. [Online]. Available: https://www.unmannedtechshop.co.uk/product/matek-h7a3-slim-flight-controller/, (accessed: 7.05.2025).

[90] Freefly. [Online]. Available: https://store.freeflysystems.com/products/alta-x-pilot-pro-essentials-kit, (accessed: 8.05.2025).

[91] KDEDirecti. "Support center - faq - electronics". (n.d.), [Online]. Available: https://www.kdedirect.com/pages/support-center-faq-electronics?srsltid=AfmBOorZBq0YlfF6WHb_BVf-qKd_Z2bCMcjU7GCpWeX63ehSFJ_Cf4mj&utm_source=chatgpt.com. (accessed: 8.05.2025).

[92] P. Zipfel, "Tensor flight dynamics", Jan. 2012.

[93] C. Venkatesan, *Fundamentals of Helicopter Dynamics*. Boca Raton, FL: CRC Press, Taylor & Francis Group, 2014, eBook - PDF, ISBN: 978-1-4665-6635-4.

[94] J. Leishman, "Development of the autogiro: A technical perspective", *Journal of Aircraft - J AIRCRAFT*, vol. 41, pp. 765–781, Jul. 2004. DOI: 10.2514/1.1205.

[95] N. Aghbaloua, A. Charkib, S. Elazzouzi, and K. Reklaoui, "A probabilistic assessment approach for wind turbine-site matching", *Electrical Power and Energy Systems*, vol. 103, pp. 497–510, 2018.

[96] MathWorks, *Dryden wind turbulence model (continuous)*, https://se.mathworks.com/help/aeroblks/drydenwindturbulencemodelcontinuous.html, Accessed: 2025-04-20, 2025. [Online]. Available: https://se.mathworks.com/help/aeroblks/drydenwindturbulencemodelcontinuous.html.

[97] R. Stull, *Practical Meteorology*. University of British Columbia, 2025, Compiled on 03/26/2025. [Online]. Available: https://www.libretexts.org/.

[98] X. Li, D. Hui, X. Lai, and T. Yan, "Power quality control in wind/fuel cell/battery/hydrogen electrolyzer hybrid micro-grid power system", in Apr. 2011, ISBN: 978-953-307-236-4. DOI: 10.5772/14559.

[99] D. of Defense, *Mil-std-810g: Environmental engineering considerations and laboratory tests*, NOT MEASUREMENT SENSITIVE, AMSC N/A AREA ENVR, Oct. 2008. [Online]. Available: https://www.milstandards.org.

[100] North Atlantic Treaty Organization (NATO), *STANAG 2895: Extreme Climatic Conditions and Derived Conditions for Use in Defining Design/Test Criteria for NATO Forces Materiel*, Standardization Agreement (Edition 1), MAS/048-MMS/2895, Promulgated by A. J. Melo Correia, Major-General, POAF, Chairman, MAS, Brussels, Belgium: Military Agency for Standardization (MAS), Feb. 1990.

[101] National Weather Service, *Beaufort wind scale*, Accessed: 2025-04-20, 2024. [Online]. Available: https://www.weather.gov/mfl/beaufort.

[102] D. T. Greenwood, *Advanced Dynamics*. Cambridge University Press, 2003.

[103] P. Pounds, R. Mahony, and P. Corke, "Modelling and control of a large quadrotor robot", *Control Engineering Practice*, vol. 18, no. 7, pp. 691–699, 2010. DOI: 10.1016/j.conengprac.2010.01.010. [Online]. Available: https://doi.org/10.1016/j.conengprac.2010.01.010.

[104] A. Alaimo, V. Artale, C. Milazzo, A. Ricciardello, and L. Trefiletti, "Mathematical modeling and control of a hexacopter", in *2013 International Conference on Unmanned Aircraft Systems (ICUAS)*, 2013, pp. 1043–1050. DOI: 10.1109/ICUAS.2013.6564793.

[105] H. M. Kandeel, E. A. Abdelmaksod, and A. O. Elnady, "Modeling and control of x-shape quadcopter", *IOSR Journal of Mechanical and Civil Engineering (IOSR-JMCE)*, vol. 19, no. 1, pp. 46–57, 2022. DOI: 10.9790/1684-1901034657. [Online]. Available: https://www.researchgate.net/publication/358635499_Modeling_and_Control_of_X-Shape_Quadcopter.

[106] Y.-M. Kwon, J.-S. Park, S. Y. Wie, H. J. Kang, and D.-H. Kim, "Aeromechanics analyses of a modern lift-offset coaxial rotor in high-speed forward flight", *International Journal of Aeronautical and Space Sciences*, vol. 22, pp. 338–351, Apr. 2021. DOI: 10.1007/s42405-020-00300-8.

[107] nucelar-power. "Critical reynolds number". (n.d.), [Online]. Available: https://www.nuclear-power.com/nuclear-engineering/fluid-dynamics/reynolds-number/critical-reynolds-number/. (accessed: 7.05.2025).

[108] R. D. Blevins, *Applied Fluid Dynamics Handbook*. Krieger Pub Co, 2003.

[109] P. Williams, "Cable Modeling Approximations for Rapid Simulation", en, *Journal of Guidance, Control, and Dynamics*, vol. 40, no. 7, pp. 1779–1788, Jul. 2017, ISSN: 0731-5090, 1533-3884. [Online]. Available: https://arc.aiaa.org/doi/10.2514/1.G002354 (visited on 03/03/2025).

[110] B. Buckham, F. R. Driscoll, and M. Nahon, "Development of a finite element cable model for use in low-tension dynamics simulation", *Journal of Applied Mechanics*, vol. 71, no. 4, pp. 476–485, Sep. 2004, ISSN: 0021-8936. DOI: 10.1115/1.1755691. eprint: https://asmedigitalcollection.asme.org/appliedmechanics/article-pdf/71/4/476/5471132/476_1.pdf. [Online]. Available: https://doi.org/10.1115/1.1755691.

[111] S. C. P. Gomes *et al.*, "Dynamic modeling of cables with external forces applied to the terminal load", *Journal of the Brazilian Society of Mechanical Sciences and Engineering*, vol. 42, no. 9, p. 472, Aug. 2020. DOI: 10.1007/s40430-020-02559-0. [Online]. Available: https://doi.org/10.1007/s40430-020-02559-0.

[112] Z. Azaki, J. Dumon, N. Meslem, A. Hably, and P. Susbielle, "Modelling and control of a tethered drone for an AWE application", in *ICCAD 2022 - 6th International Conference on Control, Automation and Diagnosis*, Lisbon, Portugal: IEEE, Jul. 2022, pp. 1–6. DOI: 10.1109/ICCAD55197.2022.9853858. [Online]. Available: https://hal.science/hal-03759486.

[113] S. Doroudgar, "Static and dynamic modeling and simulation of the umbilical cable in a tethered unmanned aerial system", 2016. [Online]. Available: https://api.semanticscholar.org/CorpusID:113604767.

[114] M. H. Jalali and G. Rideout, "Three-dimensional dynamic modelling and validation for vibration of a beam-cable system", *Mathematical and Computer Modelling of Dynamical Systems*, vol. 27, no. 1, pp. 87–116, 2021. DOI: 10.1080/13873954.2020.1871372. eprint: https://doi.org/10.1080/13873954.2020.1871372. [Online]. Available: https://doi.org/10.1080/13873954.2020.1871372.

[115] D. Cline, *Rayleigh's dissipation function*, Online, Accessed: 2025-03-19, 2025. [Online]. Available: https://phys.libretexts.org/Bookshelves/Classical_Mechanics/Variational_Principles_in_Classical_Mechanics_(Cline)/10%3A_Nonconservative_Systems/10.04%3A_Rayleighs_Dissipation_Function.

[116] S. F. Hoerner, *Fluid-Dynamic Drag: Practical Information on Aerodynamic Drag and Hydrodynamic Resistance*. Midland Park, N.J., 1965.

[117] R. H. Vaz and A. J. Mestel, "Some similarity solutions for three-dimensional boundary layers", *Proceedings of the Royal Society A: Mathematical, Physical and Engineering Sciences*, vol. 475, no. 2229, p. 20 190 267, 2019, Epub 2019 Sep 11, PMID: 31611722, PMCID: PMC6784388. DOI: 10.1098/rspa.2019.0267. [Online]. Available: https://doi.org/10.1098/rspa.2019.0267.

[118] N. Andersson, *Fluid mechanics - mtf053, lecture 16*, Lecture, Chalmers University of Technology, Department of Mechanics and Maritime Sciences, Division of Fluid Mechanics, Gothenburg, Sweden, 2025.

[119] M. Rinaldi, S. Primatesta, and G. Guglieri, "A comparative study for control of quadrotor uavs", *Applied Sciences*, vol. 13, no. 6, p. 3464, 2023. DOI: 10.3390/app13063464. [Online]. Available: https://doi.org/10.3390/app13063464.

[120] M. Esmail, M. Merzban, A. A. M. Khalaf, and H. Hamed, "Comparison of various control techniques applied to a quadcopter", *Journal of Advanced Engineering Trends*, vol. 42, pp. 233–244, Jul. 2023. DOI: 10.21608/jaet.2022.122064.1141.

[121] T. Glick and S. Arogeti, "Control of tethered drones with state and input constraints - a unified model approach", in *2018 International Conference on Unmanned Aircraft Systems (ICUAS)*, Authorized licensed use limited to: Chalmers University of Technology Sweden. Downloaded on January 23, 2025 at 08:29:35 UTC from IEEE Xplore. Restrictions apply., IEEE, Dallas, TX, USA: IEEE, Jun. 2018, Dallas, TX, USA. DOI: 10.1109/ICUAS.2018.8453434.

[122] N. H. Sahrir and M. A. Mohd Basri, "Modelling and manual tuning pid control of quadcopter", in *Control, Instrumentation and Mechatronics: Theory and Practice*, N. A. Wahab and Z. Mohamed, Eds., Singapore: Springer Nature Singapore, 2022, pp. 346–357, ISBN: 978-981-19-3923-5.

[123] B. Douglas, *How do you get a drone to hover? | drone simulation and control, part 2*, https://se.mathworks.com/videos/drone-simulation-and-control-part-2-how-do-you-get-a-drone-to-hover--1539323448303.html, From the series: Drone Simulation and Control, Oct. 2018.

[124] M. McKay, R. Niemiec, and F. Gandhi, "Control reconfiguration for a hexacopter experiencing single rotor failure", in *Proceedings of the 27th International Conference on Adaptive Structures and Technologies (ICAST)*, Rensselaer Polytechnic Institute, Lake George, New York, USA, Oct. 2016.

[125] G. M. Smith. "What is an inertial navigation system?" (2023), [Online]. Available: https://dewesoft.com/blog/what-is-inertial-navigation-system. (accessed: 19.05.2025).

A

Requirement specification

Requirement specification list (R=Requirement, D=Desire)

Nr	Requirement	Justification	Evaluation/verification
1	Transportation		
R1.1	Must be able to be safely transport drone within given dimensions, 1500x2000xoptional* [mm]	Safety, flexibility	Measure model
R1.2	Must be able to transport the base (generator, tether etc.) of given dimensions**	Safety, flexibility	Dimensions of reference systems
2	Modularity (in usage)		
R2.1	Must have a tether length > 70 [m]	Increase coverage/range of usage	Measure tether
D2.1	Should have a tether length > 100 [m]	Increase coverage/range of usage	Measure tether
R2.2	Must have modular payload capabilities	Within given blackboxes, top and bottom mounted	Model assessment
R2.3	Must be able to carry a top mounted payload of 300x300x500 [mm]	Increase the range of usage	Measure model
R2.4	Must be able to carry a bottom mounted payload of 400x400x400 [mm]	Increase the range of usage	Measure model
R2.5	Must be able to carry a combined payload weight of 15 [kg]	Increase the range of usage	Based on chosen systems
R2.6	Must have great maneuverability in z-direction	Perform within its main functionallity	Based on chosen systems
D2.2	Should have great maneuverability in xy-plane	Increase the range of usage	Based on chosen systems, simulations of model
3	Safety		
R3.1	Must be designed with redundancy, such that it is operable with loss of one motor	To ensure safe usage of the product	Based on chosen systems, simulations of model
R3.2	Must contain backup systems such as onboard battery if supply of power is interupted	To ensure safe usage of the product	Engineering assessment
R3.3	Must protect propellers in xy-plane	To ensure safe usage of the product	Engineering assessment
R3.4	Must not be harmful to the user	To ensure safe usage of the product	Engineering assessment
R3.5	Must minimize heat development	To ensure safe usage of the product	Based on chosen systems
4	Competition		
D4.1	Should have a competitive price	To be an order winner	Benchmarking
D4.2	Should have a differentiating factor in the market	Promote customer purchase	Benchmarking
5	Maintenance		
D5.1	Should use as much standardized componets/systems as possible (COTS)	Reduce price, increase availability	Model assessment
R5.1	Must in most cases be maintainable on site	Increase availability of drone (decrease complexity and time)	Engineering assessment
R5.2	Must have sparse maintenance	Increase continous usage	Based on chosen systems
6	Weight		
D6.1	Should have a low drone weight	No unnecessary limitation of payload	Model assessment
D6.2	Should have a low tether weight	No unnecessary limitation of payload	Model assessment
7	Reliability/Robustness		
R7.1	Must have disturbance free information exchange	To minimize risk for loss of communication with drone, for safety	Based on chosen systems
R7.2	Must have high speed data exchange (through tether)	Reliable and improved range of usage	Based on chosen systems
R7.3	Must be able to get power supplied from (COTS) power supply	Accessibility and price	Based on chosen systems
D7.1	Should meet Saab quality standards	Durability and reliability in unity with present product range, to be competitive	Based on chosen systems/materials
R7.4	Must be designed with redundancy, such that it is operable with loss of one motor	Increase continous usage	Based on chosen systems, simulations of model
D7.2	Should have tether mounted close to drones CoG	Stability	Model assessment
8	Environment		
D8.1	Should give away minimal noise	Not disturb people, wildlife etc.	Based on chosen systems
R8.1	Must be operable in harsh environments	Operate in, and withstand harsh weather	Based on chosen systems, simulations of model
R8.2	Must be operable in AECTP-230, zones A3, C0***	Increase the range of usage, and to ensure proper functionality of the product	Based on chosen systems
D8.2	Should be operable in AECTP-230, zones A1, A2, A3, C0, C1, C2, M1, M2, M3****	Increase the range of usage, and to ensure proper functionality of the product	Based on chosen systems
R8.3	Must be operable under continous wind conditions, including the occurrence of strong gusts	Increase the range of usage, and to ensure proper functionality of the product	Simulations of model
9	Life in service		
D9.1	Should achieve a long service life	Increased competitiveness and reliability	Based on chosen systems
10	Material		
R10.1	Must have weather resistant materials (water resistant, wind resistant, etc.)	Ensure proper functionality of the product in a wide range of applications	Based on chosen systems
D10.1	Should use renewable/environmental friendly materials	To achieve SDG (sustainable development goals)	Based on chosen systems
11	Ergonomics		
D11.1	Should promote comportable and efficient handling	To increase user friendliness of product	Engineering assessment
12	Deployment/Retraction/Landing		
R12.1	Must have fast deployment capabilities	Fast to operation for coverage, increased range of usage	Simulations of model
R12.2	Must be able to deploy from and land on uneven terrain (non-leveled base rotated along its width)	Increase the range of usage environments	Simulations of model
R12.3	Must have fast retraction capabilities	Safety, flexibility	Theoretical assessment
R12.4	Must be able to land in case of tethered communication failure (tether breaks)	For safety if connection is lost	Based on chosen systems
13	Manufacturing		
D13.1	Should be able to be produced by common manufacturing processes	Reduce costs and time-to-market	System assessment
D13.2	Should be able to source parts locally	Reduce costs and time-to-market	System assessment
14	Geometry		
R14.1	Must dimension drone to fit within 1500x2000xoptional* [mm] after it has landed	Safety of drone	Measure model
R14.2	Must dimension drone to be within the given 1500x2000xoptional* [mm] footprint in 1 direction, whilst landing, not considering propellers	Available space at landing	Measure model
D14.1	Should have a minimized footprint whilst deployed	To not be to conspicuous and disturb	Measure model
15	Legal		
D15.1	Must secure data output from system, from data breach	Protect the data of stakeholders	Based on chosen systems
16	Other		
D16.1	Should minimize heat development	Minimize energy loss	Based on chosen systems
R16.1	Must not obstruct mounted payload to a higher degree	Increase the range of usage	Based on chosen systems/design

*) "optional" is based on the total available height during transportation (the optional height of the drone + the optional height of the top of the base have a combined limitation)
**) 2000x1500xoptional* on top of 1100x1500x600 [mm]
***) AECTP = Allied Environmental Conditions and Test Publications. Zones correspond to a total temperature range of -19 to 39 [°C], and a relative humitidy of 43 to 100 [%]
****) AECTP = Allied Environmental Conditions and Test Publications. Zones correspond temperature range of -46 to 49 [°C], and a relative humitidy of 3 to 100 [%]

B

Final iteration

HEXACOPTER CONFIGURATION 2 (3-BLADED FOLDING PROPELLERS)

AVAILABLE PROPELLER SIZE - ANY YAW-ANGLE		OPTIONAL COMMENT:
Propeller size (inch):	25.31	

THRUST DEMAND (FROM LAST ITERATION)		
Thrust demand (kg/motor):	11.168	*2:1 thrust-to-weight*

COTS PROPELLER		
Propeller model:	KDE-CF245-TP	
Radius (mm):	311.15	
Weight (prop) (g):	104.7	
Propeller adapter model:	KDE-TPAHL-ML	
Propeller adapter weight (g):	40	
Total propeller weight (g):	144.7	

MOTOR-PROPELLER MATCH		
# Arms/rotors:	6	
Motor (recommended for propeller):	KDE8218-120kV	
Thrust (g):	13939	*Maximum estimated thrust at sea-level*
Efficiency (g/W):	4.22	*Estimated based on power calculations*
Motor weight (g):	845	*Wires/Bullets included*
Voltage (V):	50.4	
Current (A):	65.54	*P = I/A*
Current @hover @weight (A):	15.962	*Current @hover weight from previous iteration*
	7727 & 5224 g thrust	*Interpolated between these*
	5584 g req.	*With initial required thrust*

CURRENT LOOP ON SEPARATE SHEETS (WITH UPDATED WEIGHT)

ESC | BATTERY		
ESC:	KDE-UAS95HVC	
ESC current rating (A):	95	*With a peak of 165 A (5 s)*
ESC weight (g):	114	*Including wires/bullets*
LiPo:	6-12S	*# of cells, ≈ 3.7 - 4.2 V/cell*
Battery size needed (mAh):	9004.5	
Reference battery:	Battery Pilotix Lipo 6S 16000mAh 60C XT90	
Required battery number of cells (S):	12	
Reference battery voltage (V):	44.4	*Rated*
Reference battery size (mAh):	16000	
Reference battery weight (g) for correct S:	3400.0	*In series*
Battery weight (total) (g):	2172.0	*Includes difference between battery rated- and motor voltage*

WEIGHT		
Power required (kW):	19.8	*@max thrust. Only considering motor power, other is disregarded*
Tether weight (g):	3352.8	
Arm weight (g):	602.0	
Motor, propeller, ESC weight (g):	6622.2	
Propeller protection weight (g):	628.8	

TOTAL WEIGHT | THRUST DEMAND | DISK LOADING		
Weight (total) (kg):	36.444	
Thrust demand (kg/rotor):	12.148	
Disk loading (N/m^2):	195.91	*Lower is considered more efficient/stable*

SUFFICIENCY (for set thrust-to-weight ratio)

Non-coaxial:	Yes	
Extra thrust required (%):	Sufficient (+14.74%)	
Extra weight capabilities/margin (kg):	5.37	*Using set thrust-to weight ratio*

POWER SUPPLY

Min. power required (kW):	19.8	
Min. power req. @power supply (kW):	21.96	
Power-supply:	WINCO WL22000VE-03/C 19000W	
Running power (kW):	19	
Peak power (kW):	22	
Amount, n:	1	$n \in Z \wedge n \geq 1$
Peak power (total) (kW):	22	
Runtime (h) @50% load:	8	*50% load is more than 50% throttle*
Power supply width (mm):	732.8	
Power supply length (mm):	1092.2	
Power supply height (mm):	732.8	
Fit within base dimensions?	Yes	*Height considered as non-limiting*
Fit within base in practice:	Yes	*Can only fit ONE power supply*

SUFFICIENT THRUST, PEAK POWER, AND POWER SUPPLY FIT WITHIN BASE

Non-coaxial:	Yes	*Sufficient solution*

WEIGHT INPUT		OPTINAL COMMENT / ADDITIONAL UNIT
Weight (g)		
Fixed:		
Payload:	15000	*INS considered part of this*
Tether (air module)*:	4300	
IMU:	150	
Flight controller:	75	
Frame (base chassis, feet):	1541	
Additional weight*:	2000	
Total:	23066	
Variable:		
Tether (cable)*:	2900	/100m (for 12kW output)
or Tether average:	241.67	/(100m*1Kw)
Propeller protection*:	0.34	/1 mm rotor radius * # of rotors
Frame (arm config 1/2)*:	100.33	/arm (Foldable prop)
Frame (arm config 3/4):	52.71	/arm (Non-foldable prop)
ESC:	*In table*	
Motor:	*In table*	
Propeller:	*In table*	
Battery weight:	*In table*	

**) Updated after previous iterations for increased accuracy*

INPUT PARAMETERS	
Tether length (m):	70
Flight time (min):	5
Thrust-to-weight ratio:	2:1
Propeller protection (y/n):	y
Additional weight (kg):	2
Payload weight (kg):	15
AC-to-DC converter efficiency:	0.95
DC-to-DC converter efficiency:	0.95
Base width (mm):	1100
Base length (mm):	1500

ITERATION OF CURRENT @HOVER (2:1 THRUST-TO-WEIGHT)

STOP CONDITION: ΔWEIGHT ≤ 0.05 %

WEIGHT 1	Non-coaxial hexacopter configuration 2
Weight (total) (kg):	36.55

CURRENT 2		
Current @hover @new weight (A):	18.075	*Only look at 2:1 thrust-to-weight ratio (hover at 50% thrust)*
Values in performance data:	7227 & 5224 g thrust 6092 g req.	*Interpolated for increased accuracy*

Stop condition is lowered for accuracy

WEIGHT 2		WEIGHT DIFFERANCE	ΔWEIGHT > 0.05 % -> CONTINUE
Weight (total) (kg):	36.452	Weight difference (%):	0.27

CURRENT 3		
Current @hover @new weight (A):	18.009	*Only look at 2:1 thrust-to-weight ratio (hover at 50% thrust)*
Values in performance data:	7227 & 5224 g thrust 6076 g req.	*Interpolated for increased accuracy*

Stop condition is lowered for accuracy

WEIGHT 3		WEIGHT DIFFERANCE	ΔWEIGHT ≤ 0.05 % -> STOP
Weight (total) (kg):	36.444	Weight difference (%):	0.02

C

Motor-propeller performance data sheet

MOTOR VERSION	VOLTAGE LiPO [V]	PROPELLER SIZE	THROTTLE RANGE	AMPERAGE [A]	POWER INPUT [W]	[HP]	THRUST OUTPUT [g]	[N]	[lb]	EST. THRUST AT SEALEVEL* [g]	[N]	[lb]	RPM [rev/min]	TORQUE [Nm]	Efficiency [g/W]
KDE8218-120kV	50.4V [12S]	24.5" x 8.1 TRIPLE-EDN (KDE)	25.00%	3.3	164	0.22	1714	16.82	3.78	1880	18.44	4.15	1980	0.57	10.47
			37.50%	6.8	344	0.46	3065	30.07	6.76	3362	32.98	7.41	2640	0.97	8.92
			50.00%	12.5	632	0.85	4764	46.73	10.51	5224	51.25	11.52	3270	1.52	7.54
			62.50%	19.7	993	1.33	6590	64.64	14.53	7227	70.89	15.94	3830	2.09	6.64
			75.00%	30.2	1523	2.04	8668	85.03	19.12	9506	93.25	20.96	4410	2.73	5.69
			87.50%	44.6	2250	3.02	10888	106.81	24.01	11940	117.14	26.33	4970	3.52	4.84
			100.00%	56.9	2867	3.84	12711	124.69	28.03	13939	136.75	30.74	5400	4.17	4.43

Figure C.1: KDE8218-120 Kv motor-propeller performance

Parameter	**Value**
K_v (Motor Velocity Constant)	120 RPM/V
K_t (Motor Torque Constant)	0.0796 Nm/A
K_m (Motor Constant)	0.3883 Nm/$\sqrt{\text{W}}$
Maximum Continuous Current*	110 A (180 s)
Maximum Continuous Power*	5695 W (180 s)
Voltage Range	22.2 V (6S LiPo) – 60.9 V (14S LiHV)
I_0 (@10V)	0.8 A
R_m (Wind Resistance)	0.042 Ω
Stator Poles	24 (24S28P, HE)
Magnetic Poles	28 (24S28P, HE)
Bearings	Triple, 6901-2RS/7901C/7001C
Mount Pattern	M5 × ∅40 mm, M6/M5 × ∅55 mm
Stator Class	8218, 0.2 mm Japanese
Shaft Diameter	∅10 mm (∅12 mm Internal)
Shaft Length	9.5 mm
Motor Diameter	∅89 mm
Motor Rotor Inertia	3.260 kg·cm^2
Motor Length	54.2 mm
Motor Weight	760 g (845 g with Wires/Bullets)
Propeller Blade Size	Up to 30.5”-TP (27.5”-TP Maximum on 14S)
Motor Advance Timing	22° – 30°
Motor Drive Frequency	16 – 32 kHz

Table C.1: Motor specifications.

D

Calculations of projected area

x- or y-direction

The area of the first rectangle, A_1, is made up of the tip-to-tip width of the drone, together with the height of the propeller protection (which is assumed to be 40 [mm]).

$$A_1 \approx 2033.3 * 40 = 81332 \text{ mm}^2$$

The area, A_2, consists of the arm-tip to arm-tip distance, and height of the arm.

$$A_2 \approx 1411 * 30 = 42330 \text{ mm}^2$$

The area, A_3, is made up of the diameter of the central chassis cylinder, together with the vertical distance between the arms and the underside of the chassis cylinder.

$$A_3 \approx 600 * 30 = 18000 \text{ mm}^2$$

The rectangle with area A_4 is the averaged width of the tether air module, calculated as $(302 + 200)/2 = 251$, times the height of the module.

$$A_4 \approx 251 * 68 = 17068 \text{ mm}^2$$

The area A_5 utilizes the projected area of the three legs, together with a fourth (horizontally oriented) rectangle that aims to encapsulate the size of the tether-to-body attachment.

$$A_5 \approx 4 * (498 * 30) = 59760 \text{ mm}^2$$

This results in a total projected area in the x- or y-direction, A_{xy}.

$$A_{xy} \approx 218508 \text{ mm}^2 \approx 0.2185 \text{ m}^2$$

z-direction

The area of the central circle, A_1, uses a diameter that is aimed to hold the size of payloads given their black-boxes, with addition to some extra margins.

$$A_1 \approx \pi * (600/2)^2 \approx 282743 \text{ mm}^2$$

The area, A_2, is based on the length and diameter of the arm, times the number of arms.

$$A_2 \approx 6 * (405.5 * 30) = 72990 \text{ mm}^2$$

The area, A_3, consists of the diameter of the motor, times the number of motors.

$$A_3 \approx 6 * (\pi * (89/2)^2) \approx 37327 \text{ mm}^2$$

This results in a total projected area in the z-direction, A_z.

$$A_z \approx 393060 \text{ mm}^2 \approx 0.3930 \text{ m}^2$$

E

Beaufort Wind Scale

Force	m/s	Description	On Land	At Sea
0	<0.4	Calm	Smoke rises vertically	Sea like a mirror
1	0.4–1.3	Light Air	Smoke drifts, vanes still	Ripples, no foam
2	1.8–3.0	Light Breeze	Leaves rustle	Small wavelets
3	3.0–4.5	Gentle Breeze	Flags extend, twigs move	Large wavelets
4	4.9–7.2	Moderate Breeze	Small branches sway	Small waves, whitecaps
5	7.1–9.6	Fresh Breeze	Small trees sway	Moderate waves, many whitecaps
6	9.9–13.2	Strong Breeze	Large branches move	Large waves, foam streaks
7	13.2–14.9	Near Gale	Trees sway, hard to walk	Sea heaps up, foam streaks
8	14.9–18.1	Gale	Twigs break, walking difficult	High waves, blowing foam
9	18.6–21.6	Strong Gale	Damage possible, branches break	Rolling seas, dense foam
10	21.8–25.2	Storm	Trees uprooted	Very high waves, sea rolls
11	25.4–29.0	Violent Storm	Widespread damage	Exceptionally high waves
12	≥29.3	Hurricane	Extreme destruction	Enormous waves, spray fills air

F

Simulation performance Comparison Using RMSE and Mean State Values for varying N_t

Parameter	**Unit**	$N_t = 1$	$N_t = 2$	$N_t = 3$	$N_t = 4$
x	m	-5.141e-03	-5.146e-03	-5.143e-03	-5.144e-03
y	m	-4.709e-04	-4.678e-04	-4.658e-04	-4.660e-04
z	m	72.543	72.543	72.543	72.543
ϕ	rad	-2.742e-06	-3.968e-06	-3.729e-06	-4.029e-06
θ	rad	2.963e-03	2.977e-03	2.976e-03	2.978e-03
ψ	rad	3.568e-05	3.513e-05	3.512e-05	3.508e-05
$\sum T$	N	75.543	75.544	75.544	75.544
F_t	N	75.424	75.426	75.426	75.426
P_{sys}	W	5593	5593	5593	5593

Table F.1: Mean values of state and output variables for varying N_t

Parameter	**Unit**	$N_t = 1$	$N_t = 2$	$N_t = 3$
x	m	1.1071e-05	1.3959e-05	5.739e-06
y	m	1.9825e-05	9.7987e-06	6.4259e-06
z	m	1.9688e-06	9.4436e-07	1.358e-06
ϕ	rad	3.1792e-06	2.0178e-06	1.2743e-06
θ	rad	3.6907e-05	1.8487e-05	1.271e-05
ψ	rad	1.6788e-06	8.6202e-07	5.3632e-07
$\sum T$	N	5.9848e-04	3.1939e-04	5.7948e-04
F_t	N	5.7216e-03	2.3528e-03	2.1699e-03
P_{sys}	W	1.3564e-02	7.3588e-03	1.3294e-02

Table F.2: Root Mean Square Error (RMSE) of state and output variables for $N_t = 1$–3, relative to the reference model ($N_t = 4$)

G

Open–loop controller vs closed–loop controller

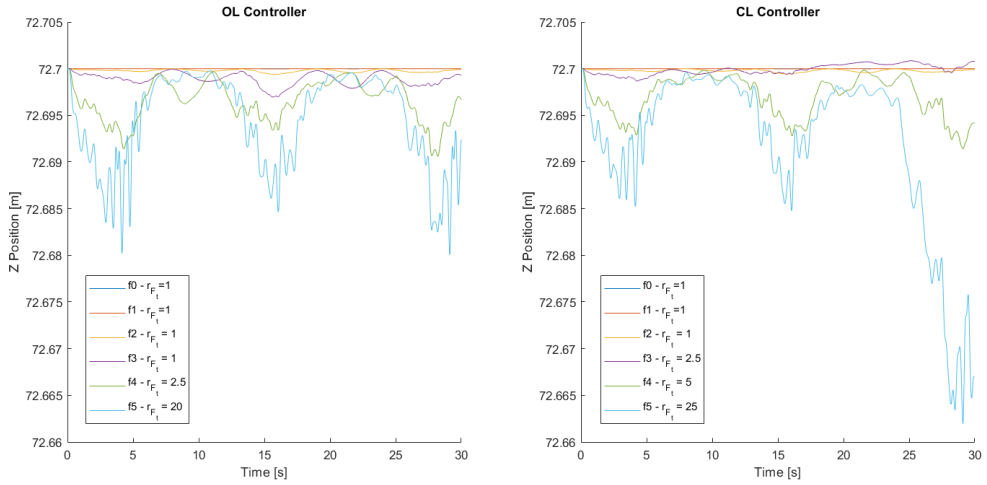

Figure G.1: Simulation z-position results at the lowest tension levels that maintain system stability for both open-loop and closed-loop controllers.

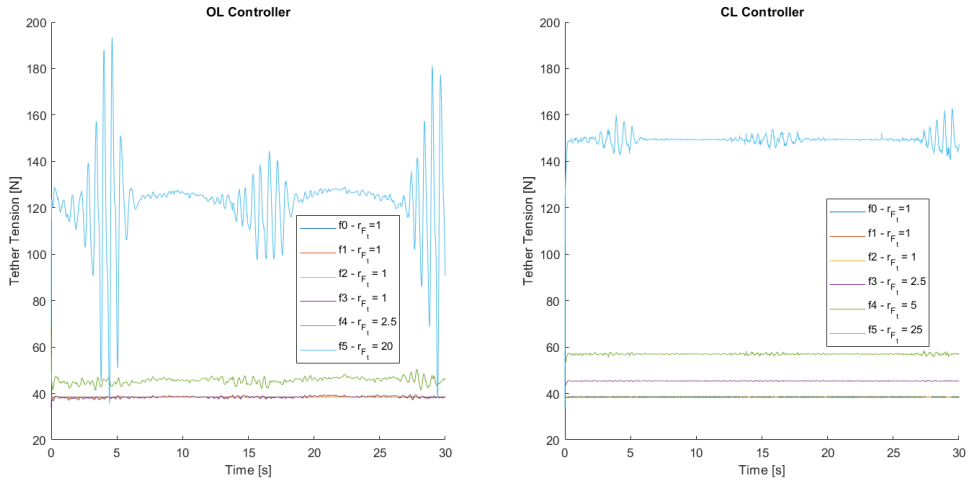

Figure G.2: Simulation tether tension F_t results at the lowest tension levels that maintain system stability for both open-loop and closed-loop controllers.

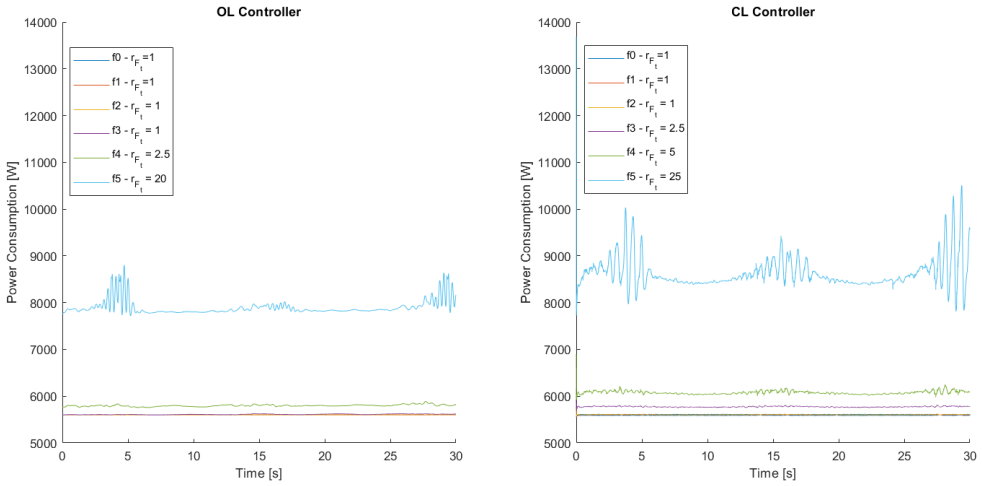

Figure G.3: Simulation Power consumption P_{sys} results at the lowest tension levels that maintain system stability for both open-loop and closed-loop controllers.

H

Requirement fulfillment

Requirement specification fulfillment (R=Requirement, D=Desire)

Nr		Requirement	Evaluation/verification	Fulfillment	Reference
	1	Transportation			
R1.1		Must be able to be safely transport drone within given dimensions, 1500x2000xoptional* [mm]	Measure model	Fulfilled	Sec 4.5
R1.2		Must be able to transport the base (generator, tether etc.) of given dimensions**	Dimensions of reference systems	Fulfilled	Sec 4.5.4
	2	Modularity (in usage)			
R2.1		Must have a tether length > 70 [m]	Measure tether	Fulfilled	Sec 4.5
D2.1		Should have a tether length > 100 [m]	Measure tether	Fulfilled	Sec 4.5
R2.2		Must have modular payload capabilities	Model assessment	Fulfilled	Sec 4.5
R2.3		Must be able to carry a top mounted payload of 300x300x500 [mm]	Measure model	Fulfilled	Sec 4.5
R2.4		Must be able to carry a bottom mounted payload of 400x400x400 [mm]	Measure model	Fulfilled	Sec 4.5
R2.5		Must be able to carry a combined payload weight of 15 [kg]	Based on chosen systems	Fulfilled	Sec 4.5
R2.6		Must have great maneuverability in z-direction	Based on chosen systems	Fulfilled	Sec 4.5
D2.2		Should have great maneuverability in xy-plane	Based on chosen systems	Fulfilled	Sec 4.5
	3	Safety			
R3.1		Must be designed with redundancy, such that it is operable with loss of one motor	Simulations of model	Fulfilled	Sec 4.5 & 8.3
R3.2		Must contain backup systems such as onboard battery if supply of power is interupted	Engineering assessment	Fulfilled	Sec 4.4
R3.3		Must protect propellers in xy-plane	Engineering assessment	Fulfilled	Sec 3.5.5 & 4.2.2
R3.4		Must not be harmful to the user	Engineering assessment	Fulfilled	Sec 3.5.5 & 4.2.2
R3.5		Must minimize heat development	Based on chosen systems	Fulfilled	Sec 4.5.5
	4	Competition			
D4.1		Should have a competitive price	Benchmarking	Fulfilled	Sec 4.5.2
D4.2		Should have a differentiating factor in the market	Benchmarking	Inconclusive	Sec 4.5.2
	5	Maintenance			
D5.1		Should use as much standardized componets/systems as possible (COTS)	Model assessment	Fulfilled	Sec 4.5.2
R5.1		Must in most cases be maintainable on site	Engineering assessment	Fulfilled	Sec 4.5.3
R5.2		Must have sparse maintenance	Based on chosen systems	Fulfilled	Sec 4.5.3
	6	Weight			
D6.1		Should have a low drone weight	Model assessment	Fulfilled	Sec 4.4
D6.2		Should have a low tether weight	Model assessment	Fulfilled	Sec 4.2.2
	7	Reliability/Robustness			
R7.1		Must have disturbance free information exchange	Based on chosen systems	Fulfilled	Sec 3.4.1
R7.2		Must have high speed data exchange (through tether)	Based on chosen systems	Fulfilled	Sec 3.4.1
R7.3		Must be able to get power supplied from (COTS) power supply	Based on chosen systems	Fulfilled	Sec 4.4
D7.4		Should meet Saab quality standards	Based on chosen systems/materials	Not evaluated	-
R7.4		Must be designed with redundancy, such that it is operable with loss of one motor	Based on chosen systems, simulations of model	Fulfilled	Sec 4.5 & 8.3
D7.2		Should have tether mounted close to drones CoG	Model assessment	Inconclusive	Sec 5.4.5
	8	Environment			
D8.1		Should give away minimal noise	Based on chosen systems	Not fulfilled	Sec 4.5.5
R8.1		Must be operable in harsh environments	Based on chosen systems, simulations of model	Fulfilled	Sec 4.5.5 & 8.2
R8.2		Must be operable in AECTP-230, zones A3, C0***	Based on chosen systems	Inconclusive	Sec 4.5.5
D8.2		Should be operable in AECTP-230, zones A1, A2, A3, C0, C1, C2, M1, M2, M3****	Based on chosen systems	Not fulfilled	Sec 4.5.5
R8.3		Must be operable under continous wind conditions, including the occurrence of strong gusts	Simulations of model	Fulfilled	Sec 8.2
	9	Life in service			
D9.1		Should achieve a long service life	Based on chosen systems	Fulfilled	Sec 4.5.3
	10	Material			
R10.1		Must have weather resistant materials (water resistant, wind resistant, etc.)	Based on chosen systems	Fulfilled	Sec 4.5.5
D10.1		Should use renewable/environmental friendly materials	Based on chosen systems	Not fulfilled	Sec 4.5.3
	11	Ergonomics			
R11.1		Should promote comportable and efficient handling	Engineering assessment	Not evaluated	-
	12	Deployment/Retraction/Landing			
R12.1		Must have fast deployment capabilities	Simulations of model	Fulfilled	Sec 8.4
R12.2		Must be able to deploy from and land on uneven terrain (non-leveled base rotated along its width)	Simulations of model	Fulfilled	Sec 4.5
R12.3		Must have fast retraction capabilities	Theoretical assessment	Fulfilled	Sec 5.1.3 & 8.4
R12.4		Must be able to land in case of tethered communication failure (tether breaks)	Based on chosen systems	Fulfilled	Sec 4.4
	13	Manufacturing			
D13.1		Should be able to be produced by common manufacturing processes	System assessment	Not evaluated	-
D13.2		Should be able to source parts locally	System assessment	Not evaluated	-
	14	Geometry			
R14.1		Must dimension drone to fit within 1500x2000xoptional* [mm] after it has landed	Measure model	Fulfilled	Sec 4.5
R14.2		Must dimension drone to be within the given 1500x2000xoptional* [mm] footprint in 1 direction, whilst landing, not considering propellers	Measure model	Fulfilled	Sec 4.5
D14.1		Should have a minimized footprint whilst deployed	Measure model	Not fulfilled	Sec 4.5
	15	Legal			
D15.1		Must secure data output from system, from data breach	Based on chosen systems	Fulfilled	Sec 3.4.1
	16	Other			
D16.1		Should minimize heat development	Based on chosen systems	Fulfilled	Sec 4.5.5
R16.1		Must not obstruct mounted payload to a higher degree	Based on chosen systems/design	Fulfilled	Sec 4.5.5

*) "optional" is based on the total available height during transportation (the optional height of the drone + the optional height of the top of the base have a combined limitation)
**) 2000x1500xoptional* on top of 1100x1500x600 [mm]
***) AECTP = Allied Environmental Conditions and Test Publications. Zones correspond to a total temperature range of -19 to 39 [°C], and a relative humitidy of 43 to 100 [%]
****) AECTP = Allied Environmental Conditions and Test Publications. Zones correspond temperature range of -46 to 49 [°C], and a relative humitidy of 3 to 100 [%]

DEPARTMENT OF ELECTRICAL ENGINEERING
CHALMERS UNIVERSITY OF TECHNOLOGY
Gothenburg, Sweden
www.chalmers.se

CHALMERS
UNIVERSITY OF TECHNOLOGY